Universidad
Carlos III de Madrid

TESIS DOCTORAL

Contributions to the improvement of image quality in CBCT and CBμCT and application in the development of a CBμCT system

Autor:
Alejandro Sisniega Crespo

Director:
Juan José Vaquero López

DEPARTAMENTO DE BIOINGENIERÍA E INGENIERÍA AEROESPACIAL

Leganés, 5 de junio de 2013

TESIS DOCTORAL

CONTRIBUTIONS TO THE IMPROVEMENT OF IMAGE QUALITY IN CBCT AND CBμCT AND APPLICATION IN THE DEVELOPMENT OF A CBμCT SYSTEM

Autor: **Alejandro Sisniega Crespo**

Director: **Juan José Vaquero López**

Firma del Tribunal Calificador:

Firma

Presidente:

Vocal:

Secretario:

Calificación:

Leganés, de de

Agradecimientos

Durante estos años que han desembocado en el desarrollo de esta tesis he tenido la suerte de contar con la ayuda y apoyo de un montón de excelentes personas, todas las cuales han aportado su grano de arena.

En primer lugar me gustaría agradecer a Juanjo y a Manolo por la oportunidad que me ofrecieron de entrar en este mundo. Desde ese momento han sabido guiarme y ofrecerme su apoyo en todo momento a la vez que libertad absoluta para proponer ideas y explorar caminos. Es muy difícil encontrar directores de su categoría científica y personal y sin ellos no habría despertado en mí la pasión por la investigación.

En cuanto al LIM, he de decir que no imagino un ambiente mejor en todos los sentidos, es un gustazo contar con estos compañeros, que no son sólo compañeros, sino amigos dispuestos igualmente a echarte un cable en lo que sea o a echarse unas birras entre risas. Todos habéis contribuido a que estos años hayan sido unos de los mejores. Empezando por mis principios en el LIM, voy a intentar recordar a todos. Edu, con el que he compartido mil cosas, desde sudores Suinseros hasta las playas de Costa Rica (ya te comerás una rima *ca…*). Judit, que me ha soportado estoicamente como compañero de mesa desde el principio y en lugar de matarme todavía me recibe con una sonrisa todos los días. Juanolas, hijo, sabes que siempre apoyaré tu cruzada taurina (por cierto, cómo nos ha quedado el FMT-CT, muy coorrecto, ¿eh?). Vero, que siempre está dispuesta a echar una mano y que se acordará de los colegas cuando conquiste el mundo. Josete y Gus, que están perdidos por esas tierras de Mordor, pero siempre tienen un rato para los amiguetes cuando pasan por aquí. Alvarico que siempre sabe poner su toque especial cuando quedamos. Angelico, que estoy en el autobús de camino… ponme otra. Tra, esa jefa que lo mismo es capaz de dirigir el labo con mano de hierro como de darlo todo en la Santina. Cris, con su *swing*, su karaoke, y con la que es imposible aburrirse aunque la conozca desde hace mil años. Gonzalo, gran amiguete con el que mantener una conversación siempre es un placer. Chema, friqueando juntos desde el Eurielec. Yasser, ¿te acuerdas cuando éramos jóvenes allá por el CASEIB del 2009? (Hay pudghpo, hamón con pan…). Javi, sin el que la vida sería mucho más aburrida, con sus chistes, su Bruno y sus cosas. Joost, ese holandés que siempre habla de cerebros, que tan bien me cae y que tan buenos consejos me da. Quique, que aunque ahora esté en las antípodas, dejó una amistad que perdura. Eu, que aunque parezca el mal, en realidad es un cacho de pan. Fidel, ese andaluz sin acento que tan buen amigo es. María, un amor de persona y la mejor guía de Montreal, aunque se vuelva nazi cuando ve las noticias. Susana, que acaba de llegar pero ya parece una amiga de toda la vida. Marco, compañero inseparable en los terrenos de juego. Juan, que reconstruye lo que quieras con el 5 % de los datos y es un compañero de despacho insuperable. Rigo, detrás de ese cubano de Cartagena con melena al viento y gusto gótico, hay un gran tipo. Mónica, compañera CTera de la que he aprendido un montón. Claudia y Aurora, que aunque os hayan separado y tengáis cara de buenas seguís siendo el dúo con más peligro del LIM. Juanjo pequeño, tu paso por el LIM ha dado pie a una amistad que se mantiene. Crespillo y Martín, que se han encargado de llevar el legado del LIM allende los mares. Eva, la chica de Minaya, ¡más buena gente no se puede ser! Paula, la chica más dulce del labo, que gobierna la reso como nadie. Lorena, que opera una rata a corazón abierto como quién pide una caña. Sandra, una gran compi desde el primer día que la conocí y mi técnico favorita. Ángela, que aunque estés en Francia se te echa de menos por aquí. Yolanda y Ángel, que siempre están por ahí abajo, pero dejan su huella en todos. Natalia, que te seguiremos viendo por la Santina. Iván, el tipo más agradable que he conocido en mi vida. Diego, que ha sabido conectar desde el principio. Ana y Asier, los dos primeros que sufren mi intento de dirección con pasmosa entereza, además de ser dos personas de lo más majo y una caja de sorpresas, que lo mismo una surfea que el otro toca reggae. Elena, esa médico nuclear con curiosidad por todo y siempre dispuesta echar un cable. Santi, un gran tipo para currar, echar un partidillo, una caña, o lo que sea. Marisa, esa jefa bio super maja. Javi Pascau, un gran tío del que siempre he podido aprender. Jorge, que acaba de llegar pero ya ha demostrado ser de lo más enrollado. También agradecérselo a toda la gente del buffer que he conocido menos, pero que también se merecen estar por aquí.

Para cerrar el capítulo del LIM, me gustaría recordar a Santi y Carmen, dos grandes personas que se nos fueron antes de tiempo dejando un gran vacío que nunca seremos capaces de llenar.

El trabajo de estos años tampoco habría sido posible sin la colaboración y amistad de la gente de la UCM (Jose Manuel, Joaquín, Samuel, Elena, Esteban, Jacobo, Paula, Vicky, Vadym, Richi, Maylin…) y sin la gente de Suinsa (ahora Sedecal).

Me gustaría mencionar también a la gente que hizo que en las estancias en el extranjero me sintiera como en casa: Laura, Antonio, Irene, Pepe y Andrea y Michel (guys, you're awesome).

Un lugar muy especial en este apartado de agradecimientos es para todos mis amigos de toda la vida (esos Goofys) que sois con los que mejor me lo he pasado desde que tenemos catorce años y a vosotros me une una amistad que pervivirá pase lo que pase. Vosotros sabéis que somos como hermanos.

Por último, pero no por ello menos importante, he de agradecer todo lo que me ha dado a Esther, que siempre me ha aguantado, apoyado y alegrado cuando lo he necesitado (y sin casi nunca mandarme a dormir al sofá) y a la que quiero con locura… y a toda mi familia, especialmente Laura y mis padres que son el eje de mi vida y los que me han enseñado a ser como soy y siempre han estado y estarán ahí pase lo que pase.

I want to thank Dr Boone for giving me the opportunity of joining his lab where I learned a lot from him. He has always been willing to help with anything I ask him. I also want to thank everyone at the UC Davis lab for being really kind and make me feel at home during my time there.

Thanks to Dr Siewerdsen for hosting me at his lab for a whole summer, giving me the chance of working with him and improve my skills, to Wojciech for all his countless hours of mentorship, his good advice and his friendship and to all the people in the lab for making me feel real comfortable during my stay.

Contents

Abstract

During the last years cone-beam x-ray CT (CBCT) has been established as a widespread imaging technique and a feasible alternative to conventional CT for dedicated imaging tasks for which the limited flexibility offered by conventional CT advises the development of dedicated designs. CBCT systems are starting to be routinely used in image guided radiotherapy; image guided surgery using C-arms; scan of body parts such as the sinuses, the breast or extremities; and, especially, in preclinical small-animal imaging, often coupled to molecular imaging systems.

Despite the research efforts advocated to the advance of CBCT, the challenges introduced by the use of large cone angles and two-dimensional detectors are a field of vigorous research towards the improvement of CBCT image quality. Moreover, systems for small-animal imaging add to the challenges posed by clinical CBCT the need of higher resolution to obtain equivalent image quality in much smaller subjects.

This thesis contributes to the progress of CBCT imaging by addressing a variety of issues affecting image quality in CBCT in general and in CBCT for small-animal imaging (CBμCT).

As part of this work we have assessed and optimized the performance of CBμCT systems for different imaging tasks. To this end, we have developed a new CBμCT system with variable geometry and all the required software tools for acquisition, calibration and reconstruction. The system served as a tool for the optimization of the imaging process and for the study of image degradation effects in CBμCT, as well as a platform for biological research using small animals. The set of tools for the accurate study of CBCT was completed by developing a fast Monte Carlo simulation engine based on GPUs, specifically devoted to the realistic estimation of scatter and its effects on image quality in arbitrary CBCT configurations, with arbitrary spectra, detector response, and antiscatter grids. This new Monte Carlo engine outperformed current simulation platforms by more than an order of magnitude.

Due to the limited options for simulation of spectra in microfocus x-ray sources used in CBμCT, we contributed in this thesis a new spectra generation model based on an empirical model for conventional radiology and mammography sources modified in accordance to experimental data. The new spectral model showed good agreement with experimental exposure and attenuation data for different materials.

The developed tools for CBμCT research were used for the study of detector performance in terms of dynamic range. The dynamic range of the detector was characterized together with its effect on image quality. As a result, a new simple method for the extension of the dynamic range of flat-panel detectors was proposed and evaluated. The method is based on a modified acquisition process and a mathematical treatment of the acquired data.

Scatter is usually identified as one of the major causes of image quality degradation in CBCT. For this reason the developed Monte Carlo engine was applied to the in-depth study of the effects of scatter for a representative range of CBCT embodiments used in the clinical and preclinical practice. We estimated the amount and spatial distribution of the total scatter fluence and the individual components within. The effect of antiscatter grids in improving image quality and in noise was also evaluated. We found a close relation between scatter and the air gap of the system, in line with previous results in the literature. We also observed a non-negligible contribution of forward-directed scatter that is responsible to a great extent for streak artifacts in CBCT. The spatial distribution of scatter was significantly affected by forward scatter, somewhat challenging the usual assumption that the scatter distribution mostly contains low-frequencies. Antiscatter grids showed to be effective for the reduction of cupping, but they showed a much lower performance when dealing with streaks and a shift toward high frequencies of the scatter distributions.

Resumen

A lo largo de los últimos años, el TAC de rayos X de haz cónico (CBCT, de "cone-beam" CT) se ha posicionado como una de las técnicas de imagen más ampliamente usadas. El CBCT se ha convertido en una alternativa factible al TAC convencional en tareas de imagen específicas para las que la flexibilidad limitada ofrecida por este hace recomendable el desarrollo de sistemas de imagen dedicados. De esta forma, el CBCT está empezando a usarse de forma rutinaria en varios campos entre los que se incluyen la radioterapia guiada por imagen, la cirugía guiada por imagen usando arcos en C, imagen de partes de la anatomía en las que el TAC convencional no es apropiado, como los senos nasales, las extremidades o la mama, y, especialmente el campo de imagen preclínica con pequeño animal. Los sistemas CBCT usados en este último campo se encuentran habitualmente combinados con sistemas de imagen molecular.

A pesar del trabajo de investigación dedicado al avance de la técnica CBCT en los últimos años, los retos introducidos por el uso de haces cónicos y de detectores bidimensionales son un campo candente para la investigación médica, con el objetivo de obtener una calidad de imagen equivalente o superior a la proporcionada por el TAC convencional. En el caso de imagen preclínica, a los retos generados por el uso de CBCT se une la necesidad de una mayor resolución de imagen que permita observar estructuras anatómicas con el mismo nivel de detalle obtenido para humanos.

Esta tesis contribuye al progreso del CBCT mediante el estudio de usa serie de efectos que afectan a la calidad de imagen de CBCT en general y en el ámbito preclínico en particular. Como parte de este trabajo, hemos evaluado y optimizado el rendimiento de sistemas CBCT preclínicos en función de la tarea de imagen concreta. Con este fin se ha desarrollado un sistema CBCT para pequeños animales con geometría variable y todas las herramientas necesarias para la adquisición, calibración y reconstrucción de imagen. El sistema sirve como base para la optimización de protocolos de adquisición y para el estudio de fuentes de degradación de imagen además de constituir una plataforma para la investigación biológica en pequeño animal.

El conjunto de herramientas para el estudio del CBCT se completó con el desarrollo de una plataforma acelerada de simulación Monte Carlo basada en GPUs, optimizada para

la estimación de radiación dispersa en CBCT y sus efectos en la calidad de imagen. La plataforma desarrollada supera el rendimiento de las actuales en más de un orden de magnitud y permite la inclusión de espectros policromáticos de rayos X, de la respuesta realista del detector y de rejillas *antiscatter*.

Debido a las escasas opciones ofrecidas por la literatura para la estimación de espectros de rayos X para fuentes microfoco usadas en imagen preclínica, en esta tesis se incluye el desarrollo de un nuevo modelo de generación de espectros, basado en un modelo existente para fuentes usadas en radiología y mamografía. El modelo fue modificado a partir de datos experimentales. La precisión del modelo presentado se comprobó mediante datos experimentales de exposición y atenuación para varios materiales.

Las herramientas desarrolladas se usaron para estudiar el rendimiento de detectores de rayos tipo flat-panel en términos de rango dinámico, explorando los límites impuestos por el mismo en la calidad de imagen. Como resultado se propuso y evaluó un método para la extensión del rango dinámico de este tipo de detectores. El método se basa en la modificación del proceso de adquisición de imagen y en una etapa de postproceso de los datos adquiridos.

El simulador Monte Carlo se empleó para el estudio detallado de la naturaleza, distribución espacial y efectos de la radiación dispersa en un rango de sistemas CBCT que cubre el espectro de aplicaciones propuestas en el entorno clínico y preclínico. Durante el estudio se inspeccionó la cantidad y distribución espacial de radiación dispersa y de sus componentes individuales y el efecto causado por la inclusión de rejillas *antiscatter* en términos de mejora de calidad de imagen y de ruido en la imagen. La distribución de radiación dispersa mostró una acentuada relación con la distancia entre muestra y detector en el equipo, en línea con resultados publicados previamente por otros autores. También se encontró una influencia no despreciable de componentes de radiación dispersa con bajos ángulos de desviación, poniendo en tela de juicio la tradicional asunción que considera que la distribución espacial de la radiación dispersa está formada casi exclusivamente por componentes de muy baja frecuencia.

Las rejillas *antiscatter* demostraron ser efectivas para la reducción del artefacto de *cupping*, pero su efectividad para tratar artefactos en forma de línea (principalmente formados por radiación dispersa con bajo ángulo de desviación) resultó mucho menor. La inclusión de estas rejillas también enfatiza las componentes de alta frecuencia de la distribución espacial de la radiación dispersa.

Motivation and Objectives

During the last decade, cone-beam CT (CBCT) has experienced an important proliferation in clinical and preclinical imaging scenarios [1] mainly as a standalone technique in applications requiring structural information or as a complement to other imaging modalities. For this reason a range of CBCT systems has been developed using a variety of embodiments and geometrical configurations adapted to application-specific imaging scenarios such as high-resolution small-animal imaging (CBμCT) [2-4], interventional C-arm imaging [5-6], musculoskeletal extremities imaging [7-8], otolaryngology imaging [9-11], breast imaging [12-13] and radiotherapy in-line imaging [14-15].

In parallel with the development of CBCT technology and its establishment as a reliable imaging technique, a large number of animal models for human disease have arisen, with widespread use for the investigation of new drugs or disease evolution. The needs of studying biological processes using animal models, and to do so in a non-invasive way, have encouraged the advance of molecular imaging techniques in the preclinical environment, with the design of high-resolution systems suitable for imaging of small-animals. Among the preferred molecular imaging techniques for small-animal studies are the Positron Emission Tomography (PET) [16] and the Single Photon Emission Computed Tomography (SPECT) [17]. Besides PET and SPECT, optical imaging techniques and, in particular, Fluorescence Diffuse Optical Tomography (FDOT) has been a subject of intensive research during the last few years owing to their promising capabilities for the development of new probes aimed at biological targets [18-19] and for the simplicity of its hardware and the fact that no radioactive tracers need to be used. While being essential for studying biological processes, molecular imaging techniques lack anatomical information that is of paramount importance for the location of the molecular data within the body and, in some cases, for the improvement of the information provided by molecular imaging. That is the case for attenuation correction in PET or SPECT [20-21] or, more challenging, the inclusion of accurate anatomical data as prior information for mathematical reconstruction algorithms in FDOT [22-23].

Anatomical information complementary to molecular data is usually obtained by means of CBCT due to the degree of development experienced by the technique, the relatively low-cost of the technology, and the ease of integration when compared to other anatomical imaging modalities, such as Magnetic Resonance Imaging (MRI) which is also the subject of intensive research [24].

Despite the significant advancements experienced by CBCT in the last years, the differences with conventional CT pose major challenges for the improvement of image quality and the reduction of dose in these kinds of systems. The use of two-dimensional detectors fixes a large cone angle in the axial direction of the beam, which is the source for increased scatter and for more complicated scatter distributions, as well as inconsistencies of acquired data depending on the acquisition trajectory. The detectors used in CBCT can also be a source of non-idealities, arising, for instance, from the comparatively slower acquisition time of two-dimensional detectors that make motion artifacts more conspicuous; from the more complicated corrections for uniformity equalization; from the presence of defective elements; or from limited dynamic range since CBCT systems usually do not include bow-tie filters.

CBμCT systems for small-animal imaging add to the aforementioned issues the need of ~10-50 fold higher resolution and a larger variety between samples making more impractical the use of bow-tie filters. To achieve such a high resolution value, the pixels of the detector are smaller and the maximum size of the focal spot of the source is more limited, forcing the use of microfocus sources. Since the integrated signal is a function of the pixel area, photon flux and integration time, to achieve similar noise levels, small-animal systems have to either increase the photon flux or the image integration time which, in turn, increases the total acquisition time. The increase of the photon flux is impractical due to the low power delivered by microfocus sources and, therefore, the signal level is usually increased by extending the image integration time and by properly optimizing the system for the particular imaging application. In any case, to obtain comparable noise levels, the dose delivered to the subject will be proportionally larger for small-animal systems.

The main goal of this thesis is to identify key factors degrading image quality in CBCT in general and CBμCT in particular and to study their impact on image quality. Possible mitigation strategies to improve the performance of CBCT systems for a given imaging task and acquisition geometry are also examined.

With all the presented considerations in mind, the specific objectives of this thesis are:

1. To optimize CBμCT systems for the imaging tasks of obtaining basic structural information and more accurate soft-tissue images to be used as *a priori* information for molecular imaging reconstruction methods.
2. To design and build a CBμCT system combined with a FDOT system for the acquisition of inherently registered CBμCT and FDOT data and develop all the tools required for data acquisition, reconstruction and system calibration.
3. To evaluate the performance of the system for the defined protocols in comparison with other previously reported systems validating its use as a tool for the exploration of further factors affecting image quality.
4. To develop new dedicated acquisition and data post-processing techniques to alleviate the effect of the reduced dynamic range of the flat-panel detector.
5. To develop simulation tools that accurately simulate the image acquisition chain in CBμCT and CBCT systems with analytical and Monte Carlo methods using Graphic Processing Units (GPUs) to exploit the parallelization capabilities of the Monte Carlo photon transport process and variance reduction techniques to accelerate the simulation of scatter distributions.
6. To study the properties of scatter and the image degradation caused by it, as a function of the configuration of the system, for generic CBCT embodiments, and to evaluate the potential of classic and Monte Carlo scatter reduction techniques for the mitigation of scatter-induced quality degradation.

The work included in this thesis is framed on one of the lines of research carried out at the Laboratorio de Imagen Médica at the Departamento de Bioingeniería e Ingeniería Aeroespacial of the Universidad Carlos III de Madrid. Part of the work included in chapters 5 and 6 was carried out at the I-Star Laboratory of the Department of Bioengineering of the Johns Hopkins University.

A significant part of the developments presented in this thesis has been or will be integrated into the preclinical high-resolution scanners manufactured and distributed worldwide by Sedecal (Madrid, Spain).

The author of this thesis has been funded by a grant from the FPU program (Formación de Profesorado Universitario, Ministerio de Educación), ref. AP2008-03148.

Outline of the document

The present document is organized in six chapters. Chapter 1 presents an introduction to image formation in x-ray imaging in general and in CT and CBCT in particular, including image reconstruction and common image degradation sources. Chapter 1 finishes with a brief introduction to the simulation of x-ray imaging systems using Monte Carlo techniques.

Chapter 2 presents the design, optimization and assessment of the CBμCT system coupled to the FDOT system. The hardware structure of the system is detailed together with the software developments for the data acquisition. It is also described the implementation of the reconstruction algorithm, using GPUs to reduce its computational burden. The next sections detail the calibration methods, some of them also new to the literature, and the software tools implemented for the calibration of the system. Then a comprehensive description of optimization process for the different imaging tasks is presented, and the last sections evaluate the performance of the individual hardware components of the system and of the complete system.

In chapter 3 the author presents a new method for the extension of the dynamic range of x-ray flat-panel detectors by means of a dual-exposure acquisition and a subsequent data processing stage based on maximum likelihood approach. The performance of the method is assessed theoretically for generic flat-panel detectors, and experimentally for a particular flat-panel detector, evaluating the effect of the dynamic range extension in the quality of planar two-dimensional data and CBCT reconstructed data.

Chapter 4 describes the modification of an empirical x-ray spectrum simulation method for the simulation of spectra generated by microfocus x-ray sources with tungsten anode. The modification method is based on the iterative adjustment of the spectral model to minimize the error between simulated and measured exposure and attenuation data. The new model for microfocus sources is then validated against experimental data for different attenuating materials and x-ray sources.

A new Monte Carlo and analytical simulation engine for CBCT is presented in chapter 5. The simulation engine is based on an existent, GPU based, publicly available code, to which we incorporated an analytical model for the inclusion of arbitrary spectra, detector response and antiscatter grids. The engine was accelerated for the simulation of primary signal by including an analytical model for attenuation measurement. The simulation of scatter was also accelerated by incorporating variance reduction techniques and by modifying the photon tracking process to fit the particular features of GPUs.

Chapter 6 presents a detailed study of the nature, properties and effects of scatter and antiscatter grids in CBCT, for a representative range of configurations ranging from small-animal systems to on-board CBCT systems used in Linear Accelerators for radiotherapy. The study makes use of the accelerated simulation platform described in chapter 5, profiting from the computational power offered by the accelerated engine to span a range of parameters affecting scatter not covered by any previous work in the literature.

1 Principles of x-ray CBCT

1.1 Introduction to x-ray CBCT

The discovery of x-ray radiation by Wilhelm Roentgen in 1895 brought a major advance to medical science, since this technology offered the possibility of visualizing structures inside the body in a non-invasive way. This discovery opened the way to medical imaging techniques by recording the x-ray radiation through an object obtaining a two-dimensional (2D) representation of the attenuation of x-rays within the body, creating x-ray radiography. For a long time x-ray radiography was the only technique available for the inspection of internal anatomy.

Being revolutionary as it was, confirmed by the fact that it is still widely used in medical practice today, x-ray radiography has a major limitation arising from the projection of the 3D structure of the body onto a 2D plane where the different individual structures are superimposed, reducing the visibility of the object of interest.

Tomographic imaging was developed in response to this limitation. In tomography (derived from the word *tomos*, Greek for section) a cross-sectional plane, or slice, of an object is imaged without the disturbance by surrounding structures as in radiography. The outcome of the tomographic imaging process would be equivalent to sectioning the object by the plane of interest and taking a photograph of it.

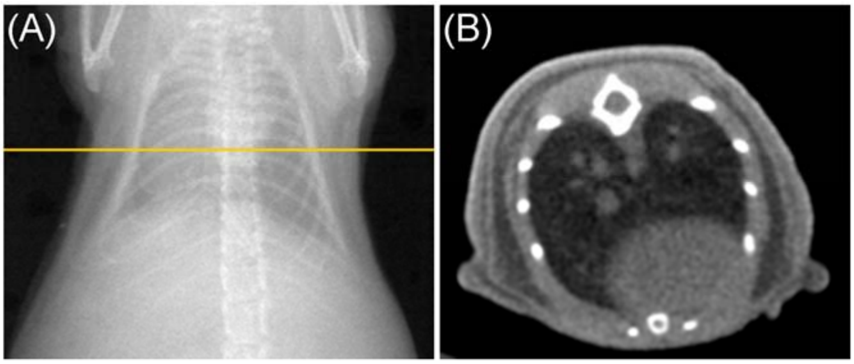

Figure 1.1. 2D radiograph of a mouse chest (A) where the overlap between superimposed structures reduces the visibility that are clearly visible in a CT slice of the same specimen (B). The horizontal line in (A) shows the approximate position for the slice depicted in (B). Data were obtained using the CBμCT system described in chapter 2.

In the particular case of x-ray computed tomography (CT) the physical property displayed in the resulting slice images is the x-ray attenuation coefficient for each site of the object, as compared to the total attenuation of x-rays in radiography. Examples of a conventional radiograph and a tomographic slice for a small-animal are shown in figure 1.1.

The following paragraphs provide a brief overview of the historical development of CT. However, there is a large quantity of literature devoted to the description of CT systems and their historical evolution where the interested reader can obtain a deep insight beyond the scope of this chapter, with dedicated books, such as those by W. Kalender [25], by J. Hsieh [26] or by S. Webb [27]; and dedicated review articles [1, 28].

First attempts for obtaining tomographic images date back to the early years of the twentieth century when several approaches were developed based on acquiring data for different linear movements of the x-ray source and detector, designed in such a way that the plane of interest was the only one focused throughout the complete acquisition. The different datasets were then combined obtaining a focused plane with the superimposed tissues showing as a low frequency blur on top of it. One of the first examples of this kind of systems was the one proposed by Bocage in 1921 [29].

While better than simple radiography, the limitations of systems such as the one by Bocage are obvious, since the blurred data on top of the focused plane reduced the visibility of structures.

In 1940, G. Frank [30] described a device closely resembling the structure of modern CT systems in which he proposed the intuitive concept of extracting information from the internal structures by observing the object from different angles.

However, to obtain accurate, not-blurred images, the early systems lacked the mathematical tools –see section 1.3– as well as the computational power required for the reconstruction of the tomographic data from the set of radiographs (projections from now on) acquired.

The first modern-like CT scanners credited in the literature were developed by two independent researchers almost simultaneously, Allan M. Cormack and Godfrey N. Hounsfield. The former developed a mathematical method for the reconstruction of CT data that was based on different roots as modern reconstruction techniques, not being aware of the work by Radon [31] that described the reconstruction of an object from its line integrals. He tested his method with a dedicated device in 1964.

The work by Hounsfield yielded the first clinical, computer-based x-ray CT scanner, which was developed between 1967 and 1971 and was built at the Central Research Laboratories of EMI, Ltd. in England [32].

From that moment, x-ray CT has undergone a large improvement that can be summarized as a sequence [33-35] of generations each of them introducing new concepts in the development of CT systems.

First generation systems followed the original design of the EMI scanner. This kind of systems made use of a pencil-beam x-ray source opposed to a single detector. The source-detector assembly was linearly moved in steps, recording the x-ray intensity traversing the object at each linear position. Once the whole set of linear positions were obtained, the system performed a rotation movement around the object of e.g. 1 degree. Then a new set of linear translations and measurements were performed and the process continued until a whole rotation around the object was performed. The concept is illustrated in figure 1.2(A).

The time required for performing the whole set of movements was very large and that motivated the development of second generation scanners. In this generation the beam of the source was opened, forming a fan-beam and instead of a single detector a set of detectors were placed in front of it to record the x-ray intensity. This way, while there was still necessary to carry out linear movements, several measurements were acquired at the same time, reducing the time for each angular projection. A schematic depiction of a second generation scanner is shown in figure 1.2(B).

The concept of fan-beam introduced in second generation scanners was extended for the design of third generation scanners. In this kind of systems, the angle of the fan beam was larger and a set of detectors forming an arc was placed in front of the x-ray source. The fan-beam in this case was large enough to span the whole subject in each view, avoiding the need of linear translation, further reducing the acquisition time from about 5 minutes per slice in second generation scanners to roughly 5 seconds in third generation scanners [25]. The design concept of third generation scanners is shown in figure 1.2(C).

A fourth generation design was proposed in which a complete ring of detectors were used, illuminated by a single x-ray source that was the only moving part of the system. It offers several advantages for reduction of image artifacts, especially those arising from stability and gain differences between the detectors. However it had limited success due to the large costs introduced by the use of such a large number of detectors and to the reduction in artifacts achieved by the improvement in the detection technology. For this reason, third generation design concepts are the basis for modern CT systems.

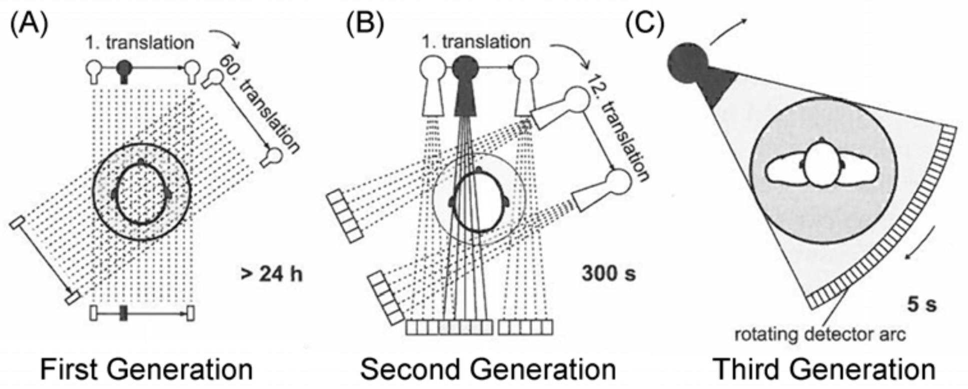

Figure 1.2. Schematic depiction of the acquisition technology for first (A), second (B) and third (C) generation CT scanners. Labels show the average acquisition time for a single slice in the first examples of each generation. The figure has been extracted and adapted from [25].

Later advances in CT technology led to lower acquisition time for single slices, but, if more than one slice was to be acquired the bed holding the subject needed to be moved and a new rotation performed to obtain data for the new slice. This process was repeated for the number of required slices. In the late 80s this problem was overcame by the introduction of helical or spiral scanning techniques [36-37] that combine the rotation of the source-detector assembly with a continuous movement of the patient bed, reducing the acquisition time and minimizing artifacts due to patient motion.

The extension of the detector by adding rows [38] and extending the x-ray beam in the axial direction –i.e. the direction perpendicular to the plane of the fan-beam– involved another breakthrough in the development of x-ray CT technology further reducing the acquisition time and turning x-ray CT into a true volumetric imaging modality that no longer provided slice data but whole volumes.

Recently, x-ray CT is experiencing a new leap with the advent of true area detectors, especially those based on flat-panel technology. This kind of detector offers the possibility of acquiring volumetric data without linear translation of the patient in a single rotation of the system, opening the x-ray beam in the axial direction to form a cone instead of a fan and introducing what is called Cone-Beam CT (CBCT) [39].

While CBCT can be of great potential for x-ray CT imaging it also poses several challenges that must be addressed prior to be turned into the standard technology for x-ray CT data acquisition. First, the large angle of aperture of the cone can generate artifacts due to incomplete sampling (see section 1.3) and to partial volume effects [40]; second, the larger cone aperture also makes it much more difficult to reduce the effects of scatter in image quality (see chapter 6); and the image acquisition time is still longer for area detectors, making CBCT acquisition slower when compared with multi-row scanners.

Despite these inconveniences, a great effort is being devoted to the improvement of CBCT technology and data processing, and its use is starting to become commonplace in several imaging environments, such as interventional C-arm imaging [6, 41], otolaryngology imaging [9, 11], imaging of extremities [8], breast imaging [12-13], imaging in radiotherapy [14-15], and, especially, micro-CT (CBμCT) imaging that provides very high resolution CT data for small samples, either in vitro –e.g. geologic samples or isolated biological tissues– [42-44], or in vivo in small-animal imaging [2-4, 45].

In the next subsection specific considerations for CBμCT in small-animal imaging are provided.

1.1.2 Small-animal x-ray CBμCT design considerations

Small-animal x-ray CBμCT imaging systems are usually designed to provide complementary information for molecular imaging systems. The main design goals are to maximize image quality while reducing as much as possible the radiation delivered to the animal.

Early implementations of x-ray CBμCT systems were aimed at non-destructive testing for industrial applications or for in vitro study of biological tissues [25]. The main design goal for these systems was to achieve high image quality (resolution and contrast), regardless of the radiation dose delivered. They were not designed to facilitate the use of equipment for in vivo imaging, such as anaesthesia equipment or vital sign monitoring devices. Thus, the mechanical setup was such that the x-ray source and detector were fixed while the sample was rotated between these devices. This made system calibration easier and ensured long-term stability.

In-vitro CBμCT scanners can achieve very high spatial resolution values (~5 μm) using micro-focus x-ray sources and area detectors such as CCDs or flat-panel detectors.

However, to obtain an appropriate signal-to-noise ratio, it is necessary to perform long acquisitions at high radiation doses. Furthermore, the desired resolution in the reconstructed volume is commonly obtained in practice by using a high magnification factor (>3), which require the detector to be situated at some distance from the sample; therefore, such mechanical arrangements are only feasible if the x-ray source and detector are assembled on a horizontal flat surface. A typical configuration for an x-ray in vitro system is depicted in figure 1.3.

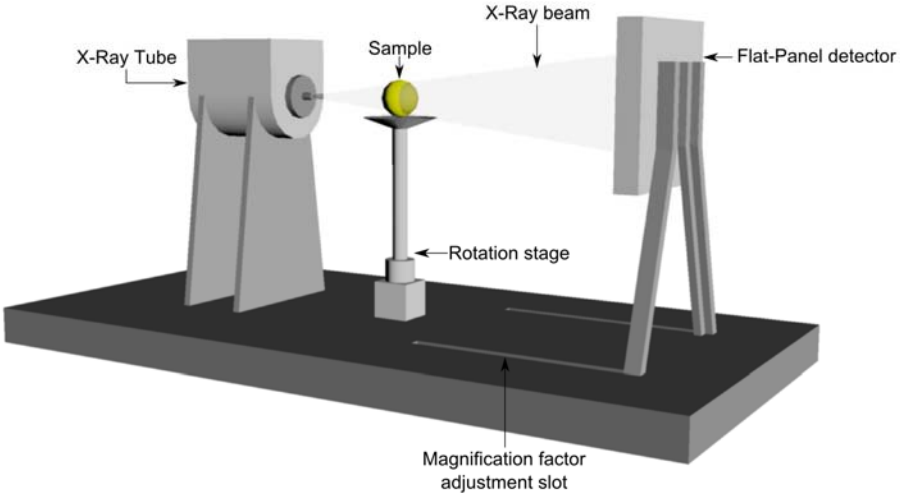

Figure 1.3. Typical configuration of an in vitro CBμCT scanner. The magnification factor can be adjusted by varying the distance between the sample and the flat-panel detector.

Small-animal CBμCT scanners also offer a reasonably high spatial resolution with sufficient image quality, although they require acquisition time and radiation dose to be as low as possible. These two additional constraints reveal the need for a new approach to the implementation of the system. Therefore, a compromise must be sought between image quality, spatial resolution, acquisition time, and dose delivered. Furthermore, during the acquisition process, the animal must be kept steady which requires the gantry holding the x-ray source and detector to rotate around it. This is an important requirement, since it is necessary to minimize the disturbance to the animal and to avoid inconsistent projection data derived from any organ displacement that may occur if the animal is moving. Anaesthesia equipment and monitoring devices (heartbeat, breathing rate, temperature…) must be correctly placed, as monitoring becomes somewhat challenging if the animal is rotating.

The constraints imposed by in vivo requirements demand a more sophisticated and careful design if the system is to be compact. This requirement is even more important when space is scarce. In this setting, the mechanical features of the x-ray source and detector become more important, since these devices should be placed on a rotating gantry to keep the subject in a fixed position. To avoid instability during rotation, the weight and size of the devices should be as low as possible, and mechanical elements are necessary to counterbalance the system. Although some scanners make use of slip rings, this is not the most common solution, as they are expensive and rotation speed is not the most constraining factor. Therefore, the signal and power cables must be placed in such a way that they do not disturb the image acquisition process. This usually involves an extension of cable lengths, thus increasing signal losses and deteriorating the signal-to-noise ratio in the acquired data.

Sensor specifications are also an important issue. Fast and sensitive detectors are extremely desirable for small animal CBμCT, given that acquisition time and dose delivered are paramount.

Since the acquired x-ray CBμCT projection data must be highly stable along the acquisition path, it is necessary to use highly stable x-ray sources and detectors. If the detector is not stable, it becomes necessary to acquire several correction datasets during a single acquisition process, thus increasing total acquisition time.

Different approaches can be adopted in the selection of the detector. Nowadays, CCDs connected optically to a scintillation screen are widely used in small-animal CBμCT systems. These detectors show good spatial resolution (usually depending on the coupling between scintillator and sensor) and the fastest image rate. However, these devices are usually too bulky to integrate in a moving gantry. Another drawback is that the sensor can be seriously damaged by x-ray radiation [46] and must be carefully shielded, thus increasing the size and weight of the system.

Modern designs make use of the so-called flat-panel x-ray detectors (semiconductor-based light detector matrices coupled to scintillator screens [47] or direct conversion semiconductor detectors), due to their high resolution (equal to or better than that achieved by CCDs) and image quality, combined with a compact design and low weight that simplifies integration in the rotating gantry. Their main drawback is that most of them are slower than CCDs.

Some experimental developments [48-51] make use of photon-counting detectors based on cadmium telluride (CdTe) or cadmium zinc telluride (CZT) sensors. These devices are able to classify the incoming photons according to their energy, enabling accurate correction of energy-related artifacts, such as beam hardening or scatter. Much effort is being made in the development of x-ray photon-counting detectors for CBμCT systems, but these are still at an early stage. The quality and image rate of the data acquired by state-of-the-art devices is not sufficient to allow them to be used in commercial pre-clinical imaging systems.

1.2 Physical background

This section provides a brief overview of the physical principles involved in the generation of x-ray radiation, its interaction with matter and its detection. For a more in-depth discussion of the physical processes involved in the formation of x-ray image the reader is referred to a collection of books, such as the one by Johns and Cunningham [52] that provides a detailed explanation of the physical basis of x-ray imaging, or the one by S. Webb [27] and the first volume of the Handbook of Medical Imaging [53] that extend the principles overviewed here.

1.2.1 Production of x-rays

X-rays are a form of electromagnetic radiation which energy range falls above the visible range and in the range of the ionizing radiation, i.e. radiation able to remove an electron from an atom and, therefore, create an ion pair [54]. The energy range covered by x-ray radiation used in medical imaging goes from a few keV (~10 keV) to about 150 keV or, equivalently from a wavelength of around 0.1 nm (12.4 keV) to 0.01 nm (124 keV).

X-ray radiation in the vast majority of medical imaging systems is produced by bombarding a metal target with particles, usually electrons, accelerated to a high speed. When a high-speed electron hits the target, several interactions involving energy transfers can take place. Most of the interactions yield heat as the primary output but some of them will produce x-ray radiation. In x-ray tubes radiation is produced by two main interactions.

The first process yielding x-ray photons consists in the interaction between a high-speed electron and the coulomb field of a nucleus of an atom in the target. As a consequence of the interaction the electron suffers a deceleration and its direction changes. During this process the electron loses part or all of its kinetic energy and, as a consequence, an x-ray photon is produced. The radiation produced by this kind of interaction is called *bremsstrahlung* radiation (German for "braking radiation") and forms the continuous energy spectrum of photons. *Bremmsstrahlung* radiation contains a larger quantity of low energy photons due to the larger probability for the electron of undergoing several partial deceleration events instead of a single event releasing all of its kinetic energy. The total intensity of *bremsstrahlung* radiation resulting from a particle of mass *m* and charge *ze*, incident on a target with charge *Ze* is proportional to [26, 54]:

$$I \propto \frac{Z^2 z^4 e^6}{m^2} \tag{1.1}$$

As a consequence, particles with low mass generate a larger quantity of *bremsstrahlung* radiation, making electrons a suitable particle for the generation of x-ray radiation in x-ray tubes.

The second type of interaction involves the collision of the high-speed electron with one of the inner shell electrons of an atom of the target, ejecting it. When the hole is filled with an electron from an outer shell, a photon is emitted. The radiation yielded by this kind of process is called characteristic radiation.

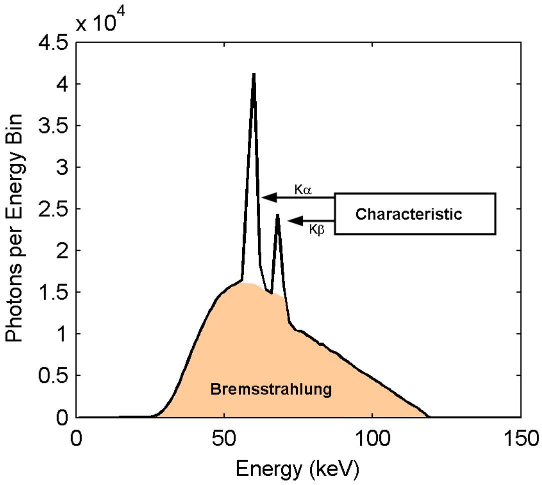

Figure 1.4. Simulated spectrum for a radiology x-ray source with a tungsten anode; the voltage of the x-ray source was set to 120 kV and the added filtration to 2.0 mm Al. In the figure the fraction of the spectrum generated by *bremsstrahlung* is shaded and the two peaks of characteristic radiation are clearly visible.

Photons generated by this process have an energy value equal to the difference between the binding energies of the two shells involved in the transition of the electron. Since the energy of electrons at each shell is defined at discrete, quantized values, in accordance to the classical Bohr model for the atom [54], the energies of characteristics x-rays are discrete and unique for each element of the periodic table.

Figure 1.4 shows an example of an x-ray spectrum generated for a radiology x-ray tube, simulated using an analytical model [55]. The *bremsstrahlung* fraction as well as the characteristic peaks can be clearly identified.

1.2.2 Interaction of x-rays with matter

Ionizing radiation can interact with matter in several ways that can result in the deposition of energy and, in some cases, in a secondary x-ray. The interactions between ionizing radiation and matter are [54] the photoelectric effect, Rayleigh scattering, Compton scattering, pair production and triplet production; whereas for the energies used in x-ray imaging only the first three are possible and are reviewed in this section.

In the photoelectric effect –first described by Albert Einstein in 1905– the x-ray photon interacts with an electron in the medium, releasing all of its energy. The energy is transferred to the electron which is ejected from the atom with a kinetic energy equal to the excess energy after unbinding the electron from the atom, i.e. the energy of the photon minus the binding energy of the electron. As a consequence, if the energy of the x-ray photon is lower than the binding energy of the electron, the photoelectric effect is not feasible. The ejected electron leaves a hole and a subsequent cascade of events, analogous to the one described for the generation of characteristic radiation, takes place. This can result in a secondary x-ray. However, the binding energy of electrons in biological tissues is low and the resulting photon is most likely absorbed within a few micrometers.

The probability of the photoelectric effect is roughly inversely proportional to the cubic of the excess energy of the photon [26], making the probability of photoelectric effect maximal when the energy of the photon matches the binding energy of the electron. Furthermore, the probability of the photoelectric effect is roughly proportional to the cubic of the atomic number [56], being a source of image contrast for materials with significantly different atomic numbers.

The second type of interaction between an x-ray and the medium is the Compton –also known as incoherent or inelastic– scatter. In this type of interaction the energy of the photon is considerably larger than the binding energy of the outer electrons of the atom. The photon hits an electron and it is deflected, transferring in the process part of its energy to the electron which is ejected from its shell. Therefore, the outcomes of a Compton event are a recoil electron, an ion, and a secondary x-ray propagating in a different direction and with lower energy than the original x-ray. Compton scatter is an interaction mainly involving outer electrons and, thus, it depends on the electron density instead of atomic number of the material [26].

The deflection angle of the photon and the energy transferred in the process are related by the next expression:

$$\frac{E'}{E_0} = \frac{1}{1 + (E_0 / m_0 c^2)(1 - \cos\theta)}, \tag{1.2}$$

where E' and E_0 are the energy of the scattered and impinging photon, respectively, θ is the angle of deflection of the scattered photon, and m_0c^2 is the rest mass of the electron, equal to 511 keV. Equation 1.2 implies that the energy of the scattered photon is smaller for large deflection angles and the effect is more pronounced for higher energy photons.

The differential cross-section for Compton scatter can be estimated using the Klein-Nishina equation:

$$\frac{d\sigma_C}{d\Omega} = \frac{r_e^2}{2}\left(\frac{E'}{E_0}\right)^2 \left(\frac{E'}{E_0} + \frac{E_0}{E'} - \sin^2\theta\right), \tag{1.3}$$

where $d\Omega$ is the differential solid angle for the deflection, and r_e is the classical electron radius.

Equation 1.3 assumes a simplification of the situation in real materials and is exact only in the case of scattering from a free electron at rest. In real situations electrons are bound to atoms and also they are not at rest. These two implications must be taken into account when studying Compton scatter. However, the explanation is beyond the scope of this introduction and the author refers the interested reader to further references, such as [57-58].

The third mechanism of interaction is the Rayleigh –coherent or elastic– scatter. The main characteristic of Rayleigh scatter is that the atom does not undergo ionization and, therefore, there is no transfer of energy from the x-ray to the medium. In Rayleigh scatter the oscillating electric field associated to the x-ray sets electrons on an atom of the medium into temporary vibration. As a consequence of the oscillation of the electrons, they emit radiation with the same wavelength of the incident x-ray but in a slightly different direction. Deflection angles for Rayleigh scattering are small and they are smaller the larger the energy since the recoil imparted to the atom must not produce ionization. For the last reason, Rayleigh scattering is more likely for low energy x-rays and high Z materials [54, 59].

Figure 1.5 shows the relative probability of deflection angles for Compton and Rayleigh scatter in water. Figure 1.5 has been extracted from [54].

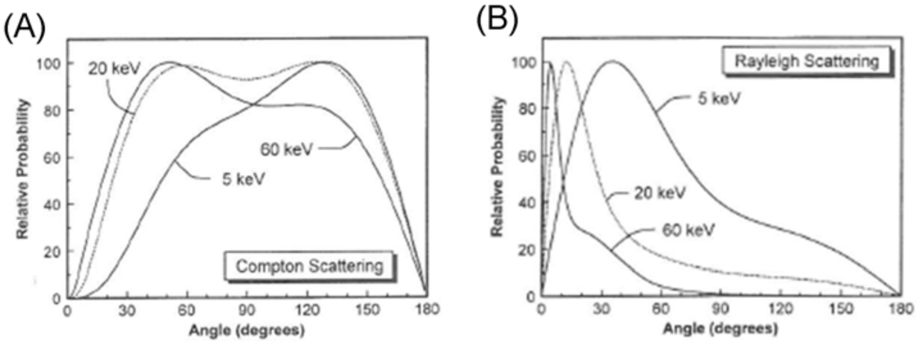

Figure 1.5. Probability of deflection angles for Compton (A) and Rayleigh (B) scatter. Note the broader distribution of deflection angles for Compton scatter and how the distribution is more biased toward forward directions for larger energies. On the other hand, the angular distribution of Rayleigh scatter is broader for low energy values. The figure has been adapted from [54].

1.2.2.1 X-ray attenuation coefficient

The net effect of the interactions described above is that the intensity of x-rays measured in a straight line from the source and after crossing an object is reduced compared to the intensity exiting the source; either because some of the x-rays have been absorbed, they have deposited part of their energy and escape the object in a different direction, or just because their direction of propagation has changed. Summarizing, the x-ray photon beam has been attenuated as it passes through matter.

As derived in [54], when x-rays pass through a material with a probability of interaction μ, the attenuation can be posed in terms of a differential equation which solution is the so-called Beer-Lambert law, yielding,

$$I = I_0 e^{-\mu L}, \tag{1.4}$$

where I_0 is the x-ray intensity –or analogously the number of photons– entering the material, I is the x-ray intensity after crossing through the material and L is the traversed thickness of material.

The value of μ is usually denoted as the linear attenuation coefficient of the material and represents the probability of interaction per unit length of material and, therefore, it must be expressed in inverse length units, usually cm^{-1}. Since μ is the probability for all the interactions together, it is the combination of the individual probabilities for each of the interactions, and it is given by:

$$\mu = \tau + \sigma_C + \sigma_R, \tag{1.5}$$

where τ is the probability of photoelectric absorption, σ_C is the probability of Compton scatter and σ_R is the probability of Rayleigh scatter.

The linear attenuation coefficient represents the attenuation of x-rays for a particular material at a specific energy, but it linearly depends on density. Since the same material can show different density values in different situations while the rest of its properties are kept untouched, μ is commonly normalized by density (ρ), yielding the mass-attenuation coefficient, (μ/ρ). Units for mass-attenuation coefficient are usually cm^2/g.

As can be extracted from the description of the types of interactions between x-rays and matter, the attenuation coefficient –as well as its individual components– depends on the energy of the x-ray photons crossing the material. This dependency can be seen in figure 1.6 that shows the variation of the mass attenuation coefficient and its individual component as a function of x-ray energy for soft-tissue in the diagnostic energy range. Figure 1.6 illustrates the importance of each individual interaction as a function of x-ray energy. In accordance with the explanation above, the photoelectric effect and Rayleigh scatter are the dominant interactions for low energy photons, while the relative contribution of Compton scatter rises with photon energy, being the main source of attenuation for energies larger than ~30 keV. While Compton and Rayleigh scatter are a source of contrast in x-ray imaging, the deflected x-rays can also contaminate the measured data and generate undesired effects, as explained below and treated more in-depth for CBCT systems in chapter 6.

Another important quantity is the fraction of energy transferred to the particles in the material in the form of kinetic energy as a consequence of the interactions, given by the mass-energy transfer coefficient, and its derived mass-energy absorption coefficient. Both parameters are useful for the estimation of x-ray exposure from simulated beams and a description of them can be found in [54].

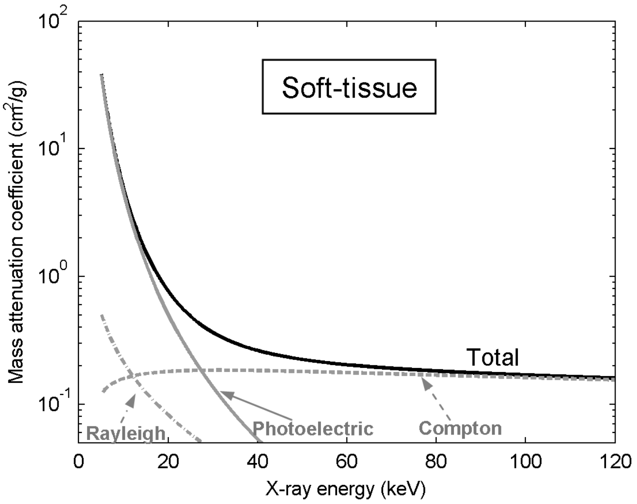

Figure 1.6. Mass attenuation coefficient and its individual components for soft-tissue. The coefficients were generated using the PENELOPE 2006 [58] physical models –see chapter 5– and material properties were extracted from the ICRP definition for soft-tissue.

1.2.3 X-ray detection

The element in charge of recording the x-ray intensity attenuated by the object is the x-ray detector. As stated above, there are several detector technologies usually associated with different imaging modalities or CT technologies.

For the sake of conciseness and given that the present work is focused on CBCT and CBμCT with flat panel detectors, an overview on the basic structure and functioning of this type of flat-panel detectors is provided below.

As stated above, flat-panel digital detectors are one of the most widely used x-ray detection devices for CBCT in general and CBμCT in the filed of small-animal imaging in particular. Several comprehensive reviews of flat-panel x-ray detector technology [1, 47, 60-61] address topics not included in the present work and could prove useful for the interested reader.

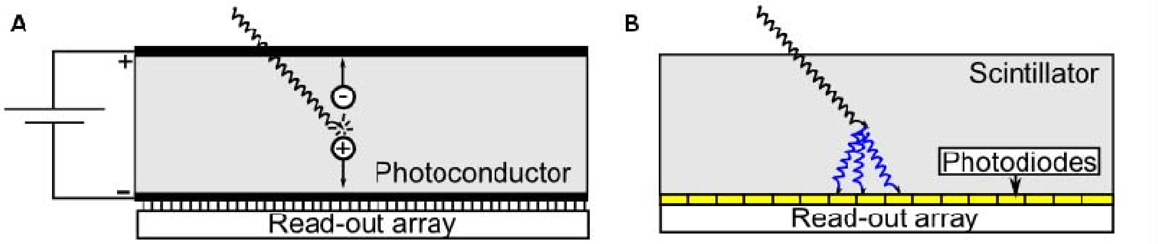

Figure 1.7. Scheme of direct (A) and indirect (B) detection approaches used in x-ray flat-panel detectors.

Flat-panel detectors can be classified as direct conversion and indirect conversion devices (see figure 1.7). A comparative study of the performance of direct and indirect conversion flat-panel detectors can be found in [62].

Since x-ray detectors can be modeled using cascaded devices [63-67] the following explanation divides signal generation into two different stages, namely, x-ray conversion and data readout. Information on the position where the x-ray photon is detected and on its deposited energy is generated at the beginning of the first stage, where the x-ray photons (primary quanta) are stopped. Subsequent steps do not add new information to form the image. Thus, it is important to have a low noise level and adequate amplification in the stages following x-ray capture to ensure that no information is lost after the x-ray photons are detected. The stage with the poorest quanta detection capability is called the quantum sink and it limits system performance in terms of signal-to-noise ratio. Since the information lost in the quantum sink cannot be recovered, a well-designed detector should have its quantum sink at the very first stage of image formation, i.e. when x-ray photons are absorbed [47].

1.2.3.1 Indirect conversion flat-panel x-ray detectors

Indirect conversion flat-panel detectors detect individual x-ray photons by generating optical photons as secondary quanta. A subsequent step is needed to convert the optical photons into electric charges on each pixel. Integrated over a period of time, this charge is then amplified and digitized.

X-ray conversion stage

The outer layer of the detector is made of a scintillation material, which provides a variable number of optical photons per x-ray photon stopped, depending on the energy involved in the interaction.

The scintillation materials used in x-ray flat-panel detectors are usually inorganic compounds such as cesium iodide (CsI) or gadolinium oxysulfide (GOS). Scintillation in such materials is based on energy transfer to the molecules of the scintillator, depending on the energy states determined by the crystal lattice of the material. In insulator or semiconductor materials, electrons remain in a discrete number of energy bands. The two main energy bands are the valence and the conduction band. Electrons with an energy state that places them in the valence band are bound to the crystal lattice and, therefore, fixed. However, those electrons with sufficient energy to reach the conduction band can move across the crystal. The band between the conduction and valence bands is the forbidden band, where no electrons can be found in a pure crystal.

If a photon with sufficient energy reaches an electron in the valence band, it can increase its energy so as to reach the conduction band, thus leaving a hole in the valence band. The excited electron returns to the valence band by emitting a photon of energy equal to the difference between the energy levels. This energy is usually too high and the emitted photon energy does not correspond to the visible light range.

To increase the number of visible light photons emitted, dopants are added to the crystal [68]. These materials create defects in the crystal lattice, where the normal energy band structure is modified, thus creating energy levels within the forbidden band. Excited electrons can fall first into one of these energy levels and later into the stable valence band, and emit photons with an energy that falls within the visible range.

Several scintillation materials have been used in flat-panel detectors. Desirable characteristics of a scintillation material for this application are the possibility of implementing large-area screens, the production of a high number of optical photons per x-ray photon detected, high sensitivity to the energy spectrum of the x-ray beam, and a high degree of correlation between the direction of propagation of the incident x-ray photon and that of the optical photons generated.

At present, the two scintillation materials most commonly used in flat-panel detectors are terbium-doped gadolinium oxysulfide (Gd_2O_2S:Tb) and thallium-doped cesium iodide (CsI:Tl).

Gd_2O_2S:Tb has traditionally been used to detect x-rays and can be manufactured easily and cost-effectively using well-known technology [47]. It comes in the form of a powder [69] composed of microscopic particles with a density of 7.3 g/cm^3.

Gd_2O_2S:Tb has one of the highest figures of merit –defined as the best balance between high light production, fast response, and appropriate energy spectra– among powder scintillators: it is highly efficient and has a very low afterglow and an appropriate energy emission spectrum, centered at 540 nm. However, achievable spatial resolution is limited by the lateral scattering of the photons generated. Thicker scintillation screens offer a longer path for the optical photons, thus increasing scattering and worsening spatial resolution, while thinner screens stop a low fraction of the received x-ray photons, thus decreasing detector sensitivity. Therefore, a compromise must be reached between x-ray stopping power and achievable spatial resolution.

Micro-structured scintillation screens based on CsI:Tl were developed to meet the main imaging needs of x-ray systems, namely, the increase in x-ray stopping power while maintaining good spatial resolution.

The manufacturing process of this type of scintillation screen is based on the deposition by thermal evaporation of long, thin, needle-shaped structures on a glass or plastic support or directly on top of the semiconductor light detectors [70]. Each of the needle-shaped structures behaves as a light pipe, confining optical photons inside it and thus avoiding most of the lateral scattering present in non-structured screens (see figure 1.8). This light confinement makes it possible to increase the thickness of the scintillation screen (up to 1-2 mm), while maintaining good spatial resolution. Furthermore, light production, needle stability and shape, and resolution of the scintillator screen are highly dependent on manufacturing conditions [71], namely thallium concentration, pressure, temperature, and post-processing.

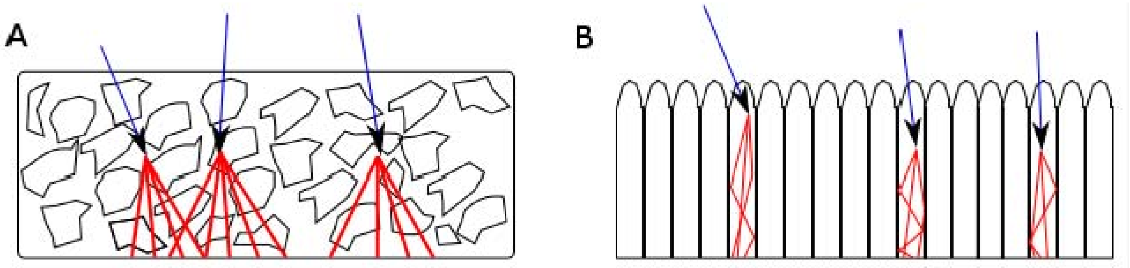

Figure 1.8. Simplified light transport in a granular non-structured scintillator screen (A) and in a microcolumnar structured scintillator screen (B).

The scintillator needle layer can be deposited directly on the semiconductor detector surface without degrading the properties of the photodetector elements in the array, thus achieving optimal spatial resolution and high x-ray detection efficiency, as optical coupling agents are not necessary to glue the scintillator screen over the semiconductor surface. Besides the aforementioned advantages of this kind of scintillator, the light production per photon stopped of CsI:Tl is among the highest known, and the peak of the emitted spectrum is at 550 nm, a value that matches the spectral response of most semiconductor photodetectors currently used in the development of x-ray flat-panel detectors [72-73]. Due to its advantages over other scintillation materials, CsI:Tl is becoming the preferred material for the x-ray photon conversion stage in flat-panel detectors.

Secondary quanta detection and readout

Secondary quanta conversion and data read-out in indirect flat-panel x-ray detectors has traditionally been implemented as a pixel array based on hydrogenated amorphous silicon (aSi:H) and thin-film transistor (TFT) technology. Each pixel consists of a reverse-biased photodiode and a TFT that acts as a switch. During exposure, charges are accumulated in the photodiode. After exposure, a gate pulse is generated for each row of pixels, thus switching the TFT of the given row of pixels to release the accumulated charges through the data line. The released charges are amplified and converted into a voltage using an array of charge-integrating amplifiers, with one amplifier per pixel in the row. The voltage signals from the row of pixels are then multiplexed and digitized.

The technology described has mainly been used for digital radiography detectors; however, devices using this technology show a long signal decay time and a poor fill factor due to the wide electrode width and switch size [72]. These drawbacks impair the development of sensors with an appropriate frame rate and small pixel size, thus hampering the use of this technology for CBμCT image acquisition.

A newer technology for the read-out of indirect x-ray flat-panel detectors consists of sensors based on CMOS technology. CMOS image sensors are composed of a matrix of identical pixels which have a photodiode and a MOS switch transistor [73], two scan circuits which address the different rows and columns of the sensor matrix, and an output amplifier.

The image formation process for the simplest CMOS image sensor, based on passive pixel elements, is quite similar to that of the pixel array based on aSi:H and TFT technology. First, the photodiodes are reverse biased. The incoming photons cause a decrease in the voltage of the photodiode, which is measured at the end of the imaging process. The drop in voltage gives an estimation of the number of photons that have reached the given pixel. After the pixel reading, the photodiode is reset.

Current CMOS sensors use more sophisticated pixel designs, where every pixel has an active element that acts as an individual amplifier, thus reducing the noise level of the final image. Improvements in active pixel design have led to the development of the pinned photodiode pixel, which is in use for most current CMOS image sensors. In this kind of sensor, two measurements are taken and subtracted for each image pixel (correlated double sampling, CDS). The first contains information about the number of photons reaching the pixel, while the second gives an estimation of the photodiode offset voltage. This kind of design allows a further reduction of the noise level and dark current of the detector. A sketch of a CMOS sensor with active pixels and CDS circuits is shown in figure 1.9.

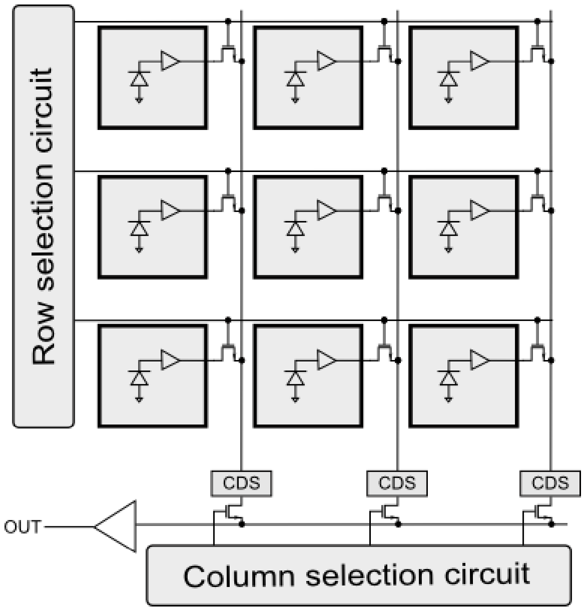

Figure 1.9. Sketch of a typical CMOS image sensor with active pixels and CDS. Adapted from [73].

1.3 CBCT image reconstruction

In this section the basics of image reconstruction in CT in general and in CBCT in particular are briefly reviewed. Extensive research efforts had been devoted to the field of tomographic image reconstruction and a more detailed treatment of the tomographic image reconstruction problem can be found in several dedicated books or book chapters such as [26, 74-76].

As stated in the introduction section of this chapter, the physical property sought in x-ray CT is the spatial distribution of the x-ray attenuation coefficient. However, the quantity recorded by x-ray detectors in the x-ray intensity behind the object to be imaged and CT systems measure this quantity for several positions –i.e. pixels of the detector– and from several angular views of the object.

When several materials and/or densities are present in the object, the measured intensity, when related with the intensity measured for the non-attenuated beam, provides the accumulated attenuation for all the materials traversed by the x-ray on its way to the detector. Recalling equation 1.4 but this time including the effect of crossing a continuous of attenuating materials –still obviating the dependence of the attenuation coefficient with photon energy– the intensity acquired is given by:

$$I = I_0 e^{-\int_L \mu(x)dx} . \tag{1.6}$$

Normalizing equation 1.6 by the non-attenuated x-ray intensity (I_0) and taking the negative log-transform of the result we arrive at the classical expression for projection data used as the starting point in transmission tomography reconstruction texts, yielding,

$$p = -\log\left(\frac{I}{I_0}\right) = \int_L \mu(x)dx . \tag{1.7}$$

Considering now a two-dimensional object recorded using a one-dimensional detector, equation 1.7, has to be represented in terms of the spatial distribution of μ in the coordinate system of the object, the projection position inside the detector and the angular view. Assuming a parallel projection geometry (see figure 1.10(A)) we arrive at the following expression [75],

$$p(t,\theta) = \int_{-\infty}^{\infty}\int_{-\infty}^{\infty} \mu(x,y)\delta\left(x\cos(\theta) + y\sin(\theta) - t\right)dxdy . \tag{1.8}$$

Projection data $p(t,\theta)$ is usually arranged into the new coordinate system formed by t and θ, building what is called a sinogram, depicted in figure 1.10(B). The name sinogram arises from the fact that the set of projections of an infinitely small point in the original coordinate system will describe a sinusoidal curve on the sinogram.

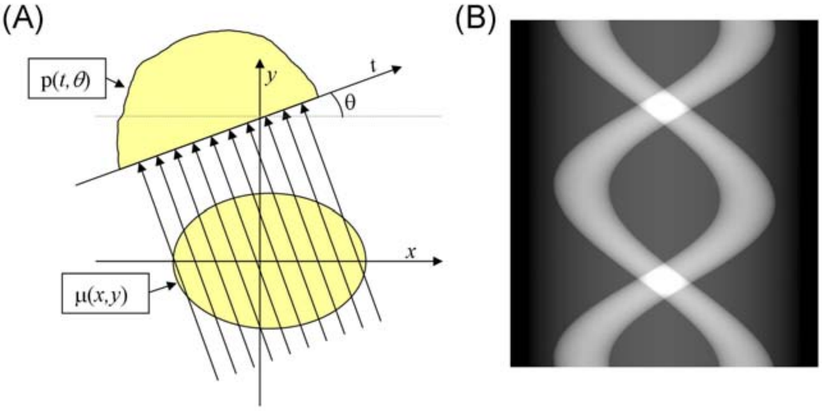

Figure 1.10. Schematic illustration of the acquisition of a projection dataset (A) for the angular position q, recorded data are the accumulated attenuation factor as a function of the x-ray travel path. In panel (B) and example of a sinogram is shown (data in (B) does not correspond to the sinogram that would be obtained in the situation depicted in (A)).

The sinogram forms the Radon transform of the object that can be inverted to obtain the original distribution of µ inside the object. The inverse Radon transform can be seen as the process of smearing back the projection value along its ray (t,θ) for each angular view and adding all the smeared rays in the original coordinate system, process known as backprojection. However, reconstructed data obtained by this process is significantly blurred.

This intuitive version of the image reconstruction process can be put into mathematical terms by introducing the Fourier slice theorem. The Fourier slice theorem (also known as central slice theorem) can be stated as [26]:

> “The Fourier transform of a parallel projection of an object $\mu(x,y)$ obtained at angle θ equals a line in the two-dimensional Fourier transform of $\mu(x,y)$ taken at the same angle.”

The proof of the theorem can be found in [26, 75]. The Fourier slice theorem provides an straightforward way of reconstructing $\mu(x,y)$ by just computing the inverse Fourier transform of the projection data. However, this approach is seldom used in practical systems since it has several drawbacks such as the non-correspondence between the sampling grid of the Fourier transform and the slice pixels, among others [26]. For this reason, backprojection algorithms are commonly used.

From the Fourier slice theorem one can elucidate the source of the blurring presented by the backprojection image. Since each projection is a radius in the 2D Fourier transform of the image –i.e. a line passing through the center of the Fourier transform– the only part of the frequency space that is sampled from every projection is the DC component, or zero frequency, and the density of sampling decreases the larger the frequency value. For this reason, when adding the data from all projections, low frequencies are overestimated while high frequency data is underestimated, causing the image to be blurred. Thus, we can add a frequency-dependent weight to the projection data to compensate the difference in sampling density. This situation is graphically depicted in figure 1.11.

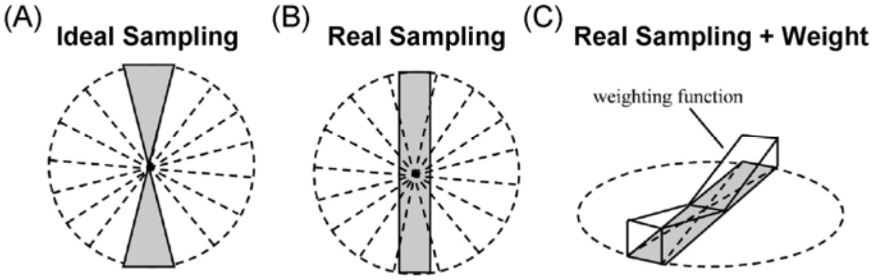

Figure 1.11. Sampling patterns of the 2D frequency space showing the ideal situation (A) and the real situation when data is acquired as a set of angular projections (B). Note the overlapping of the different projections in the low frequency area. This effect can be compensated by giving a higher weight to high frequency areas, as shown in panel (C). The figure has been extracted and adapted from [26].

The intuitive weighting value can be posed into mathematical terms by introducing the filtered backprojection algorithm (FBP), which is directly derived from the Fourier slice theorem. After some mathematical manipulation –see refs [75-76]– the expression for the FBP reconstruction is:

$$\begin{aligned} \mu(x,y) &= \int_0^{\pi} g(x\cos\theta + y\sin\theta, \theta)\, d\theta \\ g(t,\theta) = g(x\cos\theta + y\sin\theta,\theta) &= \int_{-\infty}^{\infty} P(\omega,\theta)\left|\omega\right| e^{j2\pi\omega(x\cos\theta + y\sin\theta)} d\omega \end{aligned}, \qquad (1.9)$$

where $P(\omega,\theta)$ is the 1D Fourier transform of the projection data for the angle θ. Then the reconstruction process is usually carried out as follows. First, the projection is Fourier transformed and it is multiplied by the ramp filter $\left|\omega\right|$; then the inverse Fourier transform of the filtered projection is smeared onto the image using the backprojection operation and the process is repeated for every projection in the dataset. While the ramp filtration is necessary to remove image blurring, CT data is usually band-limited and very high frequencies contain only noise that is enhanced by the filtering operation. For this reason, the ramp filter is usually apodized, multiplying it by smoothing windows, such as the Hanning or sinc windows.

For the case of non-parallel geometries several modifications have to be made to equation 1.9. When moving to fan-beam geometry, where rays diverge from a source point to reach every position of the detector, the rays have to be weighted as a function of the angle they formed with the central ray of the beam (see [75]) prior to the filtration operation.

Both the parallel and fan-beam geometries sample the whole Radon space for the slice to reconstruct and the reconstructed data obtained by using the FBP method is mathematically exact. However, when acquiring data for several slices at once using cone-beam geometry with a circular acquisition trajectory, as is the case for all the systems considered throughout this work, obtaining mathematically exact reconstructions using variations of the FBP method is not feasible due to the incompleteness of the sampling space, according to the Tuy-Smith condition [77-78], which reads:

> "Exact cone-beam reconstruction is possible if the trajectory of the cone-beam source intersects every plane intersecting the object."

The Tuy-Smith condition is not fulfilled in circular trajectories for any part of the volume except for the central slice, since rays not contained in the central slice cross several slices on their way to the detector. Whereas there is not an exact mathematical solution, in the case of acquisition trajectories where the solid angle spanned by the beam is not very large, Feldkamp, Davis and Kress [79], introduced an approximated algorithm that tries to compensate the data incompleteness by applying to the projection data a weighting factor dependent on the divergence between the trajectory of the ray for the position in the projection and the central ray of the beam. This factor is applied prior to the fan-beam weighting that is also necessary in CBCT with circular trajectory.

Due to the not so critical impact of the approximation in the FDK method and to the simplicity and high computational efficiency of the method, most CBCT systems use the FDK reconstruction algorithm. However, a lot of work has been devoted recently to the development of iterative statistical reconstruction algorithms that have a great potential for reducing the effects of incomplete trajectories, noise, low number of projections, etc. Example of these types of methods can be found in [74]. Most of iterative algorithms are not used in practical systems due to their high computational burden; however the situation is rapidly changing due to the introduction of GPUs in the field of image reconstruction, offering their massive parallel computing capabilities for the speedup of iterative algorithms [80-81].

1.4 Non-idealities in CBCT imaging

CBCT, as well as conventional CT, is not free from non-idealities that cause artifacts in the reconstructed images. The artifacts are diverse and they arise from several sources that can be attributed to the design of the system and the underlying physics, with the x-ray source, or with the image formation at the detector. Artifacts can also be induced by the subject being imaged. In this section several sources of artifacts are briefly introduced, in particular those more closely related with the work presented in the following chapters. More detailed reviews offering descriptions of the origin and impact on image quality of the different artifacts in CT can be found in [25-26, 82].

1.4.1 Beam hardening

As explained in section 1.2.1, x-ray tubes used in medical imaging generate a continuous spectrum of x-ray energies which is by no means monochromatic and contains x-ray photons with a variety of energies. In addition, the attenuation coefficient of tissues depends on x-ray energy –see section 1.2.2– and thus the attenuation of x-rays will then be different for different x-ray energies.

On the other hand, analytical reconstruction algorithms presented in section 1.3 inherently assume the beam to be monochromatic and treat the reconstruction of the attenuation coefficient as a linear problem.

If we include the effect of the polychromaticity of the beam into equation 1.4, the projection value is given by:

$$p_p = -\log\left(\frac{I}{I_0}\right) = -\log\left(\int_0^{kVp} q(E) e^{-\int_L \mu_E(x)dx} dE\right), \tag{1.10}$$

where $q(E)$ is the spectrum of the x-ray source normalized to unity area. Equation 1.10 shows that the relation between the measured attenuation and the length of material traversed is no longer linear and, therefore, treating it as linear will generate inconsistencies in the reconstructed data.

It is important to point out that the attenuation coefficient for all of the tissues is larger for low energy photons –see figure 1.6– and that makes the fraction of low energy photons in the total spectrum to be preferentially reduced for longer lengths of traversed material. The net effect is a shift towards high energy of the spectrum mean energy after being attenuated by a length of tissue and that shift is a function of the length of material. This shift means that the effective attenuation coefficient will be lower than expected for large material thickness, departing from linearity as assumed in the reconstruction algorithm. The effect is also more conspicuous for highly attenuating materials, such as bone.

The lower attenuation value measured creates cupping artifacts –i.e. reduction of the apparent attenuation coefficient for homogeneous areas towards the central part of the area, which is where crossing paths are longer– and inconsistencies for high attenuating materials (such as bone) that create streaks joining areas of this material. Streaks are a product of the different errors introduced by beam hardening when the beam crosses thick and thin parts of high attenuating material. An example of artifacts created by beam hardening is shown in figure 1.12(A).

Effects of beam hardening can be alleviated by several techniques. One of the most widespread techniques is the so-called water correction [83] which exploits the similarity between water and soft-tissue. In water correction the attenuation is measured for known lengths of water and the deviation between the curve of attenuation as a function of thickness and the ideal linear trend is estimated. This estimation is used to build a table of correction coefficients for measured attenuation that are later applied to linearize real projection data. Water correction reduces cupping but it cannot deal with the inconsistencies introduced by highly attenuating materials.

To reduce streak artifacts several methods have been proposed, most of them involving a two-step correction where a water correction is performed followed by a secondary correction for the highly attenuating parts of the object. Most of these methods are variations of the approach by Joseph and Spital [84].

Another method for the reduction of beam hardening artifacts involves the inclusion of the polychromatic nature of the spectrum in the reconstruction process, usually in the context of statistical reconstruction methods that aim at minimizing beam hardening at each iteration [85-87].

1.4.2 Scatter

The x-ray attenuation coefficient for the energy range used in medical imaging is composed to a great extent by scatter, especially Compton scatter. Scattering mechanisms attenuate the x-ray beam in the sense that the particular photon undergoing the interaction is re-directed from its original path –besides loosing part of its energy in the case of Compton scatter– and, therefore is seen as attenuation when measuring the intensity for this path. However, scattered photons can still reach the detector at a different position and their intensity will be recorded erroneously. Then, the signal detected at each location is a mixture of primary and scattered photons.

The scattered photons are incorporated into the intensity measured for a different ray –i.e. detector position– reducing the attenuation observed in this ray and making the measurements inconsistent. The situation is especially important in the case of high attenuating areas of the object surrounded by soft-tissue since in that case the relative error introduced in the measured attenuation value is larger.

Since scatter reduces the recorded attenuation and it is particularly noticeable for high attenuating parts, its effect is similar to that of beam hardening, causing the reconstructed data to show cupping and streak artifacts between high attenuating regions of the object [88-89]. Effects of scatter can be observed in figure 1.12(A).

It is straightforward to notice that scatter is a much bigger problem for large beam angles and large detectors, where scattered photons at larger deflection angles are more likely to hit the detector. This makes the problem of scatter more conspicuous in CBCT systems when compared to multi-row fan-beam systems and, in turn, in multi-row systems when compared with single-row fan-beam geometries.

At this point of the discussion a question could arise: Is there a way to distinguish scattered from primary photons? Given that x-ray sources generate polychromatic spectra and that the detectors commonly used in CBCT are energy integrating detectors, once scattered photons have reached the detector they are basically indistinguishable from primary photons. However, the impact of scatter can be mitigated by several techniques which reject scatter prior to reaching the detector (use of antiscatter grids or large air gaps [90]), or that estimate the scatter signal, either using measurements [91-92], analytical approaches [93], Monte Carlo simulation (chapter 5) [94-95], or hybrid methods [96].

While there are several methods to reduce the impact of scatter, it is still one of the major sources of image degradation in CBCT. The complicated nature of scattered radiation in some imaging scenarios prevents the accurate rejection or estimation of the spatial distribution of the scatter fluence, making the correction very challenging. The effects and nature of scatter in CBCT as a function of acquisition geometry and sample size are thoroughly studied in chapter 6 of this dissertation.

1.4.3 Incomplete projection data

For the reconstruction of CT data using the FDK algorithm it is necessary to measure all the line integrals crossing the object. It has been shown that this is not the case for the axial direction in circular trajectory CBCT, and, therefore, only approximated reconstructions are feasible.

However, the case of the interior data problem is more conspicuous. We refer to interior (or laterally truncated) data problem as the situation where part of the object lies outside the radial field of view (i.e. the circle containing the rays that are measured for all of the angular positions, as depicted in figure 1.10). When part of the object lies outside of the field of view, the reconstruction problem does not have a unique solution [77] and bright areas are generated at the boundary of the FOV in the reconstructed data. In addition to bright areas, truncated data results in low frequency drifts of the measured attenuation, as shown in figure 1.12(B).

Several methods have been proposed for the correction of artifacts arising from the reconstruction of laterally truncated data [97-99]. Throughout this work we corrected laterally truncated data by using the extrapolation approach by Ohnesorge et al. [98].

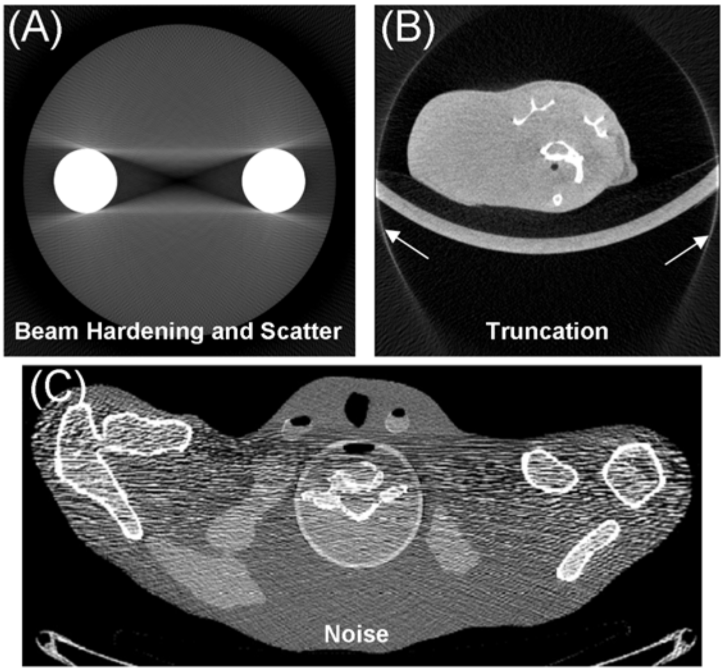

Figure 1.12. Several types of artifacts in CT and CBCT created by beam hardening and scatter (A), lateral truncation of the projection data (B), and heterogeneous noise (C). Panel (C) was extracted from [26].

1.4.4 Noise and detector non-idealities

Detectors for CT in general and in particular flat-panel detectors commonly used in CBCT integrate the energy deposited by the incoming photons within the pixel area, with no discrimination of any property of the incoming photon. In this situation the signal and noise of the measured data has been proved to follow a compound Poisson distribution –see [100] and chapter 3– where the variance of the signal is proportional to the mean, plus a fixed quantity coming from the additive noise in the electronic components [101]. In this case larger signal values show higher signal-to-noise ratios.

In addition, flat-panel detectors do not have an infinite dynamic range and in some circumstances it is not possible to obtain an appropriate signal level for the most attenuated parts of the beam without saturating the detector in less attenuated areas. When this situation arises, the level of noise is different for the different attenuation parts of the object and artifacts can be noticed in the reconstructed data. For the case of asymmetric objects –e.g. a human thorax– there can be two directions with very different attenuation values and, therefore, noise levels. This in turn generates streaks running through the more attenuating part (see figure 1.12(C)). This phenomenon is usually referred as photon starvation.

Photon starvation can be partially alleviated by automated exposure control (AEC) techniques that modulate the x-ray source current as a function of the angular position [102], or by image processing methods [103-104].

Under other circumstances, the modulation of the current is not feasible and other approaches could be used, such as methods for the extension of the dynamic range of the detector, as explained in chapter 3.

Flat-panel detectors can also be the source of image artifacts for other causes besides noise. They can contain unresponsive elements –i.e. pixels, lines or rows– or elements in which the response is far from ideal. These defective elements produce a signal which departs from that of adjacent detector elements resulting in bright or dark rings in the reconstructed image.

Another source of ring artifacts that can be seen as a milder version of the effect of defective elements is caused by small deviations between the gain curves of adjacent pixels after gain correction [105] –i.e. after normalizing the acquired data by the so-called flat-field data generated with no object in the beam– which create slight rings visible in the reconstructed slice. These small deviations usually arise from slight non-linearity of the gain curve of the pixel and several methods have been proposed to alleviate the effect in the image using interpolation techniques [106-107] or by modifying the gain correction process using more than one point [108-109].

1.4.5 Others

Among the other effects degrading image quality in CBCT one can mention aliasing, which arises when the angular sampling of the data is not large enough to accommodate the highest frequency features of the object. This causes the high frequency data to overlap with the low frequency part generating streak-like artifacts emanating from sharp edges in the object structure.

Another source of artifacts in CBCT is the partial volume effect arising from the cone shape of the x-ray beam that can make some features of the object to fall within the beam when it is observed from one angular position but to fall outside of the beam when observed from the mirror position (see figure 1.13).

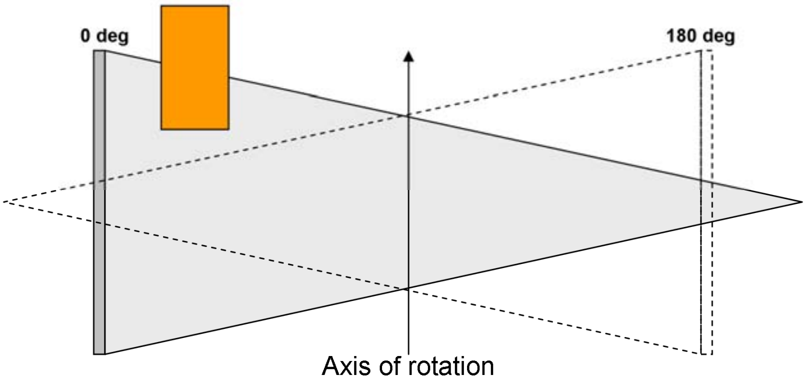

Figure 1.13. Illustration of the partial volume effect. Solid lines represent projection at the first angular position (0º) where the rectangular object enters the beam, while for the mirror projection –dashed lines– the object falls outside the x-ray beam.

Further artifacts can be generated from problems of the x-ray source such as the instability of its output, especially when the kVp of the beam is not stable, or as off-focal radiation.

The motion of the subject scanned can also turn into a source of artifacts which is more difficult to avoid when imaging moving organs into a living subject, such as in cardiac imaging or in lung imaging. While the effect of respiration and heart beat can be somewhat reduced by using gating techniques the subject can also move, degrading image quality in a more conspicuous fashion.

1.5 Monte Carlo simulation of x-ray systems

The generic name of Monte Carlo is given to a set of numerical methods in which one or several processes, physical systems and phenomena are simulated by statistical methods using random numbers [110]. The basic concept of Monte Carlo is to describe a system or process by a set of a priori known probability density functions (PDF) and connection rules between them and then predict the output of the system or process to a given input by randomly sampling the PDFs using the output of a stage as the input for subsequent stages.

In this section a brief introduction to Monte Carlo simulation in photon transport problems is provided, whereas more detailed revisions of the Monte Carlo theory and its application to medical physics can be found in [58, 110-113].

Monte Carlo provides a means to accurately simulate photon transport in x-ray systems and has been widely used, especially for dose estimation [114] and scatter characterization [96, 115-119], since those quantities are difficult to obtain using analytical methods.

Besides the mentioned studies there has been developed a collection of Monte Carlo simulation packages for the simulation of radiation transport in generic environments that are widely used in the medical imaging community, such as Geant [120], EGS [121], MCNP [122], or Penelope [58].

Monte Carlo simulations of radiation transport model each photon (or particle) as a random sequence of leaps inside a volume that end in an interaction where properties of the photon change (its direction and/or energy). After undergoing an interaction the photon can either be terminated –e.g. its energy is too low or it has been absorbed as outcome of the interaction– or start a new track according to its new properties to a new interaction point. The process continues until the photon is terminated or it leaves the volume. Every time the photon is transported or a new interaction is simulated, a sequence of PDFs is randomly sampled.

In the particular case of photon transport, the interaction model is formed by a set of differential cross sections determining the PDFs of the random variables that define the track [58] in terms of the free path between interactions, the type of interaction taking place, and the energy loss and angular deflection applying to the photon as outcome of the interaction.

While Monte Carlo simulation can provide very accurate predictions of the behavior of real systems if appropriate models are used, it is by nature a random method and, therefore, it is subject to statistical uncertainty. The uncertainty can be reduced by simulating a larger number of events, however at a larger computational cost. This need of increasing computational burden to obtain accurate simulations is the major drawback of Monte Carlo methods.

When the simulation process is aimed at the estimation of a particular quantity arising from photons undergoing a subset of the available interactions –e.g. scattered x-rays reaching the detector in CBCT–, it is possible to reduce the uncertainty of the quantity of interest by using *a priori* information favouring events more likely to end up in the addition of information to the sought parameter. This can be seen as purposely biasing the Monte Carlo process to avoid wasting time performing calculations that are useless to the particular application. Techniques that reduce the uncertainty of a given outcome of the simulation are known as Variance Reduction (VR) techniques. VR techniques, when appropriately implemented, are able to drastically reduce the noise of a given quantity without biasing its value or distribution.

The following paragraphs briefly revise the most important components of x-ray Monte Carlo simulation.

Random Number Generation

Current Monte Carlo methods build upon the capability offered by computers to generate random numbers. All the random number generators used in Monte Carlo simulations are based on mathematical algorithms which generate very long sequences of numbers that are, therefore, repeatable, making them not true random, but pseudo-random or quasi-random.

The generator of random numbers is a key component in Monte Carlo simulation, since subtle correlations between the generated numbers could lead to large errors in the estimated quantities. As stated in [110], the sequence of random numbers used in Monte Carlo simulation should have the following properties:

i. The sequences of random numbers should be uncorrelated.
ii. The generator must have a long repetition period.
iii. The sequence of random numbers must have a uniform distribution and be unbiased.
iv. The sequence must be reproducible if it is started from the same point.
v. The generator has to be as fast as possible
vi. It is also desirable for the generator to be parallelizable, allowing the computation of several numbers at the same time.

Given these requirements, a collection of methods for the generation of random numbers is available in the literature [123-125].

Sampling of PDFs

As stated above, random numbers in the Monte Carlo simulation are uniformly distributed. However, the physical interaction modelled in Monte Carlo simulation seldom show a uniform distribution and random sampling methods have to be applied for the selection of the interaction outcome as a function of the known PDF.

For this reason a collection of methods has been proposed throughout the literature for the sampling of those functions. Examples of these methods are the inverse-transform method [126] that inverts the cumulative distribution function (CDF) of the event for the sampling, the Walker's aliasing method [127] that generates a new uniform version of the PDF, keeping track of the changes, and then uses two random numbers to sample inside this uniform distribution and then within the respective modified values, or rejection methods [128] that subject the uniformly distributed random number to a test to determined whether it will be accepted or not.

Variance Reduction Techniques

As explained above, VR techniques help in reducing the uncertainty of a given quantity by modifying the Monte Carlo sampling process according to previous knowledge on the system, the process to simulate, or both.

Particular examples of this type of techniques in photon transport is the interaction forcing [129] that modifies the length of the photon track according to the distance between the photon and the boundary of the material in materials where the probability of interaction is low to force the photon to interact before leaving the area. Another widely used VR technique is Woodcock tracking [130] that avoids the explicit computation of the points where the photon crosses through a boundary between two different materials –e.g. a soft-tissue area and a bone area– by using the lower mean free path of the materials in the volume and introduce virtual interactions.

The inclusion of VR techniques in Monte Carlo simulation of scatter is illustrated in chapter 6 and [119], and examples of VR in x-ray simulation, either for scatter estimation or for dose calculations can be found in [96, 117, 131].

2 Design, optimization and assessment of a small-animal CBμCT system combined with an fDOT system

2.1 Introduction

As explained in the introductory section of this work, modern drug development techniques relies heavily on the use of small-animal models and molecular imaging techniques, PET, SPECT or fDOT, to provide the required functional information that characterizes the behavior of the drug. However, these techniques suffer from a lack of anatomical information that is commonly provided by anatomical imaging techniques such as MRI or CBμCT being the last one more widely spread due to its low cost when compared and ease of integration.

As well as complementing the information obtained using molecular imaging techniques, CBμCT by itself is a valuable tool in small-animal imaging and is commonly used in research fields associated with the morphology of the sample (e.g., bone studies). For this reason, an important amount of research effort has been put in the last years for the development, assessment and evolution of CBCT systems and acquisition techniques, not only in the preclinical environment [132-136] but also in the clinical world, where the use of CBCT is becoming more popular for special applications such as cardiac imaging [137-140], otolaryngology [9-11], interventional C-arm [6, 41], musculoskeletal imaging of extremities [8]or in-line CBCT for IGRT [15].

In the last ten years, different CBμCT systems based on microfocus x-ray tubes and semiconductor-based flat-panel detectors arranged in cone-beam geometry have been developed, and their suitability has been proved [2, 141]. Flat-panel–based cone-beam configurations present advantages over other configurations –e.g., pencil or fan-beam geometries– used in clinical applications. These advantages include reduction in acquisition time, large axial field of view (FOV) with no geometrical distortions, optimization of radiated dose per time and data acquired, and a more compact, space-saving design. Additionally, indirect conversion semiconductor flat-panels are particularly interesting for small-animal imaging due to their high-resolution capability, especially when the micro-columnar scintillation screen is directly grown on the semiconductor detector. Current advances in semiconductor technology point to improved features in the future [142-143].

Regarding molecular imaging techniques, fDOT has received significant attention due to its capability for imaging biological processes not visible with other techniques, its low cost and its innocuous nature since no ionizing radiation is used for the acquisition. However, fDOT is a low resolution technique and the reconstruction problem is highly ill-posed [144]. It has been proved that anatomical information provided by CBμCT could be used not only to properly localize the fluorescence data, but also to provide prior information for the direct fDOT problem [145] or for the inverse fDOT problem [23, 146-149], yielding higher quality reconstructed data.

For the last reason several combined fDOT-CBμCT systems have been reported in the literature during the last years [150-152], most of them using previously developed CBμCT systems. However very few details about the design and performance of the CBμCT system of these developments are available and little information was provided on the optimization of acquisition geometry and protocols for the particular imaging task.

Here we report the design in terms of hardware, software and acquisition geometry of a CBμCT system designed to be coupled to a fDOT system. The system was designed for the acquisition of structural data to provide anatomical information for localizing fDOT data and for the acquisition of high-quality soft-tissue data to be used as prior information for the fDOT reconstruction or as a research tool by itself.

We also addressed in this chapter the calibration of the system and present several methods, some of them new to the literature, to calibrate the different parameters.

We optimized the geometrical configuration of the system and the spectral conformation of the beam to maximize image quality and delivered dose.

The system was evaluated both in terms of its critical individual components and in terms of overall performance. To this end we measured the stability, linearity, resolution, and the noise and signal transfer properties of the detector; the stability of the x-ray source; and the dose, resolution, contrast and noise properties of the reconstructed data.

2.2 CBμCT system design

For the system design we took into account the imaging tasks required for the provision of complementary information to fDOT data. In particular, two different imaging tasks are contemplated, one for the provision of rough structural information mainly provided by bony structures in the animal body, and a second one for the provision of more accurate quantitative information for the provision of prior information for the fDOT data reconstruction process or to be used as standalone data. This second imaging task required the optimization of the relation between soft-tissue contrast and dose delivered to the subject.

In the following sections we detailed the components and building process of the system, the data acquisition and reconstruction approaches implemented for the system, the calibration methods used to obtain high quality data and the methods followed to optimize the acquisition protocols according to the imaging task.

An overall view of the fDOT-CBμCT system with the shielding elements in place but with no covers is shown in figure 2.1.

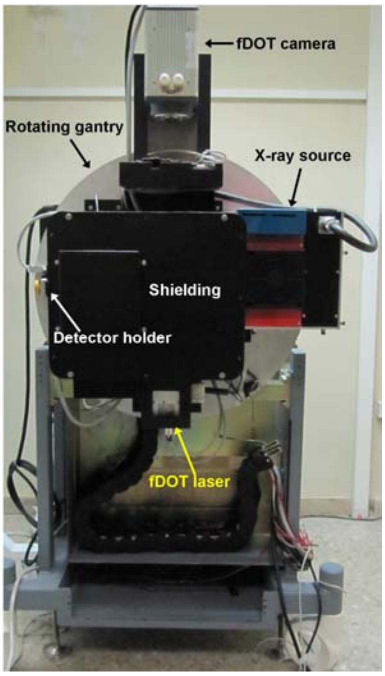

Figure 2.1. Overall view of the fDOT-CBμCT system with the shielding elements in place.

2.2.1 CBμCT system components

The main components of a CBμCT system based on flat-panel detectors are the x-ray detector and the microfocus x-ray source. The constraints imposed by the imaging application determine the type of source and flat-panel detector chosen by the designer.

In small-animal CBμCT systems, it is important to use a detector with appropriate image resolution to obtain the high-quality images necessary for preclinical applications.

The maximum pixel size and minimum resolution required for the detector depend on the geometrical configuration of the system (see below). High sensitivity and low noise level are also highly desirable features when attempting to minimize the radiation dose.

The output of the x-ray tube must be stable enough to ensure a constant radiation level during the acquisition process. Its focal spot size must be sufficiently small to not degrade system resolution. The maximum admissible size for the focal spot is determined by the detector pixel size, the geometrical configuration of the system and the required resolution for the particular imaging task.

Furthermore, highly stable motorized devices are used in the design of small-animal CBμCT systems to place the animal within the FOV and to perform the rotational movement of the x-ray source–detector assembly around the sample. Finally, control components –e.g. computer, motion control drivers or shutter– and shield elements must be incorporated to ensure simple and safe operation.

The scanner design includes a computer that controls the microfocus x-ray tube and the CMOS flat-panel detector, both of which are assembled in a common rotating gantry.

The computer synchronizes the gantry motions with the image integration in the detector. The data acquired from each angular position are captured by a digital frame grabber.

The x-ray flat-panel detector used is the C7940DK-02 model (figure 2.2 A) (Hamamatsu Photonics K.K., Hamamatsu, Japan). A complete description and an evaluation of some of the performance parameters can be found in [72, 153]. It is an indirect flat-panel detector based on a CsI:Tl scintillator screen and a high-fill-factor CMOS image sensor to detect the optical photons. The features of the flat-panel detector as reported by the manufacturer are summarized in Table 2.I.

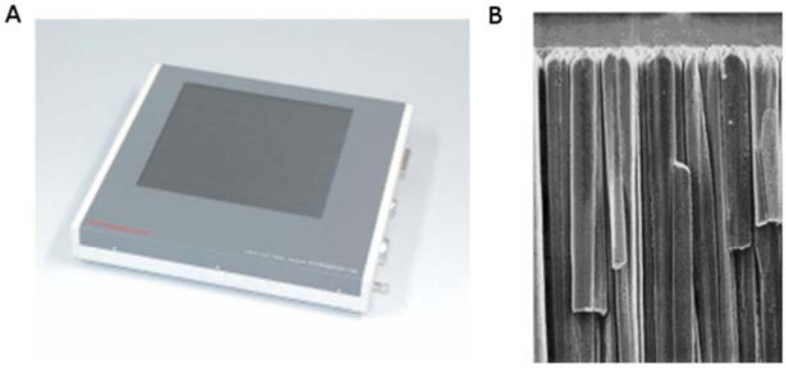

Figure 2.2. Hamamatsu C7940DK-02 X-ray flat-panel detector (A) and detail of the needle-like CsI:Tl crystal structures on the scintillator layer (B). Images courtesy of Hamamatsu Photonics K.K.

The scintillator layer of the flat-panel detector is a 67.6 mg/cm^2 microcolumnar CsI:Tl layer directly deposited over the CMOS photodiode matrix surface (figure 2.2 B). A photodiode matrix with active pixel elements connected to CMOS transistor switches enables detection and read-out of the visible photons generated on the scintillation screen. The photodiode CMOS matrix has 2x2 and 4x4 binning capabilities and a high fill-factor (79%). The on-chip signal amplification channels have a low noise level, and an offset suppression circuit based on CDS is assigned to each of these channels. This design achieves a high degree of image uniformity and a low noise level. However, correction tasks must be performed after acquisition of an image in order to obtain the best achievable quality.

Table 2.I. X-ray flat-panel detector characteristics.

Parameter	***Value***
Pixel size	0.05, 0.1, 0.2 mm (Binning 1x1, 2x2, 4x4)
Photodiode area	120 x 120 mm
Number of pixels (Total/Active)	2400 x 2400 / 2240 x 2344
Frame rate	2, 4, 9 fr/sec (Binning 1x1, 2x2, 4x4)
Noise (rms)	1100 electrons
Saturation charge	2.2 M electrons
Dynamic range	2000
Sensitivity (@ 80 kV)	50 LSB/mR

The detector is placed on top of a 95 mm-long linear motion stage that allows its displacement in order to modify the acquisition geometry. The linear stage is the model LTM 80 (Owis GmbH, Staufen, Germany) equipped with a stepper motor.

The CBµCT system makes use of a tungsten anode microfocus x-ray source (L9631-MOD2, Hamamatsu Photonics K.K., Hamamatsu, Japan). The source has 40 to 110 kVp energy range and maximum anode current of 1 mA, limited as a function of kVp to deliver a maximum power of 50 W. The focal spot size of the x-ray beam varies linearly between 15 and 80 µm with the power set, for power values larger than 6 W.

A fixed collimator made of a tungsten-bismuth alloy shapes the x-ray beam to cover the detector area and a filter holder is included to place filter materials for the x-ray beam.

As stated above, the detector and x-ray source are mounted onto a rotating gantry. This gantry consists of an 80 cm-diameter aluminum plate that holds both components and a rotating motion stage model RV350PP (Newport Corp., Irvine, CA).

The sample is placed inside the FOV of the system by means of a 295 mm-long linear motion stage, model LTM 80 (Owis GmbH, Staufen, Germany) equipped with a stepper motor.

The motorized stages included in the system are managed by servo drives with integrated motion controller boards, model ISCM 4805 (Technosoft S.A., Neuchatel, Switzerland). The individual drives communicate via a CAN bus which end side is connected to the acquisition computer by a RS-232 serial link.

All the components included in the system were connected to a regular personal computer in charge of the control of the whole system. The acquisition computer ran a Linux operating system (Fedora Core 9).

2.2.2 Data acquisition

Several acquisition schemes make it possible to obtain the projection data for the different angular positions. There are two main trends for the acquisition of CBµCT data. Most of the current systems use a continuous acquisition scheme, most of the times using continuous x-ray beam flux [154]. This approach has the advantage of faster acquisition times when a fast detector is used, although the effect of image lag, mechanical imperfections and synchronization flaws are more conspicuous.

An alternative is the acquisition of a stack of frames for each angular projection, with the gantry steady during the acquisition (step-and-shoot). While the gantry rotates, no image is acquired and the radiation beam is blocked to minimize the effect of image lag and to avoid the delivery of useless dose to the subject under study. Some of the systems reported in the previous literature followed this approach [4].

We implemented both approaches for data acquisition in the system presented in this chapter. The data acquisition software was implemented in C language using a multi-thread approach that guarantees the maximum data throughput provided by the detector and the correct synchronization between gantry movement and image acquisition, assuring that no frames are lost during the acquisition process. Continuous or step-and-shoot acquisition can be selected by the user together with the rest of acquisition parameters by setting the proper flags when launching the application.

The acquisition task was split into two different tasks each one associated to an execution thread generated by the main application. The two threads were synchronized using POSIX semaphores and used a shared memory area to share data. One of the threads was in charge of carrying out the movement of the system while synchronizing it with the flat-panel detector and transfer the data provided by the detector from the frame grabber memory to the shared memory area.

Figure 2.3 shows a schematic description of the acquisition process for both the continuous (figure 2.3 A) and the step-and-shoot (figure 2.3 B) acquisition approaches.

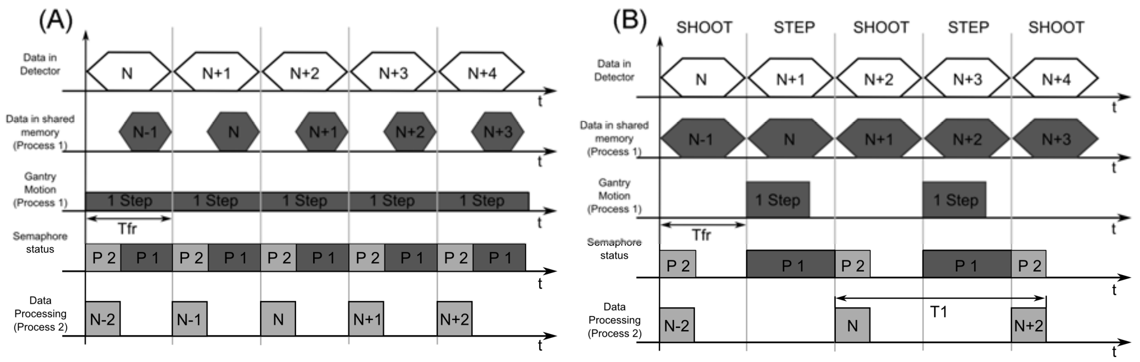

Figure 2.3. Schematic representation of the acquisition protocol for continuous (A) and step-and-shoot (B) acquisition.

Figure 2.3(A) shows a schematic description of the different tasks and their temporal synchronization for the acquisition of CBμCT data using the continuous acquisition approach. As explained above there are two threads involved in the acquisition process. The first of the threads is in charge of launching the continuous rotation of the gantry around the subject, and of grabbing the acquired data from the frame-grabber dedicated memory area and move them to the shared memory area where they are left for the second thread to process them. The second thread accesses the shared memory area, performs the required processing (if any) on the data and save the data to disc before a new dataset is delivered by the acquisition thread.

In order to properly synchronize the acquisition process, the rotation speed of the gantry must be set as a function of the number of angular positions to acquire, N_p, and the angular span, A_s, to be covered during the rotation. If we denote the image integration of the detector by T_{fr}, the rotation speed is given by the following expression:

$$\omega_g = \frac{A_s}{N_p \cdot T_{fr}} . \tag{2.1}$$

Every time a projection is available at the frame-grabber memory, the acquisition thread records the angular position where it has been acquired by interrogating the motion controller about the gantry encoder position. Immediately after recording the angular position, the thread locks the shared memory area, copies the acquired data to it and adds the angular position stamp to the dataset. Once the data has been moved, it releases the semaphore to the shared memory area, indicating the processing thread that a new dataset is available for processing.

The time taken by the acquisition is only set by the acquisition thread, since the frame period of the detector is longer than the time needed for the basic processing and asynchronous writing to disc.

If the sample is too large to fit inside a single axial FOV, the whole volume can be acquired by performing rotations combined with axial shifts of the bed. From the parameters of the detector and the requirements of the given acquisition, it is possible to calculate the time taken by the acquisition process. This effective acquisition time (excluding warm-up and sample positioning) is given (in seconds) by the following expression:

$$T_{acq} = T_{fr} \cdot N_p \cdot N_{FOV} , \tag{2.2}$$

where N_{FOV} is the number of bed positions to acquire.

The step-and-shoot approach used was very similar to the one presented in [155], which was in turn based on the approach in [4]. The acquisition thread was implemented as an event-driven finite-state machine with two possible states to take advantage of the maximum data rate provided by the detector [156], thus reducing acquisition time and delivered dose. The first state (*step*) was used to move the gantry to the next angular position and to move the just acquired data from the frame-grabber memory to the RAM shared memory area. The second state (*shoot*) performs two tasks:

a) launching the acquisition of either a single frame or a frame sequence if several frames were to be averaged in the current angular position, and
b) release the shared memory area to allow the processing thread to process the dataset acquired at the previous gantry position.

The transition between states is triggered in synchrony with the detector image integration time, T_{fr}, as shown in figure 2.3 B.

The processing tasks carried out by the processing thread are identical to those for the continuous acquisition protocol described above.

Quality of the projection images can be improved by acquiring and averaging several frames per angular position. In this case, the finite-state machine remains in shoot state for a time equal to N_{ave} times T_{fr}, where N_{ave} is the desired number of frames, until the last frame of the current projection arrives. Therefore, in the multi-frame case there are several *shoot* periods between two *step* periods. Additional pre-reconstruction processing, such as filtering, could be performed during *shoot* intervals, when the CPU is idling.

The step-and-shoot protocol has the capability of increasing the quality of projection data in terms of spatial resolution compared to the continuous protocol. This improvement is caused by the stationary position of the gantry during data acquisition, avoiding undesired motion artifacts. However the acquisition time is longer for the step-and-shoot approximation owing to the detector frame discarded during every *step* interval. In addition, the current implementation of the system does not count with a beam shutter fast enough to block the x-ray beam during the *step* intervals and, therefore, higher dose is delivered to the sample when using step-and-shoot protocols.

Analogously to the case for continuous protocols, the total acquisition time for step-and-shoot protocols is given by,

$$T_{acq} = T_{fr} \cdot \left(N_{ave} + 1\right) \cdot N_p \cdot N_{FOV} \,. \tag{2.3}$$

Note that when acquiring the same number of angular projections than using a continuous protocol, and with one frame for each of them, the total acquisition time is twice the time employed by the continuous acquisition, with the corresponding increase in dose.

2.2.3 System calibration

Acquired raw projection CBµCT data contain undesired properties that have to be corrected prior to reconstruct the tomographic volume, to obtain consistent attenuation values. In addition to the corrections performed on the raw data, a number of parameters describing the system have to be properly calibrated and applied during the reconstruction process for the generation of high quality data.

In particular, the following calibration tasks are carried out for the system presented: obtaining of the gain and dark maps for each acquisition protocol, identification of defective elements in the detector, estimation of the deviation of the geometrical parameters of the system from their nominal values, calibration of the stitching parameters to concatenate volumes from two consecutive bed positions, and calibration of the water value for each acquisition protocol to convert reconstructed data to Hounsfield units.

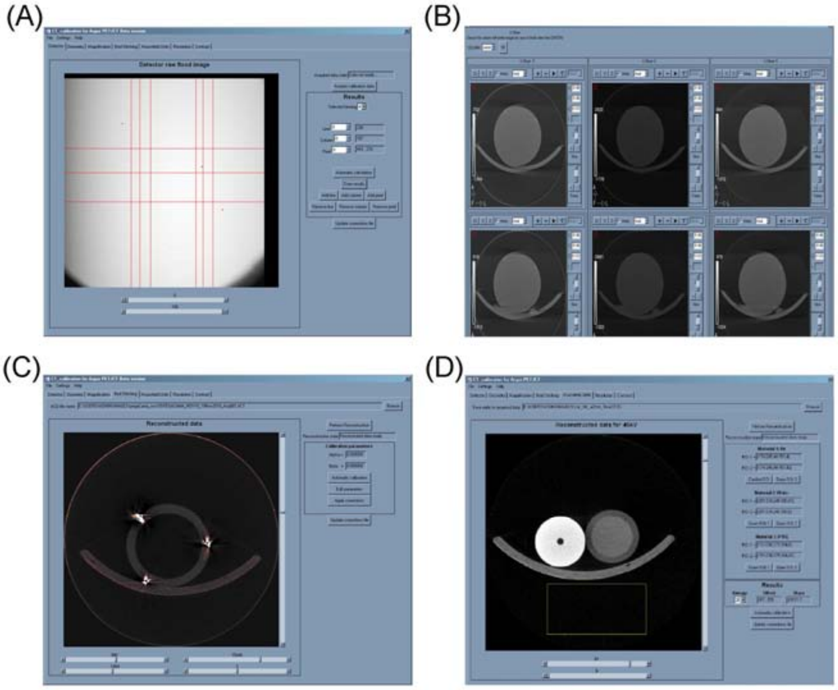

Figure 2.4. Screenshots of the software application for the calibration of the CBµCT system. Interface for the calibration of defective elements in the detector (A), for the geometrical calibration of the system (B), for the stitching parameters to concatenate consecutive bed positions (C), and for the calibration of Hounsfield units (D).

All the calibration methods, with the exception of the gain calibration which has to be performed regularly to maintain the quality of the reconstructed data, were included in a user-friendly software application that allows the calibration of the whole system in a semi-automated way, applying the methods detailed below. Figure 2.4 shows several screenshots of the application.

2.2.3.1 Gain and dark maps

Raw image data provided by the FP detector is contaminated by structured noise which shows as deterministic patterns arising from the structure of the imaging sensor. This structured noise has to be removed to enhance the quality of the projection data and avoid artifacts in the reconstructed volume. In particular the raw signal is contaminated by two types of structured noise, namely dark signal and gain map of the detector [157].

The dark signal is the image that results only from random generation of electrons and holes in the reverse bias photo-detectors in the sensor area that generates a small current even when no radiation is reaching the sensor [158]. Since this signal is always positive, it has a non-zero mean with a random component superimposed. This non-zero average signal forms an offset image that depends on the image integration time and temperature of the sensor and that must be subtracted from the acquired data. The dependence of the offset on temperature makes it advisable to acquire the correction data just prior to the CBμCT data acquisition.

The second component of structured noise arises from the small differences in gain of the different individual pixels that generate slightly different signal values for a uniform flux of radiation. The gain map of the sensor is usually estimated by averaging a set of flood images for which the detector is irradiated with the beam set at the acquisition protocol configuration in terms of kVp and filtration and for a value of exposure sufficiently separated from the saturation point of any pixel in the detector.

The straightforward way to correct the acquired data for dark and gain is the so-called flat-field correction [156, 159], which consists in the subtraction of the dark offset and the subsequent division by the dark-corrected gain map, according to the following expression [160], for a pixel with coordinates (*u*,*v*):

$$C(u,v)=\frac{R(u,v)-\bar{O}_R(u,v)}{\bar{G}(u,v)-\bar{O}_G(u,v)}, \tag{2.4}$$

where R is the acquired data, $\bar{O}_R$ is the offset data acquired for the temperature conditions of the acquired data, $\bar{G}$ is the gain map and $\bar{O}_G$ is the offset image for the temperature conditions of the gain map.

While the flat-field correction approach provides sufficient image quality for most applications, it inherently assumes a perfect linear gain curve for each pixel. In real detectors, however, it remains some degree of non-linearity in the gain curve of the pixels [109], causing the equalization of the pixel response to leave slight differences between the response of adjacent pixels that in turn translate into artifacts in the reconstructed image (see section 1.4.4). This effect is more evident for signal levels far from the calibration point.

There are several approaches to compensate the remaining non-uniformity, among which the one proposed by Seibert et al. [109] and further extended by Kwan et al. [108] has been shown to largely compensate the non-linearity of pixel response. We selected a simplified version of it for the correction of raw data in the presented scanner. The approach consists in the acquisition of several gain maps for a set of different exposure levels at the detector, by modifying the anode current for the same beam kVp and added filtration. The highest current used is equal to the one used for classic flat-field correction. Figure 2.5 depicts the deviation from ideal linear gain and how the multi-bright calibration data is obtained, for a simplified version of the approach in [109].

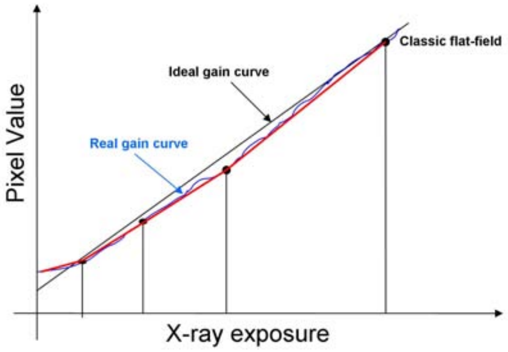

Figure 2.5. Multi-bright calibration for the compensation of non-linearity in individual pixels gain curve.

To correct a pixel of the acquired data, first, we identified the signal level in the gain maps closest (but lower) than the one of the pixel to correct; second, the pixel value is divided by the result of interpolating the identified gain value and the one for the immediately superior anode current value; and, third, the corrected value is scaled by the ratio between the interpolated gain and the one used for classic flat-field correction.

In our system we averaged 50 images for 5 exposure levels ranging from zero (dark signal) to 90 % of the saturation limit of the detector.

2.2.3.2 Calibration of defective elements of the detector

Some of the elements of the detector (isolated pixels, rows, or columns) are not responsive to the incoming radiation or their gain factor is very low and they provide an insufficient signal for appropriate image formation [156]. These elements have to be identified and corrected in the acquired data, usually by means of interpolation between the adjacent valid elements [66].

There are several methods for the identification of defective elements but most of them are proprietary and few details are available about their implementation and it is common to obtain defect maps directly from the manufacturer of the detector to which new identified pixels are added manually. We developed an automated method for the identification of defective elements from a set of images irradiated with a uniform x-ray beam, after dark and gain correction.

We developed two approaches, one for the detection of defective rows or columns and a second one for the detection of isolated pixels.

For the detection of rows (columns), the detection area is split into three regions and the average column (row) of each section is computed. We computed the 3-point derivative of the three averaged columns (rows). If two peaks separated by one position are larger than 1.3 times the average value of the derivative in one of the three averaged columns (row), the row (column) surrounded by the peaks is marked as defective. If the two peaks are larger than 1.15 times of the average value of the derivative but in more than one of the three regions, the row (column) is marked as defective.

Isolated defective pixels are found by computing the 2D Fourier transform of the flood image with the highest current and filtering it with a quadratic 2D ramp filter which frequency response is given by:

$$H(f_u, f_v) = f_u^{\,2} \cdot f_v^{\,2}, \tag{2.5}$$

where f_u and f_v are horizontal and vertical frequency, respectively.

After filtering the image, its inverse Fourier transform is computed and those pixels with a value larger than a user-selectable threshold are identified as defective.

To identify clusters of grouped defective pixels, the image area is split into groups of four pixels and their average value is calculated for each of the uniform images. If the average response of the cluster as a function of anode current is not monotonic or its linear regression has a $R^2 < 0.75$, the cluster is marked as defective. Other approaches to estimate clusters of defective pixels use the temporal stability of their response [160].

2.2.3.3 Geometrical calibration

It is well known that deviations between the expected geometrical setup of the system and the real one are a source of severe artifacts in the reconstructed data [161-162]. Therefore, correct alignment between source and detector is critical to achieve the theoretical resolution value and avoid the presence of artifacts in the reconstructed image. There are several suitable methods for estimating the differences between the geometrical parameters of the real system and those of the original design from experimental data [163-167]. These methods are usually based on the acquisition of a set of markers, usually ball bearings, placed on a phantom with a known geometry. The projection position and usually their trajectories are fitted to the theoretically predicted values, derived from the ideal geometrical arrangement, in order to calculate the deviation between the real and ideal geometry setup.

Figure 2.6 shows a schematic depiction of the geometrical parameters of a CBCT, to clarify the following explanation.

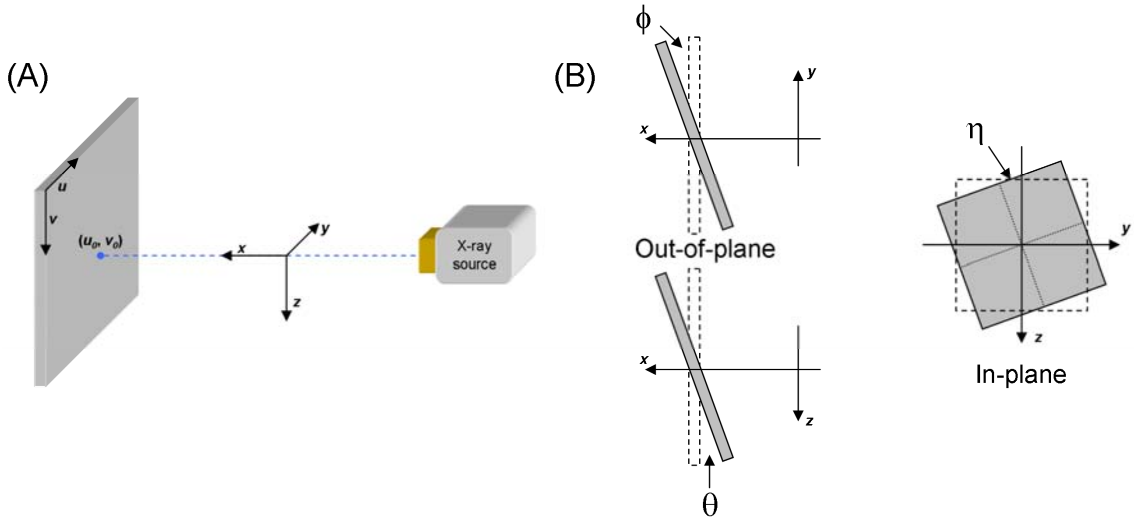

Figure 2.6. Schematic representation of the geometrical parameters of a CBCT, showing the world coordinate system (x,y,z) and the detector coordinate system (u,v). The blue dashed line in panel (A) shows the position of the central ray of the beam impinging on the detector at the piercing point (u_0,v_0). Panel (B) shows the three possible rotations of the flat-panel detector, two out of plane (ϕ,θ) and one in plane (η).

In this system, the geometrical deviation from the original design was measured by means of an analytical procedure based on the assessment of the elliptical trajectories described by two ball bearings placed in a soft material, such as foam, as described in [166]. Using this method it was possible to estimate the value of the in-plane rotation of the detector (η) and one of the two out-of-plane tilt angles of the detector (ϕ), the position of the piercing point (u_0, v_0) –i.e. the position where the central ray, which joins the x-ray source focus and the isocenter, impinged on the detector surface–, and the actual distance between the x-ray source and the flat-panel detector. The remaining angle, although not as critical as the previous two [163, 166], was first reduced as much as possible to be able to assume that its value is close to zero. The correct alignment in the direction of this angle was mechanically assessed. The estimated angular deviations are mechanically corrected. The position of the piercing point is stored to be included in the data description used by the reconstruction engine.

2.2.3.4 Calibration of the bed stitching parameters

As mentioned above, the extent of the axial FOV can be expanded by concatenating volumes acquired for two consecutive bed positions, with a small overlapping portion. While the ideal movement of the bed would be along the axis of rotation of the scanner real positioning systems present small deviations from this situation that translate into small differences in the position of overlapping structures in the two volumes to concatenate. When the volumes are concatenated and the overlapping area is fused, the discrepancies in the positions of structure arise as double contours that worsen image quality in this overlapping area

We developed a method to model the deviation between the axis of displacement of the bed and the scanner rotation axis. We modeled the deviation using two angular shifts between the ideal and actual trajectories, as depicted in figure 2.7.

We designed a dedicated phantom to estimate the angular displacements, shown in figure 2.7. The phantom was formed of a 30 mm-diameter PMMA tube with length equal to 2 times the axial size of the FOV minus the size of the overlap area. In our system we used an overlapping area of 20 mm and the size of the FOV depended on the selected magnification. The phantom was designed for an intermediate magnification factor of 1.6, yielding a total length of 130 mm.

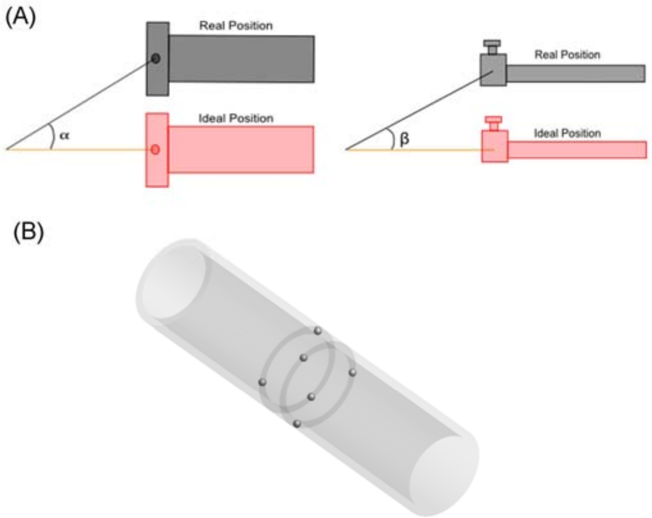

Figure 2.7. Angular displacements calculated for the calibration of the bed movement (A) and sketch phantom used for the calibration process (B).

At an axial position of half the phantom length –i.e. the central position of the overlapping area in the image– two sets of three 1 mm-diameter ball bearings were placed forming two rings. One of the rings was shifted 5 mm towards the bottom of the phantom and the second 5 mm towards the top. The bearings were positioned each with an angular distance of 120º with respect to the next and we set a phase shift of 60º between the two rings.

The phantom was scanned twice, one per bed position, in such a way that the two rings fell into the overlapping area for both acquisitions. The two bed positions were reconstructed independently, yielding two reconstructed volumes, one with the overlapping area at the final slices and one with the overlapping area at the initial slices. We extracted the overlapping area and used a threshold at half the maximum value to segment the ball bearings from the surrounding elements. The center of mass for each ball bearing was computed after identifying unconnected areas –one for each ball bearing– using morphological operations. We found the misalignment parameters by minimizing the distance between ball bearings in the two volumes in the least squares sense.

2.2.3.5 Hounsfield Units calibration

Hounsfield unit conversion was calibrated for all the acquisition protocols by measuring a phantom consisting of three materials: air, water and Teflon. The average values in two regions-of-interest drawn into the water and air regions were fit linearly according to the well-known expression for conversion to Hounsfield units [25].

2.2.4 Data reconstruction

For the reconstruction of tomographic data we used a filtered backprojection-like approximation, based on the well known FDK algorithm [79], introduced above, for circular acquisition trajectories. Our implementation of the algorithm takes profit of the highly parallelizable nature of the reconstruction process and the massive parallel computation capabilities offered by Graphic Processing Units (GPUs). Also, to speedup the computation, the algorithm employs the hardware interpolation offered by GPU’s texture memory.

The original FDK approach presented by Feldkamp, Davis and Kress [79] was intended at the reconstruction of complete circular trajectories (i.e. 360 degrees angular span) and cannot deal with laterally truncated projections, which generate artifacts in the reconstructed slices. We incorporated several modifications available in the literature to handle these types of inconsistencies in the data.

2.2.4.1 FDK implementation in GPU

As stated in section 1.3, the FDK reconstruction algorithm consists of several steps that have to be carried out sequentially. For every individual projection, the air value has to be normalized (I_0 correction), prior to log-transform the data. Every row of the pre-processed projection is then filtered by a frequency ramp-like filter yielding the high-frequency version of the original projection data. The filtered projection is then backprojected along its angular direction onto the voxel grid of the reconstructed data. These three steps must be carried out sequentially, since the output of each one of them is the input for the next. However, every step involves several computations for every pixel in the projection domain or voxel in the reconstructed data domain. The processing of an individual pixel or voxel is to a great extent independent of the rest of pixels or voxels in the data and, therefore, a great reduction in computing time can be achieved by properly process them in a parallel fashion.

Figure 2.8 shows a basic outline of the execution flow for the reconstruction of a volume. In the figure, blue boxes denote processing steps carried out on the CPU and orange boxes denote those carried out on the GPU. Most of the processing is performed on the GPU, exception made of the initial steps where the projection data is loaded and the I_0 is computed from an object-free area in the projection provided by the user.

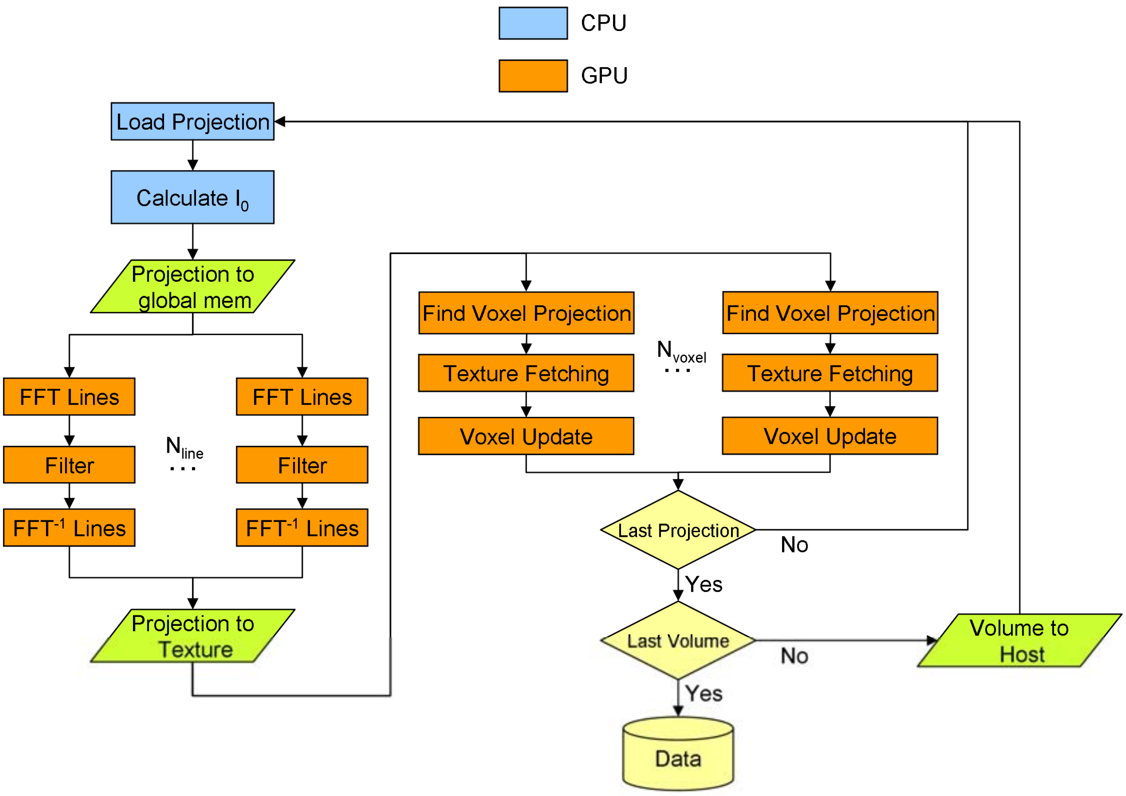

Figure 2.8. Outline of the FDK reconstruction process implemented in GPU. The tasks marked in blue are performed in the CPU, while those marked in orange are carried out in the GPU.

After the calculation of the I_0 value, the projection is loaded into an area in the global memory of the GPU. Every pixel in the projection is processed in parallel, normalizing it by I_0 and log-transforming its value.

If the projection is laterally truncated every row is extended in parallel, using the mirror extrapolation algorithm proposed by Ohnesorge et al. [98]. The extrapolation algorithm guaranteed a smooth transition from the last recorded attenuation value to zero attenuation while maintaining the noise properties of the projection data in the extrapolated region.

Every pixel in the extrapolated projection is then multiplied by the FDK weighting factor that accounts for the divergence of the radiation beam in the longitudinal direction and, if the angular span of the acquisition is lower than 360 degrees, it is multiplied by an angle-dependent weight to account for incomplete acquisition trajectories. The weight to compensate incomplete trajectories is calculated according to the approach presented by Silver et al. [168], which is based on the original work by Parker et al. [169].

The Fourier transform of each row of the processed projection is then computed using the CUFFT library (Nvidia Corp., Santa Clara, CA) and it is then filtered by a frequency-ramp filter multiplied by an apodizing window, selected by the user, to compensate the amplification of high-frequency noise caused by ramp filtration. Our implementation included Shepp-Logan and Hann apodizing windows. After performing the filtering step, the inverse Fourier transform of the filtered rows of the projection is calculated.

The filtered projection is moved from the global memory space of the GPU to a two-dimensional texture memory for the computation of its backprojection into the reconstructed volume. Texture memory offers several advantages over global memory for backprojection of the already processed projection data. First, texture memory is cached and provides faster access to data when an appropriate degree of memory coalescence is achieved within GPU execution blocks, and, second, it provides hardware-based interpolation algorithms to compute values for non-integer memory positions.

In our implementation every instance of the backprojection GPU kernel processes a column of the reconstructed volume. For each column in the volume, we calculate the position where the ray joining the first voxel and the x-ray source focus hits the detector. Since voxels of the same column are projected along a column of the detector, the equation of this projection column is computed.

The software computes the position of the projection for every voxel within the detector column and calculates the projected attenuation value using bilinear interpolation, taking advantage of the aforementioned hardware-based interpolation algorithms offered by texture memory. The estimated attenuation is added to the value in the voxel after the proper normalization.

The process is repeated for every projection in the dataset. If the volume to reconstruct is too large to fit into the GPU memory, the software splits the computation into several sub-volumes and repeats the explained process for each of them.

2.2.5 Optimization of the geometrical configuration

The selection of the appropriate geometrical configuration for the system is a key point for the performance of the CT system in terms of image quality and power requirements.

Given a set of hardware components, the choice of the geometrical configuration of the system determines the achievable spatial resolution of the reconstructed data for the detector pixel pitch and x-ray source focal spot size [34], the air gap, which dramatically impact the quantity and properties of the scattered radiation [89-90, 119], the required x-ray power to obtain an appropriate signal level at the detector, and the minimum footprint for the system.

The selection of a geometrical configuration implies the proper choice of a number of parameters which usually have opposite effects in the different outcomes to optimize. For instance, large air gaps are highly desirable to minimize the amount of scatter in the data and, therefore, the degradation of image quality caused by scatter [90, 119], but setting a large air gap forces the designer to increase the x-ray power, according to the inverse squared distance law, to achieve the required signal at the detector. A reduction in the required power is of great importance for the development of small-animal CBμCT systems owing to the close relation between focal-spot size and x-ray source power that usually imposes the use of low-power sources to meet the resolution requirements of the small-animal imaging task.

In addition to the increase in power, selecting a large air gap for a given magnification factor and/or target resolution enlarges the minimum footprint of the system which could lead to non-acceptable mechanical configurations for real systems.

Summarizing, the selection of the geometrical configuration of CBμCT is a complex problem with a non-unique solution in which a compromise between the different factors must be sought to obtain an appropriate level of image quality while keeping the system feasible to build.

In the case of the small-animal CBμCT system described in this chapter we had very strict requirements in terms of maximum size of the system, since the x-ray source and flat-panel had to be mounted on the 80 cm-diameter rotational gantry. Also, the FOV must be large enough to permit the imaging of large murines, such as rats.

Another clear restriction of our system is the explicit relation between delivered power and focal spot size which in turn limit the maximum air gap that can be accommodated for a desired resolution value.

The position of the x-ray source at the rotating gantry was fixed to make it fit completely within the aluminum plate (see figure 2.1). This constraint fixed the source-to-axis distance (SAD), which had a value of 155 mm.

Given the size of the flat-panel detector and the need of a FOV large enough to fit a large rat (~70 mm diameter) plus a small margin to allow imprecise placement of the specimen that would arouse during regular imaging practice, we selected a minimum source-to-detector distance (SDD) of 230 mm. The baseline geometrical configuration yielded a magnification factor of 1.48 and a FOV size of 80.86 mm (78.06 mm after considering the non-active part of the detector).

Provided the baseline geometrical configuration and given that the detector is mounted on a 95 mm-long motorized linear stage which permits the modification of the SDD up to 325 mm we investigated the impact of the magnification factor and focal-spot size on the spatial resolution. This study served as the basis for the subsequent optimization of the acquisition protocol by identifying the limits in power for a required resolution as a function of the magnification of the system.

We followed an approach previously described by Zbijewski et al. [8] based on a simple model that computed the MTF of the system as a combination of the presampled MTF of the detector and an analytical model for the MTF of the x-ray source focal spot. The MTF of the complete system is then computed as the product of the two MTFs at the central plane of the reconstructed volume, i.e. a coronal plane parallel to the detector which intersects the isocenter of the scanner.

The presampled MTF of the detector was experimentally measured as explained in section 2.3.1. For the focal spot blur we picked up a first-order model described in [8, 52, 170] which modeled the focal spot as a Gaussian with a width value given by the nominal focal spot size modified by the magnification factor, according to the next expression:

$$MTF_s(f_u, f_v) = \exp(-\pi[[(M-1)/M]a_s]^2(f_u^2 + f_v^2)), \tag{2.6}$$

where M is the magnification factor, a_s is the focal spot nominal size, and f_u and f_v are the horizontal (i.e. along detector rows) and the vertical (i.e. along detector columns) components of the frequency, respectively. While the assumption of a Gaussian distribution is not realistic [170], it has been proved useful for this kind of calculation [34].

To obtain the proper MTF measurement, the presampled MTF of the detector must be translated to the isocenter of the scanner, which is performed by multiplying the original spatial frequency values by the magnification factor M.

Denoting the translated presampled MTF for the detector as MTF_{FP}, the total MTF for the system is given by:

$$MTF_t(f_u, f_v) = MTF_{FP}(f_u, f_v) \cdot MTF_s(f_u, f_v)\,. \tag{2.7}$$

To evaluate the achievable spatial resolution we considered MTF_t to be symmetric. This is a reasonable assumption since the analytical model adopted for MTF_s is indeed symmetric and the presampled MTF has been shown to be also symmetric for FPs with square pixels [66]. Taking into account the symmetrical properties of MTF_s, without lose of generality and for the sake of simplicity, we evaluated the function along the horizontal frequency direction.

We assessed the achievable spatial resolution as a function of magnification and x-ray power as the cutoff frequency for values of MTF_s of 0.5 and 0.2, denoted as MTF_{50} and MTF_{20}.

2.2.6 Optimization of the acquisition protocol

The selection of the appropriate imaging protocol is of paramount importance for the minimization of dose while maintaining the desired level of image quality. While the geometrical configuration of the system, as stated above, has a major impact on the achievable resolution, fixes the maximum x-ray power to be used for a desired resolution and a given magnification factor, and plays an important role on the effect of scatter (see chapter 6), the selection of the x-ray beam peak energy and filtration must also be carefully carried out.

Depending on the imaging task the x-ray tube voltage and beam filtration must be tuned to maximize the image quality provided between the areas of interest for a target dose or, equivalently, to minimize dose for a required image quality.

Several studies were carried out at the early times of CBμCT imaging to find the optimal energy maximizing image quality as a function of sample size, assuming a monochromatic beam. Grodzins [171] used the number of photons reaching the detector as the optimization criteria, deducing a simple formula for the optimal energy for cylindrical samples. Spanne [172] used several optimization criteria on the basis of findings by Grodzins. Results in [172] showed that using the dose at the centre of the object, instead of the number of photons behind it, could yield a difference in optimal energy of a factor of 10 for large sample sizes.

Several recent works [173-175] explored the impact in image quality of x-ray energy and filtration optimization in breast CT, clinical CT and CBμCT using the dose-weighted contrast-to-noise ratio (CNRD) as the optimization criteria. CNRD is defined for a sample consisting of only one homogeneous material as,

$$CNRD = \frac{C}{N\sqrt{D}}, \tag{2.8}$$

where C is the contrast between the material of interest and water, N is the noise level in the area of the material of interest, measured as the standard deviation of the voxel values, and D is the averaged dose absorbed in the sample, usually expressed in mGy.

Hupfer showed that for imaging tasks involving the discrimination between soft-tissue materials, which was modelled as a constant difference in density for the same mass-attenuation coefficient, the selection of beam filtration played a major role, while the x-ray tube voltage affected the results to a lesser extent. For an ideal energy-response detector, i.e. a detector providing the same signal regardless of the energy of the incoming x-ray photons, a moderately hard filtration was found to provide larger CNRD values. On the other hand, for voltage values above 50 kV the performance in terms of CNRD was fairly constant.

For the case of bone imaging, the divergence in mass-attenuation coefficient for bone and soft-tissue is maximized for low energy photons. Therefore, the use of soft spectra enhanced CNRD. X-ray beam filtration in this case did not make a big difference in CNRD when compared to x-ray source voltage.

Basing our study in the results by Hupfer, we introduced in the analysis the response of the flat-panel detector. To obtain an accurate representation we used the cascaded systems theory first introduced by Johns and Cunningham [52] and further developed and adapted to flat panel detectors by Siewerdsen et al. [65-66] which has been shown to provide accurate representation of the signal formation chain in flat-panel detectors [8, 64, 66]. In this particular case we are not interested in the spatial frequency properties of the signal formation, only in the mean pixel signal. This value is given, for a known beam spectrum and after some manipulation, by [119]

$$\bar{m} = \sum_{E=0}^{E_{\max}} q_0(E) g_1(E) g_2(E) , \qquad (2.9)$$

where g_1 is the energy-dependent probability of absorption of the scintillator, g_2 is the energy-dependent number of visible photons generated per absorbed x-ray photon. The value for g_2 was selected as 50 photons per absorbed keV, as stated by Rowlands et al. [176]. For the development of equation 2.9 we only took into account the energy-dependent factors of the cascaded systems model for the detection process, since the effects of energy-independent factors play a minor role in the selection of the optimal spectral configuration of the beam.

For the selection of the optimal spectral configuration of the beam for the discerning between soft-tissue areas we proceeded as follows. Following Hupfer et al., we consider that CNRD can be considered constant from 50 kV. Taking that into account we calculated the signal provided by the detector behind two synthetic soft-tissue cylindrical phantoms, one of 32 mm diameter (mouse sized) and one of 50 mm diameter (rat sized). We performed the calculation for a range of voltage values (40 – 110 kV) and for several filtration thicknesses of aluminum (0.5 mm to 3 mm in 0.5 mm increments) and copper (0.05 mm to 0.3 mm in 0.05 increments). To generate the x-ray spectra for the optimization study we used the modified TASMIP model for microfocus sources, described in chapter 4, and applied the Beer’s law to obtain the filtered signal, using the mass energy attenuation coefficients in the NIST database [177]. We compared the signal generated by the detector to that of an ideal detector with flat energy response and gain equal to the result of averaging $g_1(E)$ across the whole energy span.

The voltage value that provided the maximum gain with respect to the ideal detector for each filtration was marked as candidate for the optimal spectrum.

As stated above, hard beams provided better CNRD values. To select the optimal beam filtration, we computed the x-ray tube power required to set the detector at a working point of 90% of the maximum pixel signal for the maximum magnification factor of the system. We selected the hardest beam permitting the use of a moderate power value achieving a compromise between CNRD and resolution requirements.

For the case of bone imaging protocols low kV values are desired to maximize the CNRD, as shown in [173]. However, for low voltages, flux reduction due to beam filtration is much more conspicuous. In addition low voltages are often associated with low efficiency of the x-ray source [52]. A compromise must be sought to use a low kV value and maintain an appropriate signal level at the detector. It is also important to keep the x-ray source power low enough to not noticeably degrade spatial resolution.

To find an appropriate spectral configuration of the beam, obtaining a compromise between the factors pointed above, we estimated the power required to set the detector at 90 % of the maximum pixel value as a function of x-ray source voltage and filtration. We used the same range of filtration and voltage described for the optimization of the soft-tissue protocol. We calculated the average signal behind the object, consisting of the soft-tissue cylindrical synthetic phantoms with a longitudinal insert of bone, with a diameter of 2 mm and 3 mm for the mouse and rat, respectively. The calculated signal at the detector provided an estimation of the maximum signal to noise ratio achievable in the projection data.

We selected the minimum voltage and softer filtration that provided a signal of about 50 times the additive noise floor, which is ~8.3 analog-to-digital units (ADU), measured as standard deviation of the pixel signal after dark subtraction [178].

2.3 CBμCT system assessment

We assessed the performance of the CBμCT system both in terms of the most critical individual components and in terms of overall CBμCT image quality and dose, as a function of acquisition protocol.

2.3.1 Assessment of x-ray source and detector performance

Since the x-ray source and detector are key components of a CBμCT scanner and they are responsible to a great extent of the final image quality, we carried out specific tasks for the evaluation of their performance.

We measured the temporal stability of the output of the source, the linearity of the response of detector pixels as a function of exposure, the stability of the detector response, the spatial resolution of the detector and its noise and signal transfer properties.

2.3.1.1 Temporal stability of the x-ray source

Temporal instability of the x-ray source can have important impact in the final image quality, depending on the nature of the instability. A small degree of temporal instability in the value of the anode current is usually observed but this kind of instability only affects the number of photons reaching the detector and, therefore, the mean signal value and the noise quantity. The deviation in mean is corrected by the I_0 correction performed during reconstruction and, if the variation is small enough, the effect of the drift in noise is negligible.

On the other hand, when the variation is not in anode current but in the tube voltage, the effects can be more difficult to compensate. In case of small deviations from the mean tube voltage, effects can be considered negligible, but the dependence of the attenuation coefficient of the different tissues on x-ray photon energy could cause inconsistencies in the attenuation data measured across different angular directions. These inconsistencies are not straightforward to compensate for, and degrade image quality.

For the reasons presented above, it is advisable to check the stability of the output of the x-ray source. To this end we measured the dose rate delivered as a function of time that must be nearly constant if the output is stable.

We measured instantaneous dose rate values using a Radcal Accu-Gold (Radcal, Monrovia, CA) multi-purpose meter to which a 10 cm-long, 3cm^3-active-volume, pencil-shaped ion chamber (Radcal 10X6-3CT) was connected. Both elements are shown in figure 2.9.

Figure 2.9. Radcal Accu-Gold digitizer module and 3cm^3 CTDI ion chamber used for exposure measurements.

We measured the output stability for a range of kV values within the limits recommended by the manufacturer of the x-ray source (40 to 110 kV) with 2 mm Al added filtration and no sample in the beam.

The x-ray beam showed a variation of less than 1% for all the spectral settings.

2.3.1.2 Linearity and stability of the detector response

Measurements were performed with a different source than the one included in the system, an Apogee XTG5011 (Oxford Instruments, Scotts Valley, CA). The source used for the measurements had very similar characteristics (tungsten anode and beryllium output window) than the one used in the final system, with the exception of a maximum voltage of 50 kV.

To test the linearity of the pixel signal values we acquired a series of images for the same x-ray beam configuration and different anode current values. The x-ray source voltage was set to 40 kV with 1 mmAl added filtration. The anode current was set from 0.2 to 0.5 mA in 0.025 mA steps. The images were acquired for 4x4 binning with a homogeneous radiation field and no object between the x-ray source and detector. The result of the test showed an excellent degree of linearity ($R^2 > 0.99$) over the dynamic range of the detector.

The stability of the detector output was estimated by measuring mean pixel signal across a set of flat-field images over a given period of time for a fixed x-ray source setting. We acquired 360 consecutive flat-field images for 30 kV and 0.4 mA with no object between the x-ray source and the detector. Measurements were separated by 10 s intervals.

Measurements showed a peak-to-valley ratio during the experiment lower than 0.05% of the mean pixel value.

2.3.1.3 Spatial resolution of the detector

The resolution of x-ray imaging detectors is usually expressed in terms of the presampled MTF. The presampled MTF describes the signal transfer characteristics as a function of spatial frequency taking into account all the detection stages except sampling. If the sampling stage is included in the calculation, the detector spatial response may become undersampled, leading to aliasing errors in the estimated MTF.

Among the different methods proposed to estimate the presampled MTF, those based on imaging a slanted slit or a slanted edge are the most widely used owing to their relatively easy implementation and accurate results.

The following paragraphs present a brief description of the procedure proposed in [179-180], which implements a variation of the slanted-edge method. A comprehensive review of the different versions of the slanted-edge approach can be found in [181]. The selected algorithm is based on the analysis of the edge response function (ERF), which is obtained by imaging a phantom consisting of an x-ray-opaque object with a polished edge. The phantom is placed directly over the detector surface at a shallow angle (1.5º - 3º) with respect to the pixel matrix. The edge position is estimated with sub-pixel accuracy in the image area by using linear interpolation. This position is then fitted to a straight line by linear regression.

The slope of this line is used to determine the number of rows (N_{av}) necessary for a 1-pixel lateral shift of the edge position in the original image –see figure 2.10–.

The algorithm generates an oversampled ERF using the pixel value at the edge position for N_{av} consecutive rows. As depicted in figure 2.10, the value of the pixel in the first row (red mark) corresponds to the first data point of the ERF. Then, the pixel value of the second row (blue mark) yields the second data point and so on. Finally, the pixel value of the N_{av}th row –fifth row in figure 2.10– is the last data point of the ERF.

The detector area is split up into groups of N_{av} rows, and oversampled ERFs are estimated for each of the groups according to the process explained. These calculated ERFs are then aligned by linear regression and averaged in order to reduce noise.

The line spread function (LSF) is estimated as the 3-point derivative of the average ERF. Finally, an estimation of the MTF is obtained as the Fourier transform of the LSF. The calculated estimation is corrected for the sinc function introduced by the derivative operation, and the frequency axis is corrected for the slant angle. The result is an accurate estimation of the presampled MTF.

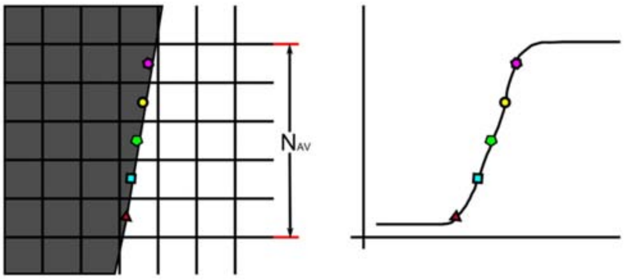

Figure 2.10. Schematic example of the calculation of the presampled MTF of the detector using the slanted edge method. Marks over the edge image (left panel) indentify the corresponding sampling points on the ERF (right panel).

Measurements of detector MTF were performed on a slanted polished copper edge of 1 mm thickness with the x-ray source voltage set to 40 kV and 1 mmAl added filtration. The source used for the measurement was the one described in section 2.3.1.2.

2.3.1.4 Noise and signal transfer properties of the detector

We measured the capabilities of the detector for the transference of noise and signal as a function of spatial frequency and for the different imaging protocols used for the acquisition of CT data. To this end, we measured the Normalized Noise Power Spectrum (NNPS), Noise Equivalent Quanta (NEQ) and Detective Quantum Efficiency (DQE).

The NNPS provides an estimation of the noise variance of the image for the different spatial frequencies. On the basis on the NNPS, overall frequency-dependent maximum signal-to-noise ratio characteristics of the image acquisition chain were estimated by including the MTF into the calculation, yielding the NEQ measurements.

Introducing in the calculation the photon flux reaching the detector surface one could provide an idea of the global signal and noise transfer characteristics of the detector for a given imaging setting. This information is provided by the DQE that can be seen as the ratio of the signal-to-noise ratio for the output image and the signal-to-noise ratio of the input radiation flux reaching the detector [182].

For this set of measurements we acquired flat-field data for the beam spectral configuration of the four CT data acquisition protocols defined for the system, i.e. bone mouse, soft-tissue mouse, bone rat, and soft-tissue rat. Anode current for the bone configurations was set to the maximum anode current contemplated in the particular protocol, while for the acquisition of data for soft-tissue configurations we set the anode current to 88% and 81% of their nominal maximum values, for the mouse and rat protocol, respectively.

Flat-field data were pre-processed prior to compute NNPS, NEQ and DQE by subtracting the dark offset and performing the gain correction. Defective elements in the images were also corrected before processing the data.

NNPS was estimated following [182-184]. We used 256 half-overlapped ROIs of 256x256 pixels distributed symmetrically from the center of the image. We fitted the data in each ROI to a 2-dimensional polynomial function. The result of the fitting was subtracted to the original ROI to remove low frequency trends contaminating noise measurements. We computed NNPS by performing the 2-dimensional Fourier transform of the data that was subsequently normalized by the dimensions of the ROI and by the squared mean signal on the ROI. The final NNPS was the average of the NNPS computed for all the ROIs. NNPS is then given by the next expression,

$$NNPS(f_u, f_v) = \frac{1}{N} \sum_{i=1}^{N} \frac{\left| DFT\left[I_i(u,v) - S_i(u,v) \right]^2 \right|}{\left[\overline{I}_i(u,v) \right]^2} \frac{\Delta u \Delta v}{N_u N_v}, \tag{2.10}$$

where N is the number of regions −256 in our case− used for the calculation, Δu and Δv are the pixel size in the horizontal and vertical direction, respectively, I_i is the part of the original image for ith ROI, S_i is the 2-dimensional polynomial fitting for detrending, and N_u and N_v are the number of pixels forming the ROI in the horizontal and vertical directions respectively.

NEQ was estimated by computing the ratio between the squared MTF calculated as described in section 2.3.1.3 and NNPS for the different protocols, and DQE was estimated by normalizing NEQ results by the estimated photon flux at the detector surface, yielding:

$$NEQ(f_u, f_v) = \frac{MTF^2(f_u, f_v)}{NNPS(f_u, f_v)}, \tag{2.11}$$

$$DQE(f_u, f_v) = \frac{NEQ}{\overline{q}_0} = \frac{MTF^2(f_u, f_v)}{\overline{q}_0 NNPS(f_u, f_v)}, \tag{2.12}$$

where $\overline{q}_0$ is the mean photon flux at the detector surface. To estimate $\overline{q}_0$ we measured x-ray exposure at the isocenter of the scanner, using a Radcal Accu-Gold (Radcal, Monrovia, CA) multi-purpose with a 10 cm-long, 3cm^3-active-volume, pencil-shaped ion chamber (Radcal 10X6-3CT) –see figure 2.9–. Exposure measurements were then translated to the detector plane by applying the squared distance law. Photon flux values were generated using spectra generated by the TASMIP model for micro-focus sources –see chapter 4– and following [52, 55], yielding

$$\frac{\overline{q}_0}{X} = \int_0^{kV} \frac{5.43 \cdot 10^{-5}}{\left(\mu_{en}(E)/\rho \right)_{air} E} p(E) dE, \tag{2.13}$$

where X is the air kerma at the detector surface in mR, μ_{en}/ρ is the mass-energy absorption coefficient for air, E is the photon energy, $p(E)$ is the unit-area normalized x-ray beam spectrum, and kV is the voltage set at the x-ray source. Final $\overline{q}_0$ values were computed by multiplying the result of equation 2.13 by the measured air kerma for the particular protocol.

2.3.2 Dose

We characterized the dose delivered to the subject for the acquisition protocols designed for the scanner using a Radcal Accu-Gold (Radcal, Monrovia, CA) multi-purpose meter to which a 10 cm-long, 3cm^3 active volume, pencil-shaped ion chamber (Radcal 10X6-3CT) was connected.

We performed two sets of measurements, one for the mouse protocols and one for the rat protocols, using two CTDI phantoms. CTDI phantoms consisted of a cylinder of PMMA with diameter of 32 mm for mouse and 50 mm for rat. A longitudinal cylindrical opening with diameter of 12 mm was drilled at the center of each phantom to place the ion chamber (see figure 2.11). Similar phantoms have been used in previous publications [185] and are commercially available for the evaluation of dose properties of CBµCT scanners [186].

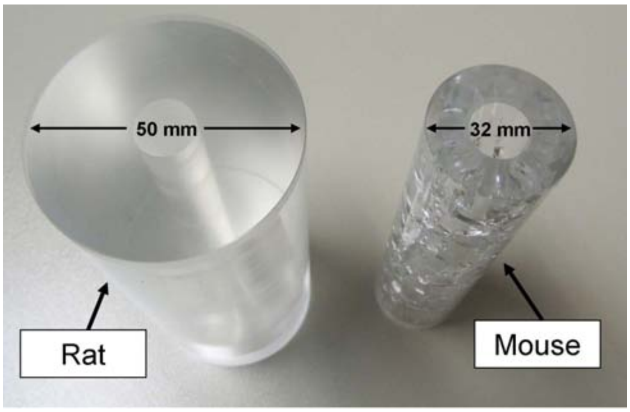

Figure 2.11. CTDI phantoms used for dose estimation for the rat and mouse protocols. Phantoms are made of PMMA (ρ = 1.18), mimicking soft tissue, and the ion chamber is placed in the central opening.

Phantoms were placed as close to the isocenter as possible and two datasets were acquired for each phantom (rat and mouse) and associated acquisition protocol (soft tissue and bone), one for complete rotation (360º) and one for partial rotation (220º) adding to a total of four datasets per phantom. The Accu-Gold meter provided instant dose measurements, allowing the estimation of dose rates and total dose as a function of the angular position of the system. To compensate for deviations between isocenter and the actual position of the phantoms, values at the isocenter were obtained as the average dose rate across all the acquired projections.

CTDI measurements were used as the gold standard for dose evaluation, providing a measured value comparable with data in previous literature for other scanners. We extended the dose study by using realistic Monte Carlo dose estimation using the modified MC-GPU [187] Monte Carlo simulation package described in chapter 5 and [95, 119]. The simulated data provided the energy deposited in each voxel in eV. Energy values were converted first to Joules and afterwards to dose units normalizing them by the mass of the voxel in kg.

We simulated the CTDI phantoms for equivalent acquisition conditions in terms of x-ray beam spectral properties and acquisition geometry. CTDI simulated data provided a means to found the proper scaling factor relating mAs and number of photons in monte-carlo simulation, and dose at the isocenter.

Dose distribution and absolute value in realistic imaging conditions was evaluated using monte-carlo simulation for realistic murine-like digital phantoms. The phantoms were generated from the Digimouse dataset [188] scaled to an average diameter of 32 mm and 50 mm for the mouse and rat protocols, respectively. The simulation included a set of tissues resembling those present in real animals, namely generic soft-tissue, lung, brain, muscle, skin, bone marrow and cortical bone. Cross sections for the different tissues were obtained from the Penelope database [58], except for bone marrow that was extracted from data in [189]. Adipose tissue was not included in the study due to the lack of identification of this type of tissue in the Digimouse dataset.

Table 2.II shows the simulation parameters used for the dose estimation in the CTDI and realistic phantoms.

Table 2.II. Parameters for the monte-carlo dose estimation.

Parameter	***Rat Protocols***		***Mouse Protocols***	
	Soft-Tissue	*Bone*	*Soft-Tissue*	*Bone*
X-ray beam	68 kV (0.2 mm Cu)	50 kV (1.0 mm Al)	66 kV (0.2 mm Cu)	60 kV (1.0 mm Al)
Number of projections	360	360	360	360
Angular span	360º	360º	360º	360º
Photons per projection	10^8	10^8	10^8	10^8

2.3.3 Assessment of tomographic image quality

2.3.3.1 Spatial resolution

The system resolution was measured using a variation of the standard test method ASTM E1695-95 [190], which is based on the examination of the CT image of a uniform disc of polycarbonate. In our case we substituted the polycarbonate disc by a rod made of PMMA due to the possibility of access to this material at our institution.

We carried out acquisitions of the PMMA rod placed as close as possible to the isocenter of the scanner for the two extreme geometrical configurations of the scanner, i.e. for minimum and maximum magnification.

The MTF of the reconstructed image is obtained from the average ERF of an axial view of the rod. To compute the average ERF we proceeded as follows. We resampled the reconstructed slice in a 14 times denser grid, i.e. pixel size is reduced to 0.071 times its original size. We found the center of the circular area in the resampled data by computing the centroid of the rod area in the image. Prior to calculate the centroid, we binarized the image using a threshold of 0.3 times the maximum value in the slice. The binary image then underwent a morphological closing operation using a circular kernel with a diameter of 12 pixels and an erosion operation to remove outliers outside the area covered by the rod.

From the estimated center position, 720 equiangularly spaced radial profiles were traced toward the edge of the circular region. To obtain accurate subpixel measurements we aligned the profiles using the same method described in section 2.3.1.3. The aligned profiles were subsequently averaged, obtaining the average ERF for the circular area.

The calculated average ERF formed the basis for the MTF estimation that was computed using the same procedure described in section 2.3.1.3. The use of a circular edge for the estimation of the ERF implicitly assumes isotropic resolution at a radial distance from the isocenter inside a single slice, which is a reasonable assumption in CBCT, as shown in [26].

The cut-off point where the MTF decreases below 20% of its maximum value was used as the standard resolution value. The cut-off point at 10% was also calculated.

The performance of the system in terms of MTF was measured for three different configurations. We designed the set of measurements in such a way as to cover the whole span of expected resolutions for the system. We measured the MTF for a detector pixel size of 0.05 mm –i.e. no pixel binning–, for the minimum (M_1) and maximum (M_2)

magnification factor of the system, viz. 1.48 and 2.10, providing the limits for the highest resolution values as a function of geometry; and for a detector pixel size of 0.2 mm –i.e. pixel binning 4x4–, for the minimum magnification factor, showing the lower limit in resolution for the system.

We estimated the influence in resolution of the reconstruction filter, by measuring MTF for each of the experiments on data reconstructed using the three filters included in the system, namely Ram-Lak filter, Ram-Lak windowed using a Shepp-Logan window with cutoff frequency at the Nyquist frequency, and Ram-Lak windowed with a Hann window with cutoff frequency at the Nyquist frequency.

2.3.3.2 Contrast, noise and HU uniformity

We evaluated the impact of noise in image quality for the optimal acquisition protocols contemplated in the system by exploring the contrast and noise properties of the reconstructed data.

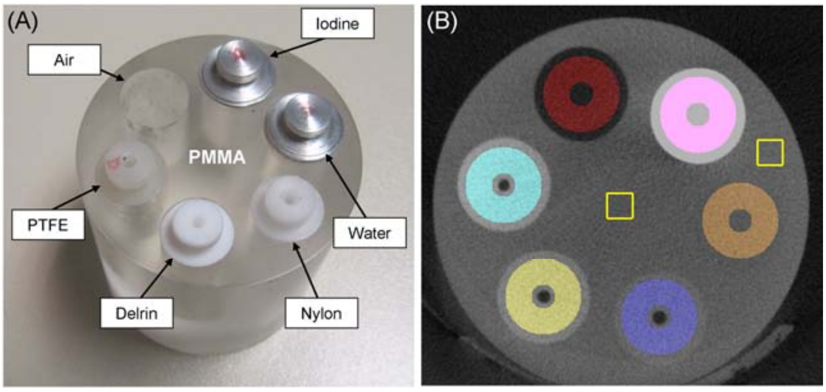

Figure 2.12. Phantom for the evaluation of CNR (A) and ROIs used for the estimation of contrast and noise values.

Figure 2.12 shows the phantom used for the evaluation of contrast and noise. It consists of a 60 mm-diameter rod of PMMA (ρ = 1.18 g/cm^3) with six 15 mm-diameter cylindrical openings containing 4 rods of plastic materials and two empty volumes that can be filled with liquids. In our experimental setup we included plastic rods made of Nylon (ρ = 1.15 g /cm3), Polyoximethilene (Delrin, ρ = 1.41 g/cm3), and PTFE (ρ = 2.2 g/cm3). One of the empty volumes was filled with water and the second one with a mixture of water and an iodinated contrast agent (Iopamidol, Iopamiro 300, Bracco, Italy) at a concentration of 15 mg I/ml.

We acquired CT data of the phantom for all the acquisition protocols contemplated for the scanner with the detector configured in binning 4x4 –i.e. pixel pitch of 0.2 mm- each at four different mAs values, namely 0.25, 0.50, 0.75 and 1.00 times the maximum mA usable for the protocol all of them for 720 angular projections with an integration time of 111 ms and evenly distributed on an angular span of 360º. The datasets were acquired using the continuous acquisition approach. We generated three reconstructed volumes for each dataset, one for each reconstruction filter used in the system.

The figure-of-merit used to estimate image quality was the contrast-to-noise ratio (CNR). CNR was calculated using the following expression,

$$CNR = \frac{|\mu_1 - \mu_2|}{\sqrt{\sigma_1^2 + \sigma_2^2}}, \tag{2.14}$$

where μ_1 and μ_2 are the average attenuation coefficients of the two materials for which the calculation is performed, measured on the reconstructed image, and σ_1 and σ_2 the standard deviation for the attenuation values measured on the image for the two materials.

For the calculation of CNR we used the water insert as the reference tissue (μ_1, σ_1). We measured average value and standard deviation inside the ring-shaped ROIs depicted in figure 2.12(B) for all the materials in the phantom, exception made of the PMMA background to exclude the biasing of the results by deterministic quality degradation effects not related with noise, such as cupping. Calculations were performed on the reconstructed data in attenuation units, i.e. prior to the conversion to HU.

To take into account the dose delivered to the sample for the acquisition, we introduced a redefinition of CNRD –see section 2.2.6–, including this time the contrast between two materials instead of one material and its theoretical contrast with water. In this case, we used our definition of CNR, which includes the noise properties of the two materials under assessment, and weighted it by the CTDI for the acquisition protocol used which is a surrogate of the dose delivered at the central area of the phantom. This way, CNRD is defined as:

$$CNRD = \frac{|\mu_1 - \mu_2|}{\sqrt{D}\sqrt{\sigma_1^2 + \sigma_2^2}}, \tag{2.15}$$

where D is the CTDI value for the acquisition protocol and mAs value used in the experiment.

In addition to CNR and CNRD we evaluated the level of noise in the water insert for the different protocols and reconstruction kernels as a function of dose (mAs). We estimated noise as the standard deviation of the HU values for the water ROI shown in figure 2.12(B).

To investigate the uniformity of HU values across the volume we measured the degree of cupping in the reconstructed data. Following [119, 191], defining μ_{center} and μ_{edge} as the mean value of a 30x30 voxel ROI at the center and close to the edge of the PMMA area, respectively –square ROIs in figure 2.12(B)–, cupping was estimated by,

$$t_{cup} = 100 \times \frac{\mu_{edge} - \mu_{center}}{\mu_{edge}} . \tag{2.16}$$

2.4 Results

2.4.1 Geometrical configuration of the system

Figure 2.13 shows the dependence of system MTF_{50} and MTF_{20}. Data show that a maximum resolution of ~8.2 lpmm, measured as MTF_{20}, can be achieved for the lowest magnification factor in the system (M = 1.48). For this case, the increase of the focal spot size with power has a moderate impact, reducing the maximum attainable resolution to 7.8 lpmm.

As the magnification factor is increased, the effect of using a larger power is much more noticeable and the degradation in image resolution is larger. For the case of the maximum magnification factor in the system (M = 2.10), the maximum attainable resolution is ~11.5 lpmm and it is degraded to ~9.8 lpmm if the tube is set to deliver its maximum power. Thus, the MTF_{20} cutoff frequency value is degraded by 15% compared to 5% for lower magnification.

As expected from the shape of MTF curves for detector and focal spot, the degradation caused in the MTF_{50} by increasing power is lower, yielding a better performance for mid-frequency imaging tasks.

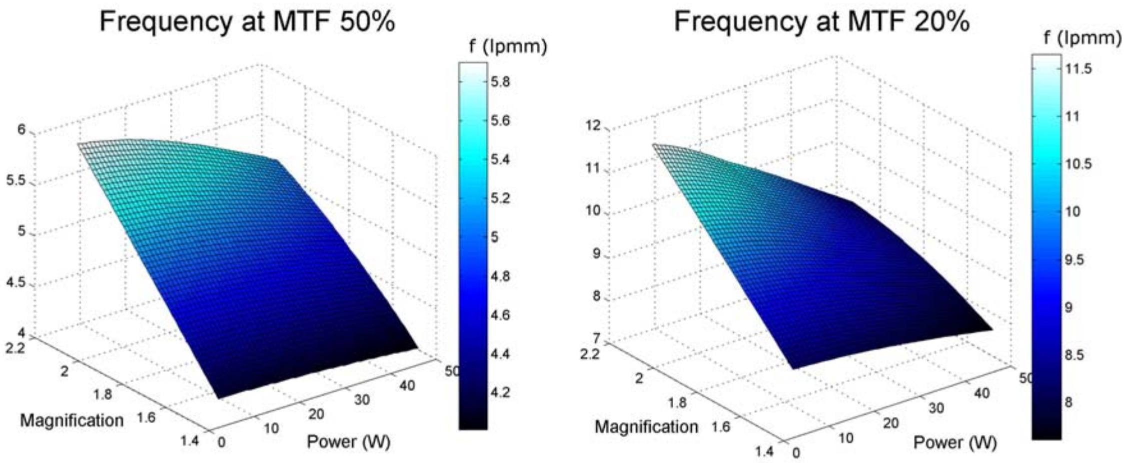

Figure 2.13. Estimated MTF cutoff frequency at 50 and 20 % of the MTF for *f* = 0, as a function of the magnification factor and the x-ray source power, that determines the focal-spot size.

2.4.2 Optimization of the acquisition protocol

The optimal working point for the x-ray source can be extracted from the plots in figure 2.14, where we compared the signal provided by the detector used in the system to that provided by an ideal detector with flat energy response and gain equal to the average gain across energy for our detector. The maxima of the curves –marked by red dots in figure 2.14– identified the kV value for each filtering configuration that yielded the maximum signal, maximizing the signal-to-noise ratio of the projection data.

Curves show that optimal x-ray source depended on filtration and sample size but, in any case it is located between 62 and 78 kV. Also, copper filters showed better performance in the maximization of the signal at the detector. For this reason we selected copper as the filtering material for soft-tissue imaging protocols.

To obtain an appropriate signal at the detector we selected the working point that provided a pixel signal of around 90% for the nominal integration time of the detector for 1x1 binning (500 ms), for the maximum power of the x-ray source and for the maximum source-to-detector distance of the system (SDD = 325 mm for *M* = 2.10).

The aforementioned factors led to the selection of 0.2 mm Cu as the appropriate x-ray filtration for soft-tissue imaging. Optimal voltage working points for the selected filtration were 68 kV and 66 kV for the mouse and rat configurations, respectively. The anode current needed to get a signal level of 90% of the saturation signal for maximum SDD were 0.68 mA and 0.74 mA, for the mouse and rat configurations, respectively, yielding output powers of 46.2W and 48.8 W, both below the 50 W limit of the source.

When pixel binning was applied the 90% saturation anode current dropped to 50% of its original value for 2x2 binning and 25% of its original value for 4x4 binning.

Power values were reduced by a factor of 2 when minimum SDD was set for the acquisition, in accordance with the inverse squared distance law.

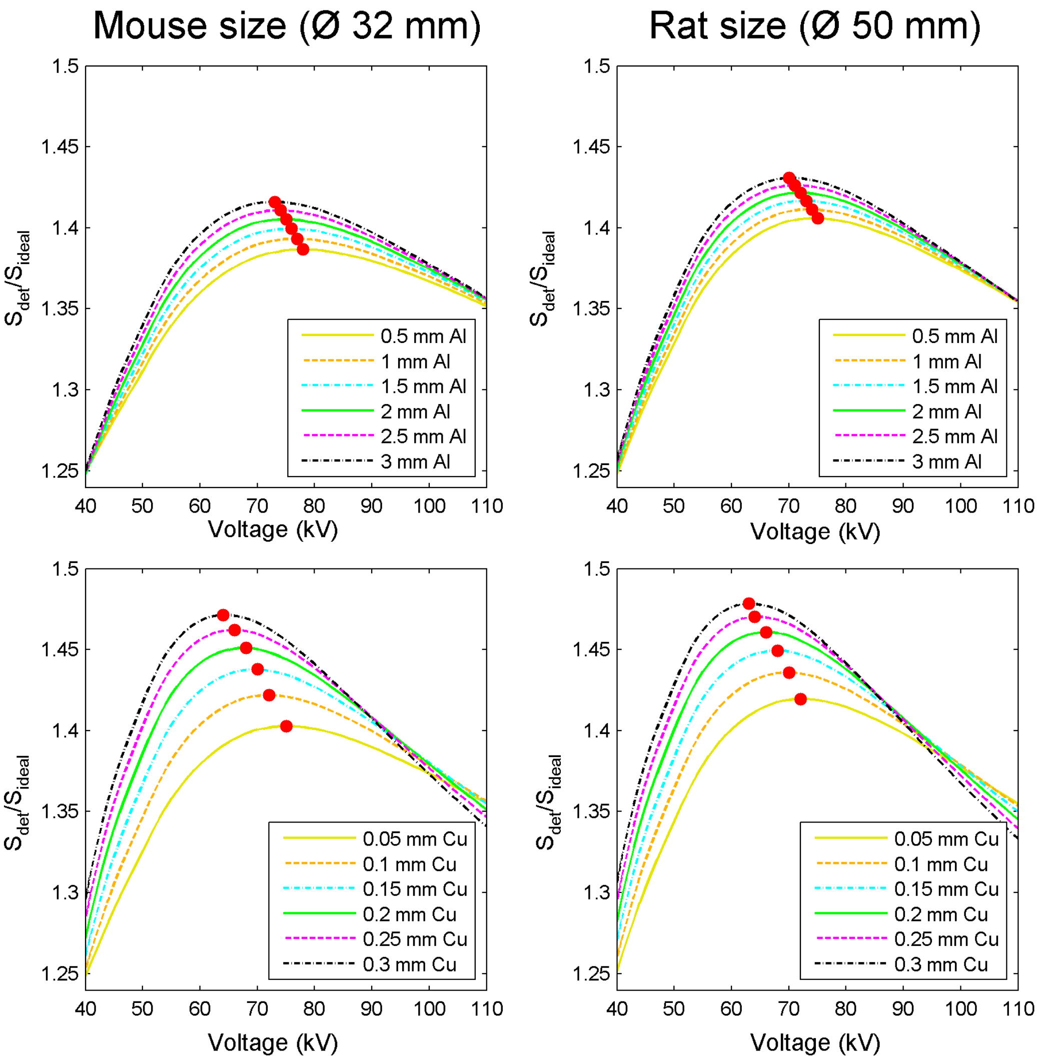

Figure 2.14. Relative signal compared to an ideal, flat-energy response detector as a function of x-ray tube working voltage and x-ray beam filtration. The column on the left shows the results for the soft-tissue cylinder with the size of a typical mouse and the column on the right for the cylinder with the size of typical rat. Top row shows the results for aluminum filtration and bottom row for copper filtration.

For the case of bone imaging, as shown by Hupfer et al. [173], CNRD was larger the lower the voltage set at the x-ray source. To select the optimal working point we computed the x-ray source power needed to set the detector air signal at 90% of the saturation point for maximum SDD, and the signal behind the object for this working point, both shown in figure 2.15.

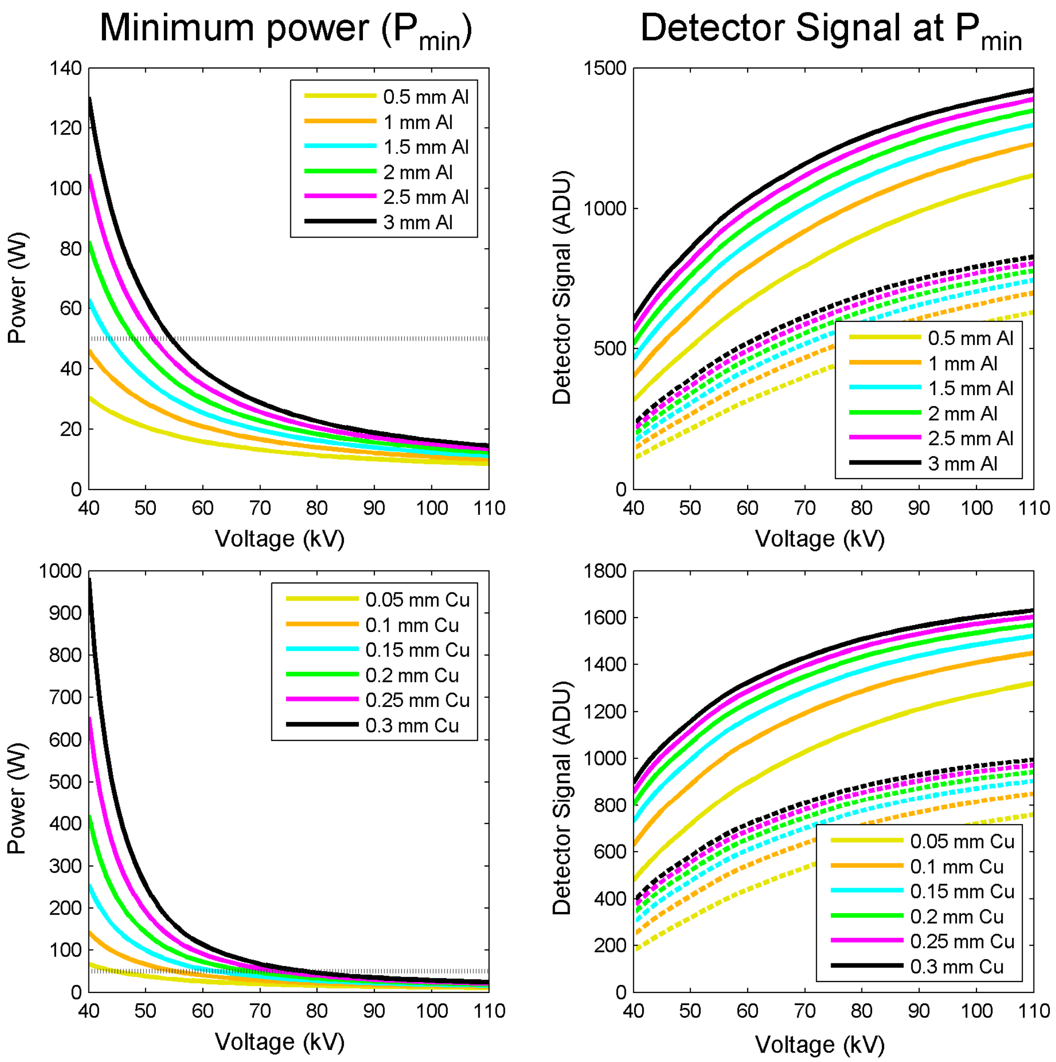

Figure 2.15. Minimum power needed to obtain a signal of 90% of the detector saturation point (left column) and signal behind the object (right column) for the mouse size (solid lines) and for the rat size (dashed lines). The dotted horizontal line in left column plots marks the power limit of the x-ray source.

Results by Hupfer et al. showed no clear benefit from variations in filtering, but the plots showing detector signal behind the object in figure 2.15 show that using a very low filtration reduced the necessary power and could help in reducing the required voltage, but the attenuation suffered by the beam is very high, yielding very low signal values behind the subject. When using copper filters, the minimum voltage for which the required power falls below the x-ray source limit is of 50 kV for 0.05 mm Cu, but it grows up to 60 for 0.1 mm Cu. Given the low improvement provided by harder filtration, we chose to be on the safe side and use a lower filtration that allowed to use lower power and to achieve better resolution values. For practical usage of the system we also selected only one filter for the bone imaging task, for it was impractical to use two different filters depending on sample size. We selected 1 mm Al filtration for the bone imaging task. For this filtration, we selected 50 kV for the mouse configuration, requiring a power of 28.7 W that yields a signal of ~75 times the noise floor (~620 ADU). The signal at the detector for this voltage in the case of the rat phantom was ~250 ADU, too low to provide sufficient image quality. For this reason we decided to increase the x-ray source voltage to 60 kV for the case of rat-sized subjects, requiring a power of 20.8 W and providing a signal of ~46 times the noise floor (~379 ADU). For samples of intermediate size, the x-ray source voltage can be tuned between the mouse and rat values, to maximize CNR while obtaining sufficient signal.

2.4.3 Detector resolution and signal and noise transfer properties

The detector included in the system showed a good resolution in terms of MTF for no pixel binning, as depicted in figure 2.16.

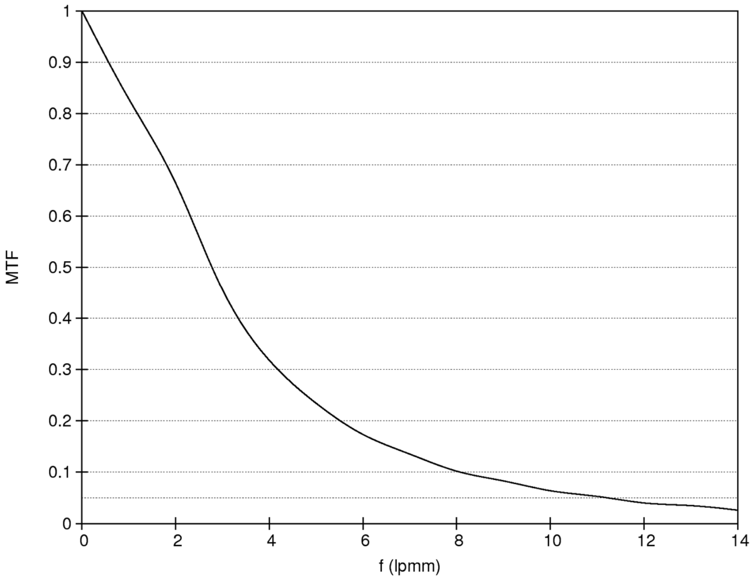

Figure 2.16. Presampled MTF for the Hamamatsu C7940-DK02 measured using the slanted-edge method. The spatial frequency at MTF_{10} was 8.1 lpmm, a figure compatible with the manufacturer's specifications.

Good resolution characteristics were expected due to the columnar structure of the scintillator and its small thickness (~150 μm), properties that minimized the spread of the visible light photons on their travel from the x-ray photon interaction point to the sensor surface. Frequency cutoff at MTF_{20} is 5.6 lpmm, at MTF_{10} (MTF = 0.1) is 8.1

lpmm and the frequency cutoff for MTF_5 (MTF = 0.05) is above the Nyquist frequency for a pixel pitch of 0.05 mm, i.e. 10 lpmm. The MTF curve is shown in figure 2.16.

We evaluated the frequency-dependent noise transfer properties of the detector for the four acquisition protocols by the NNPS distributions displayed in figure 2.17.

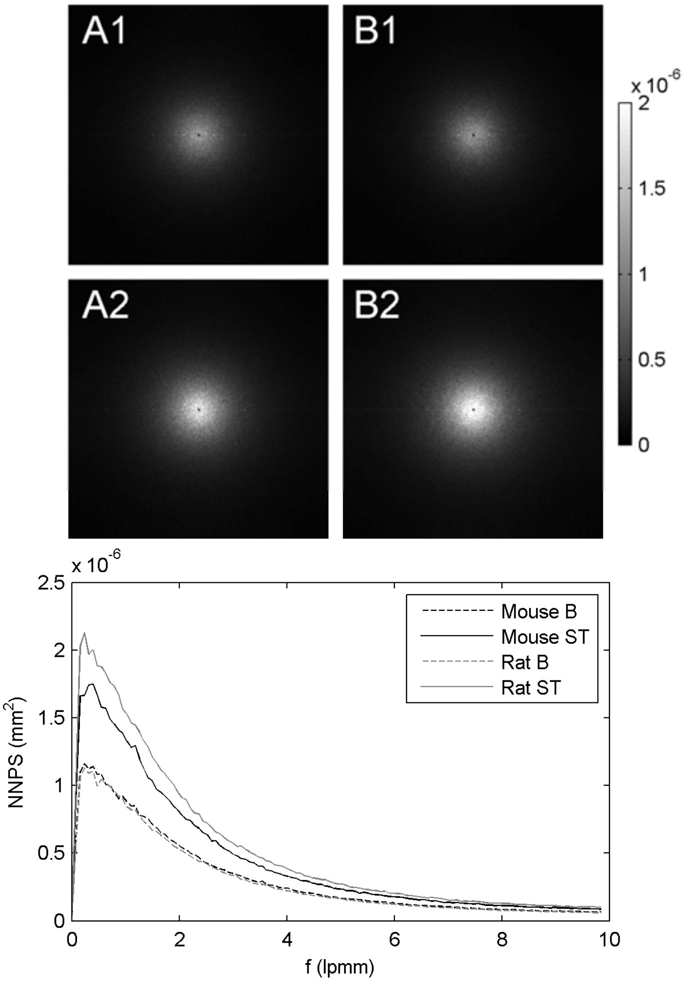

Figure 2.17. NNPS 2D distributions for the mouse bone (A1) and soft-tissue (A2) protocols and for the rat bone (B1) and soft-tissue (B2) protocols. Plot shows the radial average of the two dimensional distributions. NNPS values for the soft-tissue protocols (solid curves) are larger and more concentrated around low frequencies while for bone protocols (dashed curves) the peak NNPS is lower and the distribution is slightly more spread.

As expected from an isotropic pixel detector, NNPS 2D distributions showed radial symmetry, indicating isotropic frequency-dependent noise properties across the detector. It is worth noting the slight deviation from this situation of the central horizontal row of the distribution, corresponding to vertical zero frequency ($f_v = 0$). This row showed a relatively low frequency peak and an overall higher value. As we detailed in the discussion section below, we believe this is generated by residual image structured noise not eliminated by gain and offset corrections.

The high radial symmetry allowed the computation of the radially averaged NNPS curve, shown also in figure 2.17. We averaged 90 profiles evenly distributed along 360º to reduce noise and improve the visibility of the results. While all the experiments were carried out for pixel signal values well above half the dynamic range of the detector, where additive electronic noise have a minor effect and the noise in the image is dominated by photon detection statistics, data for bone protocols were acquired for higher signal values. This is shown in the NNPS distributions as a decrease in the peak value of the distribution. Noise power for the different protocols showed a very similar distribution in frequency with a slightly larger quantity of low frequency noise for soft-tissue protocols, i.e. harder spectra.

NEQ and DQE data are depicted in figure 2.18 for all the protocols. NEQ peak values were larger for the bone protocols, in accordance to NNPS results. NEQ provides an estimation of the maximum signal-to-noise ratio achievable for the acquisition conditions and it is, therefore, affected by the exposure level. While NEQ was larger for bone protocols, the ratio between NEQ values for bone and soft-tissue protocols was lower that the one for NNPS values, pointing to poorer relation between signal and noise transfer for bone protocols compared to soft-tissue protocols.

For the computation of DQE, the mean number of photons per mR and mm^2, obtained using equation 2.13, was of $1.11 \cdot 10^5$ and $2.18 \cdot 10^5$ for the mouse bone and soft-tissue protocols, respectively, and of $1.35 \cdot 10^5$ and $2.13 \cdot 10^5$ for the rat bone and soft-tissue protocols, respectively. Air kerma values at the detector surface were of 23.36 mR and 3.88 mR for the mouse bone and soft-tissue protocols, respectively, and of 15.68 mR and 3.74 mR for the rat bone and soft-tissue protocols, respectively.

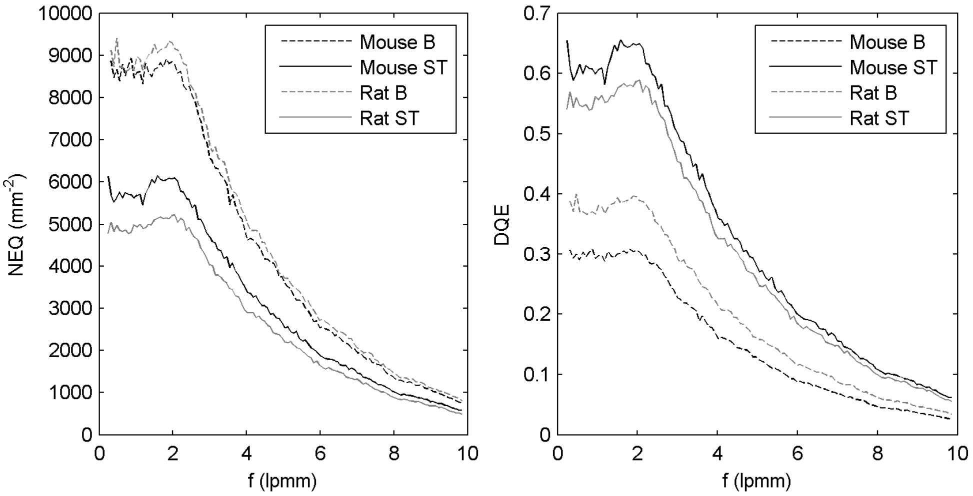

Figure 2.18. NEQ and DQE for the Hamamatsu C7940-DK02 detector and for the different acquisition protocols designed for the system. NEQ values are larger for the bone protocols due to the anode current level used for the tests. When including exposure-related considerations in the calculation –i.e. computing DQE– soft-tissue protocols showed superior performance.

DQE curves showed peak values around 0.6 for the soft-tissue protocols and around 0.3-0.4 for bone protocols. Since DQE is an estimation of the signal-to-noise ratio transfer capabilities of the detector, larger DQE values for soft-tissue protocols imply larger performance of the detector in transferring the information contained in the x-ray flux reaching its surface and potential benefits for minimizing dose for a required noise level.

2.4.4 Dose

The value of CTDI for the acquisition protocols specified above –see section 2.4.2–, was of 2.19 mGy/mAs for the mouse bone protocol, 0.79 mGy/mAs for the mouse soft-tissue protocol, 2.15 mGy/mAs for the rat bone protocol and 0.61 mGy/mAs for the rat soft-tissue protocol.

Figure 2.19 shows the estimated dose distribution in the CTDI phantom obtained from the monte-carlo simulations assuming a homogeneous cylinder of soft-tissue. It is important to notice the larger difference between the doses deposited near the edge of the phantom and at its central part, for both the mouse and rat bone protocols when compared to the dose distribution for soft-tissue protocols that is much more even. This spatial variation of dose arises from the lower mean energy of the spectrum for bone protocols that reduces the mean free path of photons in the phantom making them more likely to interact near its surface. On the other hand, the harder spectra used for soft-tissue protocols make the photons to traverse a longer distance before interacting.

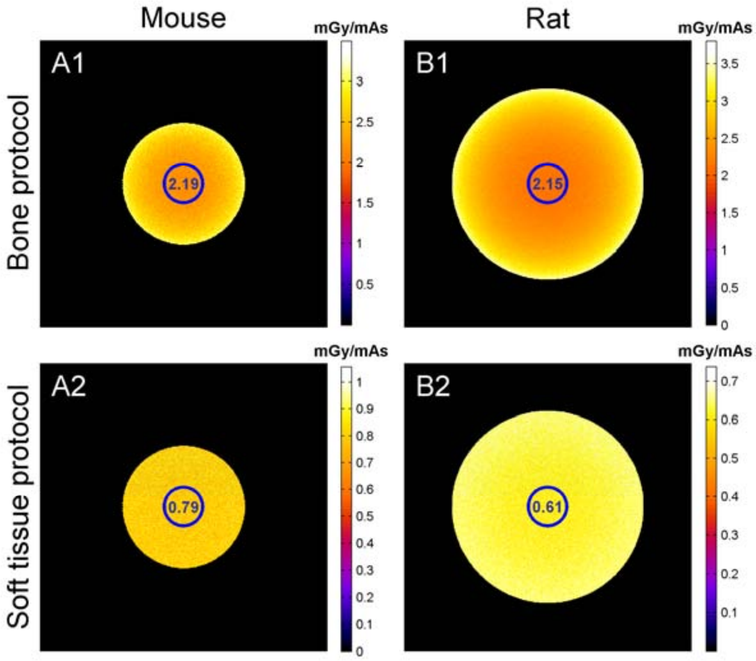

Figure 2.19. Measured CTDI per mAs and Monte Carlo estimated dose distribution at the central slice, for the mouse (A) and rat (B) phantom sizes and for the bone (1) and soft-tissue (2) protocols. Blue circumferences show the position and extent of the ion chamber placed inside the CTDI phantoms. Numbers show CTDI measurements normalized by mAs.

Simulated dose distribution on realistic murine phantoms reproduced to a large extent the trends observed in CTDI data (see figure 2.20). Dose distribution for complete trajectories –i.e. 360º angular span– showed peak soft-tissue dose values near the skin of the subject and very high differences (~10 fold) between soft-tissue dose and bone dose, as expected from the larger attenuation coefficient shown by bone for soft spectra, responsible of the superior contrast achieved for bone imaging tasks. This effect is more pronounced in the case of rat sized subjects, due to the larger length of material traversed by photons.

Also, the dose distribution is biased towards the surface of bone areas, for the same reasons, but, in this case, the difference between the surface and the interior part of the bone is larger owing to the small mean free path of photons in bone, making them much more likely to interact very close to the surface. This effect is more pronounced for the skull area that contained thicker bones.

For the case of soft-tissue imaging protocols the dose is more evenly distributed along the subject, as expected from CTDI simulated data, and the difference between dose delivered to bone and to soft-tissue areas is less pronounced (~6 fold).

Dose values measured on a circular ROI of the same size of the CTDI ion chamber (12 mm diameter) are in agreement with CTDI measurements, being on the range of 2 to 3.5 mGy/mAs for bone protocols, around 1 mGy/mAs for soft-tissue mouse protocol and somewhat lower (~0.7 mGy/mAs) for the soft-tissue rat protocol.

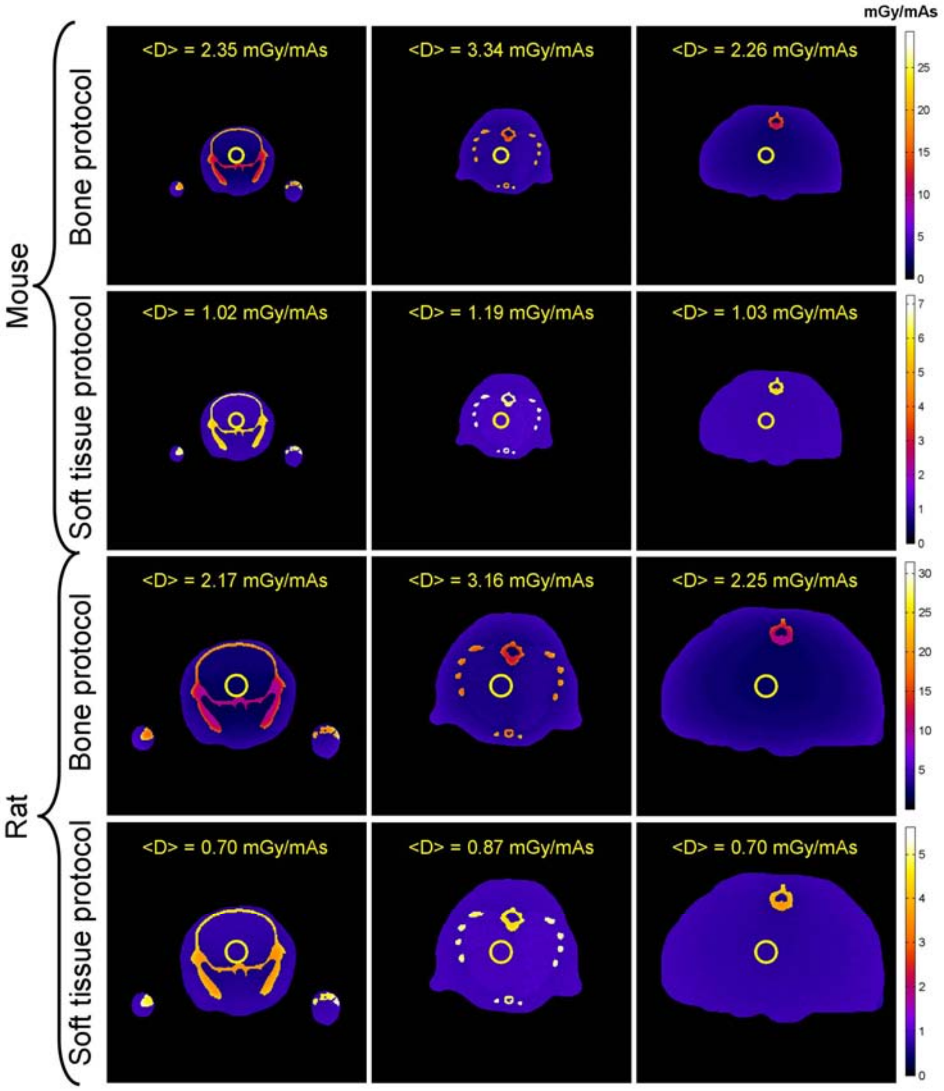

Figure 2.20. Monte Carlo simulated dose for complete trajectory acquisition protocols, normalized by mAs. Average dose values measured over the circular ROIs depicted on the central part of the distributions are labeled on top of them. Dose distributions are shown for a slice at the brain area, one at the thorax and one at the abdomen.

Figure 2.21 shows the dose distribution for partial acquisition trajectories, spanning 220°. The distributions showed a significant anisotropy, being higher the dose deposited for parts of the subject close to the x-ray source during its trajectory. This effect is more pronounced for bone imaging protocols, as expected from the large anisotropy shown by their dose distribution for complete trajectories.

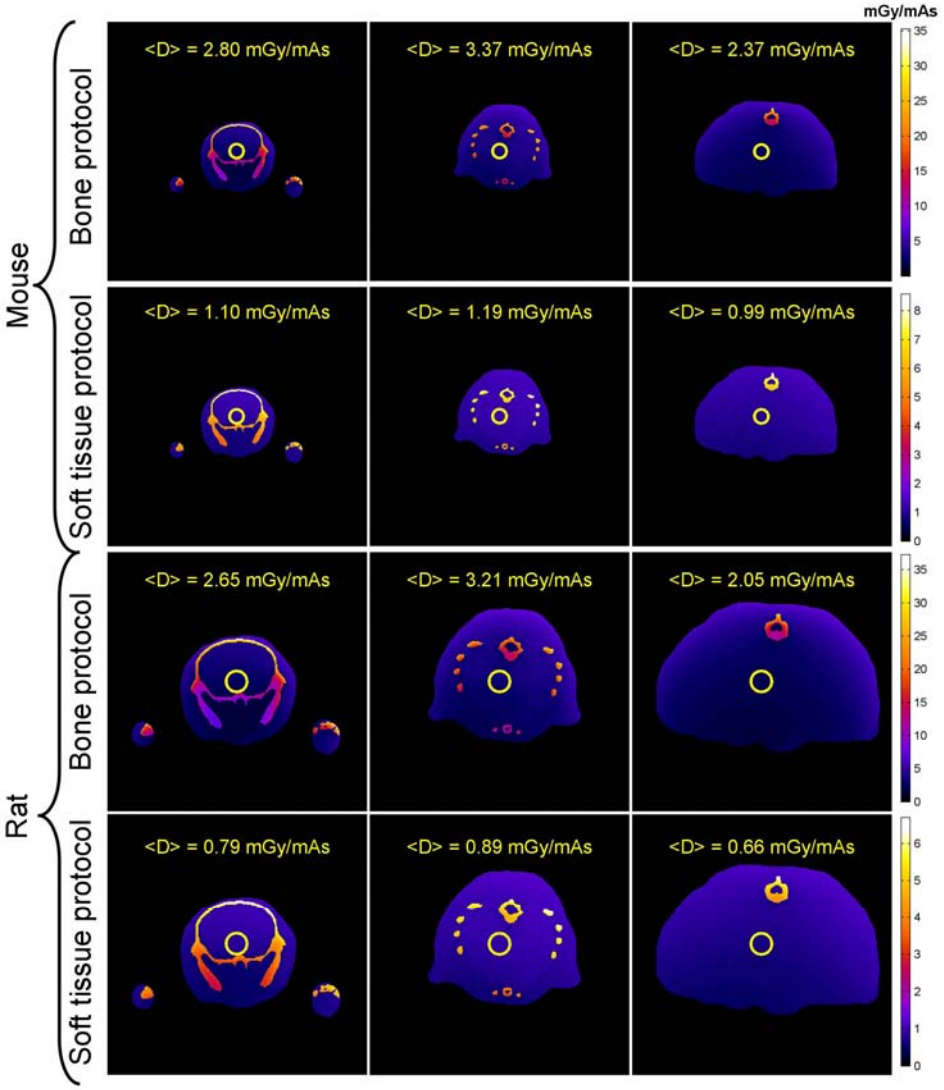

Figure 2.21. Monte Carlo simulated dose for partial trajectory acquisition protocols covering an angular span of 220º, normalized by mAs. Average dose values measured over the circular ROIs depicted on the central part of the distributions are labeled on top of them. Dose distributions are shown for a slice at the brain area, one at the thorax and one at the abdomen.

2.4.5 Tomographic data resolution

Figure 2.22 shows the MTF curves for the three configurations included in the experimental study. As expected, the MTF is better for the binning 1x1 configuration and, inside it for the larger magnification factor, in accordance with results in section 2.4.1.

Cutoff frequencies at 0.2 (0.1) MTF when using the Ram-Lak filter are 12.1 (13.5), 7.1 (8.4) and 2.7 (3.3) lpmm for binning 1x1 and *M₂* magnification, binning 1x1 and *M₁* magnification, and for binning 4x4 and *M₁* magnification, respectively.

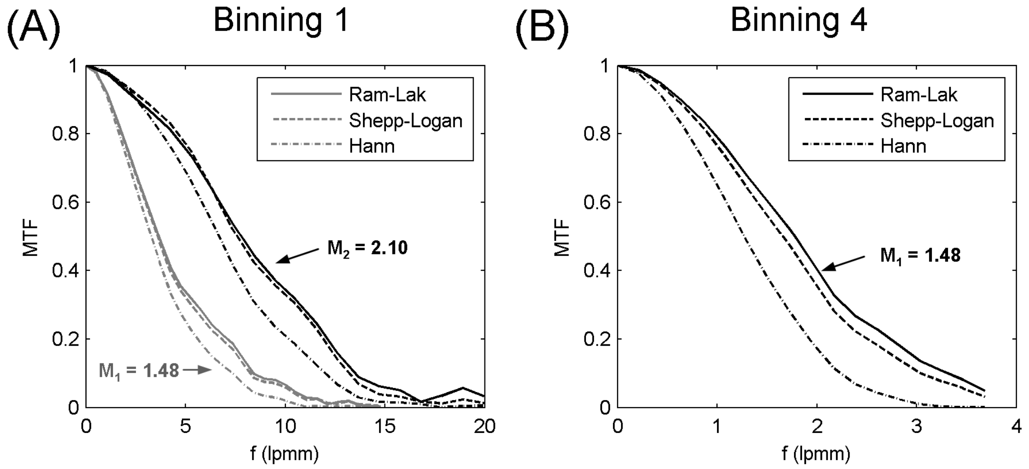

Figure 2.22. MTF of the reconstructed data for the native detector pixel size of 0.05 mm – binning 1x1– (A) and for a detector pixel size of 0.2 mm –binning 4x4– (B). The effect of the reconstruction filter kernel on resolution is shown for three filtering kernels, namely pure Ram-Lak (continuous curves), Ram-Lak multiplied by a Shepp-Logan window (dashed curves), and Ram-Lak multiplied by a Hann window (dash-pointed curves). Binning 1 data was measured for the two limit magnification factors in the system, M_1 = 1.48 and M_2 = 2.10.

Effects of the reconstruction filter on the resolution of the system can be extracted from figure 2.22. For binning 1x1, the effect of windowing the ramp filter is shown as a reduction in resolution which is larger for the M_2 configuration than for the M_1 configuration. Specifically, the frequency value at 0.2 (0.1) MTF is reduced to 11.9 (13.2) and 10.2 (12.0) lpmm for the Shepp-Logan windowed filter and for the Hann windowed filter, respectively, for the M_2 configuration; for the M_1 configuration they are reduced to 6.8 (8.2) and 5.6 (7.3) lpmm for the Shepp-Logan and for the Hann windows, respectively.

For the case of binning 4x4, the reduction in resolution caused by smooth filters is larger, being the 0.2 (0.1) MTF cutoff frequency reduced to 2.5 (3.0) and 1.9 (2.2) lpmm for the Shepp-Logan and Hann windows, respectively.

2.4.6 Contrast, noise and HU uniformity

We acquired tomographic data for the CNR phantom using the four acquisition protocols –mouse bone, mouse soft-tissue, rat bone, and rat soft-tissue– and for four exposure settings. Exposure was of 1.3, 2.6, 3.9 and 5.2 mAs for the mouse bone protocol; 1.7, 3.4, 5.1 and 6.8 mAs for the mouse soft-tissue protocol; 1.6, 2.4 and 3.2 mAs for the rat bone protocol; and 1.9, 3.8, 5.7 and 7.6 mAs for the rat soft-tissue protocol. Only three exposure settings were used for the case of the rat bone protocol due to the not guaranteed stability of the beam for very low anode current values.

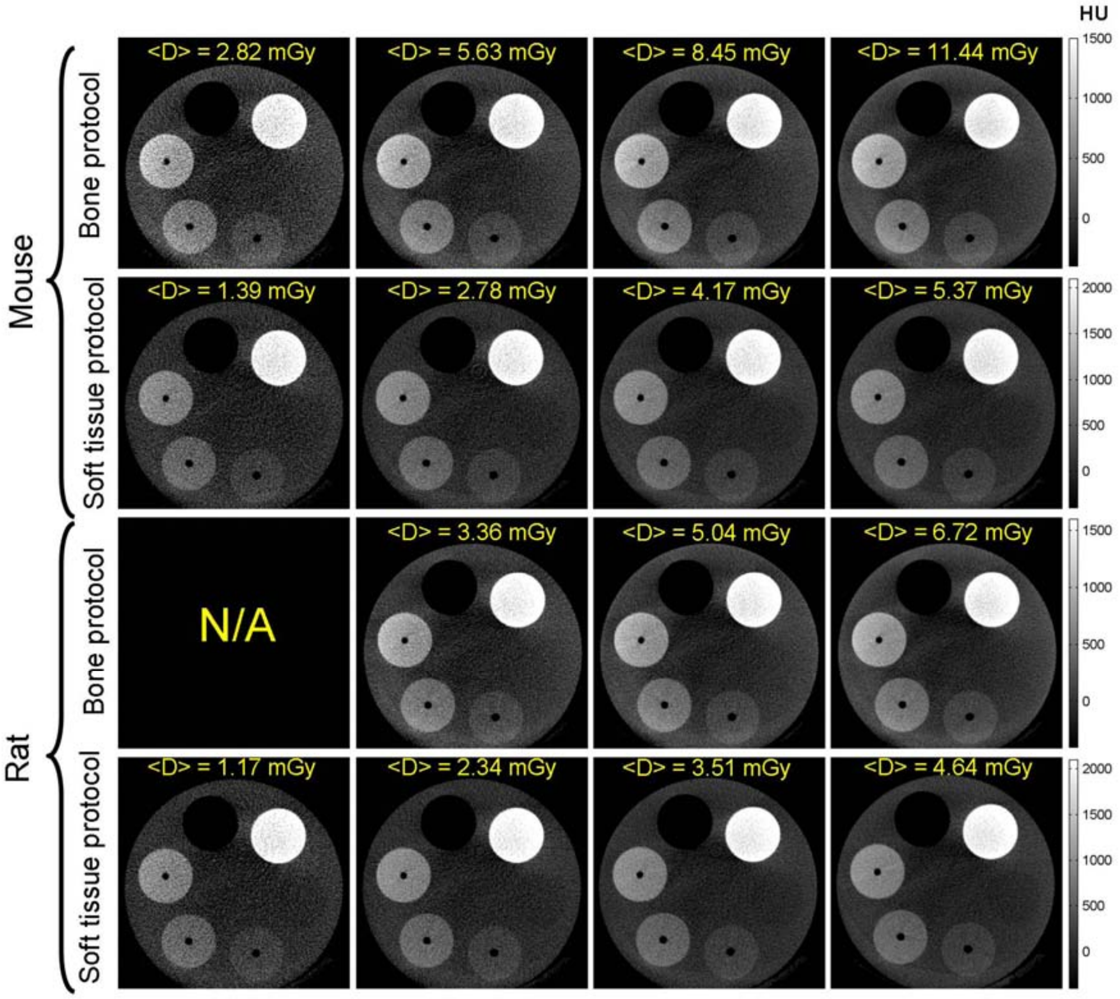

Figure 2.23. Central slice of the reconstructed volume of the CNR soft-tissue phantom for the four acquisition protocols and for 0.25, 0.5, 0.75 and 1.0 times the nominal mA value for each protocol. Yellow labels provide the dose delivered to the center of the sample for each dataset, estimated from CTDI measurements.

The dose delivered to the center of the sample for each of the acquisitions was estimated from the CTDI measurements in section 2.4.4 scaling them by the mAs value. Delivered dose values were 2.82 mGy, 5.63 mGy, 8.45 mGy and 11.44 mGy for the mouse bone protocol; 1.39 mGy, 2.78 mGy, 4.17 mGy and 5.37 mGy for the mouse soft-tissue protocol; 3.36 mGy, 5.04 mGy and 6.72 mGy for the rat bone protocol; and 1.17 mGy, 2.34 mGy, 3.51 mGy and 4.64 mGy for the mouse soft-tissue protocol.

Figure 2.23 depicts the central slice of reconstructed volume data for each of the acquisition protocols –reconstructed with the Hann filter– together with the dose delivered during the acquisition.

Image data showed a similar noise level across acquisition protocols, for the four exposure bins. This is the expected result, since mAs values used for each protocol yielded similar signal levels at the detector. While noise level is similar in all datasets soft-tissue protocols showed superior contrast between tissues and lower deposited dose, proving better performance for imaging the soft-tissue-like materials included in the phantom. Thus, materials are more easily identified when using the two soft-tissue acquisition protocols, being the more obvious improvement the capability of identifying the water region that was not visible for the bone protocols.

Cupping artifacts are more evident for bone protocols, as can be observed in the drop of image intensity toward the interior part of the inserts in the images generated for the bone protocols.

CNR and CNRD quantitative results, shown in figure 2.24, follow the trends hinted by visualization of the reconstructed data. Soft-tissue protocols showed larger CNR and CNRD values for all the materials in the phantom. The use of the soft-tissue protocol for mouse increased CNR values by factors 2.5-3.0 for Nylon, for the lowest and highest mAs setting, respectively, 1.5-2.0 for Delrin, 1.5-2.1 for PTFE, and 2.0-3.6 for the iodinated contrast. When including dose in the estimation of performance, ratios of CNRD between soft-tissue and bone protocols rose to 3.6-4.4 for Nylon, 2.2-3.0 for Delrin, 2.1-3.1 for PTFE, and 2.9-5.2 for Iodine.

Results for the rat protocols were very similar, showing very similar gains in CNR and slightly lower gains in CNRD, being those of 2.9-4.1 for Nylon, 2.2-2.8 for Delrin, 2.2-2.7 for PTFE and 3.3-4.0 for the iodinated contrast, reflecting the average lower dose/mAs delivered by the rat bone protocol compared to the mouse bone protocol.

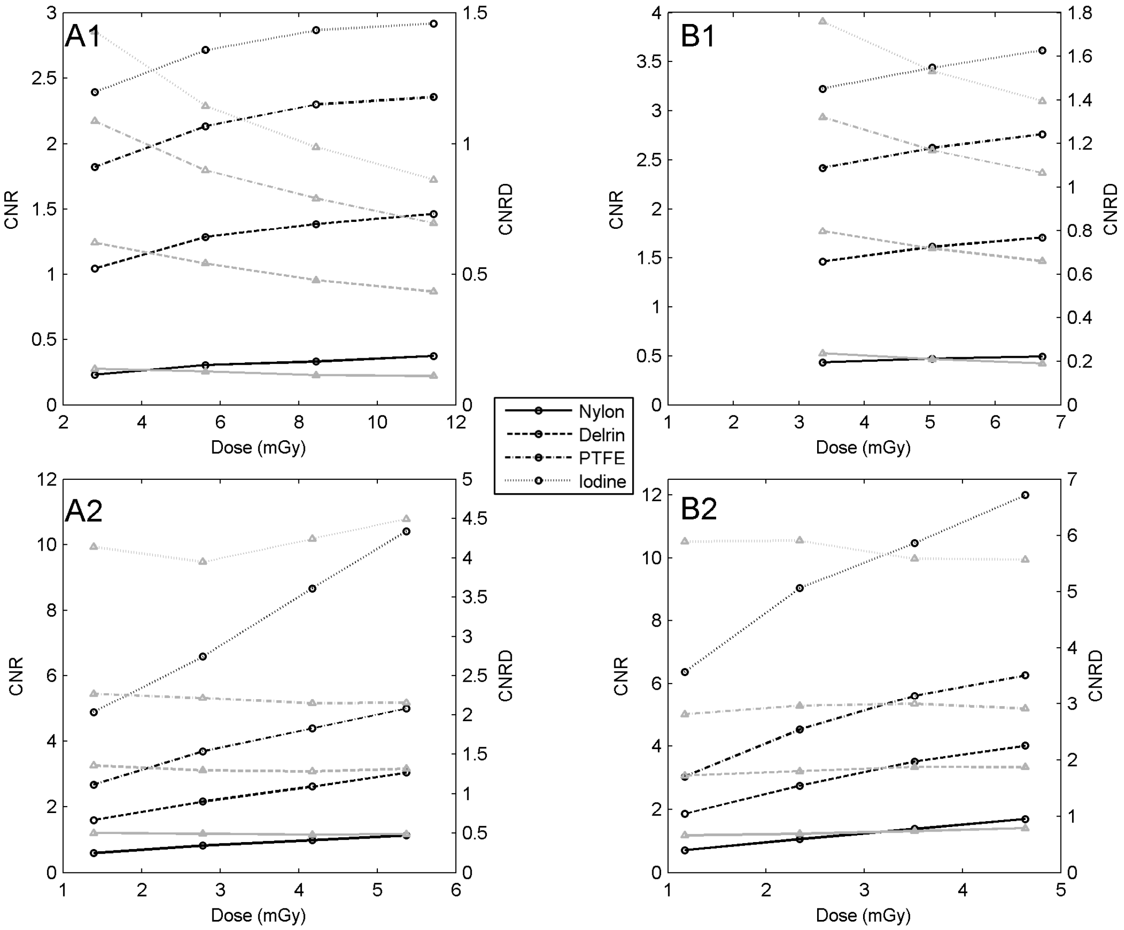

Figure 2.24. CNR and CNRD curves for the defined image acquisition protocols, as a function of dose, for data reconstructed with the Hann filter. Panel A1 shows the curves for mouse bone protocol, A2 for mouse soft-tissue protocol, B1 for rat bone protocol, and B2 for rat soft-tissue protocol. CNR curves are drawn in black and CNRD curves are drawn in gray. Continuous curves depict results for the Nylon area, dashed curves for Delrin, dash-point curves for PTFE, and point curves for iodinated contrast.

HU standard deviation as a function of dose is shown in figure 2.25, for the four acquisition protocols and for the three reconstruction filters, viz. Ram-Lak, Shepp-Logan and Hann. Noise values were reduced by a factor of ~2 for all of the protocols when using the Hann window and by a factor of ~1.20 for the Shepp-Logan window. The noise reduction provided by windowed filters did come at the cost of a lower resolution, as shown by results in section 2.4.5.

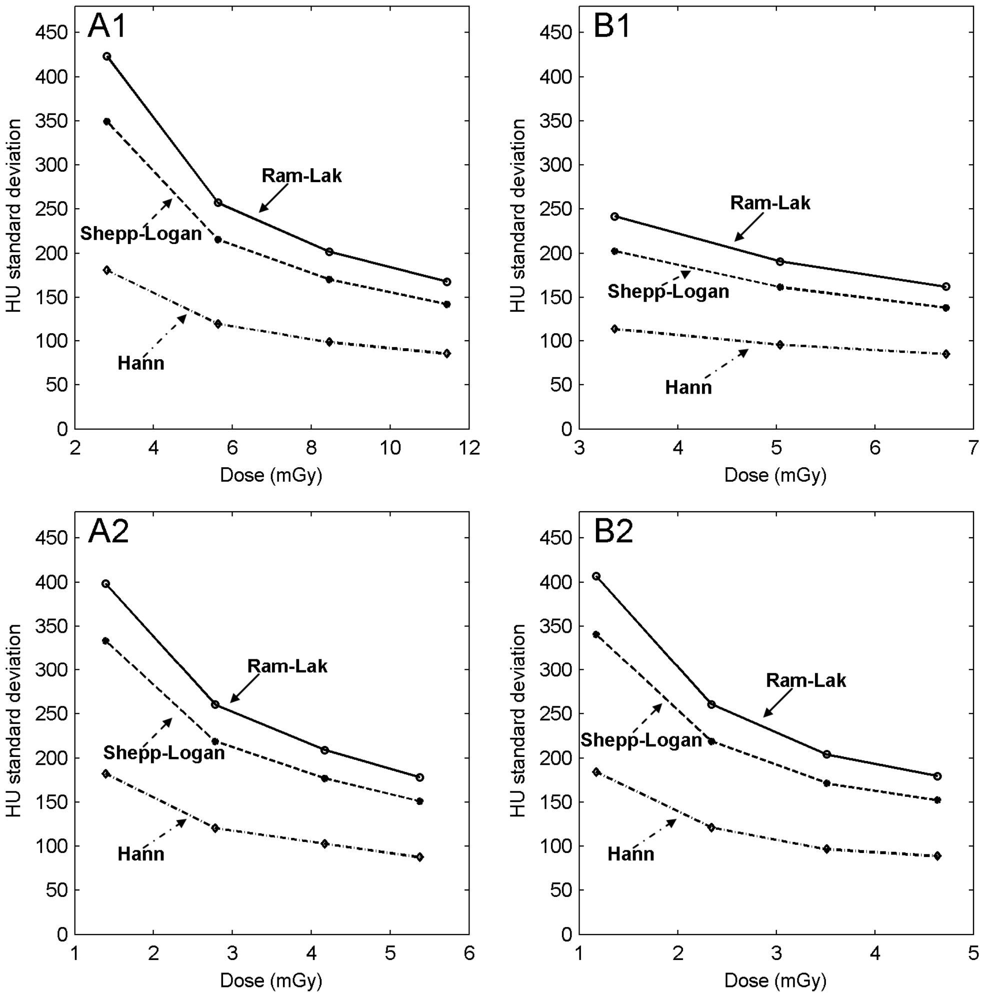

Figure 2.25. Noise in the reconstructed data as a function of dose for the water area of the CNR phantom. Noise was measured as standard deviation in the HU values for the mouse bone (A1) and soft-tissue (A2) protocols and for the rat bone (B1) and soft-tissue (B2) protocols. Data show the impact in noise of the reconstruction filter, showing a reduction in noise when apodizing the frequency response of the Ram-Lak filter.

Cupping measurements (t_{cup}) confirmed the visual trends that pointed to a more uniform distribution of HU values for the soft-tissue imaging protocols, compared to bone protocols. Average t_{cup} in PMMA was of 0.25 for mouse bone protocol and it reduced to 0.21 for mouse soft-tissue protocols, and rat bone protocol showed a t_{cup} value of 0.24 that was reduced to 0.22 for the soft-tissue protocol.

2.4.7 Small-animal CBμCT data

Figure 2.26 shows an example of a reconstructed volume of a mouse acquired using the presented system and the bone protocol. Data were reconstructed using the Shepp-Logan and Hann filters to illustrate the impact in noise and resolution of the filtration.

Data were acquired with a total of 5.2 mAs, estimated dose from CTDI of 4.38 mGy, 720 projections and 4x4 binning.

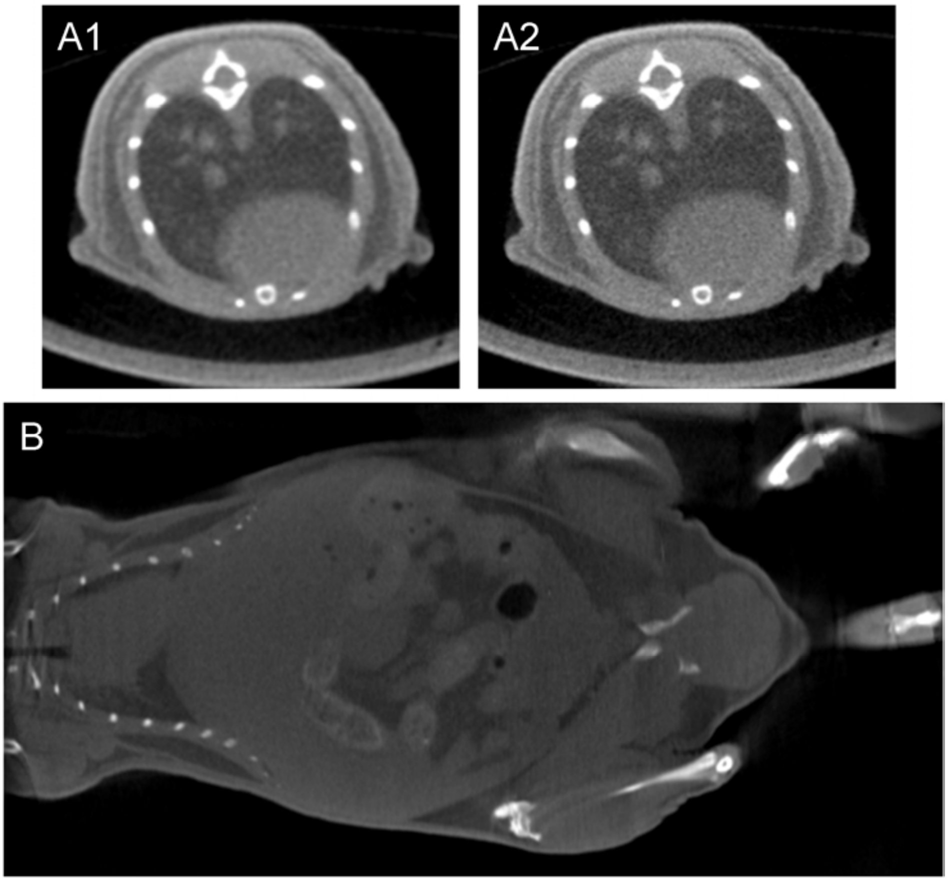

Figure 2.26. Example of a mouse CBµCT dataset using the bone protocol. Axial slice at the thorax reconstructed with a Hann window (A1) and with a Shepp-Logan window (A2) and coronal slice reconstructed with a Shepp-Logan window (B).

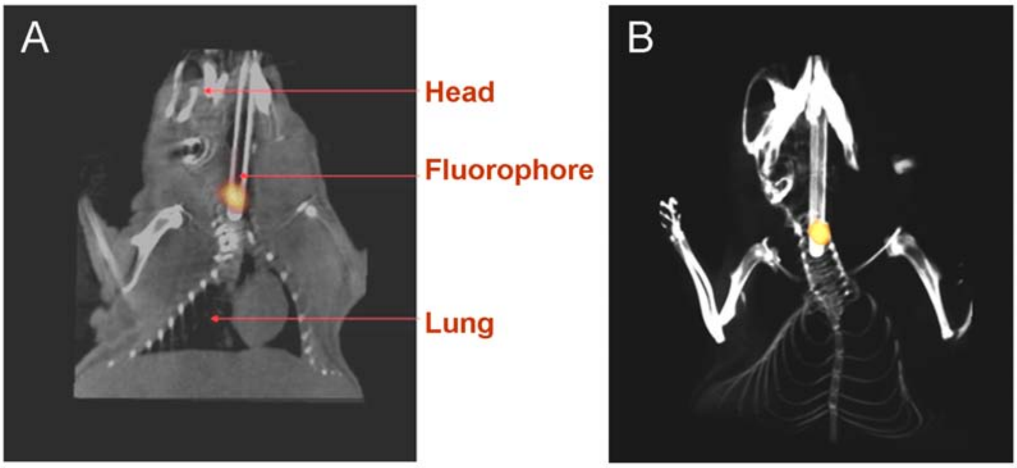

Figure 2.27. Example of a mouse CBµCT combined with a fDOT volume. Coronal slice (A) and volumetric render (B).

Figure 2.27 shows an example of a CBμCT image fused with a fDOT reconstruction acquired with the presented system. The fluorescence compound was confined into a capillary tube and both datasets were reconstructed separately and subsequently fused.

2.5 Discussion and conclusions

We have designed and built a new CBμCT system to be used in combination with a fDOT system. The system provides a high capability of adaptation to the imaging task by allowing the user to optimize the geometrical configuration and the acquisition protocol, covering from fast, low-dose, low-resolution protocols for the provision of anatomical landmarks based on bone structure, to the provision of high-resolution data with a competitive low contrast resolution for the visualization of soft-tissue structures.

The CBμCT system presented was based on a microfocus x-ray source and a flat-panel detector with a CsI:Tl scintillator and a CMOS sensor. The system permitted the movement of the detector to modify the magnification factor and, as a consequence, the FOV and resolution of the reconstructed volume. To achieve the maximum versatility for the use of the system we implemented two acquisition approaches one making use of a step-and-shoot acquisition scheme, where the slight blurring caused from motion is eliminated, and a continuous acquisition scheme that reduces the acquisition time and delivered dose. Both implementations used a multi-thread structure that maximizes the data throughput while guaranteeing the synchronization between data acquisition and processing.

While we have not found evident resolution loss from the use of continuous rotation approaches, thorough investigation of the appropriateness of the acquisition technique to the imaging task must be carried out for special situations requiring very high resolution or involving the acquisition of a low number of projections over a large angular span [192-193], where the use of a step-and-shoot approach could be beneficial. For those cases it would be mandatory to include a fast beam chopper to minimize the dose delivered to the subject. The development of such device is a subject of current research at our institution.

For the reconstruction of the acquired image data we developed a fast implementation of the well-known FDK method that takes profit of the highly parallel nature of the reconstruction process and of the massive parallel computing capabilities offered by modern GPUs. The reconstruction engine included the most common projection data preprocessing tasks (I_0, geometrical corrections and log conversion). In addition to standard processing we included correction techniques to allow the reconstruction of incomplete trajectories, following the approach in [168], and laterally truncated data that could arise when targeting the acquisition to a small ROI on the subject by increasing magnification. Laterally truncated data was extrapolated according to [98].

The system can be calibrated in a semiautomatic way using methods previously reported on the literature (geometry and gain maps generation) or designed specifically during the development of the system (defects, bed stitching). The calibration process can be carried out using a single software application and simple phantoms allowing the performance of calibration tasks by non-specialized staff.

The CBμCT system was specifically designed for providing both low quality data for the positioning of the optical functional information on its anatomical site as well as for the acquisition of high-quality data that could be used by itself or as a source of prior information to be incorporated into the functional data reconstruction. Information in the first case is achieved mainly by the contrast between soft-tissue and bone areas of the subject. For the second case it was necessary to maximize the contrast between soft-tissue structures since the optical properties can change drastically between different soft-tissue areas that have much more similar x-ray properties [194].

To achieve a good balance between image quality and suitability of the acquisition protocol to the imaging task we sought the spectral configuration that theoretically maximized the CNRD of the reconstructed data between bone and soft-tissue or between soft-tissue areas, basing our study on results by Hupfer et al. [173]. We found that voltages between 66 kV and 68 kV combined with copper filtration were the most appropriate for soft-tissue imaging because they maximized the detector signal while not exceeding x-ray source maximum power for the most extreme imaging conditions. However, the large power required for maximum magnification will diminish image resolution according to data in figure 2.11, providing a maximum resolution of ~9 lpmm at MTF_{20}. This inconvenient might be overcome by increasing the image integration time of the detector while reducing the anode current by the same factor, at the cost of a larger acquisition time and a lower dynamic range of the projection data [178] which impact must be further assessed.

For the case of bone imaging, voltage values between 50 and 60 kV were found to be the lowest providing a sufficient signal value at the detector and were selected according to their higher CNRD for low photon energies.

The evaluation of the individual components of the system showed the suitability of the x-ray source and detector for the acquisition of CBμCT data in terms of temporal stability and signal linearity that is further corrected by the multi-bright gain correction employed in the system.

The evaluation of the signal and noise transfer characteristics of the detector indicated a DQE(0) ranging from 0.3 (mouse bone protocol) to 0.6 (mouse soft-tissue protocol). These results are in agreement with data in the literature. Konstantinidis [159] reported a DQE(0) of 0.25 for a 28 kV and 1.5 mm Al added filtration beam for a very similar device and Siewerdsen et al. reported a DQE(0) of ~0.65 for harder beams [65-66] and similar scintillators.

The measured NEQ showed an overall slight higher value on the row for zero vertical frequency, together with a peak at an intermediate-low frequency. The structured noise shown by the flat-panel detector consists of a group of vertical bands of the same size. For this reason we believe the source of these effects in NEQ is the residual part of the structured noise remaining after the dark and gain corrections. However, no visible artifacts were observed on the corrected image.

DQE results also pointed at the suitability of the soft-tissue imaging protocols for maximizing the signal-to-noise transfer capabilities, as shown by the larger DQE values obtained.

Measured dose and CNRD values for the different acquisition protocols are in the same range or below data reported in previous literature, specially when using the soft-tissue imaging protocols. Vaquero et al. [4] reported a dose value of 33 mGy for a similar spatial resolution protocol compared to ~5 mGy when using the rat soft-tissue protocol and Hann window for a similar noise level. Hupfer et al. [185] reported CTDI values for a 32 mm-diameter PMMA phantom of ~3.5 mGy/mAs for a 50 kV with 0.5 mmAl added filtration beam and a system with SAD = 170 mm. This result is comparable to the CTDI of 2.19 mGy/mAs measured in our system for the mouse bone protocol (50 kV, 1.0 mmAl added filtration and SAD = 155 mm).

Zbikewski et al. [8] showed a signal-difference-to-noise ratio of ~1 for a dose value of ~10 mGy and for an adipose insert –which provided a theoretical signal difference of ~115 HU– and water and a 90 kV with 0.3 mmCu added filtration (harder than the beams used here) for a 250 mg/cm^2 detector, compared to a signal difference of ~180 HU between Nylon and water for the rat soft-tissue protocol and a similar CNR value for 5 mGy.

Analysis of the tomographic resolution achieved by the system showed slight degradation with respect to the theoretical maximum resolution for the minimum magnification factor that provided a resolution of 7.1 lpmm (at MTF = 0.2) compared to the theoretically achievable of 8.7 lpmm. This effect however is not reproduced for the higher magnification factor. One possible explanation is the presence of subpixel misalignments left after the geometrical calibration for this magnification factor. However, no apparent artifacts or blurring is observed in the data and a more in-depth study must be carried out in order to find the actual cause for the apparent loss in resolution.

Another conclusion that can be extracted from the resolution and noise data is the effect in reducing noise caused by the reconstruction filters which, under some circumstances, overcome the loss in resolution. As an example, the use of the Shepp-Logan windowed filter reduced noise by 20% while the resolution remains almost untouched, suggesting the use of this filtration for regular imaging practice. On the other hand, the Hann windowed filter indeed reduced the resolution of the data but also reduced the noise by a factor of two and it could provide very important dose reduction capabilities for not-very high frequency imaging tasks. In addition, there exists a tradeoff between magnification, resolution, noise and filtration. Noise is increased by increasing magnification owing to the inverse squared distance law, but resolution is also increased. In this case, the use of a smooth filtration could provide better resolution at a lower noise for the same dose.

There are some important factors beyond the scope of this work that affect image quality and must be studied or implemented for the improvement of image quality and/or the reduction of dose. One of them is the quantity and nature of x-ray scatter in such a compact geometry as the one presented here. Several hints are provided in chapter 6 and [119, 195] but a dedicated study has to be carried out to assess the impact of scatter for this particular configuration and the possible scatter reduction techniques.

As a further example, for making the most out of the variable geometrical setup of the system it must be studied the development and application of advanced data completion schemes involving the acquisition of partial high-resolution datasets and their completion with low-resolution, very low-dose datasets. Examples of such data completion techniques can be found in [196-197].

3 Expansion of the dynamic range of flat panel detectors for small-animal cone-beam CT: a dual-exposure technique

3.1 Introduction

Analytical reconstruction algorithms used in CBμCT, such as FDK [79], produce severe artifacts in the reconstructed slices when the field of view (FOV) covered by the acquired projections truncates the object under examination [10, 79]. Thus the scanner FOV should be larger than the size of the sample. If the subject has a high attenuation region, it is not possible to obtain a sufficient signal-to-noise ratio (SNR) inside this area without saturating the detector elements in the object-free region. Such a problem can arise in any CT scanner, when the dynamic range of the subject exceeds that of the detector.

Several approaches have been proposed to address this issue. Most were originally developed for optical imaging –i.e. photography and video– and are based on hardware modifications or special detector designs. Some implementations include the use of a non-conventional pixel design [198], multiple sensors inside a single pixel [199], spatially varying pixel sensitivity [200], or combinations of special scintillator and pixel designs [201]. In addition to the methods mentioned above, a small number of software-based methods have been developed. An example can be found in [202], who mathematically estimated a high dynamic range (HDR) dataset from the low dynamic range image.

Some of the most widely used software-based techniques for extending the dynamic range of optical image detectors are based on the acquisition of several images, each with a different exposure to incident radiation [203]. The acquired data are then combined to obtain a new HDR image. The combination algorithm to obtain the value of a pixel of the HDR image can be as simple as the selection of the best sample from the original dataset [204] or a more elaborate process, which takes advantage of all the information contained in the acquired data [205-206].

The use of multi-exposure–based techniques to extend the dynamic range of flat-panel detectors in CBμCT has been reported elsewhere [207]. However, the algorithm for obtaining the HDR data from datasets with different exposures was not fully developed, the performance of the method was not compared with that achieved by conventional scanning methods, and discontinuities were observed in the HDR data.

We introduce a dual-exposure technique based on a maximum likelihood approach to extend the dynamic range of flat-panel detectors. The method combines two projection datasets using a maximum likelihood estimation based on previous knowledge of the detector response to incoming radiation. The detector response is described using an existent analytical model [101] for pixel mean and variance which was extended to include the effect of saturation. The validity of the detector model was assessed using experimental data, and a parametric description was generated for a real flat-panel detector. The performance of our method in extending the dynamic range and its potential limits were evaluated using simulated data. In addition, the performance of the method in realistic imaging scenarios was assessed using experimental projection and CT data from a commercial CBμCT scanner.

3.2 Materials and methods

3.2.1 Generation of HDR projection data

The aim of the method is to measure x-ray projection data with a dynamic range that is larger than that achieved by the detector using a regular acquisition protocol.

In order to generate the HDR data, a minimum of two datasets must be acquired at two x-ray exposure levels (different mA value for the same kVp value). First, a regular acquisition is performed, followed by the acquisition of a partially saturated dataset.

Figure 3.1 outlines the workflow of the HDR data generation process. The following subsections detail the different steps.

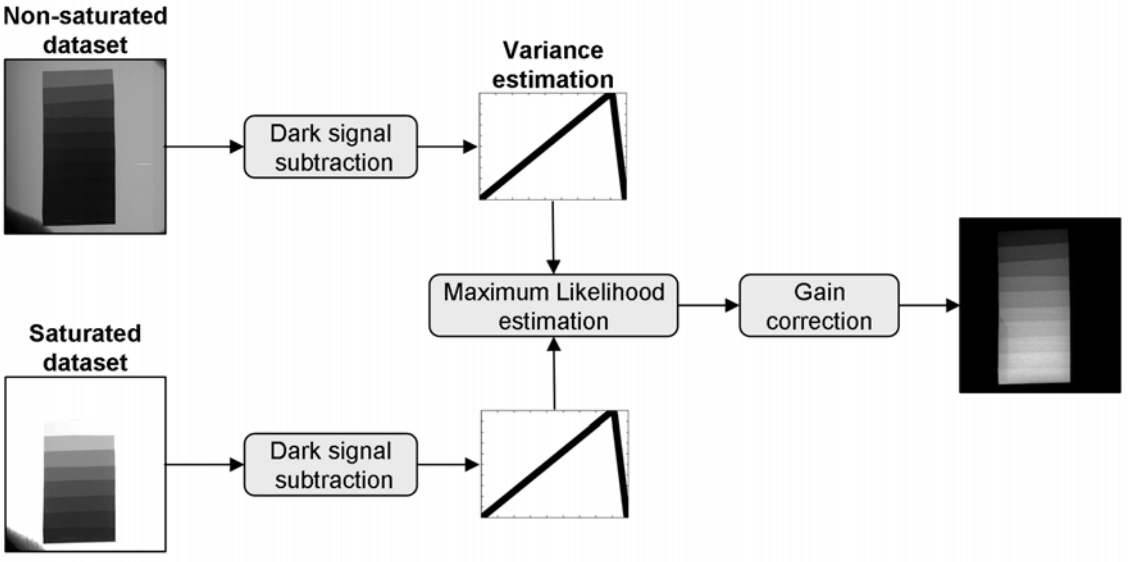

Figure 3.1. Outline of the dual-exposure method to obtain an HDR projection. Two datasets are acquired at different x-ray flux levels, and the dark signal is subtracted from both of them. After estimating the variance for each pixel in the dataset—according to the detector model—both datasets are combined using a maximum likelihood approach, thus generating the HDR data, which eventually undergo a standard gain correction step.

The mA for the first scan is set to the regular value according to the acquisition protocol. This value would be close to the maximum value not saturating any pixel of the projection images. At this mA setting, parts of the image showing very high attenuation can be underexposed and, therefore, may not provide a suitable signal.

A second scan is carried out at a higher mA value, which makes it possible to obtain a partially saturated dataset that provides improved information about all or, at least, some of the underexposed areas of the first scan. The ratio of the mA value for the second acquisition to the mA of the first one –i.e. the Bucky factor for the second acquisition– is denoted as A_2. The original dataset is combined with the partially saturated dataset following the method described below, which is based on the proposal in [206] modified to meet the particular features of x-ray flat-panel detectors.

While the method presented here aims to combine two datasets, it can easily be extended to any number (N) of datasets with A_i ($i = 1, \ldots, N$) values.

3.2.1.1 Pixel model

Flat-panel detectors show a linear relationship between the energy integrated within the pixel area and the pixel signal. Furthermore, the statistics of the incoming photons follow a compound Poisson model [100], for which the classic linear relationship between variance and mean, which is characteristic of Poisson processes, still holds. Given these premises, we assume a simple linear model for the pixel mean response (*m*) and its variance (*v*), following [101],

$$m(X) = gX + p\,, \tag{3.1a}$$

$$v(X) = h\left[m(X) - p\right] + n\,, \tag{3.1b}$$

where X is the exposure to incident radiation, g is the linear gain factor of the pixel, p is the mean dark offset of the pixel (i.e. the mean pixel signal in the absence of radiation), h is the linear factor relating mean and variance of the pixel signal, and n is a noise component accounting for all additive noise sources of the pixel that do not depend on exposure. These additive noise sources include quantization noise, a consequence of the digitization of the integrated energy, which depends on the bit depth of the detector [208].

In the present context, we are interested in the expansion of the dynamic range of the sensor to maximize the span of discernible x-ray attenuation factors. The attenuation value is obtained after the gain correction of the acquired data; therefore, we are not interested in the characterization of the gain properties of the detector and consider the product gX as a single variable whose range is determined by the dynamic range. Consequently, we can rewrite equations 3.1a and 3.1b as,

$$m(gX) = gX + p\,, \tag{3.2a}$$

$$v(gX) = h\left[gX\right] + n\,, \tag{3.2b}$$

Pixel values read from the detector are then assumed to be realizations of a Gaussian variable with mean and variance given by equations 3.2a and 3.2b.

The detector can enter the saturation part of the curve if gX is large enough to yield pixel values above the maximum. In that case, the pixel signal behaves as a clipped or censored Gaussian variable (i.e. realizations above the maximum yield the same pixel value), and the linear relation in equation 3.2b no longer holds. The point where the linear relation is no longer valid is considered the upper limit for the dynamic range.

Expressions for the variance of the censored variable as a function of the mean, $m(gX)$, and original variance for a non-truncated detector, $v(gX)$, provided by equations 3.2a and 3.2b, can be found in Appendix 3.A.

3.2.1.2 Joint probability density function and maximum likelihood estimation

To extend the dynamic range of the recorded image using the proposed method, we defined a joint probability density function (j-pdf) for the acquired data.

According to the previously described pixel model, each pixel observation can be considered a realization of a Gaussian-distributed random variable [100], with mean and variance given by equations 3.2a and 3.2b if the signal lies inside the non-saturated range.

Since values of a single pixel for the acquired datasets are independent, the j-pdf of the multi-exposure data can be expressed as the product of the pdfs of *N* Gaussian-distributed random variables, yielding

$$P(\mathbf{Y_j}) \propto \exp\left(-\sum_{i}^{N} \frac{\left(Y_{ij} - m(A_i gX_j)\right)^2}{v(A_i gX_j)} \right), \tag{3.3}$$

where Y_{ij} is the recorded pixel value for pixel j and acquisition i and $\mathbf{Y_j}$ is the vector of the N values recorded for pixel j.

The HDR signal for pixel j is estimated as the value of gX_j that maximizes the probability of observation of the acquired data or, equivalently, minimizes the absolute value of the exponent in equation 3.3, yielding the following expression for the objective function:

$$O(gX_j) = \sum_{i}^{N} \frac{\left(Y_{ij} - m(A_i gX_j)\right)^2}{v(A_i gX_j)}. \tag{3.4}$$

Equation 3.4 could be minimized by iterative approximations, but the proposed method is aimed at the raw data processing stage, which is usually highly demanding in terms of processing time. For this reason, we propose to replace the gX_j term in the denominator by the actual pixel value after dark correction ($Y_{ij} - p_j$). Deriving equation 3.4 with respect to gX_j after performing the approximation in the denominator and leaving the resulting equation equal to zero, the expression for the maximum likelihood estimation of gX_j becomes:

$$gX_j = \frac{\displaystyle\sum_{i}^{N} \frac{A_i (Y_{ij} - p_j)}{h(Y_{ij} - p_j) + n}}{\displaystyle\sum_{i}^{N} \frac{A_i^2}{h(Y_{ij} - p_j) + n}}. \tag{3.5}$$

In the present case, two datasets with two different A_i values (i = 1, 2; and A_1 = 1) are combined. However, to obtain a valid signal over a continuous range, A values must be properly selected to ensure some degree of overlap between the gain curves of the acquisitions, i.e. pixels below the dynamic range of the detector for the ith acquisition must not be saturated for the (i+1)th acquisition.

3.2.2 Experimental setup and data analysis for the detector model

We validated the analytical model for the detector and the HDR extension method using a commercial small-animal multimodality imaging system, the Argus PET/CT (Sedecal, Madrid, Spain). To assess the validity of the model, we acquired image data for several exposure levels and fitted the measured parameters (p, h, and n in equations 3.2a and 3.2b) to the detector model. Using the acquired data, we obtained a set of typical parameter values that characterize the performance of the detector for a configuration suitable for small-animal imaging scenarios.

3.2.2.1 Cone beam micro-CT system

The CBμCT subsystem of the Argus PET/CT is a small-animal CT designed to provide anatomical information that is complementary to functional PET data. A thorough description and evaluation of the system can be found in [4].

The system incorporates a microfocus x-ray source (Oxford Instruments, Oxfordshire, UK) based on a tungsten anode with maximum peak energy of 50 kVp that is capable of delivering a continuous power of 50 W (anode current range 0-1 mA). The energy spectrum is conformed using a 1-mm Al filter, which adds to the 0.125-mm–thick Be output window.

The x-ray signal is detected using a CMOS-based flat-panel detector (Hamamatsu Photonics K.K., Japan). The detector contains a CsI:Tl scintillation crystal grown directly on top of the sensor, with an active area of 12x12 cm^2 and pixel size of 0.2 mm, 0.1 mm, or 0.05 mm depending on the selected binning configuration (4x4, 2x2, or no binning). Binning also sets the minimum integration time of the detector, which is 0.125 s, 0.25 s, and 0.5 s for 4x4, 2x2, and no binning, respectively. Image integration time can be extended up to 10 s regardless of the binning configuration. The detector signal is formed by 12 bits.

3.2.2.2 Characterization of the flat-panel detector and estimation of parameters for the linear model

We acquired series of images for 25 x-ray exposure levels and set 4x4 binning for three image integration times, viz. 125, 500, and 1000 ms. Exposure on the detector surface was set by changing the anode current of the tube from zero to above the saturation point of the detector. We acquired 50 images for each exposure level, and, to avoid potential lag effects, the x-ray flux was turned off for two seconds between acquisitions of consecutive series of images. Data were acquired for 35 kVp (a common setting for small-animal imaging) with no object in the FOV, thus obviating object-related effects such as beam hardening or scatter.

Mean pixel value and variance were computed for every pixel of the detector at each of the exposure levels. We estimated the dark signal value, p (intercept of the gain curve), as the mean value for 0 mA. To obtain the dynamic range properties of individual pixels, and allowing for the effects caused by non-uniform distribution of radiation, we arranged the variance of each pixel in a histogram as a function of the mean value of the particular pixel for the same exposure setting. The resulting variance curve was adjusted to the linear model to provide values for n (intercept of the variance curve) and h (slope of the variance curve). For large exposure values, a considerable fraction of events fell into the saturated part of the gain curve of the detector, forcing the variance of the pixel value to depart from the expected linear trend and creating an elbow in the variance curve, in agreement with the previously introduced censored Gaussian model. The position of the elbow was considered to be the upper limit for the pixel dynamic range. According to [209], the lower limit for the dynamic range was estimated as the signal level necessary to obtain an SNR of one.

The validity of the censored Gaussian model for the completion of the linear model for variance at areas near saturation was proved by theoretically calculating the variance of a censored Gaussian variable limited to 4095—the maximum pixel value for a bit depth of 12 bits—as a function of gX, using the n, h, and p parameters calculated.

We investigated the overall properties of the detector as a function of x-ray exposure by averaging the mean and variance curves of individual pixels and proceeded with the individual pixel analysis (see above) to obtain the parameters for the averaged detector.

As an alternative to anode current modification, exposure can be increased by extending the integration time of the detector for a constant anode current. We characterized the performance of the detector in terms of dark signal and additive noise as a function of integration time. To this end, we acquired series of 50 images for integration times ranging from 0.125 s to 2 s using 4x4 binning. Mean pixel value and variance were computed for each pixel, and the average across all the pixels in the detector was assumed to reflect the overall behaviour of the detector.

3.2.2.3 Impact of dark signal and additive noise on detector dynamic range

The impact of the dark signal level and additive noise on the dynamic range of the detector was estimated using an analytical calculation of the minimum and maximum pixel values. We obtained the lower limit for the pixel signal by making the SNR equal to one, i.e. $m(gX)^2 = v(gX)$, and we used the censored Gaussian model to find the elbow of the variance curve $v(gX)$, which is the upper limit for the pixel signal. Dynamic range was computed as the difference between the upper and lower limits, and the resulting value was normalized by the maximum pixel value for the bit depth of the detector.

3.2.3 Assessment of the performance of the HDR method

We evaluated the potential performance of the HDR method by means of simulated data obtained using the detector analytical model for generic detectors with ideal properties, i.e. limited only by quanta statistics. The effects of detector non-idealities on the performance of the HDR method were analyzed.

The actual performance of the method in realistic small-animal imaging scenarios was assessed for both planar and tomographic imaging using two dedicated phantoms. Experimental data were acquired using the previously described Argus PET/CT scanner. Each test protocol included the acquisition of a dataset using the dual-exposure technique presented here and a second dataset using a regular single-exposure technique. All acquisitions were performed in such a way that the number of frames acquired per angular position for the single-exposure data was chosen to match the mAs values used for dual-exposure data. Therefore, the same dose was delivered to the sample for both the single- and the dual-exposure data acquisitions.

3.2.3.1 Analysis of the performance of the HDR method for generic detectors

The performance analysis was carried out for an ideal detector with the h value obtained for the Argus PET/CT detector and $p=n=0$. For this ideal detector, simulations of pixel signal were carried out as a function of the attenuation of the x-ray beam. To this end, the theoretical air exposure (gX_a) was set at around 90% the saturation limit for the pixel value, and the beam was assumed to be attenuated by a range of water thicknesses (x) from 0 cm to 25 cm at 0.5 cm intervals. We performed 500 realizations of a Gaussian-distributed random variable for each thickness value. According to Beer's law, we set the mean of the Gaussian function to $m=gX_a\cdot\exp(-\mu_w x)$, where μ_w is the linear attenuation coefficient of water. Variance was given by the detector model for m. For the sake of simplicity and with no loss of generality, the bit depth of the virtual detector was set to 8 bits.

For each water thickness value, dual-exposure data were simulated for different values of dose Bucky factors (A), starting at 1 and running up to $\exp(-\mu_w x)^{-1}$. The simulated signal for each value of A was combined with the original signal –i.e. A=1– using the HDR method, and the SNRs of the combined data were computed.

To confirm that the HDR method achieved an effective extension of the dynamic range of the detector, SNR values for the HDR method were compared to the theoretical improvement in SNR which would be obtained by averaging an equivalent number of frames delivering the same total dose to the subject, that is, $A^{-1/2}$.

To assess the importance of the dark signal for the dynamic range of the detector, the HDR method was applied to simulated data for which the Bucky factor (A) was set by increasing the exposure time instead of the x-ray source anode current.

Since the additive noise level of the detector is constant with integration time, its effect is limited to the reduction of the initial dynamic range of the sensor; however, the potential for dynamic range extension offered by the HDR method does not depend on the level of additive noise present in the detector.

3.2.3.2 Performance evaluation with planar projection data

We designed and built a dedicated phantom to evaluate the performance of the dual-exposure technique with planar projection data. The phantom consisted of a set of layers of copper tape of different thicknesses ranging from 0.45 to 1.125 mm. The layers were arranged to form a staircase structure as shown in figure 3.2.

The Argus PET/CT system contains a PMMA tube that protects the gantry from accidental leaking of fluids. When attenuation is very high, the signal can be contaminated by scatter generated in the protective tube from the non-attenuated part of the beam, thus masking the results. To allow proper evaluation of the algorithm using the planar phantom, the non-attenuated part of the beam was blocked by framing the phantom in a lead window 2.5 mm thick, thus practically suppressing the scattered radiation generated in the protective tube.

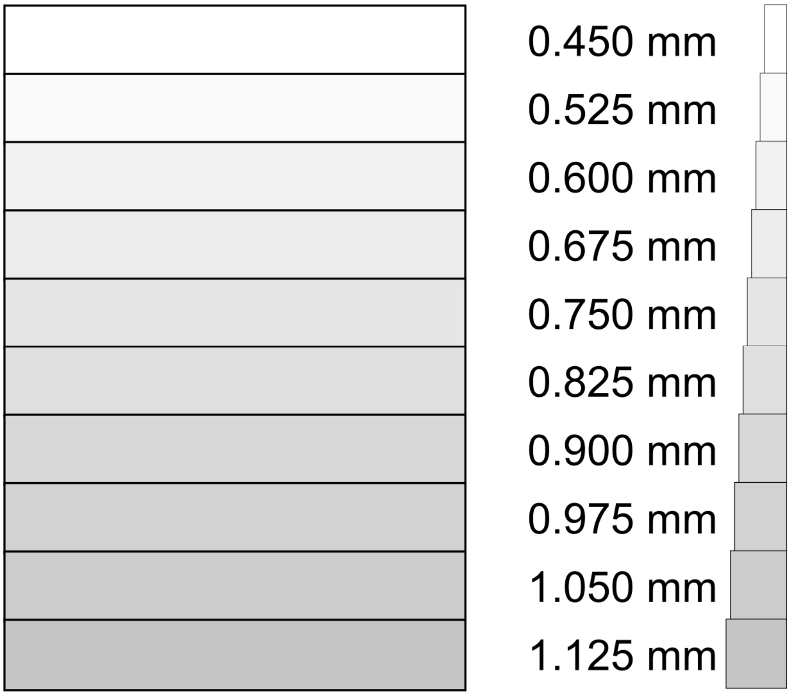

Figure 3.2. Schematic diagram of the phantom designed to evaluate the performance of the method with planar image data. Top and side view. The numbers show the thickness of the different layers. The lead frame surrounding the phantom is not shown in the diagram.

The Argus PET/CT system contains a PMMA tube that protects the gantry from accidental leaking of fluids. When attenuation is very high, the signal can be contaminated by scatter generated in the protective tube from the non-attenuated part of the beam, thus masking the results. To allow proper evaluation of the algorithm using the planar phantom, the non-attenuated part of the beam was blocked by framing the phantom in a lead window 2.5 mm thick, thus practically suppressing the scattered radiation generated in the protective tube.

We measured profiles across the staircase pattern and SNR values on each of the steps to evaluate the performance of the HDR algorithm. SNR values were estimated as the ratio of mean to standard deviation of pixel values measured on 40×20–pixel ROIs centered on each of the steps.

Table 3.I shows the acquisition parameters for the projection data. The integration time of the detector was extended to reduce the value of current saturating the detector and to obtain a larger range of anode current for the HDR method. The dark correction was

performed using 50 averaged images. For the gain correction we used 50 averaged images acquired at the nominal current of the single-exposure protocol.

Table 3.I. Acquisition parameters for projection data.

Parameter	*Protocol 1*		*Protocol 2*	
	Dual-exposure	*Single-exposure*	*Dual-exposure*	*Single-exposure*
X-ray beam energy	30 kV	30 kV	35 kV	35 kV
X-ray beam filtration	1 mm Al	1 mm Al	1 mm Al	1 mm Al
Number of exposures	2	1	2	1
X-ray tube current	0.10 / 1.00 mA	0.10 mA	0.08 / 0.96 mA	0.08 mA
Integration time	1500 ms	1500 ms	1000 ms	1000 ms
Frames per projection	1	11	1	13
Total output	1.65 mAs	1.65 mAs	1.04 mAs	1.04 mAs
Acquisition time	3 s	16.5 s	2 s	13 s

3.2.3.2 Performance evaluation with tomographic data

Contrast resolution on tomographic slices was evaluated using a dedicated phantom consisting of a homogeneous cylinder made of PMMA (density = 1190 kg/m^3). The phantom contained cylindrical openings of different diameters on the PMMA rod that were filled with an iodinated contrast agent (iopamidol 300 mg/ml, Iopamiro 300, Bracco s.p.a., Milan, Italy). A copper sheet 0.5 mm thick was fixed around the PMMA cylinder to simulate a hard bone skull. A sketch of this phantom is shown in figure 3.3.

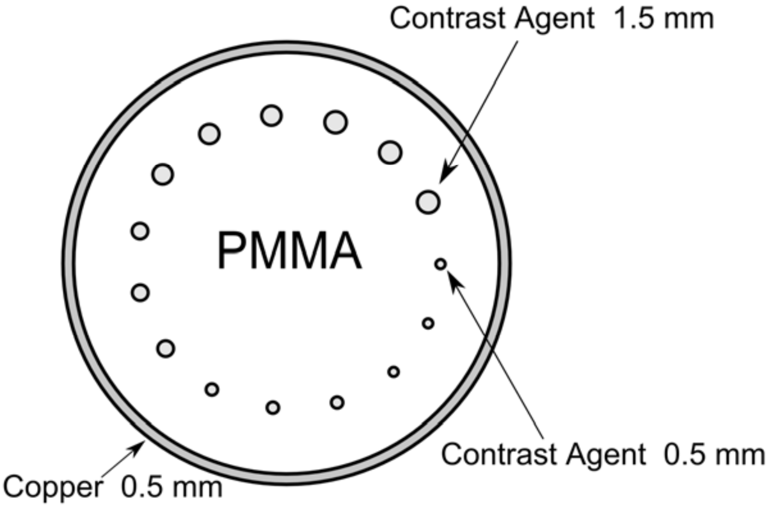

Figure 3.3. Diagram of the contrast resolution phantom. The phantom consists of a uniform PMMA background surrounded by a 0.5-mm–thick layer of copper tape. To estimate contrast inside the PMMA region, cylindrical openings of several diameters were drilled on the uniform region and filled with an iodinated contrast agent. The size of the cylindrical inserts ranged from 0.5 to 1.5 mm in 0.25 mm steps, with three inserts per size.

As in the previous case, we set the acquisition parameters for the dual- and single-exposure scans to deliver the same radiation dose to the subject under study (see Table 3.II), and the dark and gain corrections were performed equally.

Table 3.II. Acquisition parameters for the low-contrast resolution study.

Parameter	*Dual-exposure*	*Single-exposure*
X-ray beam peak energy	35 kV	35 kV
X-ray beam filtration	1 mm Al	1 mm Al
Number of angular projections	360	360
Number of exposures	2	1
X-ray tube current	0.06 / 0.96 mA	0.06 mA
Integration time	1000 ms	1000 ms
Number of frames per projection	1	17
Total output	367.2 mAs	367.2 mAs
Acquisition time	720 s	6120 s

Tomographic reconstruction was carried out using a regular FDK approach with a Shepp-Logan windowed ramp filter (see chapter 2, section 2.2.4). Reconstructed volume size was 512x512x142 voxels with a voxel size of 0.125x0.125x0.5 mm. To minimize the impact of ring artifacts in the measurements, both the single-exposure and the HDR data were processed using the ring artifact removal method described in [106], with identical parameters for both datasets.

The impact of noise on the detection of the inserts was evaluated by visual inspection. The contrast-to-noise ratio (CNR) between the 1.5-mm iodine regions and the PMMA background was measured for both datasets. The expression used to compute the CNR values was:

$$CNR = \frac{\left|\mu_{PMMA} - \mu_I\right|}{\sqrt{\sigma_{PMMA}^2 + \sigma_I^2}}, \tag{3.6}$$

where μ_{PMMA} and μ_I are the average voxel value of the PMMA and iodine insert regions respectively, and σ_{PMMA} and σ_I are the standard deviation values inside these regions. The resulting values presented below are the mean of the three CNR values calculated from each of the three 1.5-mm inserts.

3.3 Results

3.3.1 Detector model assessment

Figure 3.4 shows the overall pixel mean and variance as a function of exposure for the three image integration times set in the study (left plot) and as a function of integration time when no radiation is reaching the detector (right plot). The response of the detector in analog-to-digital units (ADU) is linear with radiation level. Detector pixel variance, averaged over the detector area, shows a linear trend that is broken at the point where some of the pixels enter the saturation area and the analytical model for variance breaks due to clipping of the pixel signal, as explained by the censored Gaussian model. The point where the variance reaches its maximum value was considered the upper limit for the exposure setting.

Variance curves in the left panel of figure 3.4 show that the extension of the integration time lowers the maximum exposure value. This effect can be explained by the trend of the dark signal as a function of the integration time shown in the right panel of figure 3.4. The increase in dark signal reduces the available dynamic range of the sensor and, therefore, the maximum exposure value saturating the detector. Variance of the dark signal does not seem to depend on integration time, suggesting that additive noise can be considered constant.

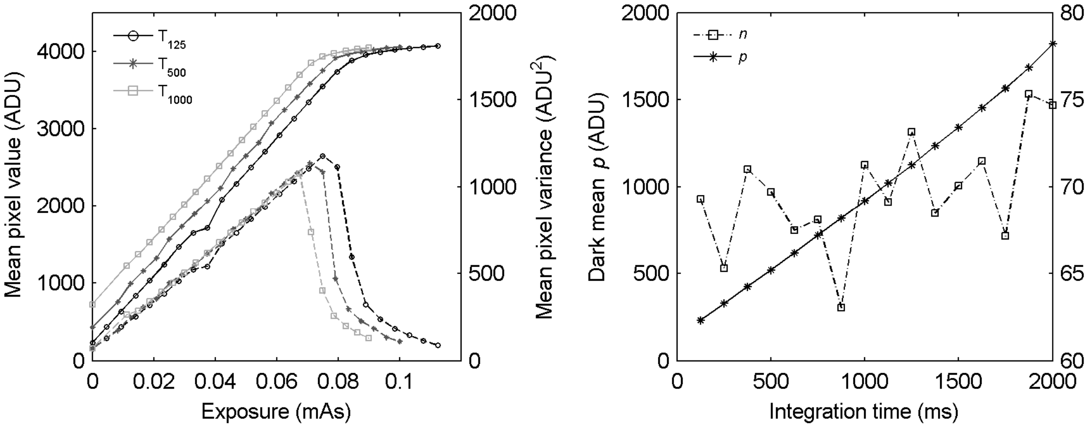

Figure 3.4. Mean response and mean variance of the detector as a function of exposure (left plot) and when no radiation is reaching the detector (right plot). The mean pixel value is represented by solid curves on the left plot; variance is represented by dashed curves.

Figure 3.4 shows the overall performance of the detector, i.e. averaging values over the detector area and not taking into account effects caused by the non-uniformity of the exposure reaching the detector surface, such as $1/R^2$ or Heel effects. The dynamic range of single pixels can be extracted from individual variance as a function of their mean value after dark signal correction, calculated as described in section 3.2.2.2. Individual pixel variance is shown in figure 3.5 for the three image integration times.

The parameters for the linear noise model (*n* and *h*) extracted from the data in figure 3.5 were found to be constant across different integration times, showing an almost constant level of additive noise $n = 68.49$ ADU^2 (as expected from the results in figure 3.4) and a slope relating signal mean and variance of $h = 0.33$.

The theoretical variance curve calculated using the censored Gaussian model (figure 3.5) shows good agreement with experimental data, thus proving its suitability for estimating pixel variance and, therefore, obtaining accurate simulated values of pixel signal and noise for generic detectors.

According to the results in figure 3.5, image integration time also affects the dynamic range of individual pixels, which is 3763:1 for an integration time of 125 ms, 3647:1 for 500 ms, and 3258:1 for 1 s. The upper limits for the dynamic range were estimated by the elbow of the gain curves and found to be 3772, 3656, and 3267 ADU above the dark signal, for 125, 500, and 1000 ms, respectively. The lower limit to obtain an SNR of one was 8.66 ADU above the dark signal, regardless of integration time.

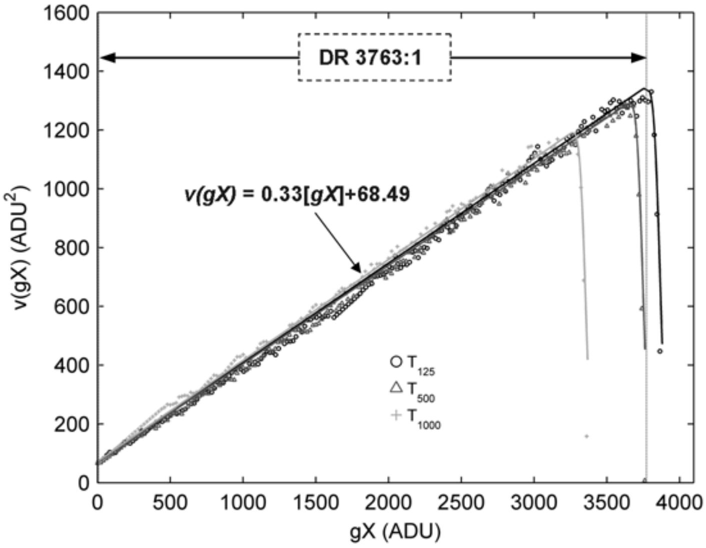

Figure 3.5. Pixel variance as a function of pixel mean, after subtraction of the dark signal, shows a linear relationship up to the saturation point of the detector. The theoretical value for pixel variance is shown by solid curves; experimental data are represented by markers. The detector shows a level of additive noise of $n = 68.49$ ADU^2, a variance slope of $h = 0.33$, and a maximum dynamic range of 3763:1.

3.3.2 Impact of dark signal and additive noise on detector dynamic range

The normalized dynamic range of the detector as a function of the dark signal and additive noise is shown as a two-dimensional distribution in figure 3.6.

As expected from previous results, the normalized dynamic range in figure 3.6 shows a much larger dependence on the dark signal than on additive noise, owing to the squared relation with the latter. According to this finding, the dynamic range of the detector is set to a large extent by the level of the dark signal in the detector unless the value of additive noise is so large that it almost reaches unfeasible values. The relatively low impact of additive noise in the dynamic range, despite being a considerable source of noise when a low number of photons reach the detector [101], justifies the exclusion of additive noise in the assessment (shown below) of dynamic range extension capabilities offered by the HDR method.

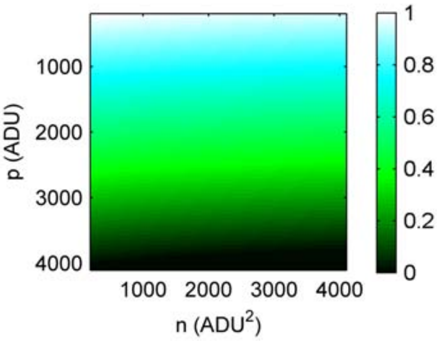

Figure 3.6. Normalized dynamic range as a function of dark signal, *p*, and additive noise, *n*, for a 12-bit detector.

3.3.2 Performance of the HDR method for generic detectors

The results extracted from the simulated data are shown in figure 3.7. When the attenuation of the beam is high enough, the number of photons reaching the detector is not sufficient to exceed the noise level. Since the signal provided by any single frame does not contain valid information, the increase in dose from the acquisition of a larger number of frames does not translate into a benefit in terms of SNR. This finding is shown in figure 3.7-A, when the beam is attenuated by more than 17 cm of water.

Figure 3.7-B shows how the HDR method makes it possible to extend the dynamic range of the detector, since the SNR of the data can be maintained constant throughout attenuation by increasing the dose by the appropriate factor. As opposed to frame averaging, the increase in dose is translated into a recovery of SNR regardless of attenuation if the Bucky factor is large enough to provide a valid signal. When the Bucky factor is below that value, the use of the HDR method has the same effect as frame averaging (see lower left corner in figure 3.7-B).

Note that the SNR obtained by the HDR method is larger than that achieved by frame averaging, even when the signal is not below the minimum level. For instance, the maximum SNR achieved by averaging frames for 5 cm of water is 25.16; using the HDR method, the SNR increases to 28.47. The larger SNR shows the denoising effect of the maximum likelihood estimation, which adds to the dynamic range extension.

In cases where it might not be feasible to increase the current of the x-ray source, the increase in exposure can be obtained by extending the image integration time of the detector. However, when the overexposed image for the HDR method is obtained using a longer integration time, the performance of the method undergoes notable degradation (see figure 3.7-C). The rise of the dark signal narrows the dynamic range of the overexposed image, reducing it to zero when the Bucky factor needed to obtain a valid signal is too large.

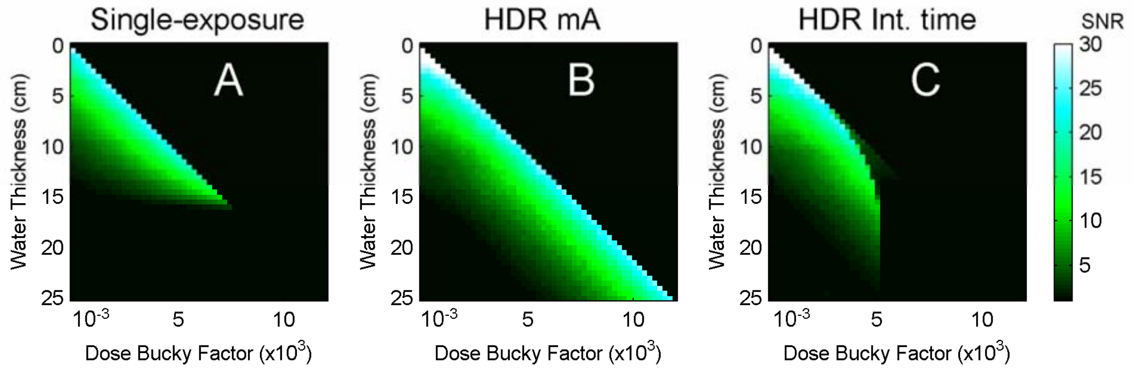

Figure 3.7. Performance of the HDR method for the extension of detector dynamic range estimated by the SNR of the acquired data for different attenuation values (B, increasing the x-ray source current and C, increasing the image integration time) compared to the SNR obtained by averaging techniques for the same attenuation values (image A). When the attenuation of the x-ray beam is large enough, an insufficient number of photons reach the detector, no information is registered in the image, and the SNR falls to zero owing to the lack of signal. Using the HDR method, the SNR of the image can be maintained almost constant, provided the current span of the x-ray source is large enough.

3.3.3 Results for planar projection data

Figure 3.8 shows a planar image of the bar pattern phantom, for both the single- and the dual-exposure data, acquired using protocol 1 in table 1 (30 kVp).

Profile data across the bar pattern for both acquisitions, plotted in figure 3.9, show how the signal is masked by noise for high attenuation values, thus concealing the transition between consecutive copper thickness values. As expected from the analytical results above, frame averaging cannot improve SNR in these areas, owing to the lack of valid photons. The steps become visible when the HDR method is applied.

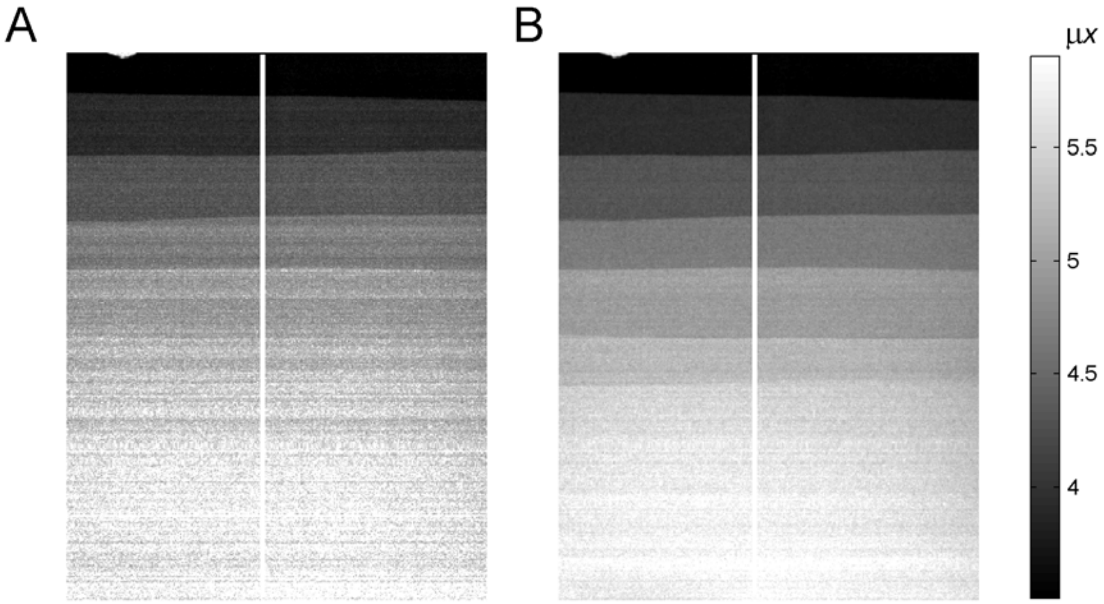

Figure 3.8. Copper stair phantom acquired using the single-exposure protocol (A) and the dual-exposure protocol (B) for acquisition protocol 1 (30 kVp). The lead frame is not shown in the image. The white line denotes the position where the profile data were measured. Note the extension in the dynamic range provided by the HDR method which translates into an enhancement of the visibility of the high attenuation regions of the phantom. The acquisition of both datasets delivered the same radiation dose to the sample.

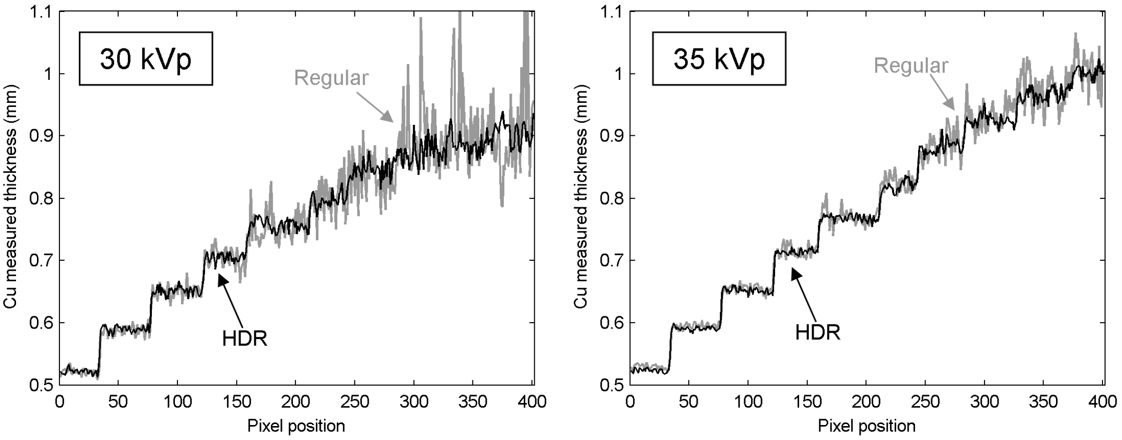

Figure 3.9. Profile plot across the bar pattern phantom projection for the single-exposure protocol (grey curves) and the dual-exposure protocol (black curves) for 30 kVp (left) and 35 kVp (right), i.e. protocol 1 and 2, respectively (table 1). Image log values have been normalized by the attenuation factor of copper at the mean energy of the beam to show the estimated thickness of copper. Deviations from real thickness values could arise from the impossibility of knowing the exact composition of the phantom material and from physical effects such as beam hardening. HDR data show a lower noise level for large thickness values, at both energy levels.

SNR measurements as a function of mean pixel value of the ROI are shown in figure 3.10. Using the HDR method, the detector achieved a dynamic range that provides a useful signal for most of the attenuation values, while single-exposure data do not provide a valid signal for large thickness values. Besides the extension in dynamic range, SNR values show better denoising capabilities for the HDR method than for frame averaging, even when the signal is large enough to allow the increase in SNR by averaging. However, as the signal level grows, the SNR curve for the HDR data shows asymptotic behaviour, and the performance of frame averaging approaches that of the HDR.

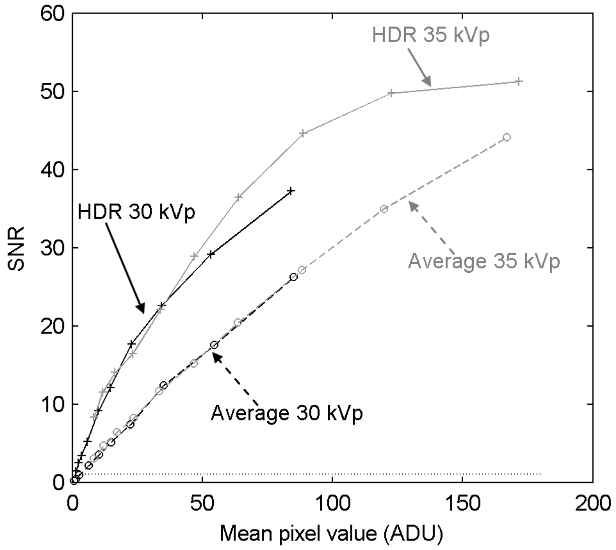

Figure 3.10. SNR measured inside the ROIs for each of the thicknesses as a function of the mean value for the HDR and frame averaged data. Data perform better when the HDR method is used, especially for a high thickness value (low mean pixel value). When the attenuation value is too high, the lack of a valid signal (even in the overexposed data) makes it impossible to obtain an appropriate SNR (even when using the HDR method). Such is the case for the first four points in the 30 kVp curve in accordance with the image and profile data that show poor quality inside those areas. Once the number of photons in the overexposed data is large enough, the SNR of the HDR data grows fast, and the curve departs from the averaging curve.

3.3.4 Results for tomographic data

Figure 3.11 depicts a slice of the reconstructed volume for the single-exposure and for the dual-exposure scans, with and without ring artifact correction. The single-exposure image has a poorer contrast resolution, and most of the inserts are masked by noise and artifacts (see zoom-in window in figure 3.11). Using the HDR technique, we can observe a marked reduction in the level of ring artifacts and noise present in the data. The mean CNR value inside the 1.5-mm inserts for the single-exposure data is 0.58, which grows to 1.71 when the HDR method is used.

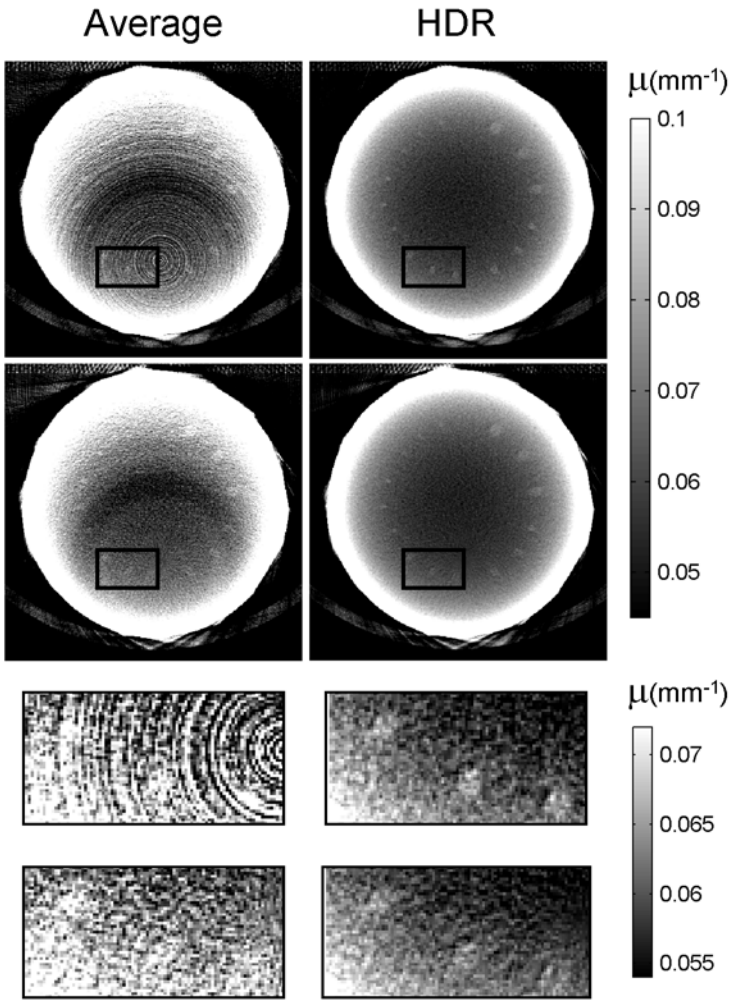

Figure 3.11. Slice of the contrast resolution phantom acquired using a regular single-exposure protocol (left column) and the dual-exposure protocol developed in this study (right column). The high level of artifacts and noise makes it difficult to discern the inserts from the surrounding background. If a ring artifact reduction method is applied, visibility improves but remains low. When the HDR method is used, artifacts are almost suppressed and the CNR becomes larger, making the inserts visible.

If the post-processing method (see section 3.2.3.3) is applied to suppress ring artifacts, the quality of the resulting single-exposure data is greatly improved (see second row in figure 3.11). Suppression of the artifacts eases the visual detection of low contrast features at the expense of slight blurring. One side effect of ring reduction that is directly associated with the aforementioned blurring effect is the reduction in the overall noise level of the dataset, which also helps to improve the visibility of the inserts. All these effects increase the original CNR value to 0.98.

On the other hand, when the ring reduction algorithm is applied to the HDR dataset, minor quality improvement is achieved, owing to the low level of artifacts present in the original data. While the less intense ring artifacts are reduced, the degradation caused by blurring is much more noticeable and the CNR value is reduced to 1.66.

3.4 Discussion

The method presented in this study extends the dynamic range of flat-panel detectors such as those used in small-animal CBμCT. This extension is achieved by means of a modified acquisition process and an additional processing stage using the acquired data, thus obviating the need for hardware modifications that may be difficult and expensive to implement in commercial devices.

In order to form the HDR image, we propose the combination of two datasets using maximum likelihood estimation based on a previously published theoretical model for the mean and variance of pixel signal. The model was extended to take into account the effect of saturation in the variance of pixel signal. The model for detector response showed good agreement with experimental data, thus proving its validity for the realistic simulation of theoretical detectors.

The detector showed a linear response that broke at the saturation point and a reduction in dynamic range for longer integration times. Since additive noise and variance slope were found to be constant across integration time, the reduction in dynamic range came solely from the increase in dark signal with integration time.

Theoretical results on the effect of dark signal and additive noise on the dynamic range of the sensor showed that the upper limit for the detector signal is set to a large extent by the offset imposed by the amount of dark signal in the pixel value. A further contribution comes from the increase in pixel variance induced by a larger value of additive noise according to equation 3.2b and the censored Gaussian model. The lower limit for pixel value (after dark subtraction) set by equaling the SNR to one depended only on the level of additive noise.

Simulated data showed that, using the HDR method, the dynamic range of the detector could be theoretically extended to infinity provided that the anode current of the x-ray source could be increased with no limit. Since a longer integration time reduced the dynamic range of the detector, the performance of the HDR method degraded when the detector exposure was increased by extending the image integration time instead of the anode current. This in turn hampered the method when the limit of the x-ray source current was too low to obtain a valid signal behind the parts of the sample with the highest attenuation values.

Experimental results showed enhanced image quality for projection and tomographic data in samples containing areas of high attenuation. This enhancement resulted from an increase in the dynamic range of the detector.

The results for the copper staircase phantom showed that the signal inside the high attenuation areas was masked by noise in the single-exposure data owing to the lack of a valid signal inside the area in any of the frames acquired. This lack of signal prevented enhancement of the visibility of the phantom structure by frame averaging. After applying the dual-exposure technique, the overexposed image provided a valid signal in some of the highly attenuated areas, revealing the part of the structure that was not visible with the single-exposure data and, therefore, extending the dynamic range of the detector.

SNR curves displayed asymptotic behaviour as the signal grew, meaning that highly attenuated areas benefited more from the improvement in dynamic range and that for large signal values the noise reduction provided by the HDR method would be much lower. This result implies homogenization of the noise properties across high and low attenuation areas, a desirable property for subsequent data processing stages.

With regard to tomographic data, the contrast and noise obtained using the method presented here was better than the one obtained using single-exposure methods, when applied on samples containing high attenuation materials that exceed the dynamic range of the detector. The poor contrast resolution in the single-exposure data can be explained by the lack of photons reaching the detector for highly attenuated areas in some of the acquired projections. This lack of photons in the single-exposure data caused the signal level to be low and more homogeneous in highly attenuated areas. During gain correction, the small differences between individual pixel gains, instead of being attenuated, were introduced into the near zero areas, thus causing ring artifacts to be much more conspicuous and conceal details inside areas surrounded by high attenuation material in the reconstructed volume. Besides the boosting of ring artifacts, low signal levels yielded lower SNR owing to the rise in the relative contribution of additive noise, in accordance with the theoretical results, thus degrading the noise properties of the reconstructed dataset.

Since all the data acquired were used in the combination process, no discontinuities were observed in the reconstructed slices. Discontinuities were observed in previous proposals, which used a cut-and-paste approach for the combination of the acquired datasets [207].

We were unable to compare the performance of our method with that of hardware-based approaches, which would certainly be more effective, especially in terms of acquisition time, since only one dataset is acquired. However, our approach is much less expensive and could be included as a minor modification to the image processing chain of any system based on a flat-panel detector, regardless of the particular hardware implementation.

Other approaches aimed at minimizing the effect of the limited dynamic range of the detector on image quality try to reduce the dynamic range of the radiation reaching it. The most widespread approach is bow-tie filtering, which modifies the spatial properties of the beam before it is attenuated by the sample [210] in an attempt to obtain a more even distribution of radiation at the detector surface. When compared with dynamic range extension techniques, such as the one presented here, it is noteworthy that the effect of bow-tie filters is reduced when the acquisition conditions depart from the expected scenario. For instance, if the shape or size of the sample is significantly different from the expected one or there are unexpected high attenuation objects, the dynamic range of the attenuated beam could still be too high for the flat-panel detector. On the other hand, the HDR method presented does not impose any prior condition on the sample properties, offering the same potential for the accommodation of a subject with a larger dynamic range independently of the attenuation distribution of the imaged sample.

The dual-exposure technique proposed here could be further extended to a multi-exposure approach based on several exposure levels to obtain a similar SNR in all the parts of the projection image. However, the maximum mA achievable by the x-ray tube limits the maximum dynamic range that can be obtained using a multi-exposure method.

3.5 Conclusions

We propose a new dual-exposure technique to extend the dynamic range of x-ray flat-panel detectors, which are commonly used in small-animal CBμCT.

Our results show that the method proposed effectively extends the dynamic range of the detector, thus increasing performance with respect to conventional protocols when there are areas of high attenuation inside the subject under study.

Future works will assess the performance of the technique on small animals. Different combination algorithms and models for the probability density functions are under study.

Appendix 3.A

According to the model presented for mean and variance of the pixel signal, the value of a single pixel for a set of acquisitions maintaining a constant radiation flux follows a Gaussian distribution with mean m and variance v given by equation 3.2. If a significant part of the distribution lies above the maximum pixel signal, all the potential values falling on that part of the curve would receive the maximum pixel value, thus concentrating the upper tail of the distribution in that single value, as shown in figure 3.A.1.

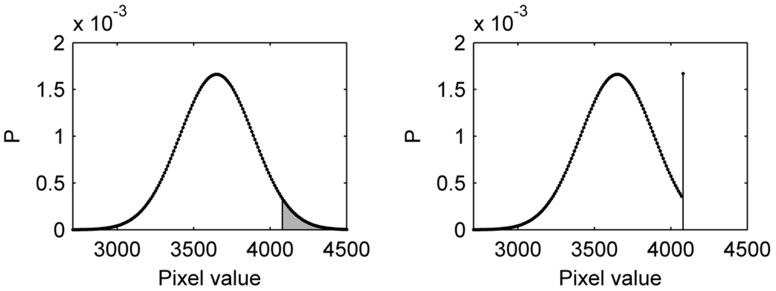

Figure 3.A.1. Probability density function of a Gaussian distribution with μ = 3650 and σ = 240 representing the distribution of a pixel signal for a 12-bit detector, thus limiting the maximum pixel value to 4095. The plot on the left shows the original distribution of pixel values, while the plot on the right shows the real distribution of pixel values after censoring the upper part (shaded on the left plot).

Analytical expressions for mean and variance of Gaussian censored distributions can be found in [211] and are reproduced below.

Let a be the censoring value, i.e. the maximum pixel value, and $m_o(gX)$ and $v_o(gX)$ the mean and variance of the original non-censored distribution, according to equation 3.2. The mean of the censored pixel distribution is given by

$$m(gX) = \left(1-\Phi\right)a + \Phi\left(m_o(gX) + v_o(gX)^{1/2}\lambda\right), \tag{3.A.1}$$

where Φ is the cumulative distribution function at point a and λ is given by

$$\lambda = -\frac{\phi(\alpha)}{\Phi(\alpha)}, \text{ with } \alpha = \frac{a - m_o(gX)}{v_o(gX)^{1/2}}, \tag{3.A.2}$$

where ϕ is the probability density function for the non-censored pixel value distribution. The value for the variance of the censored distribution yields the next expression,

$$v(gX) = v_o(gX)\Phi\left[\left(1-\delta\right) + \left(\alpha-\lambda\right)^2\left(1-\Phi\right)\right], \tag{3.A.3}$$

where $\delta = \lambda^2 - \lambda\alpha$.

4 Modification of the TASMIP tungsten anode x-ray spectral model for the simulation of microfocus x-ray sources

4.1 Introduction

The ability to obtain accurate estimations of the x-ray spectrum for a given voltage and added filtration is of paramount importance for the simulation and optimization of x-ray imaging systems [64, 173-175, 212-213].

A variety of methods has been reported in the literature for predicting x-ray spectra, especially for sources containing tungsten anodes. The spectra generation methods made use of several strategies for estimating the parameters of the spectrum. They can be empirical, based on adjustment to measured data, such as methods that aimed at estimating the shape of the spectrum from attenuation measurements using different approaches, such as the Laplace transform [214], analytical models [215] or maximum likelihood estimations [216], or a combination of analytical models and iterative optimization [217]. Another empirical method, the TASMIP model [55, 218], provided a set of polynomial curves that generated the shape of the spectrum as a function of x-ray source voltage, after fitting the curves to experimentally measured spectra.

Other methods use semi-empirical approaches, making use of physical models somewhat modified or completed by measured data. Methods that fell into this category include the earliest attempt to model *bremsstrahlung* intensity, developed by Kramer [219] and models that build upon this one, such as the one by Birch and Marshall [220] and its evolution by Tucker et al. [220-222]. Poludniowski [223] reported a spectral model based on physical models that described more accurately the process of x-ray generation in metal targets than previous, semi-empirical, attempts and need no empirical information.

The third category of x-ray spectra generation models is based on the simulation of the x-ray generation process, tracking the emitted electrons in the target, by Monte Carlo techniques. Examples of this kind of methods can be found in [224-225]. While Monte Carlo simulation has the potential to accurately describe the x-ray generation process and create very accurate spectra it also has a large computational burden that can hamper their use when a large number of spectra have to be generated.

Among the aforementioned spectra simulation methods, TASMIP is widely used [8, 95, 119, 226-229] due to its accuracy, simplicity, and to its integration in a publicly available software package, called Spektr [230], that provides extended functionalities for the generation of realistic x-ray spectra and derived quantities, such as photon fluence or exposure. However, the TASMIP model provided means to generate x-ray spectra for typical x-ray sources used in radiology and for x-ray sources used for mammography but it lacks a dataset for the generation of spectra for microfocus x-ray sources. Microfocus sources present a low inherent filtration, similar to that of mammography x-ray sources, and a large x-ray voltage span, comparable to the one shown by radiology x-ray sources.

In this chapter we report the adaptation of the TASMIP empirical model for the simulation of x-ray spectra in microfocus x-ray sources. We generated a new set of spectra by estimating the value of inherent filtration affecting the radiology dataset and combining both models, the one for mammography and the one for radiology. The new dataset was further corrected for variations in inherent filtration and anode roughness to match experimental measurements of exposure and attenuation. The modified spectra were used to generate a new set of polynomial coefficients analogous to those used by the TASMIP models for radiology and mammography.

4.2 Materials and methods

4.2.1 TASMIP model for the generation of x-ray spectra

TASMIP is an empirical model proposed by Boone et al. for x-ray sources with tungsten anode for radiology [55] and mammography [218]. The model uses polynomials to estimate the photon output in an x-ray energy bin as a function of x-ray source voltage. The coefficients of the polynomials were obtained by fitting experimentally measured spectra to the highest order polynomial (maximum order of 3) that best represented the data given the available number of data points for each energy bin. Then, the photon output for the *i*th energy bin –with energy E_i– is computed as:

$$q(Ei) = a_{i0} + a_{i1} \cdot kV + a_{i2} \cdot kV^2 + a_{i3} \cdot kV^3, \tag{4.1}$$

where a_{in} is the n-order coefficient of the polynomial for the ith energy bin and kV is the voltage set at the x-ray source.

The dataset used as reference for radiology spectra was published by Fewell et al. [231] and the one used for mammography was measured specifically to build the TASMIP model. The main differences between the x-ray sources used for both models were the inherent filtration of the source and the usable voltage range.

The model for radiology is defined for voltages between 30 and 140 kV in 1 keV energy bins while the model for mammography is defined for voltages between 18 and 40 kV in 0.5 keV energy bins.

An example of spectra generated using TASMIP for mammography and radiology is shown in figure 4.1.

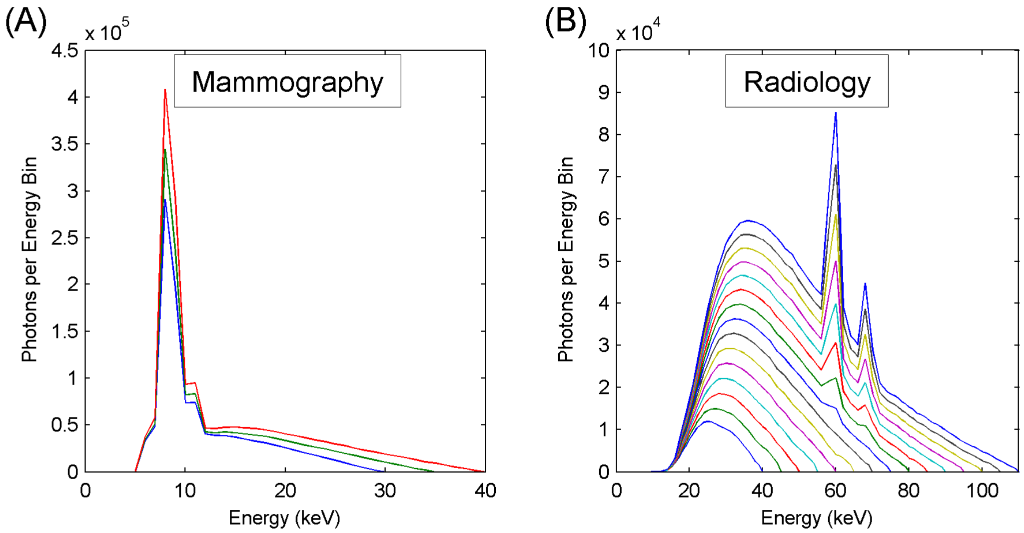

Figure 4.1. Spectra generated by the TASMIP model for mammography (A) and radiology (B) x-ray sources. The divergence between both sets of spectra is manifest, especially in the low energy part which is the part of the spectrum more affected by inherent filtration. Mammography spectra were scaled prior to display to obtain consistent units between the two datasets.

For the simulation of spectra throughout this work we used the publicly available Spektr [230] implementation of the TASMIP model. Spektr included the TASMIP model for radiology and a set of complementary functions for the calculation of derived quantities such as exposure or attenuated spectra. For the generation of the mammography spectra we included a new function in Spektr to read the polynomial coefficients for mammography and rebin them to a grid with 1 keV bins.

4.2.2 Air Kerma measurements

For measurements of Kerma in air we made use of the CBμCT scanner described in chapter 2. The x-ray source of the system was a tungsten anode-based microfocus source; model Hamamatsu L9631-MOD2 (Hamamatsu Photonics K.K., Hamamatsu, Japan). The voltage of the source could be set between 40 and 110 kV for guaranteed stable output and the maximum delivered power was 50 W. The only nominal inherent filtration included in the source was a beryllium output window 0.5 mm thick.

We measured air Kerma at the isocenter of the scanner –i.e. at a distance of 155 mm measured from the focal spot of the source– using an Accu-Gold multi-purpose meter (Radcal, Monrovia, CA) and a 10 cm-long pencil-shaped ion chamber (Radcal 10X6-3CT). The bottom edge of the ion chamber was fixed to the center of the bed at its very beginning in such as way as to leave the active volume of the ion chamber pendant in air to avoid the contamination of measurements by scattered radiation generated at the bed. All the measurements were translated to a distance of 1 m by applying the inverse squared distance law.

To obtain absolute exposure values as well as attenuation measurements as a function of x-ray source voltage we measured air Kerma behind a set of attenuating materials.

We designed three different experiments, one for the measurement of data for the modification of the TASMIP model and two for the validation of the beam spectra simulated using the modified model.

One dataset for each of the experiments consisted of acquired exposure data for x-ray source voltages between 30 and 110 kV in 5 kV increments, with an anode current of 0.4 mA.

For the first experiment we acquired 9 datasets with the beam attenuated by different thicknesses of aluminum, namely 0, 0.5, 1.0, 1.5, 2.0, 2.5, 3.0, 3.5, and 4.0 mm Al. Incremental thickness values were obtained by piling up individual plates of aluminum with a thickness of 0.5 mm, as shown in figure 4.2(A). Aluminum plates were extracted from a HVL attenuator set, model 115 A (Gammex, Middleton, WI), and had a 99% purity.

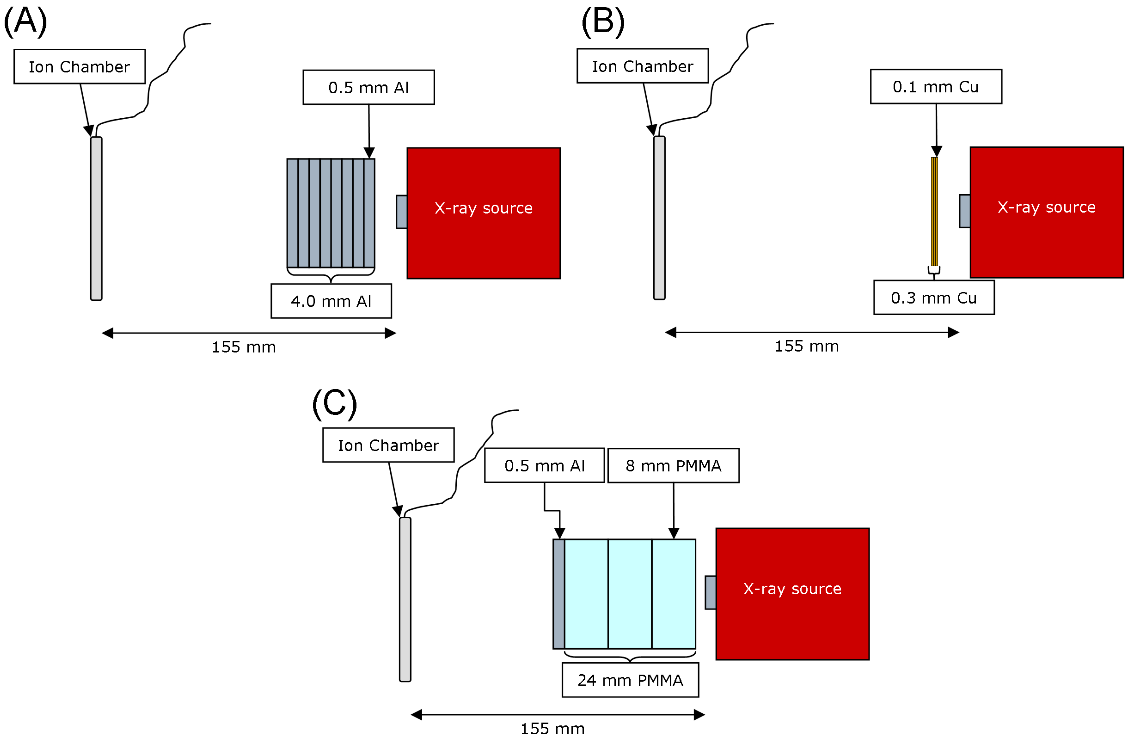

Figure 4.2. Schematic depiction of the experimental setup for the three experiments performed in the presented work. The sketches show the final state for each of the experiments, when all the attenuating plates have been stacked and the beam is undergoing maximum attenuation.

For the second experiment we measured exposure for the same voltage and current settings but in this case the beam was attenuated by copper plates. Copper thickness was varied between 0 and 0.3 mm by piling up 0.1 mm-thick copper plates, as depicted in figure 4.2(B). Copper plates were extracted from a pure copper HVL attenuator set, model 116 (Gammex, Middleton, WI).

In the third experiment we attenuated the beam using three different thicknesses of PMMA, namely 8, 16 and 24 mm; obtained from stacking individual PMMA plates with a thickness of 8 mm. The reference beam contained 0.5 mm Al added filtration to mimic the minimum filtration used in realistic imaging environments. The aluminum filter was placed behind the PMMA plates to absorb most of the low-energy scattered photons generated at them and prevent the scatter flux to reach the ionization chamber and thus to contaminate the measurements. The arrangement for the third experiment is shown in figure 4.2(C).

4.2.3 Estimation of the inherent filtration and generation of the polynomial coefficients

In accordance with the hypothesis that tungsten spectra generated by the TASMIP radiology model, the TASMIP mammography model and those produced by microfocus x-ray sources differ only in inherent filtration and probably in anode roughness and/or angle. We defined a three step fitting process for the generation of the modified spectra that formed the basis for the new interpolation polynomials.

The first step of the process was aimed at finding the best match between the spectra generated by the TASMIP model for mammography and the ones generated by the model for radiology, in terms of aluminum filtration, tungsten filtration and scale factor due to the different units used for the generation of both spectra.

To this end we defined a three parameter model affecting the mammography spectra and found the optimal values for the three parameters by minimizing, in the least-squares sense, the difference between the shape of the transformed mammography spectra and the one of the radiology spectra. The transformation applied to a mammography spectrum to get an estimation of the radiology spectrum is given by,

$$\hat{q}_R(E) = s \cdot q_M(E) e^{-(\mu_{Al}(E) x_{Al} + \mu_W(E) x_W)}, \tag{4.2}$$

where E is the energy bin, q_M is the original mammography spectrum, s is the scale factor to be found during the minimization process, μ_{Al} and μ_W are the x-ray attenuation factors of aluminum and tungsten, respectively, and x_{Al} and x_W are the thicknesses of aluminum and tungsten sought.

The cost-function for the minimization was built by adding the squared differences between the estimated ($\hat{q}_R$) and original (q_R) radiology spectrum for each energy bin and kVp value.

For the optimization process we generated a set of mammography and radiology spectra from 30 to 40 kVp in 1 kVp increments, since this is the range of voltage overlapping between the two models. To match the energy grid for the two spectra dataset, the mammography dataset was rebinned from its original 0.5 keV grid (see section 4.2.1) to a grid with bins of 1 keV.

Due to the lack of spectral data for energy bins below 10 keV (and to the low accuracy of the first bins) in the radiology dataset, we used energies above 15 keV for the fitting.

Optimal parameters of the model were found by minimizing the least-squares cost-function using the Levenberg-Marquardt method as implemented in the *lsqnonlin* function of the Matlab® (Mathworks, MA) package.

The second step of the process consisted in the generation of a new set of x-ray spectra ($\hat{q}_c$) by combining the mammography and radiology datasets over the whole span of kVs covered by our source. The new spectra were produced as follows.

First, a new set of radiology spectra was simulated for voltage values between 30 and 110 kV in 5 kV steps. The effects of inherent filtration were removed by applying the Beer's law for the negative values of the estimated thickness of aluminum (x_{Al}) and tungsten (x_W), i.e. by "unattenuating" the spectra.

We used data from the mammography dataset to compensate the lack of data for energy bins below 10 keV and instabilities caused by the "unattenuation" process in the low energy range due to the low values in the original radiology spectrum that were subject to numerical inaccuracy. Data by Boone et al. [218] showed a large degree of linearity for the first energy bins of the mammographic model. For this reason we removed the higher order terms of the original polynomial coefficients and linearly extrapolated the values of energy bins from 6 to 13 keV beyond the kVp range covered by the mammographic model and up to 110 kVp, matching the kVp values used to generate the radiology dataset. Values up to 13 keV in the unattenuated radiology spectra were substituted by the extrapolation of mammography data, obtaining a complete dataset for the voltage range covered by the microfocus x-ray source used in the present work.

The third, and last, step of the fitting process yielded the final spectra for the generation of the modified TASMIP model for microfocus x-ray sources. In this step the dataset arising from the previous stage was modified to match the experimental measurements by minimizing the difference between the estimated and measured attenuation –calculated as the ratio of exposures– in the least-squares sense. We used a method similar to the one proposed by Meghzifene et al. [232] that used attenuation measurements and numerical optimization to find the thickness of aluminum attenuating the spectra generated at the anode.

We obtained the exposure for the simulated spectra by integrating, across energy, the inverse of the x-ray quanta per unit of exposure, weighted by the spectra in the dataset. The number of x-ray quanta per unit exposure for a particular energy bin can be obtained using the expression by Johns [52]:

$$\frac{\Phi}{X} = \frac{5.43 \cdot 10^5}{\left(\mu(E)/\rho\right)_{en} E}, \tag{4.3}$$

where $(\mu(E)/\rho)_{en}$ is the mass-energy absorption coefficient for air, X is the exposure value in mR and Φ is the photon fluence in photons/mm^2. Using equation 4.3, the total exposure value is given by [55]:

$$X_t = \int_0^{E_{\max}} \frac{X}{\Phi}(E)\hat{q}_u(E)dE, \tag{4.4}$$

where $\hat{q}_u$ is the estimated microfocus spectra. The value of $\hat{q}_u$ was estimated by finding the aluminum and tungsten filtration that, when applied to $\hat{q}_c$, minimized the difference between estimated and measured attenuation. Analogously to equation 4.2, $\hat{q}_u$ is given by:

$$\hat{q}_u(E) = \hat{q}_c(E)e^{-(\mu_{Al}(E)x_{Al} + \mu_W(E)x_W)}. \tag{4.5}$$

We built the last fitting process on two premises: first, that the housing of x-ray sources –responsible for inherent filtration– contains several materials that are not exactly aluminum (while they have similar atomic number) and, therefore, the equivalent aluminum thickness could vary with x-ray source voltage; and, second, that anode roughness can be modeled as a voltage-independent tungsten thickness [233]. For these reasons we set as parameters for the optimization process one value of aluminum thickness per kVp and a single tungsten thickness shared for all kVp values.

Attenuation data were computed for the aluminum filtered exposure data –see section 4.2.2 and figure 4.2(A)– using 0 mm Al as the reference point (i.e. we used 8 attenuation points, namely 0.5, 1.0, 1.5, 2.0, 2.5, 3.0, 3.5, and 4.0 mm Al). The cost-function was minimized using the Levenberg-Marquardt method.

The estimated microfocus spectra ($\hat{q}_u$) generated after the optimization process was subsequently used to find the coefficients for the new TASMIP polynomials. The polynomial fitting was performed in an analogous fashion to the one described by Boone et al. [55], finding a polynomial (with a maximum degree of 3) that related x-ray source voltage to photon output, per energy bin. We used the *polyfit* routine in Matlab® for finding the polynomial coefficients.

Residual differences in the efficiency of the x-ray source used in this work and those used by Boone et al. were compensated by finding the average scaling factor between measured and estimated values of exposure behind aluminum attenuators.

4.2.4 Evaluation of the spectral model

We evaluated the accuracy of the spectra generated by the modified TASMIP model for microfocus sources in terms of exposure and attenuation, for the three exposure datasets described in section 4.2.2.

In particular we compared the exposure estimated by the simulated spectra to the one measured behind the aluminum and PMMA attenuators, and the attenuation factors using 0.5 mm Al as the reference beam for both materials. We also compared attenuation factors in copper using 0.1 mm Cu as the reference beam. We did not use the non-filtered beam –i.e. 0 mm Al or 0 mm Cu filtration– as the reference from the attenuation analysis to enhance the visibility of the data due to the large dynamic range of attenuation values if the non-filtered beam was included in the study.

To further assess the validity of the model we compared the estimated and measured exposure values at the isocenter of an Argus PET/CT scanner (Sedecal, Madrid, Spain) which is described in [4]. The Argus PET/CT includes a tungsten anode-based x-ray source, model Apogee 5011 (Oxford Instruments, Oxfordshire, UK) with a maximum voltage of 50 kV and maximum power of 50 W. The beam is filtered with 1 mm Al.

Measurements were performed in an analogous fashion to the one described in section 4.2.2, for voltages between 30 and 50 kV in 5 kV steps and for an anode current of 0.4 mA. The data were obtained without the protective PMMA tube –see chapter 3, section 3.2.3.2– which was removed for technical service, preventing the data to be contaminated by scatter generated at the PMMA tube.

4.3 Results

The new set of coefficients for the polynomial curves of the modified TASMIP model can be found in Appendix A1 of the present document.

Figure 4.3 shows a set of spectra generated using the modified TASMIP for microfocus sources, with no added filtration. The spectra show a large number of photons in low energy bins, resembling the shape of the mammography spectra in that part of the energy span –see figure 4.1(A)–, and it follows the shape of the radiology spectra for high energy photons, although after removing the effect of inherent filtration.

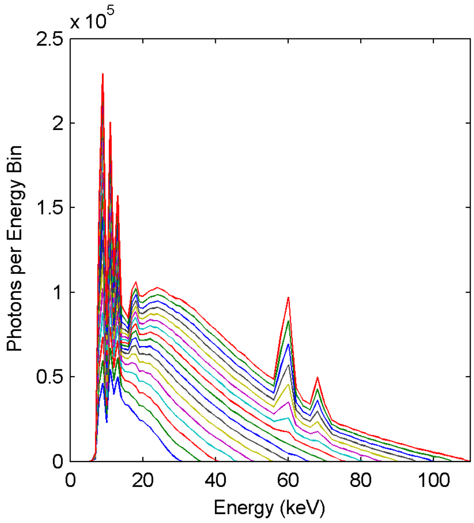

Figure 4.3. Spectra generated by the modified TASMIP model for microfocus x-ray sources plotted for a range of voltages between 30 and 110 kV in 5kV increments.

We found the radiology spectra to present an inherent filtration of x_{Al} = 1.68 mm Al with a negligible quantity of tungsten filtration ($x_W < 10^{-10}$ mm). The second fitting process which matched attenuation and exposure measurements to the spectra resulting from the combination of mammography and radiology data yielded a negative value of aluminum thickness for all the voltages, ranging between 0.20 and 0.22 mm Al and a value of tungsten filtration of 0.0029 mm W, which can be generated by a value of roughness of the anode of ~3 μm.

Exposure as a function of source voltage for the raw beam –i.e. 0 mm Al added filtration– is shown in figure 4.4(A). Simulated exposure shows a good agreement with measured values, with an average relative mean error of 0.03.

The exposure curve for the beam filtered by different thicknesses of aluminum is shown in figure 4.4(B). In this case the simulated data also show a good agreement with measured exposure.

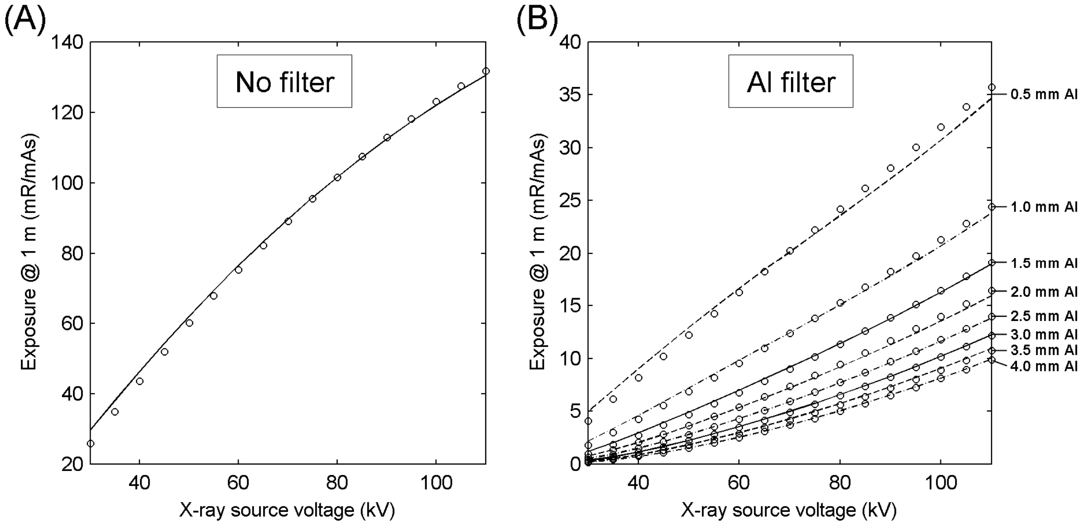

Figure 4.4. Panel (A) shows the air Kerma at a distance of 1 m away from the source measured –circular markers– and estimated –solid lines– using the spectra model for no added filtration in the beam and x-ray source voltage from 30 to 110 kV in 5 kV increments. Air Kerma measurements and estimations for a beam filtered by aluminum are compared in panel (B), for a range of added filtration between 0.5 and 4 mm Al in 0.5 mm increments.

Simulated attenuation values for aluminum –see figure 4.5(A)– showed very good agreement with measured data with a maximum average error of 0.07, for a peak energy of 35 kVp. For the case of copper, the correspondence between simulated and measured attenuation is worse, with a deviation that can be visually appreciated in figure 4.5(B). The maximum mean error in this case was of 0.1, for the data corresponding to 35 kVp.

To illustrate the difference between the modified model and the original TASMIP for radiological sources, attenuation curves are presented again in figure 4.6, comparing simulated attenuation (red curves) to measured data (blue curves). The deviation is much larger in this case and it is especially noticeable for copper, with average relative errors between 0.6 and 4.4.

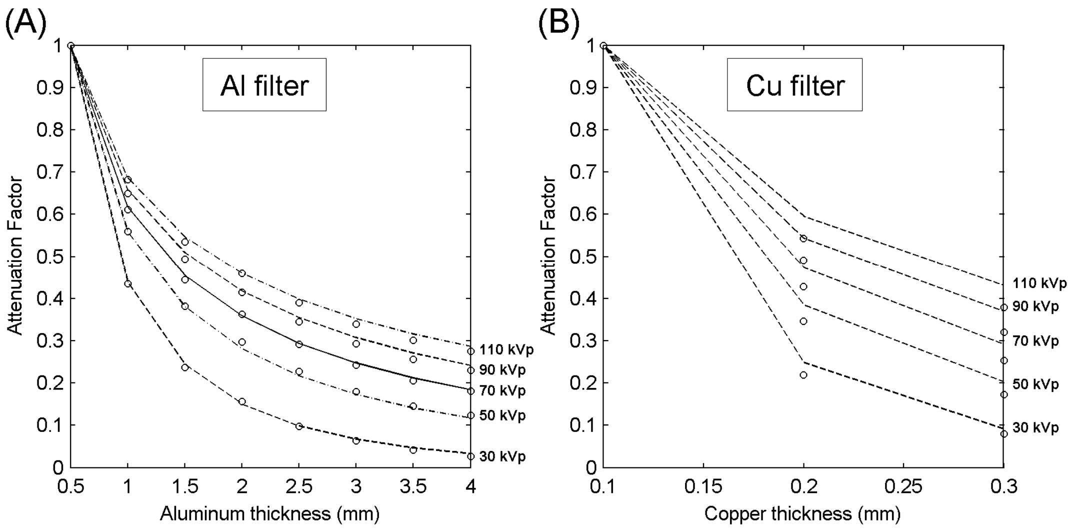

Figure 4.5. Attenuation curves from measured –circular markers– and estimated –solid line– data as a function of added filtration for different x-ray source voltages. Panel (A) show the attenuation values for different thickness of aluminum referred to 0.5 mm Al. Attenuation values using copper as attenuating material are shown in panel (B), using 0.1 mm Cu as the reference point.

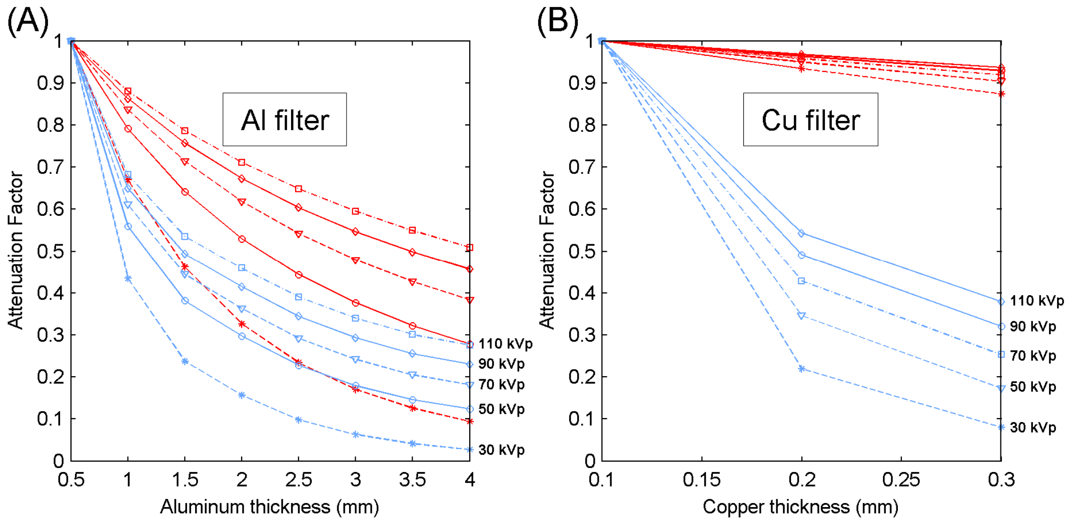

Figure 4.6. Comparison between attenuation values for aluminum –panel (A)– and for copper –panel (B)– attenuators obtained by the classic radiological version of the TASMIP model –red curves– and experimentally determined –blue curves.

Simulated exposure and attenuation for the PMMA attenuators is shown in figure 4.7, together with measured data. Simulated and measured curves present small deviations, with a maximum relative average error of 0.05 in exposure (for 8 mm PMMA) and of 0.06 in attenuation (for 24 mm PMMA).

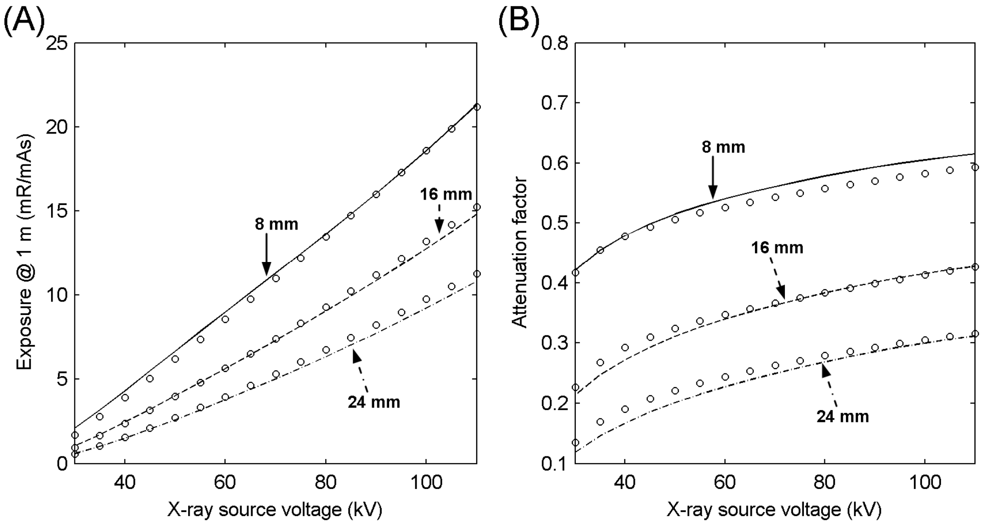

Figure 4.7. Air Kerma (A) and attenuation values (B) measured –circular markers– and estimated –curves– using the modified TASMIP model behind PMMA plates of different thicknesses, as a function of x-ray source voltage. We used 0.5 mm Al added filtration for the reference –i.e. non-attenuated– beam.

The simulated exposure for 1 mm Al added filtration agreed to a great extent with the measured data, for the Hamamatsu x-ray source (already shown in figure 4.4(B) and depicted again in figure 4.8) and for the Oxford x-ray source, shown in figure 4.8. The last point in the exposure curve for the Oxford source broke the trend and departed not only from the simulated data but also from the experimental data obtained with the Hamamatsu source.

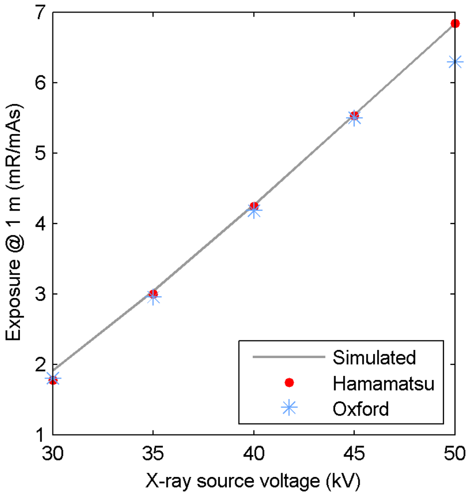

Figure 4.8. Experimentally determined –markers– and simulated –curve– air Kerma values for x-ray beams between 30 and 50 kVp and 1mm Al filtration. Red dots represent the values obtained for the Hamamatsu x-ray source and blue stars represent those obtained for the Oxford x-ray source.

4.4 Discussion and conclusions

In this chapter we have shown the modification of the TASMIP model for the simulation of x-ray spectra for tungsten anodes in the radiology and mammography environments to use it for microfocus x-ray sources. In particular we modified the model by finding the inherent filtration affecting spectra generated by the original model for radiology when compared to the model for mammography which only included the output beryllium window of the tube. After finding the inherent filtration relating the radiology and mammography datasets we built a complete dataset combining both. We then found the values of inherent filtration and anode roughness relating this new dataset to experimental attenuation values, with an approach similar to [232].

The estimated value of inherent filtration relating the radiology and mammography datasets was found to be of 1.68 mm Al, in line with the value of inherent filtration reported by Boone et al. for the spectra used to build the model, who estimated an inherent filtration of ~2.0 mm Al for the Fewell spectra, computed as the nominal 1.1 mm Al plus an extra filtration of ~0.88 mm (for voltages between 30 and 40 kV) which was necessary to match measured attenuation [55].

We found that experimental data for our microfocus x-ray source matched better for a value of inherent filtration of ~1.5 mm Al, with an extra filtration of ~3 μm W. This extra filtration from tungsten could arise from roughness in the anodes used in [55, 218] and falls in the range of values reported by Nowotny and Meghzifene [233] which found anode roughness ranging from 0 to 6 μm for a set of six anodes extracted from used x-ray sources.

Errors shown by the new model for transmission are in line with errors reported by Ay et al. [234] for other spectra generation models, however, in the radiology range, with 1.2 mm Al inherent filtration. They showed a mean error in attenuation curves for aluminum thicknesses ranging from 0 to 25 mm and for 100 kVp of 10.4% (0.104 relative error) for the IPEM model [235], 9.9% for the model by Birch and Marshall [220], 4.5% for the model by Tucker et al. [221], 0.6% for the TASMIP radiology model [55], 3.0% for a Monte Carlo model using the MCNP package [224], and 7.7% for a Monte Carlo model based on the EGS4 package [225].These values compared to a mean error of 2.9% for aluminum thicknesses up to 4 mm shown by the modified TASMIP model and to a mean error of 7.8% when using copper with a maximum thickness of 0.3 mm. While the range of thicknesses is smaller, our spectral model contained a significantly larger fraction of low energy photons, making the attenuation larger for lower thickness of material.

In conclusion, we have generated a new set of polynomial coefficients for the simulation of x-ray spectra for microfocus x-ray sources that can be used following the philosophy of the TASMIP model. As in the case of the TASMIP model, the generation of spectra is very simple, implying only the evaluation of polynomial curves as a function of x-ray source voltage. The new set of polynomials can be straightforwardly included in Spektr, taking profit of the additional features offered by this package. The results showed an accurate enough agreement with experimental data, in line with other, usually more complicated, spectral models developed for radiology or mammography.

This new model provides a dedicated tool for the generation of spectra for microfocus x-ray sources covering a large span of voltages, filling the whole range of applications for small-animal x-ray imaging.

5 Development of acceleration techniques for Monte Carlo simulation of x-ray scatter on GPUs for CBCT

The work presented in this chapter was carried out in part at the I-STAR laboratory, Department of Biomedical Engineering of the Johns Hopkins University and under the supervision of Wojciech Zbijewski PhD and Jeffrey H. Siewerdsen PhD.

5.1 Introduction

X-ray scatter in CBCT imaging has been usually pointed as one of the key physical factors limiting image quality. Specifically, x-ray scatter is recognized to impart a loss in contrast, a decrease in contrast-to-noise ratio, loss in detective quantum efficiency (DQE), a loss of spatial resolution, and an increase in cupping and streak artifacts [33, 88, 236-238].

Along the trajectory of CBCT imaging, researchers have proposed a variety of techniques for the measurement or estimation of the quantity and distribution of scatter, which can be divided in physical, analytical, Monte Carlo and hybrid methods.

Physical methods of characterizing x-ray scatter in CBCT often involve measurement of signal in the shadow of an x-ray opaque “blocker” placed between the source and the object such that the signal behind the blocker is mainly due to scatter, and the un-blocked signal arises from scatter + primary. Examples of this kind of techniques can be found in [91-92, 191, 239-242].

Analytical models for scatter estimation have also received a considerable interest. These methods cover from very simple approaches in which the scatter signal is assumed to be constant across the whole scan [237] or across a single projection [243] to more elaborate approaches where the scatter is computed as the convolution of the primary signal with an scatter point spread function which is used as the convolution kernel [93, 244].

Monte Carlo simulation is known to provide accurate estimations of scatter signals but its use has been hampered by the high computational burden and the large number of photon histories needed to obtain a reasonable signal-to-noise ratio in the estimated signal which are usually on the range of 10^9 photons [115].

Variance reduction techniques help in reducing the computational burden of Monte Carlo simulation of x-ray scatter. Examples of these techniques are forced detection [245], mean free path transformation [117], Woodcock tracking [130] or interaction splitting and Russian roulette [117]. These techniques have shown a potential decrease factor in running time, for a given level of noise, in the range of 10-100 [117]. Monte Carlo can also be combined with noise reduction techniques, taking advantage of the relatively low frequency of the scatter signal [94, 246-249], or it can be combined with analytical estimations of first-order scatter providing noise first order scatter and a coarse estimation of multiple scatter that undergoes a denoising stage [96].

MC simulation can be significantly accelerated by implementation on graphics processing units (GPUs) that provide a fast, parallel computing architecture with standard desktop workstations. We report here a new scatter simulation platform that makes used of a publicly available software library for Monte Carlo simulation of x-ray systems in GPUs [187] to which variance reduction techniques were incorporated to accelerate the generation of scatter signals. The photon tracking process was modified to increase the improvement in performance provided by variance reduction and several new capabilities were included in the platform.

5.2 Materials and methods

The simulation engine presented in this chapter was based on the MC-GPU v1.1 package that takes profit of the parallelization capabilities of the Monte Carlo photon tracking process on voxelized geometries and of the potential for parallel computing offered by GPUs.

A detailed description of the MC-GPU package can be found in [187] and the package is publicly available via the U. S. Food and Drug Administration, Center for Devices and Radiological Health (http://code.google.com/p/mcgpu/). The code employs interaction models and cross sections from PENELOPE 2006 [58], a general-purpose

Monte Carlo simulation system for electron-photon transport, and was shown to achieve a 15- to 30-fold acceleration over computation on a single CPU [187].

With the objective of improving the performance of the simulation engine for the particular task of estimating x-ray scatter distributions on CBCT we modified the code and developed several variance reduction techniques that increase the signal-to-noise ratio of the estimated scatter for a fixed simulation time.

We also extended the capabilities of MC-GPU to allow the simulation of polychromatic x-ray spectra, the inclusion of models of the detector signal formation as a function of the energy of the incoming photon, the inclusion of models for the energy and travel direction-dependent photon rejection process taking place in antiscatter grids, and the tallying of the energy deposited in the voxelized volume, yielding a basis for dose estimation.

The accelerated simulation engine was evaluated against the classic version of MC-GPU and experimental measurements. We evaluated the gain in performance provided by variance reduction. Finally we presented a practical application of the simulation engine for the correction of scatter artifacts in CBμCT.

5.2.1 MC-GPU – Inclusion of variance reduction techniques

MC-GPU tracks individual x-ray photons through the voxelized volume using Woodcock tracking [130]. The length of the step between interactions is calculated assuming a uniform object composed of the most attenuating material in the volume. Some interactions are then treated as virtual –i.e., not resulting in a change to photon energy or trajectory– depending on the material encountered at the interaction site. With this approach, explicit computation of photon path intersections with each voxel boundary is avoided, yielding algorithmic acceleration and execution speeds independent of voxel size for a fixed total volume size. Photon histories with the weighted energy –i.e. the product of the carried weight by the photon energy– falling below 5 keV are terminated. To further increase the speed in simulating x-ray scatter distributions, we implemented additional variance reduction techniques in the MC-GPU engine, namely, biasing of the photon direction sampling, forced scattering, interaction splitting, and forced detection.

(a) Photon direction biasing: In classic Monte Carlo photon tracking, the original direction of the photons generated at the x-ray source is uniformly sampled

along the x-ray cone as it happens in real systems. This is an appropriate approach when the voxelized volume covers most of the beam and does not contain a significant fraction of voxels with a very low interaction probability (i.e., it does not contain large empty areas). However, in some situations, the volume could include empty portions – e.g. the space between the fingers when simulating the acquisition of a hand– or not cover part of the beam –e.g. when simulating sagittal views of a thorax CBCT– where photons are not likely to interact.

We modified the photon generation process in MC-GPU to offer the possibility of directing more photons to those parts of the volume where they are more likely to interact. To do so, a previous analytical projection of the volume for the particular position of the source and detector is computed. The volume is projected using the approach described in section 5.2.3 but assuming a monochromatic beam with energy equal to the mean energy of the spectrum used for the simulation. The projected volume yields a two-dimensional distribution that is rearranged and normalized to unit area to generate a probability density function (pdf).

Every time a new photon is generated during the simulation its direction is sampled from the pdf using rejection sampling. To not bias results towards more attenuating paths, the generated photon receives a weight inversely proportional to the probability of the sampled direction, yielding

$$w_0 = \frac{1.0}{N_r \, p_{ray}}, \tag{5.1}$$

where N_r is the number of bins used for the generation of the pdf and p_{ray} is the probability for the particular direction of the photon, generated using bilinear interpolation from the closer bins of the pdf. Equation 5.1 provides weights larger than one for directions with probability lower than that for uniform sampling, and weights lower than one for those with larger probability values.

If very low attenuating paths are present in the volume it is possible for some photons to receive very large weights that cannot be compensated until a very large number of photons is simulated. To prevent weights from getting too large we set an upper limit for weight, according to

$$w_{\max} = \frac{N_{ph}}{N_u N_v}, \tag{5.2}$$

where N_{ph} is the number of photons to simulate and N_u and N_v are the number of pixels of the detector in the u (horizontal) and v (vertical) directions, respectively. Photons with weights larger than the value provided by equation 5.2 are rejected.

(b) Forced scattering. All non-virtual interactions were forced to be either Compton or Rayleigh scatter by eliminating photoelectric absorption from the set of possible interactions and adjusting the photon weight to correct for the resulting bias:

$$w_i = w_{i-1} \frac{\mu_c + \mu_r}{\mu_t}, \tag{5.3}$$

where w_i is the weight after interaction i, w_{i-1} is the weight carried by the photon from previous interactions, μ_c and μ_r are the Compton and Rayleigh components of the attenuation coefficient, respectively, and μ_t is the total attenuation coefficient for the voxel at which the interaction occurs.

(c) Interaction splitting [117] and forced detection [116, 118]. After selecting the interaction type, the photon was split into several (N_{split}) virtual photons, each of them with a weight reduced by $1/N_{split}$ from that of the original photon. For Compton scatter interactions, the direction of each virtual photon was forced toward a uniformly randomly selected detector pixel, thus assuring detection. Forcing toward all pixels would be prohibitively slow due to the large number of elements in the detector matrix. A weight was assigned to the photon to correct for the bias resulting from neglecting other possible directions [250]:

$$w_i = w_{i-1} \sigma_c^{-1} \frac{d\sigma_c}{d\Omega} \Delta\Omega, \tag{5.4}$$

where σ_c is the total Compton scattering cross section, $d\sigma_c/d\Omega$ is the differential Compton cross section for the direction from the interaction site to the center of the detector pixel, and $\Delta\Omega$ is the solid angle covered by the detector pixel in the direction of the photon. The differential cross section was computed with PENELOPE using the Klein-Nishina formula corrected for electron binding effects using the impulse approximation [58]. Equation 5.4 is an approximation, since the differential cross section is assumed constant across a detector pixel. For small pixels (e.g., <1 mm for flat-panel detectors), the change in scattering angle across a pixel is small and thus the error is expected to be negligible; no appreciable bias was found in scatter distributions obtained with forced detection compared to standard simulation (see section 5.3.1). The resulting virtual scattered photon was tracked toward the detector using Woodcock tracking, allowing only for virtual interactions, but weighting the photon contribution by the probability of interaction every time the transport function is sampled, and thus accounting for attenuation along the photon track. Photon splitting was also performed for Rayleigh interactions, but forced detection was not employed, since it did not significantly improve simulation speed (i.e., most photons undergoing Rayleigh scatter advanced toward the detector anyway). After an initial scattering event and scoring the resulting virtual photons in the detector, the simulation proceeded to model multiple scatter by returning to track the original photon in the usual manner to the next scatter event, scoring a new group of resulting virtual photons in the detector, and so on until the photon traversed the object.

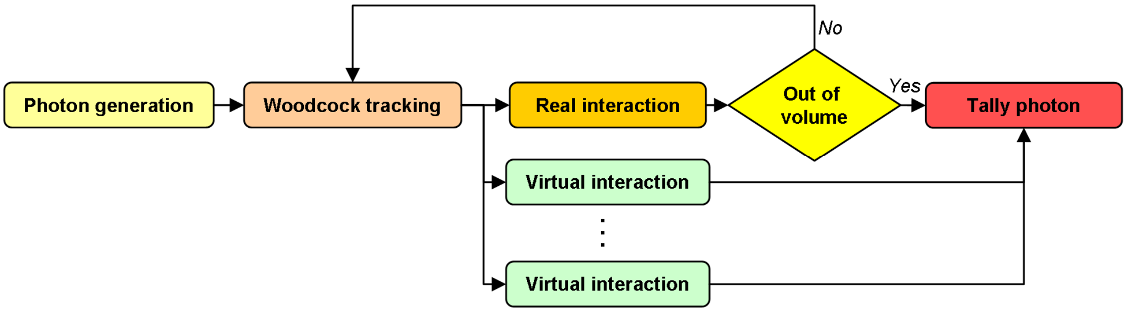

Figure 5.1. Tracking algorithm proposed. The tracking of the photon is stopped at every interaction point, and the CPU takes the control of the process. Several interactions are launched in parallel in the GPU and the photons are transported directly to the detector. One of the interaction results is assumed to be the real interaction and the photon parameters are stored to continue the tracking. The process is terminated when the photon exits the volume.

Interaction splitting can be detrimental to overall performance of a parallel Monte Carlo implementation since it breaks the continuity of each primary photon thread when the virtual scattered photons are created and transported toward the detector. The tracking process was therefore modified to optimize for parallel execution of interaction splitting on a GPU. Primary photons originating from the x-ray source were tracked in parallel until all of them reached their first interaction points. Subsequently, the status of the primary photons was stored in GPU memory and the threads associated with tracking them were terminated. A new group of threads was created for each original photon to undergo virtual interactions and to track the virtual photons to the detector in a fully parallel fashion. After all the virtual photons reached the detector, their threads were terminated and a new set of kernels was launched to continue the tracking of the original photons from their saved state. The modified tracking process is graphically depicted in figure 5.1.

5.2.2 MC-GPU – Inclusion of polyenergetic spectra, detector response models, antiscatter grids and dose tallying

We extended MC-GPU for the simulation of arbitrary spectra of the x-ray beam. The spectrum for the particular simulation is provided as a text file with 1 keV sampling intervals over the range 1-150 keV. The x-ray spectrum must be normalized to unit area, yielding a pdf, before being read by the simulation engine. The energy for each new generated photon is sampled from the spectrum pdf using the Walker's alias method [127].

Transmission through a focused antiscatter grid was included in the simulation engine by applying analytical weights to each photon reaching the detector plane. The grid response is approximated as locally parallel, oblique lamellae oriented at an angle corresponding to the angle of the focused grid at the location of photon incidence. The weight for the photon is computed according to the analytical expression of Day and Dance [251], as a function of photon incidence angle, photon energy, grid cell materials and dimensions, and local grid angle. The energy dependence of the photon transmission factor for the lamellae and interspaces is provided to the simulator as a text file for energy values between 1 and 150 keV in 1 keV increments.

The variation of the detector signal as a function of the energy of the incoming photon was included as an energy-dependent weight factor that multiplies the energy of every photon reaching the detector. The model of the detector signal is provided to the simulation engine via a text file with a format equivalent to the one used for grid transmission.

As a last feature, we incorporated into the simulation engine the possibility of generating a voxelized volume storing the energy deposited by all of the interactions undergone by photons at that place. To do so, every time a photon reaches an interaction point, the energy, if any, deposited as a consequence of the interaction is added to the voxel value, in a similar fashion as the one used by Boone et al. [114]. The final volume contains the energy in eV deposited at each of the voxel forming the volume. Conversion to dose can be performed by normalizing by the mass of the particular voxel. It is important to point out that the approach used for dose scoring is an approximation where the photon is assumed to locally deposit all the energy at the interaction point, neglecting the range traveled by the possible photo electron.

5.2.3 MC-GPU – Analytical tracking of primary photons

While variance reduction techniques are appropriate for the reduction of the variance of the scatter signal, obtaining a better relation between noise and simulation time for scatter components, they have no effect on the noise of the simulated primary signal. When variance reduction is applied to accelerate Monte Carlo simulation by lowering the number of tracked photons, the noise in the resulting primary estimates reflects this reduced photon fluence and may therefore be relatively large.

For this reason we decided to not rely on the Monte Carlo simulation of primary signal when variance reduction techniques are applied during the simulation. To obtain a primary signal free of noise we implemented an analytical polychromatic ray-tracer, based on the approach by Siddon [252]. The analytical projector employs the same source spectrum, system geometry and material properties as the Monte Carlo engine. The complete projections including primary and scatter could be generated by adding the gain corrected scatter signal to the result of the analytical ray tracing.

The implementation of the ray-tracing engine is briefly described in the following paragraphs.

The Siddon ray tracing algorithm assumes a voxelized geometry and computes the exact x-ray path of a infinitesimal width ray, in our case joining the focal spot of the x-ray source and a point on the detector plane. To achieve a good performance and accuracy, the algorithm works by computing the points of intersection between the boundaries of voxels and the distance between two consecutive points of intersection. This process takes profit of the parallel disposition of voxel boundaries, which allows the computation of the first intersection of the ray with the volume and estimate the following intersection points by recursion. The projected value is obtained by adding the set of distances between pairs of consecutive intersection points weighted by the value of the voxel traversed between the two intersections. A simplified version of the traking process is depicted in figure 5.2 for a two-dimensional slice.

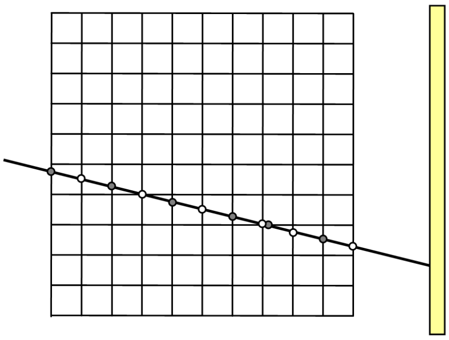

Figure 5.2. Schematic view of the Siddon tracking process. The distance and attenuation value between a grey and the next white point and viceversa is weighted by the attenuation factor of the particular voxel.

The GPU implementation traces each ray in a parallel fashion, launching a selectable number of threads per detector pixel, as set by the user. The computation of the intersection points is independent for each tracked ray, and rays with similar trajectories are grouped together in blocks. The voxelized volume is stored in a 3D texture memory that offers cached memory areas, accelerating the access to memory if a considerable degree of coalescence is achieved. The intention of grouping rays with close trajectories is to make the most out of the caching capabilities of texture memory.

5.2.4 Experiment 1: Evaluation of the performance gain and accuracy of the accelerated Monte Carlo engine

This set of experiments had two main goals. The first objective was to assess that the inclusion of the variance reduction techniques do not bias the quantity and spatial distribution of the generated scatter signal. The second objective was to evaluate the level of correspondence between experimental and Monte Carlo simulated data.

The basic MC-GPU, in which we introduced variance reduction techniques, was validated in comparison to measurements and in comparison to a CPU-based Monte Carlo implementation (PENELOPE), in the context of dose estimation [95, 253]. The Monte Carlo variance reduction techniques in our implementation of MC-GPU were validated by computing scatter distributions with and without variance reduction for a variety of CBCT configurations.

To test the correspondence between the scatter fields generated by the MC-GPU with variance reduction and the classic implementation of MC-GPU and to assess the increase in performance from variance reduction we performed a series of simulations using the phantom proposed in [119] and explained in greater detail in chapter 6, section

6.2.2. The phantom is shown in figure 5.3(A) and it consists of a homogeneous region of soft-tissue with two cylindrical inserts of bone formed by a layer of cortical bone with marrow in its interior and two further cylindrical inserts of adipose tissue and muscle, respectively. Material properties were extracted from the Penelope database [58] and from data by Woodard and White [189].

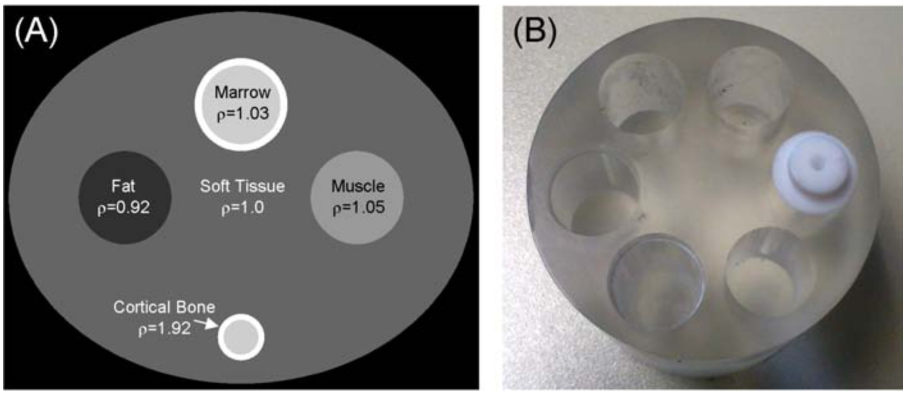

Figure 5.3. Depiction of the synthetic phantom (A) used for the evaluation of the match between the accelerated and classis version of MC-GPU and for performance measurements. The right panel (B) shows a picture of the CNR phantom with only the PTFE insert.

Simulations were carried out for two different system geometries and x-ray spectra. First we used a mid-compact geometry with source-to-axis distance (SAD) of SAD = 1000 mm and axis-to-detector distance (ADD) of ADD = 500 mm, comparable to the geometry used for on-board CBCT systems in Linear Accelerators (Linac), with a compromise spectrum (70 kVp, +2 mm Al, +0.2 mm Cu added filtration), softer than usual clinical spectra but harder than those used for preclinical image acquisition. The major axis of the phantom was set to 280 mm and projection data were obtained for a beam perpendicular to the major axis.

The second simulated dataset was obtained for a small-animal geometry of SAD = 155 mm and ADD = 75 mm and a soft spectrum (45 kVp, +1 mm Al added filtration). The major axis of the phantom was set to 70 mm, resembling a rat. Projection data were obtained for a beam aligned with the major axis of the phantom.

The simulations were performed ten times in each case with the number of photon histories per projection (N_{ph}) ranging from $5x10^6$ - $5x10^8$. An additional MC-GPU simulation obtained with 10^{10} photons/projection and no variance reduction provided a reference standard against which to assess possible bias introduced by the acceleration techniques.

We quantified the performance of the simulation engine given a number of photon histories using the following figure of merit for efficiency:

$$\varepsilon = \sum_i \left(\frac{\overline{x_i}}{\sigma_i} \right)^2 \frac{1}{\bar{t}}, \tag{5.5}$$

where σ_i is the standard deviation of pixel *i*, $\overline{x_i}$ is the mean value for pixel *i*, and $\bar{t}$ is the average execution time of the Monte Carlo simulation, all computed over ten independent Monte Carlo runs. The variance reduction techniques should yield lower noise for a given number of simulated photons compared to simulations without such acceleration, but at the cost of potential increase in run-time. The ratio (R_ε) of ε with and without variance reduction therefore assessed the gain in performance.

We also inspected the match between the total simulated signal and experimental data. The simulated signal was obtained from adding the analytically computed primary signal and the scatter signal generated by the accelerated MC-GPU. To this end we performed an acquisition of the CNR phantom shown in chapter 2, figure 2.11, and reproduced for the sake of clarity in figure 5.3(B) with only the PTFE insert in place. For the image acquisition we used the CBμCT system described in chapter 2. We used the soft-tissue rat protocol –see chapter 2, section 2.4.2– which involved the use of 66 kV and 0.2 mmCu added filtration. The spectrum was generated using the model proposed in chapter 4 and the detector response was obtained according to cascaded systems analysis, as explained in chapter 2, section 2.2.6.

We acquired a single projection with the detector set in 4x4 binning –i.e. 0.2 mm pixel size– and for the minimum magnification of the system. Projection data was corrected for defective elements, dark offset, and gain.

We simulated the same projection image using the three materials in the phantom and a segmented volume generated from a reconstructed dataset of an acquisition for 360 projections carried out just after obtaining the single projection. The material properties were extracted from the Penelope database [58]. For estimating the Monte Carlo scatter signal we used 10^7 photons.

Before adding primary and scatter data, the scatter data was normalized by the gain field computed analytically taking into account spectrum, detector response, and geometry; therefore accounting for $1/R^2$ effects.

All the simulations were carried out on a single Geforce GTX460 GPU (Nvidia Corp. Santa Clara, CA) with 1 GB dedicated memory.

5.2.5 Experiment 2: Practical application to scatter correction

To provide a practical scenario for the usage of the presented simulation platform, we applied it to the correction of scatter in CBμCT.

We designed a complete architecture for the automatic Monte Carlo-based scatter correction from an acquired volume. This correction scheme was described in more detail in [35]. The scatter correction framework presented consists of five stages that yield a scatter corrected tomographic volume as a final result requiring no interaction from the user.

The CBμCT projection data is first reconstructed by means of the well known FDK [79], using the approach described in chapter 2, section 2.2.4. The reconstructed data are then segmented automatically, yielding the voxelized volume that is used for the Monte Carlo simulation.

The data were segmented using the method proposed by Otsu [254]. This algorithm performs an unsupervised segmentation, given the number of classes present in the volume. In the original scatter correction method we used three different classes for the description of biological tissues: soft tissue, bone, and air. The histogram of the volume is computed and the two levels for the segmentation are found by maximizing the between-class variance, yielding the statistically best separation assuming there are three different tissues in the sample.

In the described implementation, each tissue class received a material description and a fixed density. It is straightforward to assign different densities inside a material according to original voxel values.

In the third stage, the scatter distribution in the CBμCT projection data is estimated using the simulation platform presented in this chapter, calculating the scatter field for a set of angular positions, previously defined by the user. The three scatter components – i.e. Compton, Rayleigh and multiple scatter– are stored in three different buffers, and they are smoothed to minimize the impact of the Monte Carlo limited number of photons, taking advantage of the relatively smooth nature of the scatter signal. The smoothing kernel is different for the Rayleigh scatter component, due to its highly forward directed distribution, which makes the smoothness assumption weaker in its case.

To minimize the simulation time, it is convenient to allow a certain amount of noise in the estimated scatter signal. Thus, a denoising step was necessary to obtain the desired noise-free scatter signal to subtract. In the present work, we have followed the approach proposed in [249]. The scatter signal was smoothed by means of several iterations of the Richardson-Lucy algorithm, stopping at the denoising step.

We propose to use different Gaussian smoothing kernels to take profit of the nature of the different types of scatter components. A wide kernel is used for the denoising of the noisier and more evenly distributed Compton and multi-scattered signals, while the forward direction of the Rayleigh signal is preserved by a narrower smoothing kernel.

The smoothed scatter signals are then divided by an analytical estimation of gain, calculated using the geometrical parameters of the system, the x-ray source spectrum, the detector response and the number of photons used for the simulation. This normalization removed the effect of the number of photons used for the simulation, detector gain, and beam anisotropy (inverse squared distance law). The scatter components are subsequently added to form the projection images which are interpolated in the angular domain to obtain the whole projection dataset to be subtracted from the original data. The corrected data are then reconstructed.

To assess the validity of the corrected volume, a new segmentation is performed. If the segmented volume differs from the one used for the MC simulation, the whole process is repeated again.

The method is outlined in figure 5.4.

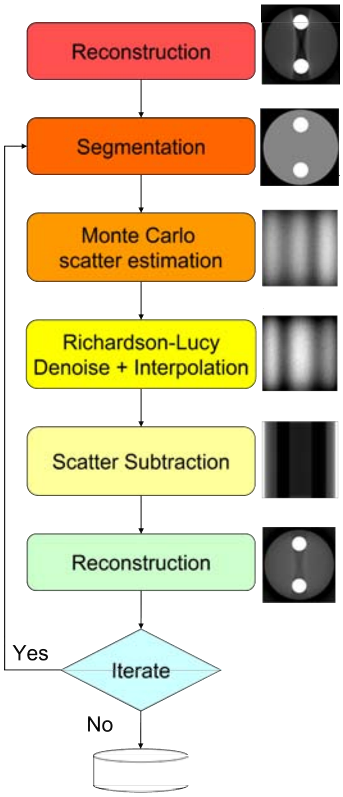

Figure 5.4. Outline of the scatter correction method proposed. For datasets highly degraded by scatter, the segmentation step could assign a wrong material to some part of the volume, then a new iteration of the method must be performed if the segmented volume is different from the one obtained in the previous iteration.

We used the same phantom, spectrum and simulation conditions described in section 5.2.4 but in this case we acquired 360 projections in 1° increments, therefore spanning a complete rotation. The anode current was set to 0.095 mA, for a total of 3.8 mAs.

For the scatter simulation we simulate 90 projections homogeneously distributed along 360°. The scatter distributions were denoised with the RL method using a 10 pixel kernel for the Compton and multiple scatter components and a 4 pixel kernel for the Rayleigh scatter component. The scatter projections for the angular position between the simulated ones were obtained by linear interpolation and a single iteration of the correction method was carried out.

We assessed the reduction in scatter by visual inspection and by quantifying the level of cupping present in the data using the t_{cup} measurement described in chapter 2, section 2.3.3.2, which expression is reproduced below:

$$t_{cup} = 100 \times \frac{\mu_{edge} - \mu_{center}}{\mu_{edge}}, \qquad (5.6)$$

where μ_{center} and μ_{edge} are the mean value of a 30x30 voxel ROI at the center and close to the edge of the PMMA area, respectively.

5.3 Results

5.3.1 Accuracy of simulated data and acceleration factor

The scatter fluence obtained by the accelerated version of MC-GPU for 5x10^6 photons is compared to the one obtained by classic MC-GPU for two different number of photons, namely 10^8 and 10^{10}, and for the Linac geometry. The scatter distributions were normalized to 10^8 photons, by dividing by the number of photons used for the particular dataset and then scale the results by 10^8. At a first glance, one can see the high degree of correspondence and the lower running time of the accelerated version of the code for similar noise levels –see panel (A1) in figure 5.5 compared to (A3)–. Deviations between classic and accelerated version of MC-GPU are quantified in panels (B) and (C) in figure 5.5. The absolute relative difference between the scatter distribution generated by the accelerated version and the one by the classic version showed a noise-like distribution with no apparent structure. Average absolute relative difference was 0.025, meaning less 2.5% discrepancy between distributions.

Profile data, measured along the central row of the detector showed equivalent trends for the three distributions with lower noise for the accelerated version of the code when compared to the result of unaccelerated MC-GPU for 10^8 photons.

The value of R_ε between the accelerated and classic versions of MC-GPU is shown in table 5.I. For the Linac geometry, the inclusion of variance reduction yielded 24~fold increase in performance when all the techniques are applied. However some techniques –direction biasing and forced scatter– were found to diminish performance in this situation and a better result was obtained when including only splitting and forced detection, achieving ~36 times better performance.

The situation for the rat geometry was different and all the variance reduction techniques provided an improvement in performance, yielding a R_ε of 28 when all the techniques were used.

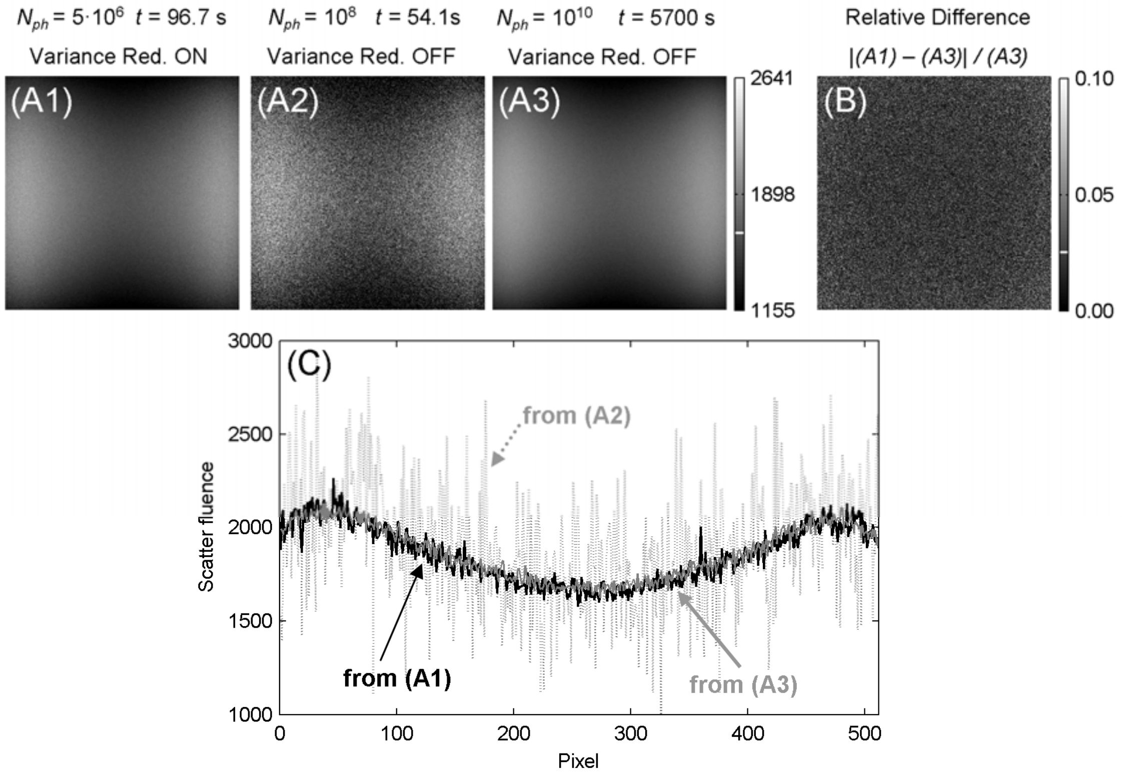

Figure 5.5. Comparison between scatter fluence obtained by the accelerated version of MC-GPU for 5x10^6 photons (A1) and the ones obtained by classic MC-GPU for 10^8 (A2) and 10^{10} photons (A3). The absolute relative difference between the distributions in (A1) and (A3) is shown in (B). Panel (C) depicts profile data measured along the central row of the detector for the three distributions. The white marks in the colorbars represent average value across the whole detector plane.

Table 5.I Performance improvement achieved for the different variance reduction techniques and system geometries

Variance Reduction Techniques	R_ε	
	Rat	*Linac*
Standard MC-GPU (Variance Red. OFF)	1.00	1.00
Interaction Splitting	12.50	10.56
Interaction Splitting + Direction Biasing	12.96	9.88
Interaction Splitting + Forced Dectection	23.03	35.54
Interaction Splitting + Forced Scatter	11.01	8.05
Interaction Splitting + Direction Biasing + Forced Detection	24.81	33.03
Interaction Splitting + Forced Detection + Forced Scatter + Direction Biasing (Variance Red. ON)	27.77	24.18

Figure 5.6 shows the projection image acquired with the CBµCT system (A1) and the one generated by the simulation engine (A2). Visual inspection of the two images yielded a good degree of correspondence, except for those areas where the segmentation of the volume yielded wrong results due to cone-beam artifacts (see the top of the image where the bed cannot be seen on the simulated projection). Also, a slight blurring can be noticed in the experimental data which is not reproduced by the simulation engine.

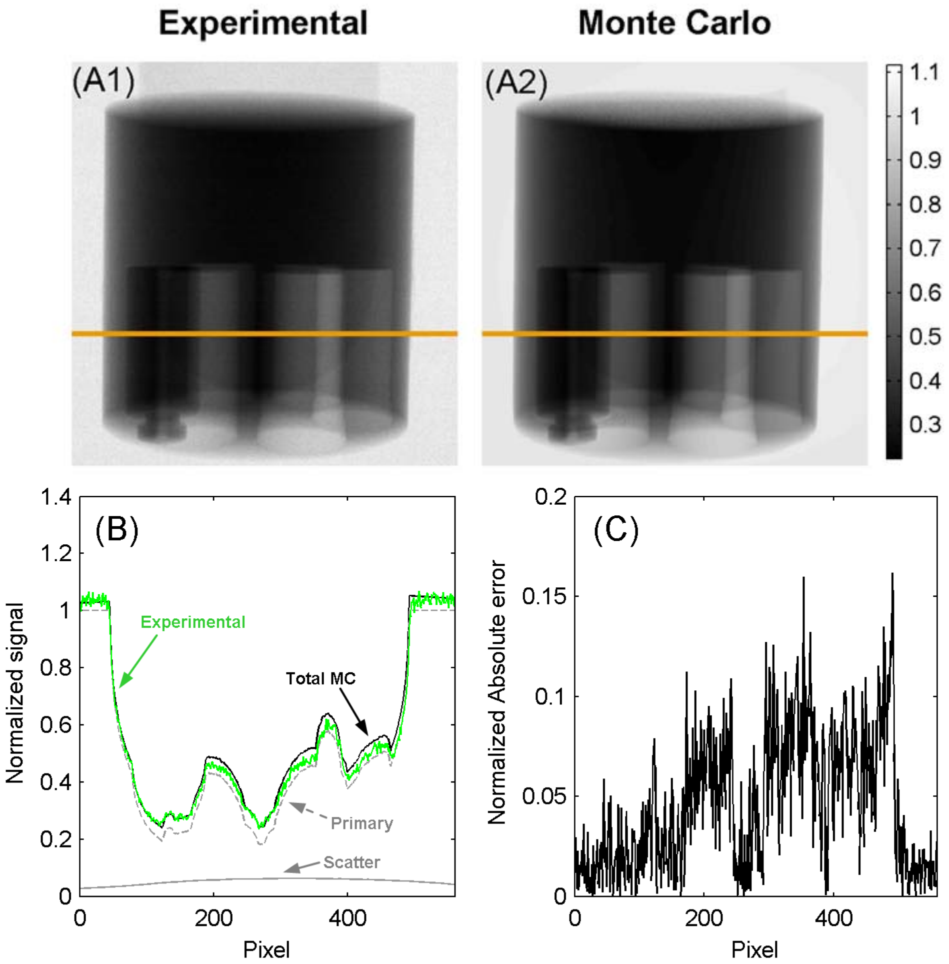

Figure 5.6. Gain normalized projection for experimental acquired data (A1) and for Monte Carlo simulated data (A2). Image profiles were measured along the orange horizontal lines shown in (A1) and (A2) and they are shown on panel (B), for experimental data (green curve), total Monte Carlo signal (black curve), Siddon primary signal (dashed grey curve) and Monte Carlo estimated scatter signal (solid grey curve). The normalized absolute error between the total Monte Carlo signal and experimental data is shown in panel (C).

Profile data across the orange lines in figure 5.6(A1) and (A2) are plotted in figure 5.6(B) and the respective absolute normalized error in figure 5.6(C). Quantitative evaluation of the profile confirmed the results pointed by visual inspection, with a good agreement between the two signals and error values that seldom reach 10 % of the signal value. The average value of difference across the profile is 0.045 (i.e. 4.5%). The difference between the two signals seems more evident for areas with high spatial variation –i.e. regions with several boundaries–.

5.3.2 Application to scatter correction

Figure 5.7 shows a reconstructed slice of the evaluation phantom after undergoing one iteration of the scatter correction algorithm (A1) and before (A2). The corrected data shows an average larger Hounsfield value, as expected from generic results for a similar geometry and spectrum in chapter 6 and in [119].

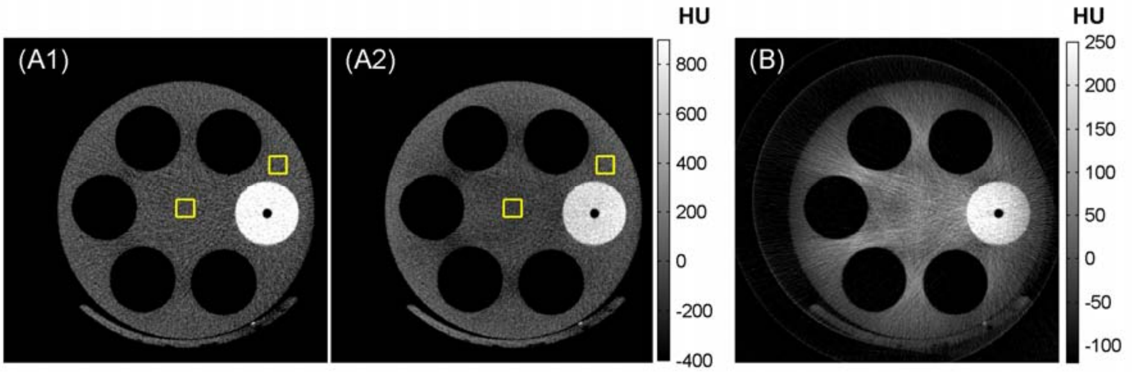

Figure 5.7. Slice of a reconstructed slice after one round of scatter correction (A1) and before (A2). The difference image (B) computed as (A1)-(A2) shows that a large part of the cupping was removed and that the dark areas between the air inserts were reduced.

In addition to the overall lower value, the original volume showed cupping and streaks artifacts that are especially noticeable in the gaps separating air inserts. When applying the scatter reduction method the image quality showed a considerable improvement, becoming more homogeneous due to reduced cupping and reducing the visibility of the dark bands.

The difference image shown in figure 5.7(B) confirmed the visual hints of reduced cupping and artifacts. Difference values on the gaps between the air inserts were larger than the surrounding area yielding a reduction in the dark bands. Also, differences follow an increasing trend towards the center of the phantom, as expected by the observed reduction of cupping. Values of t_{cup} measured using the edge and central ROIs depicted in figure 5.7(A1 and A2) further confirmed this trend, being of t_{cup} = 10.5% for the original dataset and t_{cup} = 2.2% for the corrected dataset.

The two concentric circles in figure 5.7(B) arose from the impossibility of applying the I_0 (air) correction –see chapter 2, section 2.2.4– during reconstruction, since there was not an object free area large enough to compute the value with sufficient accuracy.

The generation of a scatter distribution (i.e. projection) took ~12 s –with values ranging between 10 and 14 s for the different angular positions– for a total running time of ~1000 s. The time used for segmentation, reconstruction and scatter signal subtraction was negligible compared to the simulation time.

5.4 Discussion and conclusions

The inclusion of variance reduction techniques of scatter forcing, photon direction biasing, photon splitting and forced detection in MC-GPU yielded performance improvement factors –when all techniques are used together– of ~27 and ~24 depending on the system geometry, phantom position and x-ray spectrum without any bias in the estimated scatter fluence. This improvement factor adds to the ~15-30x increase in speed obtained by regular MC-GPU over calculations performed on a single CPU. These results are in agreement to those obtained for previous versions of the simulation engine [119].

Improvement factors of ~35 were achieved in some situations if only the appropriate subset of variance reduction techniques was used, since some of the techniques degraded performance for some scenarios.

The largest baseline gain in performance was shown to be provided by photon splitting –even given the computational burden imposed by the modified photon tracking–, in agreement with results obtained by Mainegra-Hing and Kawrakow [117] that found this technique the most effective among the techniques included in their study, viz. exponential transformation of the photon path [129], Woodcock tracking and a variation of forced detection. The combination of photon splitting with forced detection of Compton scatter provided dramatic improvements in performance, especially for the case of the Linac geometry. The larger performance improvement observed in the Linac geometry probably arises from the larger size of the sample and the higher mean energy of the x-ray beam. Larger phantoms involve more scatter interactions and a larger probability of absorption for scattered photons making larger the gain from forcing the scattered photons to reach the detector since a larger signal is integrated for high-order scatter when photons are forced to be directed towards the detector instead of letting them scatter free at directions that can be far from reaching the detector after a few interactions. Furthermore first-order scatter benefits from being translated directly to the detector since the probability of further interactions is larger for larger phantoms.

The case of forced scatter and source direction biasing is more challenging. Performance gains from forced scatter were previously reported by Colijn et al. [195] in the context of scatter estimation for small-animal CT imaging but we found degraded performance for some systems. We attributed this degradation to the lower relative probability of absorption compared to scatter for moderately hard spectra. This low absorption probability causes that only the small fraction of low energy photons likely to be absorbed benefit from forced scatter and their small contribution to the scatter signal does not compensate the time needed to transport them to the detector on a large volume. On the other hand, softer spectra contain a larger fraction of photons with an appreciable probability of absorption that benefit from forced scatter; this, combined with the lower time needed to transport the photon to the detector, could yield net benefits in performance from forced detection in small-animal systems.

Source biasing imposed a larger computational burden from the sampling of a further pdf by rejection sampling. This extra time needed per photon is compensated by the larger quantity of photons undergoing scatter interactions when a considerable part of the x-ray beam traversed only through air regions. That was the case for the rat configuration, where the beam was aligned with the major axis of the phantom. However when most of the beam crosses the sample, as in the case of the Linac experiment, performance could be degraded.

The accelerated simulator showed excellent agreement with its counterpart (classic MC-GPU) reassuring that the included variance reduction techniques indeed do not bias the estimated scatter distributions.

Simulated and experimental data showed a reasonable degree of correspondence with average relative error of 4.5 % and maximum error of ~10-12% for the lowest signal that contained few photons. Similar results were found for an intermediate version of the simulation engine by Zbijewski et al. [95].

Deviations were larger for high-frequency areas of the image. This can be explained by several effects, such as off-focal radiation or pixel cross-talk.

Practical use of the engine for scatter correction showed good results, with a 5-fold reduction in cupping and a noticeable reduction of scatter artifacts. This result is in line with previous literature on Monte Carlo scatter correction [35, 94-96, 249] which showed a great potential for artifact suppression. However, the time needed for the simulation of the complete dataset was in this case of ~15 minutes in a single medium-cost GPU, approaching acceptable running times for the use of Monte Carlo scatter correction in the regular imaging practice.

6

Monte-Carlo study of the effects of system geometry and antiscatter grids on CBCT scatter distributions

The work presented in this chapter was carried out in part at the I-STAR laboratory, Department of Biomedical Engineering of the Johns Hopkins University and under the supervision of Wojciech Zbijewski PhD and Jeffrey H. Siewerdsen PhD.

6.1 Introduction

As stated in chapter 5, x-ray scatter is one of the key sources for image quality degradation in CBCT. Therefore a detailed study of scatter as a function of system geometry and sample characteristics will help system design tasks in: i.) understanding the nature and form of x-ray scatter components (i.e., incoherent, coherent, and multiple scatter) contributing to the total scatter; ii.) the extent to which scatter rejection with antiscatter grids benefits image quality; and iii.) the effect of system geometry (e.g., source-to-object and object-to-detector distance) on the magnitude, nature, and spatial distribution of x-ray scatter and its components.

Neitzel [90] provided an analytical treatment of the question of system geometry – relative to antiscatter grids– in limiting x-ray scatter, concluding generally that systems with a short object-to-detector distance (i.e., a small "air gap") benefit most from the use of an antiscatter grid, whereas systems that can accommodate a large air gap (i.e., a large object-to-detector distance) benefit from the extended geometry in rejecting x-ray scatter, and a grid may be of little use (or actually detrimental, due to absorption of primary) to overall image quality per unit dose. Factors such as FOV, electronic noise, focal spot blur, and – of course – limitations in scanner size suitable to a given application present important additional considerations in system geometry, but the relationship between scatter and system geometry is known to be a particularly steep function of "selectivity" – e.g., scatter fluence varying by more than an order of magnitude over the range of geometries relevant in clinical CBCT.

The diversity of preclinical and clinical CBCT configurations in various applications spans a full range of such system geometries, with some featuring a compact form with a small air gap and others involving an extended geometry with a large air gap. This diversity of geometries, along with the associated variety of imaging techniques and object size implies that the susceptibility to scatter is not the same for all CBCT embodiments. This point is reflected in recent studies on the effects of x-ray scatter in such contexts. In a particular small-animal CBCT geometry, for example, Colijn et al. [195] showed scatter-to-primary ratios (SPR) of 10-20% for rat-sized objects. In musculoskeletal extremity imaging, Zbijewski et al. [8] found ~20% scatter-induced cupping and showed that antiscatter grids significantly reduce such artifact and improve contrast-to-noise ratio (CNR) without increase in imaging dose. In breast imaging, Kwan et al. [255] measured ~50% SPR at the detector for an average-size breast (14 cm diameter) and showed the benefit of a bowtie filter in reducing scatter. For mobile C-arm imaging, Schafer et al. [41] showed that an antiscatter grid did not offer an improvement in CNR per unit square root dose. Similarly, Kyriakou et al. [250] found that for low- to medium- scatter levels in C-arm CT, an increase in x-ray exposure was needed to compensate for primary absorption in the grid. In kilovoltage (kV) CBCT for image-guided radiotherapy (IGRT), Siewerdsen et al. [256] showed that although grids significantly reduced cupping and streak artifacts, image uniformity, and CT number accuracy, they did not offer an improvement in CNR per unit square root dose and offered little or no qualitative improvement in soft-tissue visibility (prostate). Similarly, Lazos et al. [245] used Monte Carlo simulations to show that antiscatter grids in CBCT for IGRT gave little or no improvement in CNR for head and neck imaging and a 10-20% improvement in CNR for pelvic imaging at a fixed dose.

That works revealed a great influence of system geometry and other design parameters that affect the quantity and distribution of scatter. They also showed that system geometry affects the form of x-ray scatter which challenges the classical assumption that most of the scatter is formed by incoherent scatter that presents a low-frequency spatial distribution and formed the basis for some scatter correction approaches [91-92, 191, 243].

The work reported below was motivated by this general backdrop of x-ray scatter within a broad diversity of CBCT scanner embodiments and applications. We leverage a modified form of the MC-GPU simulation software across a spectrum of system geometries to investigate not only the magnitude of x-ray scatter within each configuration but also the relative components (incoherent, coherent, and multiple scatter) therein. The work also sheds light on the potential merits (or detriments) of antiscatter grids within various system geometries, the influence of grid orientation on scatter rejection, and the spatial distribution of scatter at the detector – in some configurations found to be far from slowly varying. The work is intended to describe the effect of system geometry and antiscatter grids on the magnitude, form, and spatial distribution of x-ray scatter across a range of pertinent CBCT applications in broad terms that will identify key considerations in understanding the performance of current embodiments, designing new systems, and developing x-ray scatter correction methods.

6.2 Materials and methods

We used the Monte Carlo accelerated scatter simulation platform described in chapter 5 to estimate the properties of scattered radiation distribution for different configurations and applications. The following sections detailed the particularities of the study presented in this chapter.

We used a generic flat-panel detector that was modeled according to the cascaded system analysis theory based on previous, validated, results. The detection stage was completed by including an analytical model for the transmission of photons through an antiscatter grid. Both elements, included in the last stage of image formation on the simulation process, are described below.

We built a series of synthetic phantoms for the assessment of scatter in a controlled environment where results are easily comparable between different geometries, and realistic phantoms providing more accurate estimations of the real world outcomes caused by scatter. The effect of scatter is quantified by a series of metrics described below.

We performed several experiments ranging from very general trends for properties of scatter as a function of geometry to life-like acquisitions involving a large number of factors affecting scatter.

6.2.1 Analytical model for spectrum, antiscatter grid, and flat-panel detector

Inputs for the x-ray source spectrum and detector response were provided as text files to the Monte Carlo simulation platform, as described in chapter 5. The effect of including an antiscatter grid was also included in the system as a further weighting factor.

Tungsten anode x-ray spectra with arbitrary filtration were obtained from the Spektr toolkit [230] implementation of the TASMIP polynomial model [55]. The spectra were provided to the simulator as a text file with 1 keV sampling intervals over the range 1-150 keV. The x-ray spectra were normalized to unity area, yielding a probability density function.

The grid was approximated as locally parallel, oblique lamellae oriented at an angle corresponding to the angle formed by the detector plane and the ray joining the location of photon incidence and the focus of the x-ray source. Each photon was assigned a weight given by the analytical expression of Day and Dance [245, 251] for grid transmission as a function of photon incidence angle, photon energy, grid cell materials and dimensions, and local grid angle. The photon was subsequently scored in the detector with a weight representing the product of energy-dependent probability of absorption in the scintillator (quantum detection efficiency, $\overline{g_1}$), and energy-dependent optical gain in the scintillator ($\overline{g_2}$). For a flat-panel detector with a 250 mg/cm^2 CsI:Tl scintillator, the mean detector response has been accurately modeled in these terms by cascaded systems analysis [64], with $\overline{g_1}$ computed from the incident x-ray spectrum and attenuation coefficient of CsI, and $\overline{g_2}$ assuming a gain of 50 photons per absorbed keV [176]. Typically, the detection process as modeled by cascaded systems analysis also includes gain stages to account for escape efficiency of optical photons from the scintillator ($\overline{g_3}$), and coupling efficiency of the scintillator and photodiodes ($\overline{g_4}$), and pixel fill factor. Since those gains are nearly independent of photon energy and therefore cancel out in gain correction, they have no impact on the analysis of scatter distributions below and were not included in the model. The weight was chosen to yield signal levels that agreed with the measured mean detector response for a Varian 4030CB flat-panel detector within ~5-10% for spectra ranging 60 - 150 kVp.

6.2.2 CBCT System and Object Models

We explored the geometric factors governing the magnitude of x-ray scatter and the individual components therein (viz., Compton, Rayleigh and multi scatter). To this end we studied a range of CBCT configurations currently deployed in clinical and preclinical applications: 1) a small-animal scanner [4] (SA); 2) a compact musculoskeletal extremities scanner [8] (MSK); 3) an otolaryngology head scanner [9] (Head); 4) a dedicated breast scanner [12] (Breast); 5) a mobile intraoperative C-arm [41] (C-Arm); and 6) a kV CBCT imager implemented on a linear accelerator [256] (Linac). The geometries approximating such configurations are summarized in table 6.I and figure 6.1. Systems were defined by their source-to-axis distance (*SAD*), axis-to-detector distance (*ADD*), and detector size –*D*, the lateral and longitudinal extent of the flat-panel detector–. In each case, the flat-panel detector consisted of a 512x512 matrix of square pixels at pitch *d* in combination with a 250 mg/cm^2 CsI:Tl scintillator. The x-ray beam extended laterally (fan angle) and longitudinally (cone angle) to match the detector area. The configurations illustrated in figure 6.1 were not intended to model any particular system and instead reflect fairly generic CBCT geometries appropriate to a given application. The flat-panel detector was centered on the central axis of the x-ray beam in each case, and "offset-detector" geometries were not considered. A bowtie filter was not incorporated in the current work since many of the systems considered do not commonly employ a bowtie. There is therefore no simple, nominal choice of filter for each configuration that would permit a fair comparison across this range of geometry, object size, and kVp. Rather, the design of bowtie filters optimal to a particular configuration is a continuing area of work, with results indicating potential advantages in x-ray scatter for some configurations (e.g. breast CT [255] and Linac CBCT [210, 245]). For simplicity in an already broad space of parameters considered below, the simulations considered scenarios without a bowtie.

Each configuration was considered with and without an antiscatter grid. The focal distance of the grid was equal to the source-to-detector distance (SDD) in each case. Simulations were performed with grid lamellae nominally oriented perpendicular to the axis of rotation (denoted "Grid Horizontal") and alternatively oriented with lamellae parallel to the axis of rotation (denoted "Grid Vertical"). Again to limit an already broad scope of parameters, a single nominal grid design was considered in all simulations – specifically, a 10:1 grid ratio, 200 lines per inch (7.87 lines per mm), focused linear grid comprising Pb lamellae with Al interspacers. This model represents an intermediate grid of fairly standard design that provided a common basis for comparisons. Potentially more beneficial grid designs –e.g., air interspacers, variable lines per inch, 2D crosshatch, etc.–, and optimal choice of grid parameters for the particular system geometry were beyond the scope of the current work. Previous work also showed that the particular grid design –e.g., grid ratio– had only a weak effect on scatter effects, and a nominal (10:1 grid ratio) was a reasonable choice. Nevertheless, the results below can be used to provide guidance for system-specific grid design by identifying key aspects of scatter distribution and grid performance for each embodiment.

Table 6.I. Nominal geometry and phantoms for the various CBCT configurations.

								Realistic Phantom	
CBCT Configuration	*X-ray Spectrum*	*SAD (mm)*	*ADD (mm)*	*Mag*	*D (mm)*	*d (mm)*	*Common Phantom Major Axis (mm)*	*Anatomy Type*	*Major Axis (mm)*
Small Animal (SA)	60 kVp (1 mm Al)	150	50	1.3	150	0.293	70	Rat	52
Extremity (MSK)	90 kVp (0.2 mm Cu, 2 mm Al)	430	120	1.3	250	0.488	160	Knee	125
Head	90 kVp (0.2 mm Cu, 2 mm Al)	480	220	1.5	250	0.488	160	Head	235
Breast	80 kVp (0.2 mm Cu, 2 mm Al)	458	320	1.7	300	0.586	140	Breast	140
C-arm	100 kVp (0.2 mm Cu, 2 mm Al)	600	600	2.0	430	0.840	160	Head and Thorax	235 and 500 (incl. arms)
Linac	110 kVp (0.2 mm Cu, 2 mm Al)	1000	500	1.5	430	0.840	280	Thorax and Pelvis	500 (incl. arms) and 350

The digital phantoms comprised various combinations of the following materials: air, lung, adipose, soft tissue, brain, skin, muscle, cartilage, red marrow, and cortical bone. The interaction cross sections for each material were computed from the elemental composition data obtained either from the Penelope database [58] (soft tissue and fat) or from the tabulated data by Woodard and White [189]. Two categories of digital phantom were considered: 1) a generic elliptical phantom referred to as the "Common Phantom" providing a common basis of comparison among each of the CBCT configurations; and 2) a set of anatomically realistic phantoms ranging from mouse to human pelvis as detailed below.

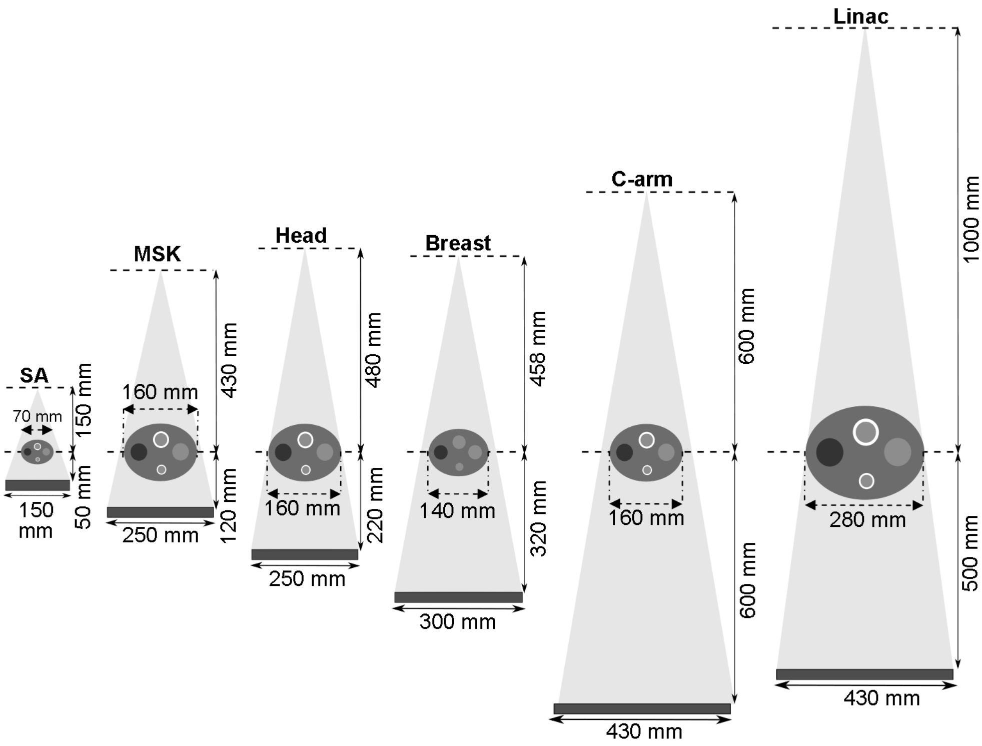

Figure 6.1. Geometric configurations illustrated to scale with the common elliptical phantom.

An axial slice of the Common Phantom is illustrated in figure 6.2. The background region consisted of soft tissue, and two low contrast (muscle and fat) inserts were included along the major axis. Two bone inserts were included along the minor axis, comprising an annulus of cortical bone around a marrow interior. For the Breast configuration, the two bone regions were replaced by glandular tissue. The size of the Common Phantom was scaled between each of the CBCT configurations as detailed in table 6.I to represent approximately the size of anatomy in each application (without lateral truncation), maintaining a constant ratio of the minor to major axes of 0.8. The phantom extended longitudinally (to infinite length) beyond the longitudinal FOV. The voxel size for the Common Phantom was chosen to minimize discretization artifacts in Siddon ray-tracing –see chapter 5– of primary x-rays: 0.03 mm for the SA configuration, 0.07 mm for the Breast, 0.08 mm for the MSK, Head, and C-arm, and 0.15 mm for the Linac.

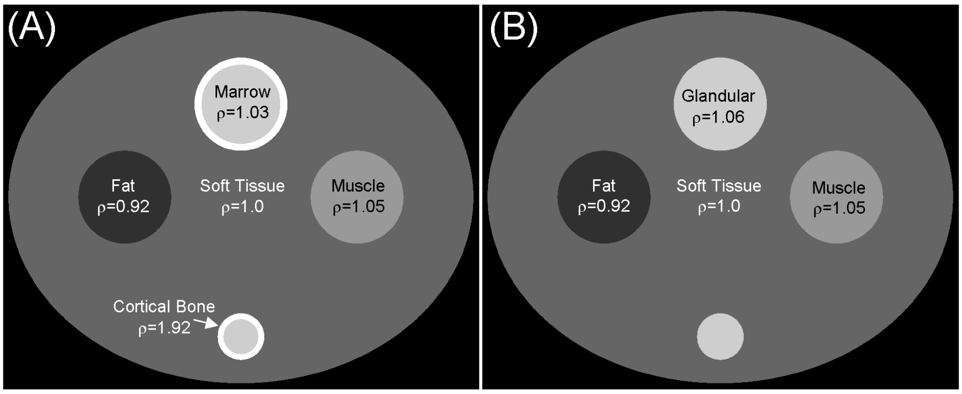

Figure 6.2. (A) Illustration of the idealized Common Phantom as used in the simulations of the SA, MSK, Head, C-arm and Linac CBCT. For the Breast configuration (B), the bone inserts were replaced by glandular tissue.

A variety of anatomically realistic phantoms were also simulated as listed in Table I. For the SA configuration, the Digimouse [188] model was scaled to simulate a rat thorax with voxel size 0.29 mm. For the MSK, Head, C-arm, and Linac configurations, anthropomorphic models of a knee, a head, a thorax, and a pelvis were built from models included in the Virtual Family Project [257-258] dataset at voxel size 1.0 mm. For the Breast configuration, a digital breast phantom was constructed from a manually segmented breast CBCT volume [259] of a breast at voxel size 0.5 mm. Materials included in the realistic phantoms included air, lung, adipose, soft tissue, brain, skin, muscle, cartilage, red marrow, and cortical bone, with cross sections computed from the same resources as described above for the Common Phantom. For all models, the original discretization of the source datasets was maintained.

6.2.3 Monte Carlo experiments

6.2.3.1 Effects of system geometry on scatter

An initial set of simulations systematically varied the system geometry across a broad range beyond the specific CBCT configurations of figure 6.1 to provide a more general understanding of the effects of system geometry on scatter fractions and grid efficacy. We varied SAD from 10-130 cm and SDD from 60-150 cm (each in ~5 cm increments, such that the former was always less than the latter). The Common Phantom was used in each case (with major axis set to 16 cm), and a single projection perpendicular to the major axis was simulated. The number of histories was N_{ph} = 5x10^6 photons, split into 512 virtual photons at each interaction. Since the spatial distribution of scatter was not analyzed in this case, only a small, centrally located, detector region of 20x20 pixels was used for scoring and subsequent computation of average SPR. All Compton photons were forced toward the detector, allowing for further reduction of simulation noise. Simulations were performed with and without an antiscatter grid using a 100 kVp (+2 mm Al, +0.2 mm Cu added filtration) spectrum and a detector of size D = 250 mm. For simulations with a grid, the focal length was equal to the SDD.

6.2.3.2 Specific CBCT configurations: Scatter distributions, image artifacts, and efficacy of antiscatter grids

The main body of experiments involved analysis and comparison of scatter properties and grid efficacy for the CBCT configurations summarized in table 6.I and figure 6.1. In each case, scatter and primary projections were simulated for both the Common Phantom and the realistic anatomical models using the nominal parameters in table 6.I, with and without the antiscatter grid. Simulations were performed for a complete circular orbit of projections at 1^o angular steps, and scatter estimation involved N_{ph} = $5x10^6$ photons per projection split into 512 virtual photons at each interaction. While the noise in scatter distributions obtained with variance reduction for this N_{ph} is low –see chapter 5, section 5.3.1–, additional denoising of the scatter fluence was performed by executing three iterations of a Richardson-Lucy (RL) fit with a Gaussian kernel [247, 249], with a kernel width of 10 pixels for Compton and multiple scatter distributions and 4 pixels for Rayleigh scatter distributions. This approach has been shown to reduce simulation noise without biasing the distributions [247]. RL fitting was used to reduce noise of the scatter distributions in the studies of various CBCT system configurations but was not used in the basic study of system geometry (section 6.2.3.1). Noiseless primary x-ray projections were computed with the Siddon algorithm and added to the total scatter distribution after a normalization of both distributions by their respective gain (air) scans. The same antiscatter grid was employed for primary and scatter simulations, as detailed in section 6.2.2. The simulated projections (scatter+primary) were reconstructed with the Feldkamp algorithm [79] on a 256x256x40 isotropic voxel grid with a Hann apodizer with a cutoff at the Nyquist frequency. The reconstruction voxel size varied between the configurations so that the side of the cubic reconstruction volume was always 110% of the major axis of the Common Phantom for that embodiment: 0.29 mm for the SA configuration, 0.69 mm for the MSK, Head, and C-arm, 0.6 mm for the Breast, and 1.21 mm for the Linac.

6.2.4 Metrics of scatter assessment

Magnitudes of total scatter, and Compton, Rayleigh and multiple scatter components therein were quantified in terms of the gain-corrected scatter magnitude (S_{tot}), the gain-corrected magnitude of each scatter component [Compton (S_{incoh}), Rayleigh (S_{coh}), and multiple scatter (S_{multi})], the fraction of each component in the total scatter signal, and the scatter-to-primary ratio (SPR). The deflection angle was measured for each scattered photon reaching the detector as the angle between the direction of travel and the line connecting the focal spot with the point of interaction with the detector. Thus a deflection angle of 0^{o} indicated travel direction parallel to the lamellae of a focused grid. For the experiments with the Common Phantom, the metrics are reported as means measured from a 20x20 pixel region of interest (ROI) located at the center of the detector, and the deflection angle was analyzed as an angular histogram weighted by the weight of each photon and normalized to unity total area. For the realistic phantoms, box plots were used to represent the distribution of metrics in the region of the projected shadow of the object. The degradation of image quality associated with x-ray scatter was evaluated by the following quantitative metrics as well as visual inspection of the reconstructed images:

(a) Cupping: Taking μ_{center} and μ_{edge} as the mean value of a 20x20 voxel ROI at the center and inside edge of the object, respectively, the magnitude of cupping artifact was assessed as:

$$t_{cup} = 100 \times \frac{\mu_{edge} - \mu_{center}}{\mu_{edge}}, \tag{6.1}$$

(b) Contrast reduction: Soft-tissue contrast between muscle and fat in reconstructions of the Common Phantom was computed as:

$$C = 2\frac{\mu_M - \mu_F}{\mu_M + \mu_F}, \tag{6.2}$$

where μ_M and μ_F are the mean values of a 20x20 voxel ROI inside the muscle and fat inserts, respectively. The reduction in contrast due to scatter was quantified by the ratio of contrast in a reconstruction of the complete simulated projection data –including primary and scatter– ($C_{prim+scat}$), to that in a reconstruction of primary-only projections (C_{prim}). Contrast and cupping were computed for the Common Phantom, where the regular elliptical shape and placement of inserts yielded a symmetric cupping pattern with respect to the major axes, and streak artifacts were localized and well separated from the muscle and fat inserts. This provided a reliable estimate of contrast from equation 6.2 without potential bias introduced by the placement of ROIs relative to a complicated pattern of artifacts in the more realistic anatomical phantoms.

(c) Contrast-to-noise ratio: The scatter and primary projections obtained by Monte Carlo simulation with variance reduction do not realistically convey the quantum noise in a projection image at a given level of radiation dose. However, consideration of image noise is important when assessing the performance of antiscatter grids because of the reduction of primary fluence and the associated increase in noise due to attenuation in the grid. We used an analytical model to analyze the relative change in contrast-to-noise ratio (CNR, including both the improvement in contrast and the increase in noise) associated with the introduction of a grid as a function of SPR. Denoting the transmission of primary photons by the grid as g_{prim} and the transmission of scattered photons as g_{scat}, the SPR in the presence of the grid is:

$$SPR_{grid} = \left(\frac{g_{scat}}{g_{prim}} \right) SPR_{no-grid} \,. \tag{6.3}$$

As derived in [89] for a circular insert of attenuation μ_1 and diameter d_1 inside a uniform circular region of diameter d_0 and attenuation coefficient μ_0, the contrast –difference in mean measured voxel values between μ_0 and μ_1– in the presence of scatter is:

$$C = \delta + \frac{1}{d_1} \ln\left(\frac{1 + SPRe^{-\delta d_1}}{1 + SPR} \right), \tag{6.4}$$

where $\delta = \mu_0 - \mu_1$ is the intrinsic material contrast, i.e. difference in true attenuation coefficient. Although equation (6.4) shows addition of a term to the intrinsic material contrast δ, the SPR-dependent natural logarithm term always has opposite sign to that of δ, and scatter always results in a reduction in the difference between reconstructed voxel values. Ignoring electronic noise, the pixel variance in the reconstructed image N^2 is inversely proportional to the detected x-ray intensity [260]. Assuming the same tube output (mAs) for image acquisition with and without the grid, and denoting the intensities of primary and scatter radiation on the detector as I^{prim} and I^{scat}, the ratio of the (squared) CNR at a fixed dose with and without a grid is:

$$\begin{aligned}\frac{CNR_{grid}^{2}}{CNR_{no-grid}^{2}} &= \left(\frac{C_{grid}\,/\,N_{grid}}{C_{no-grid}\,/\,N_{no-grid}}\right)^{2} = \frac{(I_{grid}^{prim}+I_{grid}^{scat})}{(I_{no-grid}^{prim}+I_{no-grid}^{scat})}\left(\frac{C_{grid}}{C_{no-grid}}\right)^{2} \\ &= \frac{I_{grid}^{prim}(1+SPR_{grid})}{I_{no-grid}^{prim}(1+SPR_{no-grid})}\left(\frac{C_{grid}}{C_{no-grid}}\right)^{2} = \\ &= \frac{g_{prim}(1+SPR_{grid})}{(1+SPR_{no-grid})}\cdot\frac{\left[\delta+\frac{1}{d_1}\ln\left(\frac{1+SPR_{grid}e^{-\delta d_1}}{1+SPR_{grid}}\right)\right]^{2}}{\left[\delta+\frac{1}{d_1}\ln\left(\frac{1+SPR_{no-grid}e^{-\delta d_1}}{1+SPR_{no-grid}}\right)\right]^{2}}\ .\end{aligned} \tag{6.5}$$

The dependence of the ratio of CNR with and without the grid in equation (6.5) on SPR was computed for each of the CBCT configurations for a setup approximating the Common Phantom, taking μ_0 for soft tissue (computed at the effective beam energy, equal to spectrum-weighted mean energy) and with d_0 matching the major axis. The values of attenuation coefficient and diameter of the insert (μ_1 and d_1) were taken from the muscle insert (figure 6.2). Grid transmission factors g_{prim} and g_{scat} were obtained for each CBCT embodiment from Monte Carlo simulations of section 6.2.3.2 by averaging over a 20x20 pixel ROI at the center of the detector. Note that the derivations of equation (6.4) and (6.5) assume that the introduction of the contrast insert (d_1, μ_1) into the background object (d_0, μ_0) introduces only a small perturbation that does not influence SPR or the measured value of the background attenuation in the presence of scatter. It also assumes that scatter carries no information and acts purely as an uncorrelated –i.e., equal noise-power at all spatial frequencies– additive source of projection noise as detailed in [89].

6.3. Results

6.3.1. Effects of system geometry on scatter

Figure 6.3 quantifies a number of important, general dependencies between x-ray scatter, system geometry, and the relative benefit of an antiscatter grid. Figure 6.3(A) plots the SPR at the center of the detector over a broad range of possible CBCT geometries for the Common Phantom fixed at a major axis diameter of 16 cm and a projection perpendicular to the major axis of the phantom. The steep reduction in SPR for higher ADD is clear –note the logarithmic scale in figure 6.3(A) – consistent with trends noted by Neitzel [90] and others [34, 250] that increasing the air gap is the first best defense against x-ray scatter. For compact geometries –e.g., those with ADD ~8-30 cm– in particular, the variation of SPR with ADD is dramatic such that small increases in air gap yield strong reduction in SPR. The dependence on SDD is comparatively weak, with only a slight increase in SPR at increased SDD due to a decrease in the deflection angle required for photons that undergo scatter at the object periphery to reach the detector center (where SPR is computed). This decrease in the deflection angle yields increased probability of interactions that contribute to SPR as explained below.

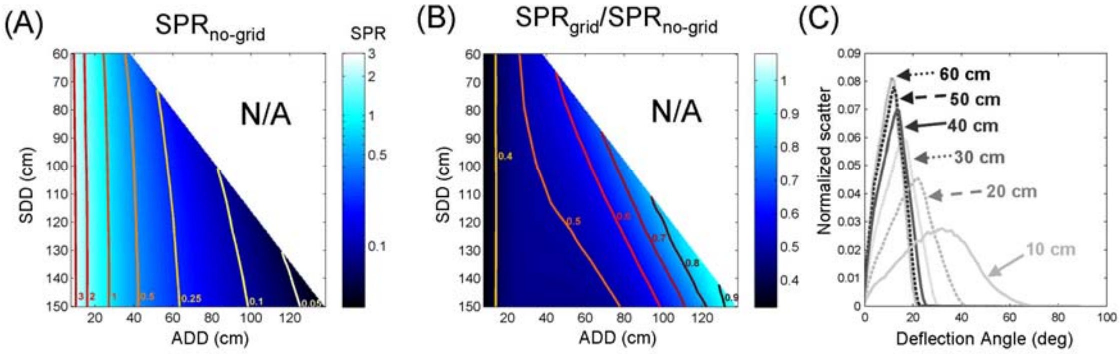

Figure 6.3. (A) SPR at the center of the detector versus SDD and ADD for systems without a grid. (B) Reduction in SPR due to an antiscatter grid (10:1 grid ratio). (C) Histogram of deflection angles of scattered photons reaching the detector plane for a projection perpendicular to the major axis of the Common Phantom.

The reduction in SPR achieved with an antiscatter grid is shown in figure 6.3(B). The benefit of grids is greater for compact systems (i.e., those with shorter ADD). As shown in the histogram of deflection angle (see figure 6.3(C)), the distribution of the direction of scattered photons reaching the detector is broader for a compact system geometry than for more extended configurations, with the peak of the histogram shifted away from 0^{o} (the direction parallel to the lamellae of a focused grid), resulting in increased scatter rejection by a focused grid. Systems with larger ADD mainly involve forward-directed scatter reaching the detector, benefitting less from the use of a grid. At a fixed ADD, grids provide less SPR reduction –higher ratio of SPR in figure 6.3(B)– for systems with shorter SDD, since the short SDD implies a steep deflection angle needed for scattered photons generated near the periphery of the object to reach the center of the detector. For both coherent and incoherent scatter, the probability of interaction is generally lower for steeper deflection angles. Therefore, compared to a configuration with long SDD, the scatter at the center of the detector for a system with short SDD contains a higher fraction of forward-directed photons that are difficult to remove by a grid.

6.3.2. Scatter in various CBCT configurations: artifacts, contrast and noise considerations

Figure 6.4 shows reconstructions of the Common Phantom across CBCT embodiments for three simulation scenarios: (i) simulation of primary photons only (providing baseline image quality for a polyenergetic x-ray beam); (ii) simulation of primary and scatter photons with no antiscatter grid; and (iii) primary+scatter photons as in (ii) but with a focused horizontal antiscatter grid. The increase in cupping and streak artifacts is apparent for all configurations when scatter is included in the simulation, particularly for the gridless scenario (ii), but the severity of scatter artifacts is strongly dependent on system geometry. The slight degree of cupping and streaks in the primary-only cases (i) are attributed to beam hardening. The images visually illustrate the effects of geometry and the presence of an antiscatter grid on image uniformity (cupping), streaks, and contrast, each quantified in figure 6.5 and discussed in detail below.

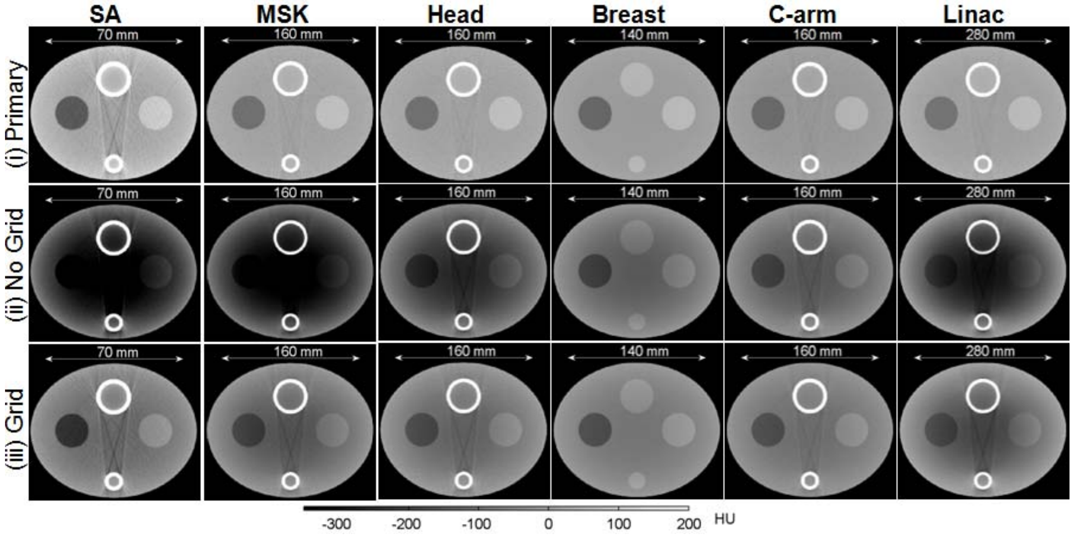

Figure 6.4. (i) Axial reconstructions of primary-only projection data for the Common Phantom. (ii) Reconstructions of projections with scatter included in the simulation (without an antiscatter grid). (iii) Reconstructions of primary+scatter projection data with an antiscatter grid.

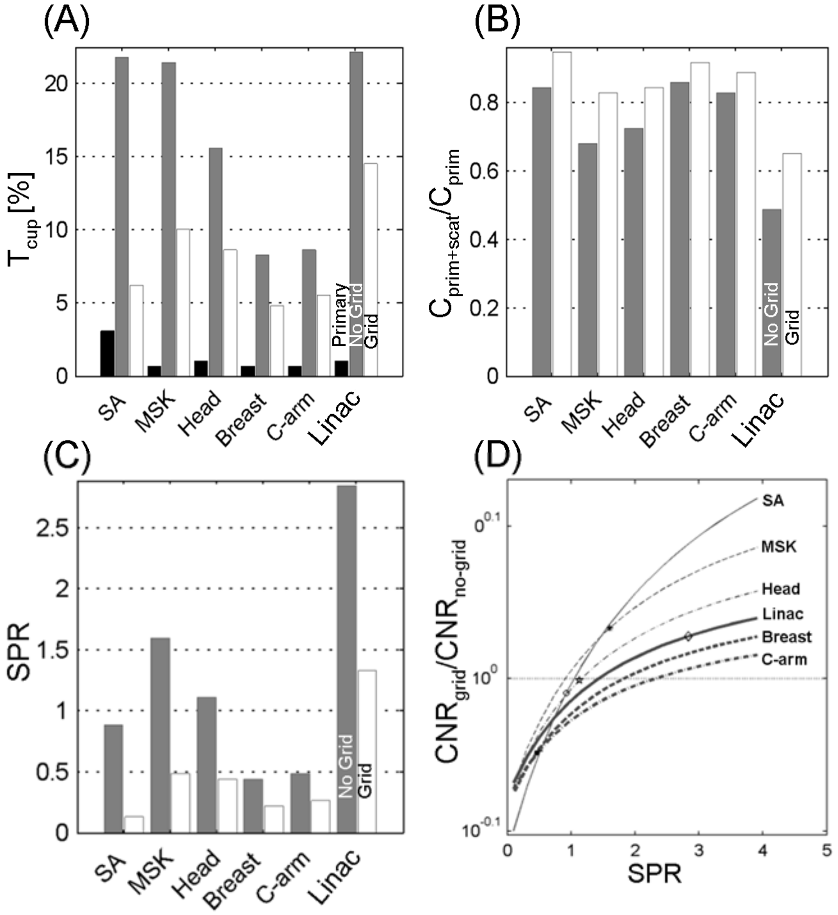

Figure 6.5. (A) Cupping artifact –equation (6.4)– in reconstructions of the Common Phantom. (B) Reduction in contrast –from equation (6.5)– in reconstructions of primary+scatter to that in primary-only. (C) SPR in projections of the Common Phantom with and without a grid. Black bars indicate simulations with primary only. Gray bars show simulations with scatter and no grid. White bars show simulations with scatter and an antiscatter grid. (D) The ratio of CNR with a grid (CNR_{grid}) to CNR without a grid ($CNR_{no\text{-}grid}$) plotted versus SPR for each CBCT configuration at fixed detector exposure. The horizontal dotted line marks CNR ratio equal to one.

As illustrated in figure 6.4, cupping is most pronounced for the more compact geometries –such as the MSK and Head scanners– and for large objects –Linac–. Figure 6.5(A) quantifies the increased cupping due to x-ray scatter, where the compact geometries exhibit artifact in the range t_{cup} ~15-22% (compared to t_{cup} ~1-3% without scatter). Similarly for the large object (280 mm) Linac case, x-ray scatter increases t_{cup} from ~1% (without scatter) to t_{cup} ~22%. As seen qualitatively in scenario (iii) of figure 6.4, introduction of a grid improves image uniformity –reduces cupping– for all configurations. Consistent with trends suggested in figure 6.3, the most pronounced benefit in image uniformity is for systems with short air gaps –SA and MSK– and large objects –Linac– and less for systems with higher magnification –Breast and C-arm–. Figure 6.5(A) quantifies the major improvement in t_{cup} by virtue of the grid for the SA, MSK, and Head configurations, whereas the improvement for the Breast and C-arm cases is more modest.

Figure 6.5 also shows that streak artifacts are evident even in the primary-only scenario (i) due to beam hardening –strongest for the SA case, which involves the softest x-ray spectrum– and are intensified in the scenarios containing scatter. Interestingly, the presence of an antiscatter grid is seen to impart greater benefit to image uniformity –reduced cupping artifact– than to streaks, most evident in the SA, MSK, and Head configurations. This reflects the sensitivity to residual scatter and the ability of grids to reduce slowly varying –low-frequency– scatter artifacts arising from high-angle scatter –Compton and multiple scatter– but lesser ability to reduce high-frequency artifacts associated with low-angle scatter –Rayleigh and, to a lesser degree, low-order Compton–.

The loss of contrast due to x-ray scatter is evident in figures 6.4 and 6.5(B), with greater degradation for the systems exhibiting larger cupping. The recovery of contrast by an antiscatter grid is strongest for the SA, MSK, Head, and Linac configurations and least pronounced for the Breast and C-arm. The lower efficiency of grids for configurations with large air gap and medium-sized FOV –i.e., Breast and C-arm– is evident from analysis of the SPR with and without grids in figure 6.5(C), where the SPR at the detector is already a factor of ~2-6 lower than for the other configurations. The results suggest the strongest benefit from the grid for the SA configuration, due not only to the compact geometry but also the soft x-ray spectrum and increased grid efficiency.

Note that the relative magnitude of cupping t_{cup} is not directly related to SPR, as evidenced by a comparison of the SA and Linac cases, which show a similar magnitude of $t_{cup,}$ despite a significantly larger SPR for the Linac configuration. This is a result of the absolute change in the reconstructed attenuation coefficient depending on SPR and object size [89] (70 mm for SA versus 280 mm for the Linac). The same dependence of reconstructed values on SPR and object size explains the different appearance of reconstructions of the Common Phantom for SA, MSK, and Linac CBCT in figure 6.4, despite similar values of $t_{cup.}$ The same t_{cup} can therefore imply a different appearance of the cupping artifact when it is accompanied by different bias in the mean reconstructed attenuation value.

Figure 6.5(D) shows the relative benefit –or degradation– in CNR associated with an antiscatter grid for each of the CBCT geometries, weighting the increase in contrast obtained by using a grid versus the associated increase in image noise. For each curve in figure 6.5(D), the system geometry is that indicated in table 6.I, but the SPR was taken as a free variable (see figure 6.5(C) for the actual SPR at the center of the detector for the posterior-anterior projection of the Common Phantom). In each case, the ratio of CNR with and without a grid was computed according to the analytical model in equation (6.5) utilizing Monte Carlo estimates of grid transmission for primary and scatter radiation. A ratio in CNR below unity implies that the grid imparts an increase in noise that outweighs the increase in contrast. For systems with a large air gap and medium-sized objects (e.g., Breast and C-arm), the grid degrades CNR over a broad range of SPR, including those typical of the Common Phantom as plotted in figure 6.5(C). Similarly for the SA configuration, the small object size yields low SPR for which the grid is seen to degrade CNR. For the more compact MSK and Head configurations, the results suggest an improvement in CNR at levels of SPR (~1.0 - 1.5) typical for those embodiments. The Linac configuration presents an intermediate case, with the large object size leading to high SPR that would make it advisable to use of a grid in terms of CNR, but a fairly long geometry for which the benefits of the grid may be small.

Considering the results of figures 6.4 and 6.5 in total reveals a mixed set of tradeoffs and considerations for each CBCT configuration as to whether or not a given system benefits from a grid. In all cases, the grid improves image uniformity (reduces cupping), but depending on the SPR may improve or degrade CNR. For the more compact geometries in human applications –MSK and Head– the results are consistent: incorporation of a grid imparts a significant reduction in artifacts and a net benefit to CNR, without increase in dose. For the more extended geometry –Breast and C-arm–, the grid has a lesser effect in artifact reduction and reduces CNR. Implications for the SA configuration are mixed: although the grid strongly reduces artifacts, it degrades CNR for the low levels of SPR typical for small subjects even in the compact geometry. Similarly for Linac, the implications are mixed, but for the opposite reasons: the grid imparts a significant reduction in artifacts but may have little benefit –or in fact, degradation– on CNR, depending on the size of the object, and an increase in dose may be required to restore CNR to that achieved by a gridless configuration.

6.3.3 Scatter in various CBCT configurations: scatter components and spatial distribution

Scatter components –incoherent, coherent, and multiple scatter of any type– are analyzed in figure 6.6 for a single projection, perpendicular to the major axis of the Common Phantom. Taking the MSK configuration for example, the fractions of each component in the total scatter are shown in figure 6.6(A). For this compact geometry, the scatter distribution is dominated by multiple scatter when no grid is present (top row).

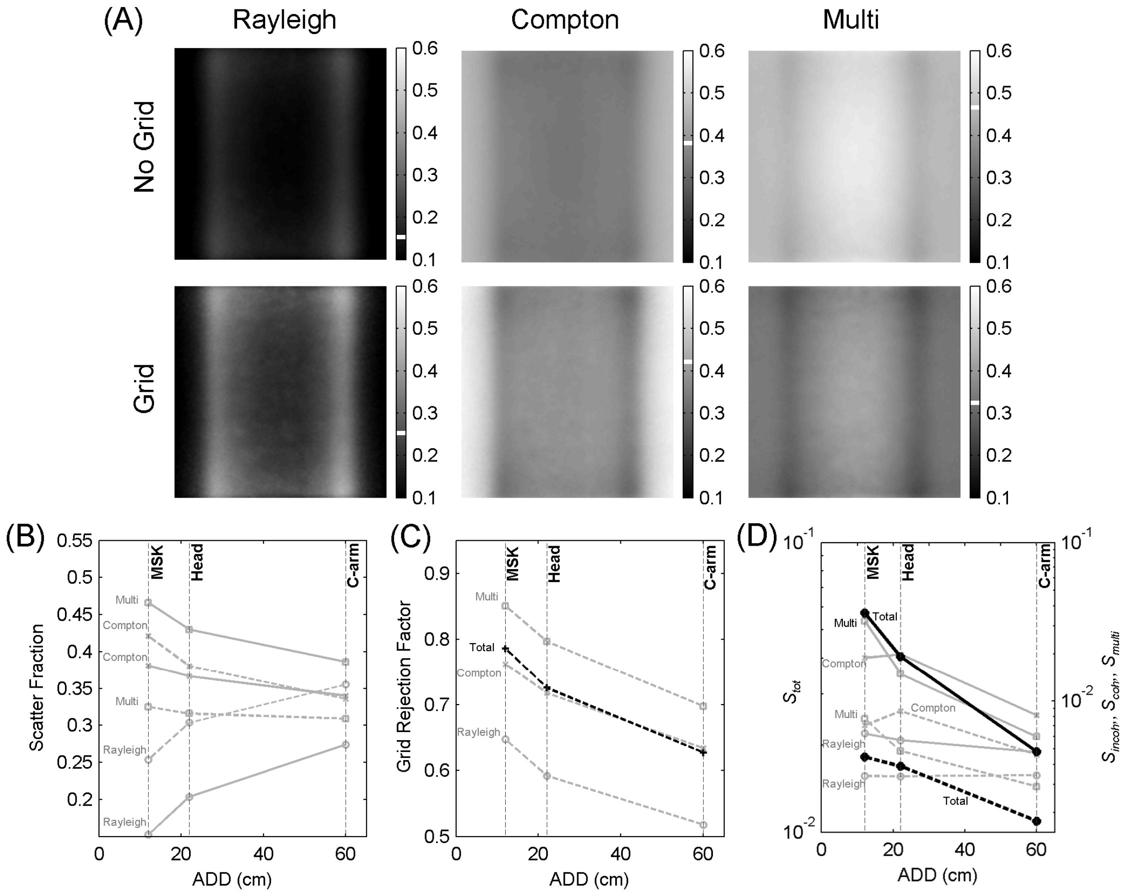

Figure 6.6. (A) Distribution (in the plane of the detector) of the fraction of total scatter associated with individual scatter components for MSK CBCT. (B) Fraction of various scatter components versus ADD. (C) Grid rejection factor (i.e., fraction of a given scatter component removed from the total) for each component. (D) Gain-corrected magnitude of total scatter, S_{tot} (left vertical axis) and of all three scatter components S_{incoh}, S_{coh}, and S_{multi} (right vertical axis). Solid lines: configuration without a grid, dashed lines: configuration with a grid, black lines: total scatter, gray lines: individual scatter components.

Introduction of a grid reduces the total scatter and changes the relative contributions of scatter components. The fraction of multiple scatter is strongly reduced, but there is a nearly two-fold increase in the relative contribution of Rayleigh scatter, reflecting lower grid efficiency for forward-directed scattered photons. By comparison, the fraction of Compton scatter is not as strongly influenced by the presence of a grid.

Figures 6.6(B-D) show the contributions of various scatter components more generally versus system geometry (ADD) showing the MSK, Head, and C-arm configurations specifically for the 16 cm Common Phantom. Figure 6.6(B) shows that the fraction of each scatter component –Compton, Rayleigh, and multiple– at the center of the detector depends on the scattering angle: Compton and multiple scatter components decrease with longer geometries, but the relative contribution of Rayleigh scatter increases significantly (with or without a grid). Figure 6.6(C) shows that the efficiency of the grid –i.e., the fraction of a given scatter component rejected– similarly depends on geometry: increasing ADD –i.e., air gap– increases the relative contribution of forward-directed scatter components –i.e., low-angle Compton and Rayleigh scatter– and results in lower grid efficiency for the more extended geometries (e.g., C-arm). Finally, figure 6.6(D) shows the relative contribution of each scatter component by comparing the magnitude of the total scatter –air scan-normalized, to allow comparison in a manner that corrects for inverse-square law– and the three components therein. The magnitude of Rayleigh scatter –corrected for inverse-square law– is almost constant across the various CBCT configurations for the fixed 16 cm phantom. The more broad angular distributions of Compton and multiple scatter diminish the amplitude of these scatter components with increasing air gap, and the same is observed for the total scatter.

6.3.3 Scatter in various CBCT configurations: Realistic anatomical phantoms

To extend and test the results above for the idealized Common Phantom within a more anatomically realistic context, projections of realistic murine and anthropomorphic phantoms were simulated for the same CBCT configurations in table 6.I. Figure 6.7 shows central axial slices of reconstructions for each phantom and scanner configuration. Overall, we note results consistent with those obtained for the Common Phantom; namely, that both the magnitude of scatter artifacts and the degree of improvement obtained through the incorporation of a horizontal grid are more pronounced for the compact geometries –MSK and Head– and/or large objects –C-arm

Thorax and Linac Pelvis–. Complex bone anatomy in the realistic phantoms underscores the magnitude of streak artifacts caused by scatter and illustrates the limited ability of grids to reduce high-frequency artifacts associated with low-angle scatter. Such strong sensitivity to bias caused by residual scatter suggests that applications involving visualization in areas near bone structures would especially benefit from some form of additional scatter correction (e.g., a high-fidelity scatter correction algorithm, perhaps based on Monte Carlo simulation). The results of figure 6.7 also extend those of figures 6.4-6.6 in anatomical contexts not approximated by the Common Phantom –viz., the C-arm configuration with a large body site (the Thorax) and the Linac configuration for imaging of a large and more highly attenuating site (the Pelvis)– each with lateral truncation. For the C-arm Thorax, increased scatter fractions are most clearly observable as a loss of quantitative accuracy in the bones compared to imaging a smaller subject as in C-arm Head. In the Linac Pelvis case, streak artifacts and other image nonuniformities are introduced in addition to cupping, despite a smaller fraction of bone in the volume compared to, for example, the head.

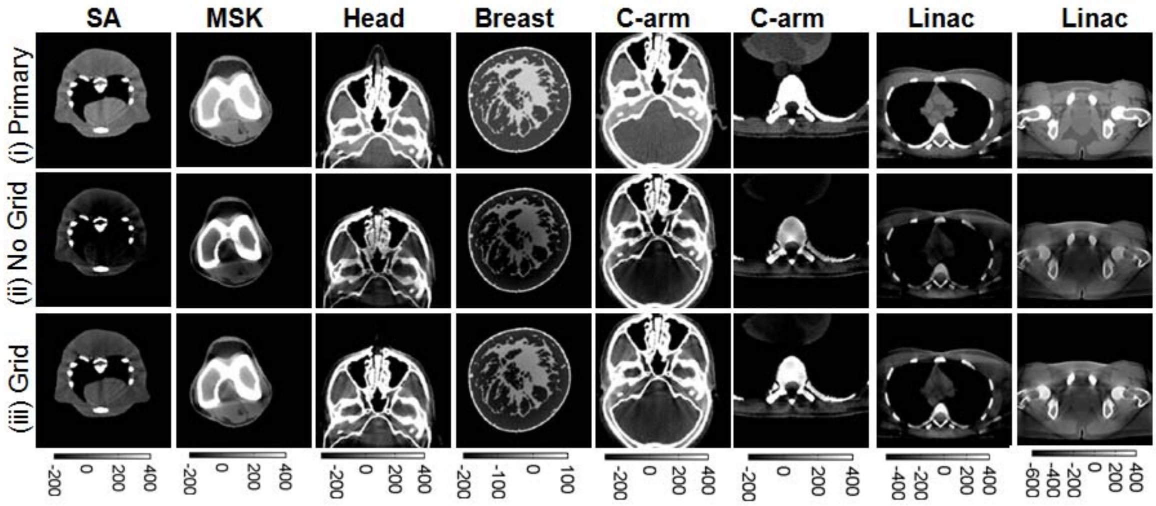

Figure 6.7. Axial reconstructions of the anatomical phantoms for the CBCT configurations in Table I. (i) Reconstructions of primary-only projection data. (ii) Reconstructions with scatter included (without an antiscatter grid). (iii) Reconstructions with primary+scatter and an antiscatter grid.

Finally, figure 6.8 shows air-scan-normalized primary and total scatter distributions in anterior-posterior (AP) projections of the realistic anatomical phantoms for each CBCT configuration. For every geometrical configuration the images show that incorporation of a grid reduces the mean intensity of scatter signal, accompanied by an increase in the relative contribution of forward-directed scatter components –i.e., Rayleigh and some single-scatter Compton–. For the horizontal grid orientation, spatial distributions of Rayleigh, Compton, and multiple scatter are shown. Rayleigh scatter distribution exhibits more high-frequency structural information –arising mainly from self-absorption– compared to other scatter components, which present a relatively slowly varying characteristic. The increase in the relative contribution of Rayleigh scatter upon the introduction of a grid therefore results in a scatter distribution exhibiting more pronounced high-frequency structural content. Figure 6.8 demonstrates that the heterogeneity in the total scatter field in the presence of a grid largely follows that of the coherent scatter distribution. The increase in high-frequency content of both coherent and total scatter distributions is most pronounced for geometries with a shorter air gap (compare, for example, the Head and C-arm cases for the same anthropomorphic head in figure 6.8), reflecting the role of an extended geometry not only in decreasing the magnitude of scatter but also in effectively "blurring" the spatial distribution of scatter as a consequence of increased distance from scattering positions.

Figure 6.8 demonstrates an additional consideration in the orientation of the antiscatter grid relative to the axis of rotations: "horizontal" (as in all previous results) in which the grid lines are orthogonal to the axis of rotation; and "vertical" in which the grid lines are parallel to the axis of rotation. The particular shape of the resulting scatter distribution depends strongly on grid orientation. The "vertical" grid orientation is aligned parallel to highly attenuating structures in several cases –e.g., the spine (for the SA, C-arm Thorax, and Linac Thorax cases) and the femur or tibia (for the MSK case)– and thus preferentially rejects scattered photons generated from outside the shadow of those structures. The vertical grid orientation thus exacerbates the effects of low-angle scatter and self-absorption and results in a scatter distribution with significantly greater high-frequency content compared to the horizontal grid orientation. Incorporation of a grid –and the particular orientation of the grid on the detector– therefore challenges the conventional, often-invoked assumption that x-ray scatter distributions follow a slowly varying (low-frequency) distribution that can be simply modeled as a slowly varying (or constant) function in scatter correction algorithms.

The magnitude of various scatter components and the overall SPR are quantified in the right column of figure 6.8 using box plots summarizing the distributions in the detector plane in the shadow of the object. As hypothesized from the Common Phantom results, the more compact configurations –i.e., shorter air gaps– suffer increased scatter magnitude for all components, and increased relative contributions of Compton and multiple scatter for objects of similar size. This effect is illustrated, for example, by comparison of the otolaryngology Head scanner configuration (3rd row of figure 6.8) and the C-arm Head (5th row of figure 6.8), where the former contends not only with higher magnitudes of all scatter components (and total scatter and SPR) but also a greater heterogeneity (high-frequency content) in the scatter distribution. This general trend of reduced scatter with increased air gap is somewhat mitigated by self-absorption in the object: compare the Head and Breast configurations, where total scatter is lower for the Head scanner (0.015 vs. 0.024, respectively), despite a shorter ADD (220 mm vs. 320 mm, respectively). For a fixed geometry –e.g., the C-arm or Linac–, the total scatter magnitude, SPR, and fraction of multiple scatter are determined by the volume of the irradiated subject –e.g., comparing the C-arm Head and C-arm Thorax (5th and 6th rows of figure 6.8)–. Compared to multiple scatter, the fraction of coherent and incoherent scatter appears to be fairly independent of object size for a fixed system geometry, e.g., the ratio $<S_{incoh}>/<S_{tot}>$ changes from 0.30 for C-arm Head to 0.29 for C-arm Thorax, whereas $<S_{multi}>/<S_{tot}>$ changed from 0.36 for C-arm Head to 0.45 for C-arm Thorax. Similarly, for the Linac configuration, $<S_{incoh}>/<S_{tot}> = 0.31$ for the thorax and 0.28 for the pelvis, compared to $<S_{multi}>/<S_{tot}> = 0.49$ for the thorax and 0.56 for pelvis.

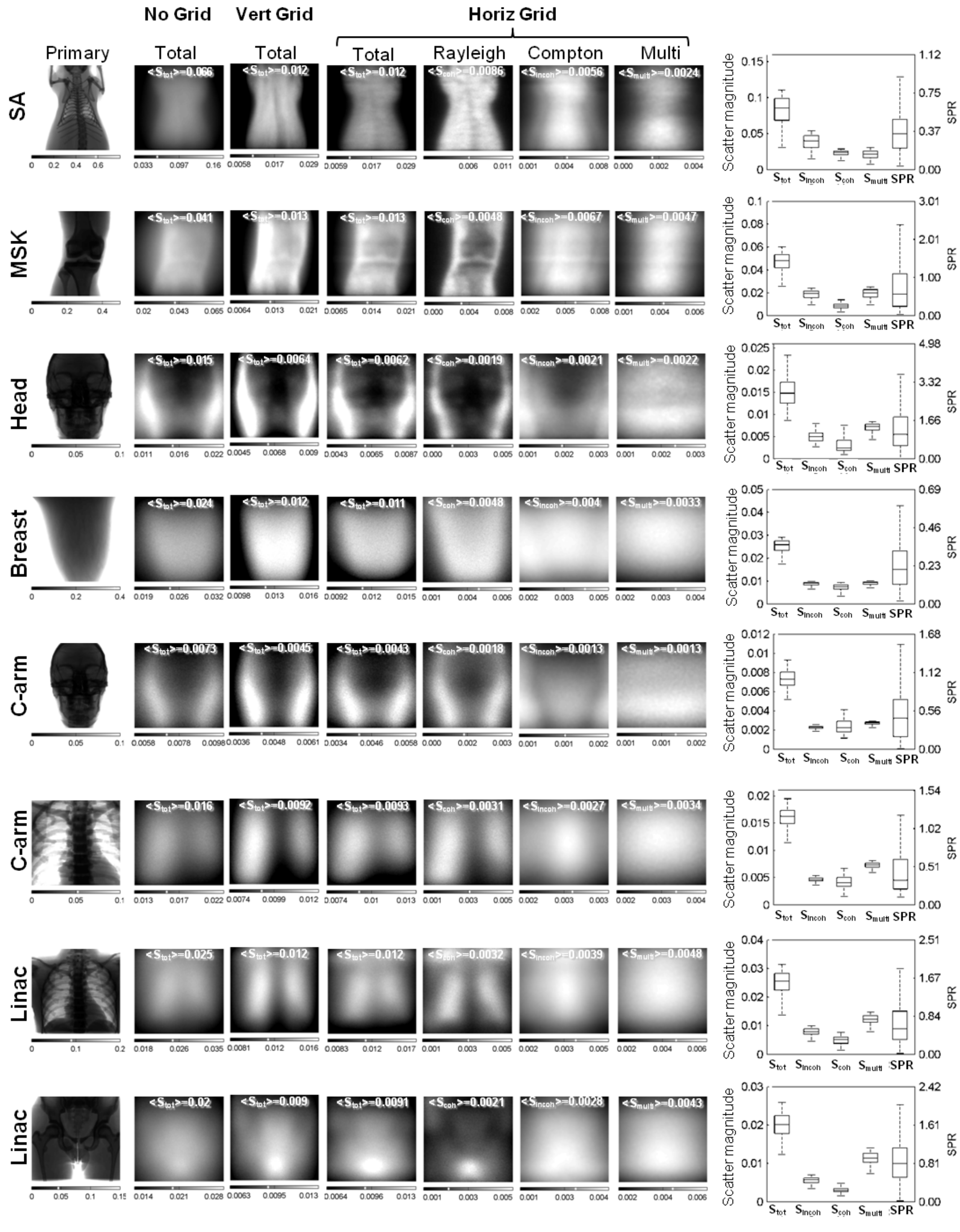

Figure 6.8. Distributions of primary, and total and individual scatter components at the detector for various scanner configurations and anatomical sites. Primary and total scatter distributions are shown without and with a grid (both for vertical and horizontal grid orientations). Individual scatter components are shown for the horizontal grid orientation only. The mean total scatter magnitude computed across the detector plane is superimposed on each distribution. The right column displays the SPR (right vertical axis) and gain-corrected intensities of each component (left vertical axis) for gridless configurations.

6.4 Discussion and conclusions

In this chapter we studied the quantity and spatial properties of scattered radiation for a representative range of CBCT configurations. The effects of scatter in image quality were also assessed.

We found a close relation between the geometry of a system and the properties of scatter. In particular, scatter in compact systems –i.e. those with a short ADD– admit scattered photons with a broad angular distribution making the scatter in these system to contain a large quantity of Compton and multiple scatter. The broad angular distribution of scatter in these systems makes antiscatter grids more effective for compact systems due to the angular dependence of the rejection factor of the grid. On the contrary, systems with a larger ADD –such as the Breast, C-arm and Linac configurations– showed a lower overall scatter and a larger relative contribution of Rayleigh scatter.

Grids modify the relative contributions of scatter components and spatial distribution of scatter: forward-directed photons –Rayleigh and single-scatter Compton– are more likely to be transmitted, shifting the spatial distribution towards higher-frequency structure. The orientation of grid lamellae also affects the shape of scatter distributions, which are more uniform for grid lines perpendicular to the dominant orientation of highly attenuating bony structures in the sample such as the femur and tibia in the MSK configuration.

Cupping artifacts induced by scatter can be removed by grids causing an improvement in contrast; both effects are more pronounced for short air gaps and for large irradiated volumes, where grids are generally more efficient. Despite the stronger relative effect of grids –i.e., improvement in contrast and uniformity– for geometries with short air gaps, the absolute magnitude of residual cupping and contrast loss for such configurations is often larger than or comparable to systems with large air gap without a grid. Analysis of CNR shows that even if grids effectively remove scatter, the CNR at fixed dose can be degraded compared to gridless acquisition due to absorption of primary radiation. Geometries with large air gaps benefit from grids in terms of CNR only for the largest subjects with high SPR. Scatter-induced streak artifacts are not effectively removed by grids, indicating a strong sensitivity to residual bias in the detector signal behind highly attenuating structures and suggesting a need for additional software corrections even in the presence of a grid.

The current study employed a common antiscatter grid of intermediate weight (grid ratio 10:1) and Al interspacers for all CBCT configurations. Other grid designs may offer potential advantages. The results outlined in this study can help to identify grid parameters that are most likely to yield improved performance as a function of geometry and thus offer a guide to optimize grid design for particular imaging tasks. For example the increase of primary transmission –while maintaining scatter rejection– is likely to yield greater benefit for more extended configurations with a long air gap. For compact configurations, a slight reduction in primary transmission –e.g., by increasing the grid ratio– may be acceptable, since the gain in CNR at fixed dose with the standard grid is already high. Finally, for grids with spatially varying grid ratio (and/or pitch) the images of figure 6.8 illustrate not only where in the image scatter is highest but also how the various scatter components –and angle of incidence– vary across the projection. The current work did not include bowtie filters in the simulation, which are in themselves a subject of research and are likely to be of greater benefit in some configurations than others. Other authors have shown that for some configurations, bowties are beneficial in terms of SPR reduction and image uniformity [118, 210, 245, 255]. Bowties were omitted from the current study because they are not commonly used in all CBCT configurations, to avoid further increasing the already large parameter space, and to maintain the focus of the current work on effects of system geometry in and of itself. Similarly, the simulations did not account for the effects of finite focal spot size. In particular, there is a trade-off between scatter reduction due to extended air gap and the associated increase in focal spot blur due to larger magnification [33-34]. Recognizing the importance of this trade-off in system design, the current study focused on specific CBCT configurations where system geometry has already been established.

The results presented here corroborate several findings from previously reported experimental and simulation studies of individual configurations. Colijn et al. [195] used Monte Carlo methods to investigate scatter in small animal systems, using a configuration with similar ADD to that assumed above (51 mm). Their results indicated SPR of 0.2-0.35 for water phantoms (60 mm diameter) and a realistic rat phantom, and a cupping level of 10-15%, whereas we found SPR of 0.35 for a rat phantom and cupping of 20%. While direct comparison is not possible due to differences in x-ray spectra –100 kVp in [195] vs. 60 kVp in this work– and size of the objects both studies indicate that scatter is a significant issue in small animal imaging, despite the small size of the subject. This is most directly attributable to short air gaps employed in SA CBCT to accommodate low power sources needed to reduce the focal-spot size and achieve the high resolution required for small-animal imaging. The MSK extremities CBCT configuration is another example of a compact geometry with short object-detector distance, so chosen to allow weight-bearing imaging in a natural standing stance [8]. Results indicate that extremities CBCT is likely to benefit from the incorporation of a grid, which provides a reduction in cupping and SPR larger than 50%, and improves CNR with no increment in dose. This is in agreement with earlier experimental studies [8] that showed ~20% improvement in soft-tissue CNR and 50% reduction in cupping in cylindrical phantoms and cadaveric knees when using antiscatter grids. Compared to other compact CBCT configurations, the Breast geometry is characterized by an extended ADD of 32 cm and provides a more favorable geometry for scatter management. As shown in figure 6.4, this ADD corresponds to the transition between the region of steep SPR reduction and the region of more modest gains from further increases in air gap. We found SPR ~0.5 for a cylindrical 14 cm phantom and for a realistic breast phantom. CNR decreased with application of a grid despite a 50% reduction in SPR and a 5-10% increase in contrast. This is similar to the experimental results of Kwan et al. [255], who found SPR of 0.5, and 2-fold reduction in SPR and 18% increase in contrast with a 10:1 grid, but concluded that grids were not beneficial for their system due to their low (56.5%) primary transmission. Further increase in ADD by 10 cm was not found to significantly reduce SPR for a 14 cm breast, consistent with our finding that the benefits of extended ADD level off at approximately 30-50 cm for a 16 cm cylindrical phantom. Kwan et al. [255] further indicated that a bowtie can be beneficial for scatter mitigation but was not considered in the study described above. Interventional C-arms provided even longer ADD than the Breast configuration (60 cm vs. 32 cm). The results show the C-arm configuration to exhibit similar SPR, cupping, and contrast as breast CBCT, with grids showing no benefit in CNR at constant dose, despite the reduction of artifacts. This is consistent with experimental results of Schafer et al. [41], who showed a ~2-fold improvement in HU accuracy with a grid, accompanied however by a loss of soft-tissue CNR –reaching up to ~40% for a 10:1 grid, depending of the tissue type– and concluded that grids were not beneficial in this configuration. In Kyriakou et al. [250], experimental and Monte Carlo studies of scatter in C-arm CBCT were also reported, showing SPR ~0.5 for a 16 cm PMMA cylinder at 60 cm object-detector distance, and demonstrating the efficacy of increased air gap in scatter, in agreement with the results above. Reduction in SPR and image artifacts with a grid was also shown, but it was concluded that for objects smaller than approx. 16 cm, an increase in dose is needed to maintain the signal-to-noise ratio obtained by a gridless configuration. This agrees with the results of figure 6.5, where grids are shown to improve CNR for C-arm CBCT only for high SPRs. Finally, the Linac CBCT configuration represents a case with a relatively long air gap (ADD=50 cm) but at large body sites likely to generate a high scatter fraction. This is reflected in our finding of high SPR (>2.5) and strong cupping (~20%) for the 28 cm Common Phantom. Grids clearly improve image uniformity and contrast for this embodiment, and the results indicate that they may be beneficial to CNR under conditions of high SPR corresponding to a ~30 cm diameter object. This is similar to the MC results of Lazos et al. [245], where SPR in excess of 2 was shown for some locations behind a pelvis, and a small improvement in CNR (10-20%) at fixed dose was reported for pelvic imaging with a grid. Siewerdsen et al. [256] also showed significant reduction in image artifacts and improvement in contrast when a grid was incorporated in the Linac CBCT configuration but found that the potential benefit of grids in terms of CNR per unit square root dose should consider the tradeoffs among noise and spatial resolution in determining whether a grid was beneficial for a particular imaging task. This result hints at the complexities of assessing the true benefit of antiscatter grids versus a number of other imaging parameters such as spatial resolution, dose, and the imaging task that are somewhat beyond the simple metric of CNR utilized in the current work.

One limitation of the current study is its reliance on the independent atom approximation (IAA) in modeling the Rayleigh scattering process. IAA is commonly assumed in Monte Carlo simulations of x-ray transport, but it neglects interference effects in the Rayleigh form factor [261], which can lead to overestimation of the intensity of coherent scatter, especially at lower x-ray energies [262-264]. To obtain initial insight into the possible effect of such IAA bias on our results, a series of preliminary simulations was carried out. The interference effects were included in the Rayleigh form factor following [264-265], and a single projection of the Common Phantom was simulated for all embodiments with $5x10^7$ photons. The root-mean-square errors due to neglecting interference were computed for all non-zero detector pixels in the Rayleigh scatter distributions and were found to be ~5-11% across all CBCT configurations without a grid. The errors in Rayleigh scatter estimation increased with a grid, reaching ~25% for the lowest-energy spectrum (SA) and were ~13-20% for configurations utilizing a higher-energy beam.

Summarizing, the results reinforce the observation that maintaining a relatively long ADD is the best primary defense against scatter when permitted by clinical constraints, the desired scanner footprint, source power, and considerations of spatial resolution. For some CBCT configurations and imaging tasks, geometry alone may provide sufficient scatter reduction to obviate the need for any additional mechanisms for scatter rejection or algorithmic correction; in fact, scatter rejection by means of a grid may be detrimental to CNR at fixed dose in the embodiments characterized by longer air gaps. Even when grids are employed, there may be a need for additional software correction of the remaining scatter, especially in applications relying on quantitative accuracy in HU for purposes of dose calculation or quantitative CT. Such correction methods should account for the often highly heterogeneous scatter distributions in the presence of antiscatter grids.

7 Conclusions

The work presented in this thesis contributes to the body of knowledge on CBCT and CBμCT imaging, in the particular fields of CBμCT systems design and optimization, development of CBCT and CBμCT ultra-fast Monte Carlo simulation, studies of the properties and impact in image quality of scatter in CBCT, and investigation of the effect of the dynamic range of flat-panel detectors in image quality and in methods to extend this dynamic range.

Getting into details, chapter 2 presents a new CBμCT system with variable geometrical configuration combined with a molecular imaging system, and its optimization process for two different imaging tasks. The optimization of the acquisition protocol for soft-tissue imaging, taking into account the response of the detector, yielded better CNRD values in soft-tissue for x-ray source voltages in the range of 65 to 70 kVp and using copper filtration. This result, based on previous findings by Hupfer et al. [173] that found constant CNRD for voltages above 50 kV for ideal detectors, showed that lower voltage values and Al added filtration commonly used in small-animal systems [266-269] are appropriate for bone imaging but may not be optimal for soft-tissue imaging tasks, as pointed, for instance, for the case of the lung in [270]. The presented system and its individual components were evaluated, obtaining limits for the resolution as a function of the geometrical configuration, dose estimation as a function of the imaging protocol and image quality limits per unit dose for the different protocols.

The next part of the thesis proposes a method to increase dynamic range of flat-panel detector, and evaluate the effect on the dynamic range of the different noise sources of flat-panel detectors and the effect of the limited dynamic range in image quality. The presented method is based on the acquisition and later combination of two datasets with different exposure values. In chapter 3 the dynamic range extension method is presented and its performance for generic flat-panel detectors is evaluated by mean of simulated data. Simulated data for the evaluation is obtained using the noise and signal characteristics of a real flat-panel detector that is characterized in terms of noise and dynamic range in chapter 3. The dynamic range extension method is assessed on real data acquired using the characterized detector, showing an effective increase of the dynamic range with a subsequent increase in image quality compared to frame averaging delivering the same dose.

The next two chapters of the thesis deal with the development of simulation tools for CBCT imaging and for CBμCT microfocus sources. Chapter 4 presents a new empirical polynomial model for the generation of x-ray spectra in microfocus x-ray sources, based on the analogous TASMIP model for the generation of spectra for sources used in radiology [55] and mammography [218]. The spectra generation model was validated against absolute exposure and attenuation measurements, showing estimation errors in line with well established models for the generation of radiologic spectra, providing a new simple tool for the generation of microfocus spectra.

In chapter 5 the inclusion of variance reduction techniques in the publicly available x-ray Monte Carlo simulation package MC-GPU showed to improved the performance of the code by a factor of ~35 for the estimation of scatter data in CBCT. The code was modified to allow the use of polychromatic spectra, energy-dependent detector response, and antiscatter grids based on an analytical model. The photon transport process of the Monte Carlo engine was redesigned to maximize the performance of the photon splitting and forced detection techniques in an environment where photons are tracked in parallel, since the classic implementation of photon tracking used in MC-GPU combined with the classic implementation of photon splitting and forced detection greatly diminished performance. The simulation platform was completed by adding an analytical polychromatic projector for the estimation of primary signal. The modified Monte Carlo engine showed no bias with respect to non-accelerated version of MC-GPU and good agreement with experimental data. Its applicability to accurate scatter correction was also demonstrated by applying a single iteration of a Monte Carlo based scatter correction method [35] to experimental CBμCT data. Scatter corrected data using the accelerated engine was obtained in ~15 minutes using an average gaming GPU, being already close to acceptable correction times for regular practice.

The last part of the thesis (chapter 6) presented a detailed study of the properties of scatter distributions in CBCT, using the Monte Carlo simulation platform presented in chapter 5. The study explored a range of geometrical configurations not covered by previous studies in the literature and presented not only distributions and effect of total scatter, but also distributions for individual components. The effect of antiscatter grids in the reduction of scatter effects, in noise, and in the spatial distribution of scatter components was also studied.

Analysis of the simulated data showed that long air gaps are the best technique to reduce the impact of scatter in image quality but their use is limited to the constraints of the system in terms of footprint, x-ray power, FOV, etc. The effect of antiscatter grids is contradictory, since they showed good performance at reducing scatter but at the cost of a higher noise due to the reduction of primary radiation that reduced CNR for a significant number of configurations. Their use is advised under some circumstances but they are by no means a general scatter correction method that can be directly included in CBCT systems without a thorough evaluation of their effects in the particular application. In addition grids showed a poor performance for the reduction of forward directed scatter and streaks artifacts.

Results showed that even using a grid, applications requiring high image quality would need the use of further scatter corrections, encouraging the development of methods such as the one presented in chapter 5.

Summarizing, the main contributions of this thesis are:

1. The development of new CBμCT system combined with an FDOT system, with variable geometrical configuration and its detailed assessment for bone and soft-tissue imaging. The development consisted of all the hardware and software components, including a GPU accelerated FDK reconstructor, and the calibration tools, with a method for detector defects calibration and a method for the calibration of the alignment between consecutive bed positions new to the literature.
2. The optimization of the acquisition protocol for CBμCT systems based on flat-panel detectors with CsI:Tl scintillators for bone and soft-tissue imaging tasks.
3. The development of a method to increase the dynamic range of flat-panel detectors, and its assessment in theoretical and experimental imaging scenarios.
4. A new model for the generation of x-ray spectra for microfocus sources, based on an existent empirical model for radiology and mammography sources, and its validation against experimental data.
5. A new accelerated Monte Carlo simulation platform for scatter in CBCT based on publicly available code to which variance reduction techniques were added, achieving large improvements in performance with no bias in the estimated quantities.

6. The design of a Monte Carlo based scatter correction based on the developed simulation platform and its validation with experimental data, obtaining corrected volumes within a reasonable computation time.
7. The study of the quantity and properties of scatter in a complete range of CBCT embodiments and the benefits and drawbacks offered by antiscatter grids. The study included detailed descriptions of the spatial distribution of scatter and relates them to the nature of the artifacts shown by the reconstructed volume and to the performance of antiscatter grids.

A1 Appendix 1

In this appendix to the thesis we report the polynomial coefficients for the model described in chapter 4 to generate spectra in microfocus x-ray sources. Table A.I shows the value of the coefficients for the different energy bins.

Table A.I. Polynomial coefficients for the modified TASMIP model for microfocus x-ray sources

Photon Energy (keV)	a_0	a_1	a_2	a_3
6.00	-6.39E+01	7.01E+00	1.07E-01	-1.15E-03
7.00	-5.98E+02	7.02E+01	5.28E-01	-6.39E-03
8.00	-1.02E+04	8.95E+02	2.61E+01	-1.87E-01
9.00	-1.59E+04	1.32E+03	3.13E+01	-2.10E-01
10.00	-1.25E+04	1.29E+03	-3.42E+00	-5.21E-03
11.00	-3.47E+04	3.34E+03	-1.27E+01	1.63E-02
12.00	-3.32E+04	3.23E+03	-2.99E+01	1.12E-01
13.00	-4.65E+04	4.18E+03	-3.65E+01	1.39E-01
14.00	-4.51E+04	4.13E+03	-5.25E+01	2.40E-01
15.00	-4.47E+04	3.77E+03	-4.38E+01	1.87E-01
16.00	-4.90E+04	3.93E+03	-4.57E+01	1.91E-01
17.00	-4.72E+04	3.47E+03	-3.37E+01	1.31E-01
18.00	-4.75E+04	3.26E+03	-2.85E+01	1.05E-01
19.00	-4.94E+04	3.25E+03	-2.95E+01	1.10E-01
20.00	-5.54E+04	3.53E+03	-3.32E+01	1.26E-01
21.00	-5.70E+04	3.45E+03	-3.09E+01	1.13E-01
22.00	-5.98E+04	3.46E+03	-2.99E+01	1.07E-01
23.00	-6.05E+04	3.32E+03	-2.73E+01	9.58E-02
24.00	-6.24E+04	3.27E+03	-2.59E+01	8.91E-02
25.00	-6.21E+04	3.07E+03	-2.24E+01	7.32E-02
26.00	-6.23E+04	2.92E+03	-1.96E+01	5.98E-02
27.00	-6.28E+04	2.78E+03	-1.72E+01	4.78E-02
28.00	-6.43E+04	2.70E+03	-1.54E+01	3.87E-02
29.00	-6.31E+04	2.57E+03	-1.41E+01	3.63E-02
30.00	-6.26E+04	2.47E+03	-1.30E+01	3.37E-02
31.00	-6.27E+04	2.43E+03	-1.32E+01	3.74E-02

Photon Energy (keV)	a_0	a_1	a_2	a_3
32.00	-6.40E+04	2.42E+03	-1.32E+01	3.84E-02
33.00	-6.32E+04	2.30E+03	-1.19E+01	3.39E-02
34.00	-6.26E+04	2.20E+03	-1.06E+01	2.95E-02
35.00	-6.36E+04	2.17E+03	-1.05E+01	2.92E-02
36.00	-6.49E+04	2.16E+03	-1.05E+01	2.95E-02
37.00	-6.58E+04	2.13E+03	-1.00E+01	2.75E-02
38.00	-6.73E+04	2.11E+03	-9.81E+00	2.64E-02
39.00	-6.64E+04	2.04E+03	-9.21E+00	2.49E-02
40.00	-6.86E+04	2.08E+03	-1.01E+01	2.94E-02
41.00	-6.50E+04	1.92E+03	-8.52E+00	2.42E-02
42.00	-6.44E+04	1.86E+03	-7.71E+00	2.07E-02
43.00	-5.58E+04	1.45E+03	-2.63E+00	0.00E+00
44.00	-5.52E+04	1.39E+03	-2.28E+00	0.00E+00
45.00	-7.24E+04	2.02E+03	-1.03E+01	3.23E-02
46.00	-7.20E+04	1.96E+03	-9.65E+00	2.87E-02
47.00	-6.73E+04	1.73E+03	-6.75E+00	1.73E-02
48.00	-6.59E+04	1.61E+03	-5.33E+00	1.17E-02
49.00	-7.36E+04	1.88E+03	-8.72E+00	2.47E-02
50.00	-8.38E+04	2.23E+03	-1.31E+01	4.14E-02
51.00	-7.86E+04	2.05E+03	-1.14E+01	3.58E-02
52.00	-7.52E+04	1.89E+03	-9.75E+00	2.97E-02
53.00	-7.78E+04	1.96E+03	-1.06E+01	3.29E-02
54.00	-8.21E+04	2.08E+03	-1.21E+01	3.86E-02
55.00	-9.11E+04	2.36E+03	-1.55E+01	5.20E-02
56.00	-7.73E+04	1.85E+03	-9.80E+00	3.10E-02
57.00	-2.90E+04	1.22E+02	7.78E+00	-1.25E-02
58.00	1.65E+04	-1.48E+03	2.38E+01	-4.98E-02
59.00	5.23E+04	-2.74E+03	3.62E+01	-7.66E-02
60.00	8.52E+04	-3.90E+03	4.73E+01	-9.88E-02
61.00	1.05E+04	-1.31E+03	2.12E+01	-3.92E-02
62.00	-5.39E+04	8.75E+02	1.62E-01	0.00E+00
63.00	-5.99E+04	1.04E+03	-1.19E+00	0.00E+00
64.00	-9.64E+04	2.29E+03	-1.51E+01	4.80E-02
65.00	-1.21E+05	3.06E+03	-2.34E+01	7.73E-02
66.00	-1.00E+05	2.33E+03	-1.53E+01	4.69E-02
67.00	-4.54E+04	4.82E+02	3.43E+00	-5.47E-03
68.00	-1.18E+03	-1.01E+03	1.83E+01	-4.39E-02
69.00	-4.93E+04	5.65E+02	2.34E+00	0.00E+00

Photon Energy (keV)	a_0	a_1	a_2	a_3
70.00	-1.62E+05	4.20E+03	-3.57E+01	1.24E-01
71.00	-1.28E+05	3.11E+03	-2.39E+01	7.82E-02
72.00	-6.87E+04	1.19E+03	-3.14E+00	0.00E+00
73.00	-7.34E+04	1.29E+03	-3.74E+00	0.00E+00
74.00	-1.34E+05	3.20E+03	-2.41E+01	7.11E-02
75.00	-1.72E+05	4.37E+03	-3.62E+01	1.13E-01
76.00	-1.53E+05	3.77E+03	-3.00E+01	9.18E-02
77.00	-7.88E+04	1.35E+03	-4.14E+00	0.00E+00
78.00	-7.92E+04	1.34E+03	-4.12E+00	0.00E+00
79.00	-1.67E+05	4.11E+03	-3.33E+01	1.02E-01
80.00	-1.56E+05	3.69E+03	-2.87E+01	8.54E-02
81.00	-2.12E+05	5.44E+03	-4.68E+01	1.47E-01
82.00	-8.26E+04	1.37E+03	-4.37E+00	0.00E+00
83.00	-7.08E+04	1.10E+03	-2.86E+00	0.00E+00
84.00	-7.87E+04	1.24E+03	-3.58E+00	0.00E+00
85.00	-2.97E+05	7.88E+03	-7.08E+01	2.26E-01
86.00	-7.88E+04	1.23E+03	-3.57E+00	0.00E+00
87.00	-7.69E+04	1.17E+03	-3.27E+00	0.00E+00
88.00	-8.16E+04	1.25E+03	-3.59E+00	0.00E+00
89.00	-8.65E+04	1.34E+03	-4.04E+00	0.00E+00
90.00	-4.27E+05	1.14E+04	-1.04E+02	3.27E-01
91.00	-5.90E+05	1.63E+04	-1.53E+02	4.91E-01
92.00	-4.52E+04	5.00E+02	0.00E+00	0.00E+00
93.00	-4.56E+04	4.97E+02	0.00E+00	0.00E+00
94.00	-4.54E+04	4.89E+02	0.00E+00	0.00E+00
95.00	-7.41E+05	2.01E+04	-1.84E+02	5.73E-01
96.00	-1.31E+06	3.67E+04	-3.46E+02	1.10E+00
97.00	-4.70E+04	4.90E+02	0.00E+00	0.00E+00
98.00	-4.85E+04	5.00E+02	0.00E+00	0.00E+00
99.00	-2.61E+06	7.30E+04	-6.86E+02	2.16E+00
100.00	-1.57E+05	2.53E+03	-9.54E+00	6.79E-12
101.00	-5.34E+06	1.49E+05	-1.40E+03	4.36E+00
102.00	-1.23E+07	3.46E+05	-3.24E+03	1.01E+01
103.00	-1.40E+07	3.93E+05	-3.66E+03	1.14E+01
104.00	-1.72E+07	4.78E+05	-4.44E+03	1.37E+01
105.00	-5.86E+04	5.58E+02	-2.51E-12	0.00E+00
106.00	-4.99E+07	1.38E+06	-1.27E+04	3.89E+01
107.00	-2.23E+06	4.05E+04	-1.84E+02	0.00E+00

Photon Energy (keV)	a_0	a_1	a_2	a_3
108.00	-7.35E+04	6.81E+02	0.00E+00	0.00E+00
109.00	4.50E+02	0.00E+00	0.00E+00	0.00E+00
110.00	0.00E+00	0.00E+00	0.00E+00	0.00E+00

Publications

Papers published in international journals and book chapters

- **A. Sisniega**, W. Zbijewski, A. Badal, I. S. Kyprianou, J. W. Stayman, J. J. Vaquero, and J. H. Siewerdsen, "Monte Carlo study of the effects of system geometry and antiscatter grids on cone-beam CT scatter distributions," *Med Phys,* **40**, 051915, 2013.
- **A. Sisniega**, J.J. Vaquero, M. Desco, " Design and Assessment Principles of Semiconductor Flat-Panel Detector-Based X-Ray Micro-CT Systems for Small-Animal Imaging," in *Integrated Microsystems: Electronics, Photonics, and Biotechnology*, K. Iniewski, Ed., ed New York: CRC Press, 309-335, 2012.
- M. Abella, J.J. Vaquero, **A. Sisniega**, J. Pascau, A. Udías, V. García, I. Vidal, M. Desco. "Software architecture for multi-bed FDK-based reconstruction in X-ray CT scanners". *Comput Meth Prog Bio*, **107**(2), 218-232, 2012.
- T. Correia, J. Aguirre, **A. Sisniega**, J. Chamorro-Servent, J. Abascal, J.J. Vaquero, M. Desco, V. Kolehmainen, S. Arridge. "Split operator method for fluorescence diffuse optical tomography using anisotropic diffusion regularisation with prior anatomical information". *Biomed Opt Express*, **2**(9), 2632-2648, 2011.
- E. Lage, J.L. Villena, G. Tapias, N.P. Martínez, M.L. Soto-Montenegro, M. Abella, **A. Sisniega**, F. Pino, D. Ros, J. Pavía, M. Desco, J.J. Vaquero. "A SPECT Scanner for Rodent Imaging Based on Small-Area Gamma Cameras". *IEEE Transactions on Nuclear Science*, **57**(5), 2524-2531, 2010.
- E. Lage, J.J. Vaquero, **A. Sisniega**, S. España, G. Tapias, M. Abella, A. Rodríguez-Ruano, J.E. Ortuño, A. Udías, M. Desco. "Design and performance evaluation of a coplanar multimodality scanner for rodent imaging". *Phys Med Biol*, **54**(18), 5427-5441, 2009.
- J.J. Vaquero, S. Redondo, E. Lage, M. Abella, **A. Sisniega**, G. Tapias, M.L. Soto-Montenegro, M. Desco. "Assessment of a New High-Performance Small-

Animal X-Ray Tomograph". *IEEE Transactions on Nuclear Science*, **55**(3), 898-905, 2008.

- C. Chavarrías, J.J. Vaquero, **A. Sisniega**, A. Rodríguez-Ruano, M.L. Soto-Montenegro, P. García-Barreno, M. Desco. "Extraction of the respiratory signal from small-animal CT projections for a retrospective gating method". *Phys Med Biol*, **53**(17), 4683-4695, 2008.

Papers submitted or in preparation for international journals

- **A. Sisniega**, M. Abella, M. Desco, J.J. Vaquero, "Expansion of the dynamic range of x-ray flat panel detectors: a dual-exposure technique," *Phys Med Biol*, (under revision), 2013.
- J.F. Abascal, M. Abella, **A. Sisniega**, J.J. Vaquero, M. Desco, "Investigation of different sparsity transforms for the PICCS algorithm in small-animal respiratory gated CT," *Phys Med Biol*, (submitted), 2013.
- **A. Sisniega**, M. Desco, J.J. Vaquero, "Modification of the TASMIP model for the simulation of microfocus x-ray sources with tungsten anode," *Med Phys*, (in preparation), 2013.
- **A. Sisniega***, J. Aguirre*, J. Abascal, M. Abella, V. Garcia, J. Chamorro, J. Ripoll, M. Desco, J.J. Vaquero, "Design and characterization of a new hybrid fDOT-XCT tomograph,", (in preparation), 2013.

International conference papers

- **A. Sisniega**, J.F. Abascal, M. Abella, M. Desco, J.J. Vaquero. "Iterative Dual-Energy Raw Data Decomposition for Slow kVp Switching: a Feasibility Study". *Abstract Book IEEE Nuclear Science Symposium and Medical Imaging Conference (NSS/MIC)*, 473, 2012.
- J. Abascal, **A. Sisniega**, C. Chavarrías, J.J. Vaquero, M. Desco, M. Abella. "Investigation of different Compressed Sensing Approaches for Respiratory Gating in Small Animal CT", *IEEE Nuclear Science Symposium and Medical Imaging Conference (NSS/MIC)*, 3344-3346, 2012.
- C. de Molina, **A. Sisniega**, J.J. Vaquero, M. Desco, M. Abella. "Complete scheme for beam hardening correction in small animal computed tomography".

IEEE Nuclear Science Symposium and Medical Imaging Conference Record (NSS/MIC), 3835-3838, 2012.

- W. Zbijewski, **A. Sisniega**, J. J. Vaquero, A. Muhit, N. Packard, R. Senn, D. Yang, J. Yorkston, J. A. Carrino, J. H. Siewerdsen, "Dose and scatter characteristics of a novel cone beam CT system for musculoskeletal extremities," *Proc. SPIE,* **8313**, 831318, 2012.
- **A. Sisniega**, M. Abella, E. Lage, M. Desco, J. J. Vaquero, "Automatic Monte-Carlo Based Scatter Correction For X-ray cone-beam CT using general purpose graphic processing units (GP-GPU): A feasibility study," *IEEE Nuclear Science Symposium and Medical Imaging Conference (NSS/MIC)*, 2011, 3705-3709.
- **A. Sisniega**, J.J. Vaquero, M. Abella, I. Vidal Migallón, E. Lage, M. Desco. "Automated Dual-Exposure Technique to Extend the Dynamic Range of Flat-Panel Detectors Used in Small-Animal Cone-Beam Micro-CT". *IEEE Nuclear Science Symposium and Medical Imaging Conference (NSS/MIC)*, 2948-2950, 2009.
- **A. Sisniega**, J.J. Vaquero, I. Vidal-Migallón, M. Abella, M. Desco. "Expanding the dynamic range of flat-panel detectors used in small-animal cone-beam CT: an automated dual-exposure technique". *Abstract book of European Society for Molecular Imaging (ESMI)*, 177, 2009.
- E. Lage, J. Villena, G. Tapias, A. de Carlos, M. Abella, I. Vidal-Migallón, **A. Sisniega**, M. Desco, J.J. Vaquero. "Development and performance of the small-animal r-SPECT prototype". *Abstract book of European Society for Molecular Imaging (ESMI)*, 170, 2009.
- M. Abella, J.J. Vaquero, **A. Sisniega**, B.W. Reutter, G.T. Gullberg, M. Desco. "Statistical 4D reconstruction of dynamic CT images: preliminary results". *Abstract book of European Society for Molecular Imaging (ESMI)*, 32, 2009.
- E. Lage, J.L. Villena, G. Tapias, I. Vidal-Migallón, M. Abella, **A. Sisniega**, N.P. Martínez, D. Ros, M. Desco, J.J. Vaquero. "rSPECT: A Compact Gamma Camera Based SPECT System for Small-Animal Imaging". *IEEE Nuclear Science Symposium and Medical Imaging Conference (NSS/MIC)*, 3126-3131, 2009.

- M. Abella, J.J. Vaquero, **A. Sisniega**, M.L. Soto-Montenegro, M. Desco. "A new algorithm for ring artifact reduction in cone-beam computed tomography: preliminary results". *Int J CARS*, **3**(Suppl 1): S11-S12, 2008.
- I. Vidal-Migallón, M. Abella-García, **A. Sisniega-Crespo**, J.J. Vaquero-López, M. Desco-Menéndez."Correction of cupping artifact for cone-beam micro-CT imaging". *Int J CARS*, **3**(Suppl 1): S12-S13, 2008.
- C. Chavarrías, J.J. Vaquero, **A. Sisniega**, A. Rodríguez, M.L. Soto-Montenegro, M. Desco."Reduction of respiratory blurring in small-animal CT scans based on a fast retrospective gating method". *Int J CARS*, **3**(Suppl 1): S13-S14, 2008.
- **A. Sisniega**, J.J. Vaquero, E. Lage, A. De Carlos, J.L. Villena, M. Abella, I. Vidal, G. Tapias, J.C. Antoranz, M. Desco. "Comparative Study of Two Flat-Panel X-Ray Detectors Applied to Small-Animal Imaging Cone-Beam Micro-CT". *IEEE Nuclear Science Symposium and Medical Imaging Conference (NSS/MIC)*, 3836-3840, 2008.
- A. Rodríguez-Ruano, J. Pascau, J. Chamorro, **A. Sisniega**, V. García-Vázquez, A. Udías, J.J. Vaquero, M. Desco. "PET/CT Alignment for Small Animal Scanners based on Capillary Detection". *IEEE Nuclear Science Symposium and Medical Imaging Conference (NSS/MIC)*, 3832-3835, 2008.
- C. Chavarrías, J.J. Vaquero, **A. Sisniega**, A. Rodríguez-Ruano, M.L. Soto-Montenegro, M. Desco."Validation of a retrospective respiratory gating method for small-animal CT scanners". *IEEE Nuclear Science Symposium and Medical Imaging Conference (NSS/MIC)*, 4303-4305, 2008.
- J.L. Villena, E. Lage, A. De Carlos, G. Tapias, **A. Sisniega**, J.J. Vaquero, M. Desco. "A Super-Resolution Feasibility Study in Small-Animal SPECT Imaging". *IEEE Nuclear Science Symposium and Medical Imaging Conference (NSS/MIC)*, 4755-4759, 2008.
- I. Vidal-Migallón, M. Abella, **A. Sisniega**, J.J. Vaquero, M. Desco. "Simulation of mechanical misalignments in a cone-beam micro-CT system". *IEEE Nuclear Science Symposium and Medical Imaging Conference (NSS/MIC)*, 5007-5009, 2008.
- J. Aguirre, **A. Sisniega**, J. Ripoll, M. Desco, J.J. Vaquero. "Design and development of a co-planar fluorescence and X-ray tomograph". *IEEE Nuclear*

Science Symposium and Medical Imaging Conference (NSS/MIC), 5412-5413, 2008.

- J. Aguirre, **A. Sisniega**, J. Ripoll, M. Desco, J.J. Vaquero. "Co-Planar FMT-CT". *Online Abstract of 2008 World Molecular Imaging Congress (WMIC),* 333, 2008

National conference papers

- A. Olmo, J.J. Sánchez, **A. Sisniega**, V. García-Vázquez, M. Desco, J.J. Vaquero. "Herramienta automática para calibrado del centro de rotación de un tomógrafo SPECT de animales de laboratorio". *Libro de Actas XXX CASEIB,* 2012.
- C. de Molina, M. Abella, J.J. Vaquero, **A. Sisniega**, M. Desco. "Un nuevo algoritmo para la reducción del artefacto de anillo en tomografía computarizada de pequeño animal". *Libro de Actas XXX CASEIB,* 2012.
- C. de Molina, M. Abella, **A. Sisniega**, J.J. Vaquero, M. Desco. "Corrección empírica de primer y segundo orden del artefacto de endurecimiento de haz en imágenes de micro-TAC". *Resúmenes del XXIX Congreso Anual de la Sociedad Española de Ingeniería Biomédica (CASEIB),* 46, 2011.
- **A. Sisniega**, M. Abella, E. Lage, M. Desco, J.J. Vaquero. "Desarrollo e implementación de una herramienta para el calibrado automático de equipos micro-TAC de haz cónico". *Proceedings del XXVIII Congreso Anual de la Sociedad Española de Ingeniería Biomédica (CASEIB),* 2010.
- I. Vidal Migallón, M. Abella, **A. Sisniega**, J.J. Vaquero, M. Desco. "Corrección del efecto del endurecimiento del haz basada en segmentación de materiales para imágenes de tomografía computarizada". *Libro de Resúmenes del CASEIB,* 103, 2009.
- E. Lage, J. Villena, G. Tapias, I. Vidal-Migallón, M. Abella, **A. Sisniega**, J. Pavía, D. Ros, M. Desco, J.J. Vaquero. "rSPECT: Diseño y evaluación de un sistema SPECT de alta resolución para animales de laboratorio". *Libro de Resúmenes del CASEIB,* 154, 2009.
- **A. Sisniega**, J.J. Vaquero, M. Abella, I. Vidal-Migallón, E. Lage, M. Desco. "Técnica automatizada para la extensión del rango dinámico de

detectores de tipo flat-panel usados en micro-TAC de haz cónico para pequeños animales". *Libro de Resúmenes del CASEIB*, 268, 2009.

- J. Chamorro-Servent, A. Rodríguez-Ruano, J. Pascau, A. Udías, **A. Sisniega**, V. García-Vázquez, J.J. Vaquero, M. Desco. "Alineamiento de sistemas PET/CT para pequeños animales basado en detección de capilares". *Libro de Actas del CASEIB*, 128-130, 2008.
- E. Lage, J.J. Vaquero, **A. Sisniega**, S. España, G. Tapias, A. Udías, V. García, A. Rodríguez-Ruano, M. Desco. "VrPET/CT: Desarrollo y Resultados Iniciales de un Nuevo Tomógrafo Multimodalidad para Animales de Laboratorio". *Libro de Actas del CASEIB*, 213-216, 2008.
- J.L. Villena, E. Lage, A. De Carlos, G. Tapias, **A. Sisniega**, J.J. Vaquero, M. Desco. "Estudio de Viabilidad para la Aplicación de una Técnica de Super-Resolución en Imagen SPECT de Pequeños Animales". *Libro de Actas del CASEIB*, 237-240, 2008.
- J. Aguirre, **A. Sisniega**, J. Ripoll, M. Desco, J.J. Vaquero. "Diseño y desarrollo de un sistema híbrido de Tomografía de Fluorescencia Molecular y CT". *Libro de Actas del CASEIB*, 329-331, 2008.
- A. De Carlos, E. Lage, J.L. Villena, G. Tapias, **A. Sisniega**, J.J. Vaquero, M. Desco. "Diseño e Implementación de una Gammacámara para SPECT de Animales de Laboratorio". *Libro de Actas del CASEIB*, 368-371, 2008.
- I. Vidal-Migallón, M. Abella, **A. Sisniega**, J.J. Vaquero, M. Desco. "Simulación de desalineamientos mecánicos en un sistema micro-CT de haz cónico". *Libro de Actas del CASEIB*, 443-446, 2008.
- **A. Sisniega**, E. Lage, A. De Carlos, J. Villena, M. Abella, I. Vidal, G. Tapias, J.C. Antoranz, M. Desco, J.J. Vaquero. "Estudio Comparativo de Dos Detectores de Rayos X de Tipo Flat-panel Aplicados a Micro-TAC de Haz Cónico para Pequeños Animales". *Libro de Actas del CASEIB*, 505-508, 2008.

Bibliography

[1] W. A. Kalender and Y. Kyriakou, "Flat-detector computed tomography (FD-CT)," *European Radiology,* **17**, 2767-2779, 2007.

[2] C. T. Badea, S. Johnston, B. Johnson, M. Lin, L. W. Hedlund, and G. A. Johnson, "A dual micro-CT system for small animal imaging," *Proc. SPIE,* **6913**, 691342, 2008.

[3] M. J. Paulus, H. Sari-Sarraf, S. S. Gleason, M. Bobrek, J. S. Hicks, D. K. Johnson, J. K. Behel, L. H. Thompson, and W. C. Allen, "A new X-ray computed tomography system for laboratory mouse imaging," *IEEE Transactions on Nuclear Science,* **46**, 558-564, 1999.

[4] J. J. Vaquero, S. Redondo, E. Lage, M. Abella, A. Sisniega, G. Tapias, M. L. S. Montenegro, and M. Desco, "Assessment of a new high-performance small-animal X-ray tomograph," *IEEE Transactions on Nuclear Science,* **55**, 898-905, 2008.

[5] R. Fahrig, R. Dixon, T. Payne, R. L. Morin, A. Ganguly, and N. Strobel, "Dose and image quality for a cone-beam C-arm CT system," *Med Phys,* **33**, 4541-4550, 2006.

[6] J. H. Siewerdsen, D. J. Moseley, S. Burch, S. K. Bisland, A. Bogaards, B. C. Wilson, and D. A. Jaffray, "Volume CT with a flat-panel detector on a mobile, isocentric C-arm: Pre-clinical investigation in guidance of minimally invasive surgery," *Med Phys,* **32**, 241-254, 2005.

[7] S. K. Koskinen, V. V. Haapamaki, J. Salo, N. C. Lindfors, M. Kortesniemi, L. Seppala, and K. T. Mattila, "CT arthrography of the wrist using a novel, mobile, dedicated extremity cone-beam CT (CBCT)," *Skeletal radiology,* **42**, 649-57, 2013.

[8] W. Zbijewski, P. De Jean, P. Prakash, Y. Ding, J. W. Stayman, N. Packard, R. Senn, D. Yang, J. Yorkston, A. Machado, J. A. Carrino, and J. H. Siewerdsen, "A dedicated cone-beam CT system for musculoskeletal extremities imaging: Design, optimization, and initial performance characterization," *Med Phys,* **38**, 4700-4713, 2011.

[9] J. Xu, D. D. Reh, J. P. Carey, M. Mahesh, and J. H. Siewerdsen, "Technical assessment of a cone-beam CT scanner for otolaryngology imaging: Image quality, dose, and technique protocols," *Med Phys,* **39**, 4932-4942, 2012.

[10] L. F. Yu, Y. Zou, E. Y. Sidky, C. A. Pelizzari, P. Munro, and X. C. Pan, "Region of interest reconstruction from truncated data in circular cone-beam CT," *IEEE Transactions on Medical Imaging,* **25**, 869-881, 2006.

[11] R. A. Zoumalan, R. A. Lebowitz, E. Wang, K. Yung, J. S. Babb, and J. B. Jacobs, "Flat panel cone beam computed tomography of the sinuses," *Otolaryngology-Head and Neck Surgery,* **140**, 841-844, 2009.

[12] J. M. Boone, T. R. Nelson, K. K. Lindfors, and J. A. Seibert, "Dedicated breast CT: radiation dose and image quality evaluation," *Radiology,* **221**, 657-67, 2001.

[13] W. T. Yang, S. Carkaci, L. Chen, C. J. Lai, A. Sahin, G. J. Whitman, and C. C. Shaw, "Dedicated cone-beam breast CT: feasibility study with surgical mastectomy specimens," *AJR Am J Roentgenol*, **189**, 1312-5, 2007.

[14] I. S. Grills, G. Hugo, L. L. Kestin, A. P. Galerani, K. K. Chao, J. Wloch, and D. Yan, "Image-guided radiotherapy via daily online cone-beam CT substantially reduces margin requirements for stereotactic lung radiotherapy," *Int J Radiat Oncol Biol Phys,* **70**, 1045-56, 2008.

[15] D. A. Jaffray, J. H. Siewerdsen, J. W. Wong, and A. A. Martinez, "Flat-panel cone-beam computed tomography for image-guided radiation therapy," *Int J Radiat Oncol Biol Phys,* **53**, 1337-49, 2002.

[16] R. Yao, R. Lecomte, and E. S. Crawford, "Small-animal PET: what is it, and why do we need it?," *J Nucl Med Technol,* **40**, 157-65, 2012.

[17] J. Woolfenden and Z. Liu, "Biomedical Significance of Small-Animal Imaging," in *Small-Animal Spect Imaging*, M. Kupinski and H. Barrett, Eds., ed: Springer US, 2005, 1-8.

[18] A. Corlu, R. Choe, T. Durduran, M. A. Rosen, M. Schweiger, S. R. Arridge, M. D. Schnall, and A. G. Yodh, "Three-dimensional in vivo fluorescence diffuse optical tomography of breast cancer in humans," *Opt Express,* **15**, 6696-716, 2007.

[19] V. Ntziachristos, A. Leroy-Willig, and B. Tavitian, *Textbook of in vivo Imaging in Vertebrates*: Wiley, 2007.

[20] P. E. Kinahan, D. W. Townsend, T. Beyer, and D. Sashin, "Attenuation correction for a combined 3D PET/CT scanner," *Med Phys,* **25**, 2046-53, 1998.

[21] J. A. Patton and T. G. Turkington, "SPECT/CT physical principles and attenuation correction," *J Nucl Med Technol,* **36**, 1-10, 2008.

[22] A. Ale, R. B. Schulz, A. Sarantopoulos, and V. Ntziachristos, "Imaging performance of a hybrid x-ray computed tomography-fluorescence molecular tomography system using priors," *Med Phys,* **37**, 1976-86, 2010.

[23] T. Correia, J. Aguirre, A. Sisniega, J. Chamorro-Servent, J. Abascal, J. J. Vaquero, M. Desco, V. Kolehmainen, and S. Arridge, "Split operator method for fluorescence diffuse optical tomography using anisotropic diffusion regularisation with prior anatomical information," *Biomed Opt Express,* **2**, 2632-48, 2011.

[24] S. R. Cherry, A. Y. Louie, and R. E. Jacobs, "The Integration of Positron Emission Tomography With Magnetic Resonance Imaging," *Proceedings of the IEEE,* **96**, 416-438, 2008.

[25] W. A. Kalender, *Computed Tomography: Fundamentals, System Technology, Image Quality, Applications,* 2 ed. Munich: Publicis, 2005.

[26] J. Hsieh, *Computed Tomography: Principles, Design, Artifacts and Recent Advances*: SPIE Optical Engineering Press, 2003.

[27] S. Webb, *The Physics of Medical Imaging*: Taylor & Francis, 1988.

[28] R. Gupta, M. Grasruck, C. Suess, S. H. Bartling, B. Schmidt, K. Stierstorfer, S. Popescu, T. Brady, and T. Flohr, "Ultra-high resolution flat-panel volume CT: fundamental principles, design architecture, and system characterization," *European Radiology,* **16**, 1191-1205, 2006.

[29] A. Bocage, " Procede et dispositifs de radiographie sur plaque en mouvement," France Patent 536464, 1921.

[30] G. Frank, "Verfahren zur Herstellung von Körperschnittbildern mittels Röntgenstrahlen," Germany Patent 693374, 1940.

[31] J. Radon, "Über die Bestimmung von Funktionen durch ihre Integralwerte längs gewisser Mannigfaltigkeiten," *Akad. Wiss.,* **69**, 262-277, 1917.

[32] J. Ambrose, "Proceedings: A brief review of the EMI scanner," *Br J Radiol,* **48**, 605-6, 1975.

[33] I. S. Kyprianou, S. Rudin, D. R. Bednarek, and K. R. Hoffmann, "Generalizing the MTF and DQE to include x-ray scatter and focal spot unsharpness: application to a new microangiographic system," *Med Phys,* **32**, 613-26, 2005.

[34] J. H. Siewerdsen and D. A. Jaffray, "Optimization of x-ray imaging geometry (with specific application to flat-panel cone-beam computed tomography)," *Med Phys,* **27**, 1903-14, 2000.

[35] A. Sisniega, M. Abella, E. Lage, M. Desco, and J. J. Vaquero, "Automatic Monte-Carlo Based Scatter Correction For X-ray cone-beam CT using general purpose graphic processing units (GP-GPU): A feasibility study," in *IEEE Nuclear Science Symposium and Medical Imaging Conference (NSS/MIC),* 2011, 3705-3709.

[36] C. R. Crawford and K. F. King, "Computed tomography scanning with simultaneous patient translation," *Med Phys,* **17**, 967-82, 1990.

[37] W. A. Kalender, P. Vock, A. Polacin, and M. Soucek, "Spiral-CT: a new technique for volumetric scans. I. Basic principles and methodology," *Rontgenpraxis,* **43**, 323-30, 1990.

[38] K. Taguchi and H. Aradate, "Algorithm for image reconstruction in multi-slice helical CT," *Med Phys,* **25**, 550-61, 1998.

[39] D. A. Jaffray and J. H. Siewerdsen, "Cone-beam computed tomography with a flat-panel imager: Initial performance characterization," *Med Phys,* **27**, 1311-1323, 2000.

[40] Y. Zou, E. Y. Sidky, and X. Pan, "Partial volume and aliasing artefacts in helical cone-beam CT," *Phys Med Biol,* **49**, 2365, 2004.

[41] S. Schafer, J. W. Stayman, W. Zbijewski, C. Schmidgunst, G. Kleinszig, and J. H. Siewerdsen, "Antiscatter grids in mobile C-arm cone-beam CT: effect on image quality and dose," *Med Phys,* **39**, 153-9, 2012.

[42] Y. Gao, E. Luo, J. Hu, J. Xue, S. Zhu, and J. Li, "Effect of combined local treatment with zoledronic acid and basic fibroblast growth factor on implant fixation in ovariectomized rats," *Bone,* **44**, 225-232, 2009.

[43] A. Sasov, "Desktop x-ray micro-CT instruments," *Proc. SPIE,* **4503**, 282, 2002.

[44] N. Tsukimura, M. Yamada, H. Aita, N. Hori, F. Yoshino, M. Chang-Il Lee, K. Kimoto, A. Jewett, and T. Ogawa, "N-acetyl cysteine (NAC)-mediated detoxification and functionalization of poly(methyl methacrylate) bone cement," *Biomaterials,* **30**, 3378-3389, 2009.

[45] M. J. Paulus, S. S. Gleason, S. J. Kennel, P. R. Hunsicker, and D. K. Johnson, "High resolution X-ray computed tomography: An emerging tool for small animal cancer research," *Neoplasia,* **2**, 62-70, 2000.

[46] D. Okkalides, "Contrast reduction in digital images due to x-ray induced damage to a TV camera's CCD image receptor," *Phys Med Biol,* **44**, N63-N68, 1999.

[47] H. K. Kim, I. A. Cunningham, Z. Yin, and G. Cho, "On the development of digital radiography detectors : A review," *International Journal of Precision Engineering and Manufacturing,* **9**, 86-100, 2008.

[48] C. Frojdh, H. Graafsma, H. E. Nilsson, and C. Ponchut, "Characterization of a pixellated CdTe detector with single-photon processing readout," *Nuclear Instruments & Methods in Physics Research Section A,* **563**, 128-132, 2006.

[49] K. Kowase and K. Ogawa, "Photon Counting X-ray CT System with a Semiconductor Detector," in *IEEE Nuclear Science Symposium and Medical Imaging Conference (NSS/MIC),* 2006, 3119-3123.

[50] Y. Onishi, T. Nakashima, A. Koike, H. Morii, Y. Neo, H. Mimura, and T. Aoki, "Material discriminated X-ray CT by using conventional microfocus X-ray tube

and CdTe imager," *IEEE Nuclear Science Symposium and Medical Imaging Conference (NSS/MIC)*, 1170-1174, 2007.

[51] J. P. Schlomka, E. Roessl, R. Dorscheid, S. Dill, G. Martens, T. Istel, C. Baumer, C. Herrmann, R. Steadman, G. Zeitler, A. Livne, and R. Proksa, "Experimental feasibility of multi-energy photon-counting K-edge imaging in pre-clinical computed tomography," *Phys Med Biol*, **53**, 4031-4047, 2008.

[52] H. E. Johns and J. R. Cunningham, *The physics of radiology*: Charles C. Thomas, 1983.

[53] J. Beutel and H. L. Kundel, *Handbook of Medical Imaging: Physics and psychophysics*: SPIE Press, 2000.

[54] J. M. Boone, "X-ray production, interaction, and detection in diagnostic imaging," in *Handbook of Medical Imaging, Volume 1. Physics and Psycophysics*, J. Beutel, *et al.*, Eds., ed Bellingham: SPIE, 2000, 1-78.

[55] J. M. Boone and J. A. Seibert, "Accurate method for computer-generating tungsten anode x-ray spectra from 30 to 140 kV," *Med Phys*, **24**, 1661-1670, 1997.

[56] C. L. Morgan and M. D. Miller, *Basic Principles of Computed Tomography*: Aspen Pub, 1983.

[57] R. Ribberfors, "X-ray incoherent-scattering total cross-sections and energy-absorption cross-sections by means of simple calculation routines," *Physical Review A*, **27**, 3061-3070, 1983.

[58] F. Salvat, J. M. Fernández-Varea, and J. Sempau, "PENELOPE - Code System for Monte Carlo Simulation of Electron and Photon Transport," presented at the Nuclear Energy Agency OECD, Issy-les-Moulineaux, 2006.

[59] R. D. Evans, *The atomic nucleus*: McGraw-Hill, 1955.

[60] S. O. Kasap, M. Z. Kabir, and J. A. Rowlands, "Recent advances in X-ray photoconductors for direct conversion X-ray image detectors," *Current Applied Physics*, **6**, 288-292, 2006.

[61] J. Yorkston, "Recent developments in digital radiography detectors," *Nuclear Instruments & Methods in Physics Research Section A*, **580**, 974-985, 2007.

[62] T. Gomi, K. Koshida, T. Miyati, J. Miyagawa, and H. Hirano, "An experimental comparison of flat-panel detector performance for direct and indirect systems (initial experiences and physical evaluation)," *Journal of Digital Imaging*, **19**, 362-370, 2006.

[63] G. Hajdok, J. Yao, J. J. Battista, and I. A. Cunningham, "Signal and noise transfer properties of photoelectric interactions in diagnostic x-ray imaging detectors," *Med Phys*, **33**, 3601-3620, 2006.

[64] S. Richard, J. H. Siewerdsen, D. A. Jaffray, D. J. Moseley, and B. Bakhtiar, "Generalized DQE analysis of radiographic and dual-energy imaging using flat-panel detectors," *Med Phys*, **32**, 1397-413, 2005.

[65] J. H. Siewerdsen, L. E. Antonuk, Y. el-Mohri, J. Yorkston, W. Huang, J. M. Boudry, and I. A. Cunningham, "Empirical and theoretical investigation of the noise performance of indirect detection, active matrix flat-panel imagers (AMFPIs) for diagnostic radiology," *Med Phys*, **24**, 71-89, 1997.

[66] J. H. Siewerdsen, L. E. Antonuk, Y. el-Mohri, J. Yorkston, W. Huang, and I. A. Cunningham, "Signal, noise power spectrum, and detective quantum efficiency of indirect-detection flat-panel imagers for diagnostic radiology," *Med Phys*, **25**, 614-28, 1998.

[67] I. A. Cunningham, "Applied Linear-Systems Theory," in *Handbook of Medical Imaging, Volume 1. Physics and Psycophysics*. vol. 1, J. Beutel, *et al.*, Eds., ed Bellingham: SPIE, 2000, 79-160.

[68] G. F. Knoll, *Radiation Detection and Measurement* 3rd ed. New York: John Wiley & Sons, 2000.

[69] M. Nikl, "Scintillation detectors for x-rays," *Measurement Science & Technology,* **17**, R37-R54, 2006.

[70] C. Bo Kyung, K. Byoung-Jik, C. Gyuseong, J. Sung Chae, B. Jun-Hyung, C. Yong Ki, L. Gyu-Ho, and K. Young-Hee, "A Pixelated CsI (Tl) Scintillator for CMOS-based X-ray Image Sensor," in *Nuclear Science Symposium Conference Record, 2006. IEEE*, 2006, 1139-1143.

[71] B. K. Cha, J. H. Shin, J. H. Bae, C. H. Lee, S. H. Chang, H. K. Kim, C. K. Kim, and G. Cho, "Scintillation characteristics and imaging performance of CsI:Tl thin films for X-ray imaging applications," *Nuclear Instruments & Methods in Physics Research Section A,* **604**, 224-228, 2009.

[72] H. Mori, R. Kyuushima, K. Fujita, and M. Honda, "High resolution and high sensitivity CMOS panel sensors for x-ray," in *IEEE Nuclear Science Symposium and Medical Imaging Conference (NSS/MIC)*, 2002, 29-33.

[73] A. Theuwissen, "CMOS image sensors: State-of-the-art and future perspectives," in *Solid State Circuits Conference (ESSCIRC)*, 2007, 21-27.

[74] J. A. Fessler, "Statistical image reconstruction methods for transmission tomography," in *Handbook of Medical Imaging, Volume 2. Medical Image Processing and Analysis*, M. Sonka and J. M. Fitzpatrick, Eds., ed Bellingham: SPIE, 2000, 1-70.

[75] A. C. Kak, M. Slaney, I. E. i. Medicine, and B. Society, *Principles of Computerized Tomographic Imaging*: IEEE Press, 1988.

[76] F. Natterer, *The Mathematics of Computerized Tomography*: Society for Industrial and Applied Mathematics, 2001.

[77] B. D. Smith, "Image-Reconstruction from Cone-Beam Projections - Necessary and Sufficient Conditions and Reconstruction Methods," *IEEE Transactions on Medical Imaging,* **4**, 14-25, 1985.

[78] H. K. Tuy, "An inversion formula for cone-beam reconstruction," *SIAM Journal on Applied Mathematics,* **43**, 546-552, 1983.

[79] L. A. Feldkamp, L. C. Davis, and J. W. Kress, "Practical Cone-Beam Algorithm," *Journal of the Optical Society of America A-Optics Image Science and Vision,* **1**, 612-619, 1984.

[80] X. Jia, B. Dong, Y. Lou, and S. B. Jiang, "GPU-based iterative cone-beam CT reconstruction using tight frame regularization," *Phys Med Biol,* **56**, 3787, 2011.

[81] J. W. Stayman, Y. Otake, J. L. Prince, A. J. Khanna, and J. H. Siewerdsen, "Model-Based Tomographic Reconstruction of Objects Containing Known Components," *IEEE Transactions on Medical Imaging,* **31**, 1837-1848, 2012.

[82] J. F. Barrett and N. Keat, "Artifacts in CT: Recognition and avoidance," *Radiographics,* **24**, 1679-1691, 2004.

[83] G. T. Herman, "Correction for beam hardening in computed tomography," *Phys Med Biol,* **24**, 81, 1979.

[84] P. M. Joseph and R. D. Spital, "Method for Correcting Bone Induced Artifacts in Computed Tomography Scanners," *Journal of Computer Assisted Tomography,* **2**, 100-108, 1978.

[85] A. I. Elbakri and A. J. Fessler, "Segmentation-free statistical image reconstruction for polyenergetic x-ray computed tomography with experimental validation," *Phys Med Biol,* **48**, 2453, 2003.

[86] I. A. Elbakri and J. A. Fessler, "Statistical image reconstruction for polyenergetic X-ray computed tomography," *IEEE Transactions on Medical Imaging,* **21**, 89-99, 2002.

[87] J. Hsieh, R. C. Molthen, C. A. Dawson, and R. H. Johnson, "An iterative approach to the beam hardening correction in cone beam CT," *Med Phys,* **27**, 23-29, 2000.

[88] P. M. Joseph and R. D. Spital, "The effects of scatter in x-ray computed tomography," *Med Phys,* **9**, 464-72, 1982.

[89] J. H. Siewerdsen and D. A. Jaffray, "Cone-beam computed tomography with a flat-panel imager: magnitude and effects of x-ray scatter," *Med Phys,* **28**, 220-31, 2001.

[90] U. Neitzel, "Grids or air gaps for scatter reduction in digital radiography: a model calculation," *Med Phys,* **19**, 475-81, 1992.

[91] K. Yang, G. Burkett, Jr., and J. M. Boone, "An object-specific and dose-sparing scatter correction approach for a dedicated cone-beam breast CT system using a parallel-hole collimator," *Proc. SPIE,* **8313**, 831303, 2012.

[92] L. Zhu, N. R. Bennett, and R. Fahrig, "Scatter correction method for X-ray CT using primary modulation: theory and preliminary results," *IEEE Transactions on Medical Imaging,* **25**, 1573-87, 2006.

[93] J. A. Seibert and J. M. Boone, "X-ray scatter removal by deconvolution," *Med Phys,* **15**, 567-75, 1988.

[94] G. Jarry, S. A. Graham, D. A. Jaffray, D. J. Moseley, and F. Verhaegen, "Scatter correction for kilovoltage cone-beam computed tomography (CBCT) images using Monte Carlo simulations," *Proc. SPIE,* **6142**, 614254, 2006.

[95] W. Zbijewski, A. Sisniega, J. J. Vaquero, A. Muhit, N. Packard, R. Senn, D. Yang, J. Yorkston, J. A. Carrino, and J. H. Siewerdsen, "Dose and scatter characteristics of a novel cone beam CT system for musculoskeletal extremities," *Proc. SPIE,* **8313**, 831318, 2012.

[96] Y. Kyriakou, T. Riedel, and W. A. Kalender, "Combining deterministic and Monte Carlo calculations for fast estimation of scatter intensities in CT," *Phys Med Biol,* **51**, 4567, 2006.

[97] J. Hsieh, E. Chao, J. Thibault, B. Grekowicz, A. Horst, S. McOlash, and T. J. Myers, "A novel reconstruction algorithm to extend the CT scan field-of-view," *Med Phys,* **31**, 2385-2391, 2004.

[98] B. Ohnesorge, T. Flohr, K. Schwarz, J. P. Heiken, and K. T. Bae, "Efficient correction for CT image artifacts caused by objects extending outside the scan field of view," *Med Phys,* **27**, 39-46, 2000.

[99] K. Sourbelle, M. Kachelriess, and W. A. Kalender, "Reconstruction from truncated projections in CT using adaptive detruncation," *European Radiology,* **15**, 1008-1014, 2005.

[100] B. R. Whiting, P. Massoumzadeh, O. A. Earl, J. A. O'Sullivan, D. L. Snyder, and J. F. Williamson, "Properties of preprocessed sinogram data in x-ray computed tomography," *Med Phys,* **33**, 3290-3303, 2006.

[101] K. Yang, S. Y. Huang, N. J. Packard, and J. M. Boone, "Noise variance analysis using a flat panel x-ray detector: A method for additive noise assessment with application to breast CT applications," *Med Phys,* **37**, 3527-3537, 2010.

[102] W. A. Kalender, H. Wolf, and C. Suess, "Dose reduction in CT by anatomically adapted tube current modulation. II. Phantom measurements," *Med Phys,* **26**, 2248-2253, 1999.

[103] J. Hsieh, "Adaptive streak artifact reduction in computed tomography resulting from excessive x-ray photon noise," *Med Phys,* **25**, 2139-2147, 1998.

[104] M. Kachelriess, O. Watzke, and W. A. Kalender, "Generalized multi-dimensional adaptive filtering for conventional and spiral single-slice, multi-slice, and cone-beam CT," *Med Phys,* **28**, 475-490, 2001.

[105] E. M. Abu Anas, J. G. Kim, S. Y. Lee, and M. K. Hasan, "Comparison of ring artifact removal methods using flat panel detector based CT images," *Biomedical Engineering Online,* **10**, 2011.

[106] M. Abella, J. J. Vaquero, A. Sisniega, J. Pascau, A. Udias, V. Garcia, I. Vidal, and M. Desco, "Software architecture for multi-bed FDK-based reconstruction in X-ray CT scanners," *Comput. Methods Prog. Biomed.,* **107**, 218-232, 2012.

[107] R. A. Ketcham, "New algorithms for ring artifact removal," *Proc. SPIE,* **6318** 3180, 2006.

[108] A. L. Kwan, J. A. Seibert, and J. M. Boone, "An improved method for flat-field correction of flat panel x-ray detector," *Med Phys,* **33**, 391-3, 2006.

[109] J. A. Seibert, J. M. Boone, and K. K. Lindfors, "Flat-field correction technique for digital detectors," *Proc. SPIE,* **3336**, 348, 1998.

[110] H. Zaidi and G. Sgouros, *Therapeutic Applications of Monte Carlo Calculations in Nuclear Medicine*: Taylor & Francis, 2010.

[111] P. Andreo, "Monte Carlo techniques in medical radiation physics," *Phys Med Biol,* **36**, 861-920, 1991.

[112] M. H. Kalos and P. A. Whitlock, *Monte Carlo Methods*: Wiley, 2009.

[113] M. Ljunberg, S. E. Strand, and M. A. King, *Monte Carlo Calculations in Nuclear Medicine: Applications in Nuclear Imaging*: Institute of Physics Publishing, 1998.

[114] J. M. Boone, "Dose spread functions in computed tomography: a Monte Carlo study," *Med Phys,* **36**, 4547-54, 2009.

[115] G. Jarry, S. A. Graham, D. J. Moseley, D. J. Jaffray, J. H. Siewerdsen, and F. Verhaegen, "Characterization of scattered radiation in kV CBCT images using Monte Carlo simulations," *Med Phys,* **33**, 4320-9, 2006.

[116] M. H. Kalos, "On the estimation of flux at a point by Monte Carlo," *Nuclear Science and Engineering (U.S.),* **16**, 111-17, 1963.

[117] E. Mainegra-Hing and I. Kawrakow, "Variance reduction techniques for fast Monte Carlo CBCT scatter correction calculations," *Phys Med Biol,* **55**, 4495-507, 2010.

[118] J. F. Williamson, "Monte Carlo evaluation of kerma at a point for photon transport problems," *Med Phys,* **14**, 567-76, 1987.

[119] A. Sisniega, W. Zbijewski, A. Badal, I. S. Kyprianou, J. W. Stayman, J. J. Vaquero, and J. H. Siewerdsen, "Monte Carlo study of the effects of system geometry and antiscatter grids on cone-beam CT scatter distributions," *Med Phys,* **40**, 051915, 2013.

[120] S. Agostinelli, *et al.*, "Geant4—a simulation toolkit," *Nuclear Instruments & Methods in Physics Research Section A,* **506**, 250-303, 2003.

[121] I. Kawrakow, "Accurate condensed history Monte Carlo simulation of electron transport. I. EGSnrc, the new EGS4 version," *Med Phys,* **27**, 485-98, 2000.

[122] X-5-Monte-Carlo-Team. (2005), "MCNP - A General N-Particle Transport Code." https://laws.lanl.gov/vhosts/mcnp.lanl.gov/index.shtml. Last Accessed: April 2013

[123] T. E. Booth, "The intelligent random number technique in MCNP," *Nucl. Sci. Eng.*, **100**, 248-254, 1988.

[124] D. H. Lehmer, "Mathematical methods in large-scale computing units," in *2nd Symposium on Large-Scale Digital Calculating Machinery*, Cambridge, 1949, 141-146.

[125] G. Marsaglia and A. Zaman, "Monkey tests for random number generators," *Computers & mathematics with applications*, **26**, 1-10, 1993.

[126] L. Devroye, *Non-uniform random variate generation*: Springer-Verlag, 1986.

[127] A. J. Walker, "An efficient method for generating discrete random variables with general distributions," *ACM Transactions on Mathematical Software (TOMS)*, **3**, 253-256, 1977.

[128] J. Von Neumann, "Various techniques used in connection with random digits," *Applied Math Series*, **12**, 1, 1951.

[129] A. Bielajew and D. O. Rogers, "Variance-Reduction Techniques," in *Monte Carlo Transport of Electrons and Photons*, T. Jenkins, *et al.*, Eds., ed: Springer US, 1988, 407-419.

[130] E. Woodcock, T. Murphy, P. Hemmings, and T. Longworth, "Techniques used in the GEM code for Monte Carlo neutronics calculations in reactors and other systems of complex geometry," in *Conference on the Application of Computing Methods to Reactor Problems*, 1965, 557-579.

[131] I. Kawrakow and M. Fippel, "Investigation of variance reduction techniques for Monte Carlo photon dose calculation using XVMC," *Phys Med Biol*, **45**, 2163-83, 2000.

[132] H. Ebina, J. Hatakeyama, M. Onodera, T. Honma, S. Kamakura, H. Shimauchi, and Y. Sasano, "Micro-CT analysis of alveolar bone healing using a rat experimental model of critical-size defects," *Oral Diseases*, **15**, 273-280, 2009.

[133] T. Engelhorn, I. Y. Eyupoglu, M. A. Schwarz, M. Karolczak, H. Bruenner, T. Struffert, W. Kalender, and A. Doerfler, "In vivo micro-CT imaging of rat brain glioma: A comparison with 3 T MRI and histology," *Neuroscience Letters*, **458**, 28-31, 2009.

[134] N. M. Harrison, P. F. McDonnell, D. C. O'Mahoney, O. D. Kennedy, F. J. O'Brien, and P. E. McHugh, "Heterogeneous linear elastic trabecular bone modelling using micro-CT attenuation data and experimentally measured heterogeneous tissue properties," *Journal of Biomechanics*, **41**, 2589-2596, 2008.

[135] H. Parameswaran, E. Bartolak-Suki, H. Hamakawa, A. Majumdar, P. G. Allen, and B. Suki, "Three-dimensional measurement of alveolar airspace volumes in normal and emphysematous lungs using micro-CT," *Journal of Applied Physiology*, **107**, 583-592, 2009.

[136] J. U. Umoh, A. V. Sampaio, I. Welch, V. Pitelka, H. A. Goldberg, T. M. Underhill, and D. W. Holdsworth, "In vivo micro-CT analysis of bone remodeling in a rat calvarial defect model," *Phys Med Biol*, **54**, 2147-2161, 2009.

[137] A. A. Isola, C. T. Metz, M. Schaap, S. Klein, M. Grass, and W. J. Niessen, "Cardiac motion-corrected iterative cone-beam CT reconstruction using a semi-automatic minimum cost path-based coronary centerline extraction," *Computerized Medical Imaging and Graphics*, **36**, 215-226, 2012.

[138] M. Kachelriess, M. Knaup, and W. A. Kalender, "Extended parallel backprojection for standard three-dimensional and phase-correlated four-dimensional axial and spiral cone-beam CT with arbitrary pitch, arbitrary cone-angle, and 100% dose usage," *Med Phys,* **31**, 1623-1641, 2004.

[139] M. Kachelriess, M. Knaup, and W. A. Kalender, "Multithreaded cardiac CT," *Med Phys,* **33**, 2435-2447, 2006.

[140] R. Manzke, P. Koken, D. Hawkes, and M. Grass, "Helical cardiac cone beam CT reconstruction with large area detectors: a simulation study," *Phys Med Biol,* **50**, 1547-68, 2005.

[141] H. K. Kim, S. C. Lee, M. H. Cho, S. Y. Lee, and G. Cho, "Use of a flat-panel detector for microtomography: A feasibility study for small-animal imaging," *IEEE Transactions on Nuclear Science,* **52**, 193-198, 2005.

[142] I. Fujieda, G. Cho, J. Drewery, T. Gee, T. Jing, S. N. Kaplan, V. Perezmendez, D. Wildermuth, and R. A. Street, "X-Ray and Charged-Particle Detection with Csi(Tl) Layer Coupled to a-Si-H Photodiode Layers," *IEEE Transactions on Nuclear Science,* **38**, 255-262, 1991.

[143] E. Miyata, M. Miki, N. Tawa, D. Kamiyama, and K. Miyaguchi, "Development of new X-ray imaging device sensitive to 0.1-100 keV," *Nuclear Instruments & Methods in Physics Research Section A,* **525**, 122-125, 2004.

[144] S. R. Arridge and J. C. Schotland, "Optical tomography: forward and inverse problems," *Inverse Problems,* **25**, 123010, 2009.

[145] D. Hyde, R. Schulz, D. Brooks, E. Miller, and V. Ntziachristos, "Performance dependence of hybrid x-ray computed tomography/fluorescence molecular tomography on the optical forward problem," *Journal of the Optical Society of America A-Optics Image Science and Vision,* **26**, 919-23, 2009.

[146] J. C. Baritaux, K. Hassler, M. Bucher, S. Sanyal, and M. Unser, "Sparsity-Driven Reconstruction for FDOT With Anatomical Priors," *IEEE Transactions on Medical Imaging,* **30**, 1143-1153, 2011.

[147] D. Hyde, E. L. Miller, D. H. Brooks, and V. Ntziachristos, "Data Specific Spatially Varying Regularization for Multimodal Fluorescence Molecular Tomography," *Medical Imaging, IEEE Transactions on,* **29**, 365-374, 2010.

[148] A. Joshi, W. Bangerth, and E. Sevick-Muraca, "Adaptive finite element based tomography for fluorescence optical imaging in tissue," *Opt. Express,* **12**, 5402-5417, 2004.

[149] A. Li, G. Boverman, Y. Zhang, D. Brooks, E. L. Miller, M. E. Kilmer, Q. Zhang, E. M. Hillman, and D. A. Boas, "Optimal linear inverse solution with multiple priors in diffuse optical tomography," *Appl Opt,* **44**, 1948-56, 2005.

[150] X. Guo, X. Liu, A. Wang, T. Feng, L. Fei, Z. Bin, H. Guangshu, and J. Bai, "A Combined Fluorescence and Microcomputed Tomography System for Small Animal Imaging," *IEEE Transactions on Biomedical Engineering,* **57**, 2876-2883, 2010.

[151] R. B. Schulz, A. Ale, A. Sarantopoulos, M. Freyer, E. Soehngen, M. Zientkowska, and V. Ntziachristos, "Hybrid System for Simultaneous Fluorescence and X-Ray Computed Tomography," *IEEE Transactions on Medical Imaging,* **29**, 465-473, 2010.

[152] X. Yang, H. Gong, G. Quan, Y. Deng, and Q. Luo, "Combined system of fluorescence diffuse optical tomography and microcomputed tomography for small animal imaging," *Rev Sci Instrum,* **81**, 054304, 2010.

[153] A. Sisniega, J. J. Vaquero, E. Lage, A. De Carlos, J. L. Villena, M. Abella, I. Vidal, G. Tapias, J. C. Antoranz, and M. Desco, "Comparative study of two flat-

panel X-ray detectors applied to small-animal imaging cone-beam micro-CT," in *IEEE Nuclear Science Symposium and Medical Imaging Conference (NSS/MIC)*, 2008, 3836-3840.

[154] A. Sasov, "Ultrafast micro-CT for in vivo small animal imaging and industrial applications," *Proc. SPIE,* **5535**, 733, 2004.

[155] A. Sisniega, J. J. Vaquero, and M. Desco, " Design and Assessment Principles of Semiconductor Flat-Panel Detector-Based X-Ray Micro-CT Systems for Small-Animal Imaging," in *Integrated Microsystems: Electronics, Photonics, and Biotechnology*, K. Iniewski, Ed., ed New York: CRC Press, 2012, 309-335.

[156] K. K. Hamamatsu Photonics, "Hamamatsu Application Manual, X-ray flat panel sensor C7912 & C7942 & C7943, rev 2.10, kr1-i50006," 2003.

[157] H. Illers, D. Vandenbroucke, and E. Buhr, "Measurement of correlated noise in images of computed radiography systems and its influence on the detective quantum efficiency," *Proc. SPIE,* **5368**, 639, 2004.

[158] S. M. Sze and M. K. Lee, *Semiconductor Devices: Physics and Technology*: Wiley, 2012.

[159] A. Konstantinidis, "Evaluation of digital x-ray detectors for medical imaging applications," PhD, Department Medical Physics and Bioengineering, University College London, London, 2011.

[160] C. Schmidgunst, D. Ritter, and E. Lang, "Calibration model of a dual gain flat panel detector for 2D and 3D x-ray imaging," *Med Phys,* **34**, 3649-64, 2007.

[161] J. Li, R. J. Jaszczak, K. L. Greer, and R. E. Coleman, "A filtered backprojection algorithm for pinhole SPECT with a displaced centre of rotation," *Phys Med Biol,* **39**, 165-76, 1994.

[162] P. Rizo, P. Grangeat, and R. Guillemaud, "Geometric calibration method for multiple-head cone-beam SPECT system," *IEEE Transactions on Nuclear Science,* **41**, 2748-2757, 1994.

[163] Y. Cho, D. J. Moseley, J. H. Siewerdsen, and D. A. Jaffray, "Accurate technique for complete geometric calibration of cone-beam computed tomography systems," *Med Phys,* **32**, 968-83, 2005.

[164] Y. Kyriakou, R. M. Lapp, L. Hillebrand, D. Ertel, and W. A. Kalender, "Simultaneous misalignment correction for approximate circular cone-beam computed tomography," *Phys Med Biol,* **53**, 6267, 2008.

[165] C. Mennessier, R. Clackdoyle, and F. Noo, "Direct determination of geometric alignment parameters for cone-beam scanners," *Phys Med Biol,* **54**, 1633, 2009.

[166] F. Noo, R. Clackdoyle, C. Mennessier, T. A. White, and T. J. Roney, "Analytic method based on identification of ellipse parameters for scanner calibration in cone-beam tomography," *Phys Med Biol,* **45**, 3489-3508, 2000.

[167] K. Yang, A. L. Kwan, D. F. Miller, and J. M. Boone, "A geometric calibration method for cone beam CT systems," *Med Phys,* **33**, 1695-706, 2006.

[168] M. D. Silver, "A method for including redundant data in computed tomography," *Med Phys,* **27**, 773-4, 2000.

[169] D. L. Parker, "Optimal short scan convolution reconstruction for fanbeam CT," *Med Phys,* **9**, 254-7, 1982.

[170] H. H. Barrett and W. Swindell, *Radiological imaging: the theory of image formation, detection, and processing*: Academic Press, 1981.

[171] L. Grodzins, "Optimum energies for x-ray transmission tomography of small samples: Applications of synchrotron radiation to computerized tomography I," *Nuclear Instruments & Methods in Physics Research Section A,* **206**, 541-545, 1983.

[172] P. Spanne, "X-ray energy optimisation in computed microtomography," *Phys Med Biol*, **34**, 679-90, 1989.

[173] M. Hupfer, T. Nowak, R. Brauweiler, F. Eisa, and W. A. Kalender, "Spectral optimization for micro-CT," *Med Phys*, **39**, 3229-39, 2012.

[174] W. A. Kalender, P. Deak, M. Kellermeier, M. van Straten, and S. V. Vollmar, "Application- and patient size-dependent optimization of x-ray spectra for CT," *Med Phys*, **36**, 993-1007, 2009.

[175] M. Weigel, S. V. Vollmar, and W. A. Kalender, "Spectral optimization for dedicated breast CT," *Med Phys*, **38**, 114-24, 2011.

[176] J. A. Rowlands and K. W. Taylor, "Absorption and noise in cesium iodide x-ray image intensifiers," *Med Phys*, **10**, 786-95, 1983.

[177] J. H. Hubbell and S. M. Seltzer. Tables of X-Ray Mass Attenuation Coefficients and Mass Energy-Absorption Coefficients [Online]. Available: http://physics.nist.gov/xaamdi

[178] A. Sisniega, M. Abella, M. Desco, and J. J. Vaquero, "Expansion of the dynamic range of x-ray flat panel detectors: a dual-exposure technique," *Phys Med Biol*, (under revision), 2013.

[179] E. Buhr, S. Guenther-Kohfahl, and U. Neitzel, "Simple method for modulation transfer function determination of digital imaging detectors from edge images," *Proc. SPIE*, **5030**, 877, 2003.

[180] E. Buhr, S. Gunther-Kohfahl, and U. Neitzel, "Accuracy of a simple method for deriving the presampled modulation transfer function of a digital radiographic system from an edge image," *Med Phys*, **30**, 2323-2331, 2003.

[181] E. Samei, E. Buhr, P. Granfors, D. Vandenbroucke, and X. H. Wang, "Comparison of edge analysis techniques for the determination of the MTF of digital radiographic systems," *Phys Med Biol*, **50**, 3613-3625, 2005.

[182] J. T. Dobbins, "Image quality metrics for digital systems," in *Handbook of Medical Imaging, Volume 1. Physics and Psycophysics*, J. Beutel, *et al.*, Eds., ed Bellingham: SPIE, 2000, 161-222.

[183] H. Illers, E. Buhr, and C. Hoeschen, "Measurement of the detective quantum efficiency (DQE) of digital X-ray detectors according to the novel standard IEC 62220-1," *Radiat Prot Dosimetry*, **114**, 39-44, 2005.

[184] K. Yang, "Development and Evaluation of a Dedicated Breast CT Scanner," PhD, University of California, Davis, 2007.

[185] M. Hupfer, D. Kolditz, T. Nowak, F. Eisa, R. Brauweiler, and W. A. Kalender, "Dosimetry concepts for scanner quality assurance and tissue dose assessment in micro-CT," *Med Phys*, **39**, 658-70, 2012.

[186] QRM-GmbH. (2008), "Micro-CT Dosimetry Phantom." http://www.qrm.de/content/products/microct/microct_dose.htm. Last Accessed: April 2013

[187] A. Badal and A. Badano, "Accelerating Monte Carlo simulations of photon transport in a voxelized geometry using a massively parallel graphics processing unit," *Med Phys*, **36**, 4878-80, 2009.

[188] B. Dogdas, D. Stout, A. F. Chatziioannou, and R. M. Leahy, "Digimouse: a 3D whole body mouse atlas from CT and cryosection data," *Phys Med Biol*, **52**, 577-87, 2007.

[189] H. Q. Woodard and D. R. White, "The composition of body tissues," *Br J Radiol*, **59**, 1209-18, 1986.

[190] ASTM, "Standard Test Method for Measurement of Computed Tomography (CT) System Performance.," ed, 2006.

[191] J. H. Siewerdsen, M. J. Daly, B. Bakhtiar, D. J. Moseley, S. Richard, H. Keller, and D. A. Jaffray, "A simple, direct method for x-ray scatter estimation and correction in digital radiography and cone-beam CT," *Med Phys,* **33**, 187-97, 2006.

[192] J. W. Stayman, W. Zbijewski, Y. Otake, A. Uneri, S. Schafer, J. Lee, J. L. Prince, and J. H. Siewerdsen, "Penalized-likelihood reconstruction for sparse data acquisitions with unregistered prior images and compressed sensing penalties," *Proc. SPIE,* **7961**, 79611L, 2011.

[193] J. F. Abascal, M. Abella, A. Sisniega, J. J. Vaquero, and M. Desco, "Investigation of different sparsity transforms for the PICCS algorithm in small-animal respiratory gated CT," *Phys Med Biol,* **(submitted)**, 2013.

[194] W. F. Cheong, S. A. Prahl, and A. J. Welch, "A review of the optical properties of biological tissues," *IEEE Journal of Quantum Electronics,* **26**, 2166-2185, 1990.

[195] A. P. Colijn, W. Zbijewski, A. Sasov, and F. J. Beekman, "Experimental validation of a rapid Monte Carlo based micro-CT simulator," *Phys Med Biol,* **49**, 4321-33, 2004.

[196] I. K. Chun, M. H. Cho, S. C. Lee, M. H. Cho, and S. Y. Lee, "X-ray micro-tomography system for small-animal imaging with zoom-in imaging capability," *Phys Med Biol,* **49**, 3889, 2004.

[197] D. Kolditz, Y. Kyriakou, and W. A. Kalender, "Volume-of-interest (VOI) imaging in C-arm flat-detector CT for high image quality at reduced dose," *Med Phys,* **37**, 2719-30, 2010.

[198] T. Lule, B. Schneider, and M. Bohm, "Design and fabrication of a high-dynamic-range image sensor in TFA technology," *IEEE Journal of Solid-State Circuits,* **34**, 704-711, 1999.

[199] T. R. Fox, D. T. Nisius, M. Z. Duncan, and M. T. Duncan, "Dynamic range extension of X-ray imaging system used in non-invasive inspection of contraband in vehicles, involves amplifying identical samples of X-ray beams using respective gain values, and forming X-ray image," US2005047546-A1; US6901135-B2, 2005.

[200] S. K. Nayar and T. Mitsunaga, "High dynamic range imaging: Spatially varying pixel exposures," in *IEEE Conference on Computer Vision and Pattern Recognition (CVPR)*, 2000, 472-479.

[201] K. Nittoh, E. Oyaizu, T. Sakurai, T. Yoshida, and K. Mochiki, "Extension of dynamic range in X-ray radiography using multi-color scintillation detector," *Nuclear Instruments & Methods in Physics Research Section A,* **501**, 615-622, 2003.

[202] N. H. Clinthorne and J. Strobel, "A simple algorithm for restoring images from pixellated radiation detectors," in *IEEE Nuclear Science Symposium and Medical Imaging Conference (NSS/MIC)*, 1998, 758-765 vol.2.

[203] S. Mann and R. W. Picard, "On being 'undigital' with digital cameras: Extending dynamic range by combining differently exposed pictures," *Is&T's 48th Annual Conference - Imaging on the Information Superhighway, Final Program and Proceedings,* 442-448, 1995.

[204] B. C. Madden, "Extended intensity range imaging," *Technical report, GRASP Lab. University of Pennsylvania*, 1993.

[205] A. Dromigny and Y. M. Zhu, "Improving the dynamic range of real-time X-ray imaging systems via Bayesian fusion," *Journal of Nondestructive Evaluation,* **16**, 147-160, 1997.

[206] M. A. Robertson, S. Borman, and R. L. Stevenson, "Estimation-theoretic approach to dynamic range enhancement using multiple exposures," *Journal of Electronic Imaging,* **12**, 219-228, 2003.

[207] P. Sukovic and N. H. Clinthorne, "A method for extending the dynamic range of flat panel imagers for use in cone beam computed tomography," in *IEEE Nuclear Science Symposium and Medical Imaging Conference (NSS/MIC),* San Diego, Ca, 2001, 1647-1651.

[208] B. R. Whiting and E. Muka, "Image quantization: statistics and modeling," *Proc. SPIE,* **3336**, 260-271, 1998.

[209] M. J. Yaffe, "Digital Mammography," in *Handbook of Medical Imaging Volume 1: Physics and Psychophysics*, J. Beutel, *et al.*, Eds., ed Bellingham, WA: SPIE Press, 2000, 329-372.

[210] N. Mail, D. J. Moseley, J. H. Siewerdsen, and D. A. Jaffray, "The influence of bowtie filtration on cone-beam CT image quality," *Med Phys,* **36**, 11, 2009.

[211] W. H. Greene, *Econometric Analysis*. Upper Saddle River, NJ: Prentice Hall, 2003.

[212] C. S. Chen, K. Doi, C. Vyborny, H. P. Chan, and G. Holje, "Monte Carlo simulation studies of detectors used in the measurement of diagnostic x-ray spectra," *Med Phys,* **7**, 627-35, 1980.

[213] R. Fahrig and M. J. Yaffe, "A model for optimization of spectral shape in digital mammography," *Med Phys,* **21**, 1463-71, 1994.

[214] B. R. Archer, T. R. Fewell, and L. K. Wagner, "Laplace reconstruction of experimental diagnostic x-ray spectra," *Med Phys,* **15**, 832-7, 1988.

[215] B. W. Soole, "A method of X-ray attenuation analysis for approximating the intensity distribution at its point of origin of bremsstrahlung excited in a thick target by incident electrons of constant medium energy," *Phys Med Biol,* **21**, 369-89, 1976.

[216] E. Y. Sidky, L. Yu, X. Pan, Y. Zou, and M. Vannier, "A robust method of x-ray source spectrum estimation from transmission measurements: Demonstrated on computer simulated, scatter-free transmission data," *Journal of Applied Physics,* **97**, 124701-11, 2005.

[217] Y. Yang, X. Mou, and X. Chen, "A robust x-ray tube spectra measuring method by attenuation data," 61423K-61423K, 2006.

[218] J. M. Boone, T. R. Fewell, and R. J. Jennings, "Molybdenum, rhodium, and tungsten anode spectral models using interpolating polynomials with application to mammography," *Med Phys,* **24**, 1863-1874, 1997.

[219] H. A. Kramers, "XCIII. On the theory of X-ray absorption and of the continuous X-ray spectrum," *Philosophical Magazine Series 6,* **46**, 836-871, 1923.

[220] R. Birch and M. Marshall, "Computation of bremsstrahlung X-ray spectra and comparison with spectra measured with a Ge(Li) detector," *Phys Med Biol,* **24**, 505-17, 1979.

[221] D. M. Tucker, G. T. Barnes, and D. P. Chakraborty, "Semiempirical model for generating tungsten target x-ray spectra," *Med Phys,* **18**, 211-8, 1991.

[222] D. M. Tucker, G. T. Barnes, and X. Z. Wu, "Molybdenum target x-ray spectra: a semiempirical model," *Med Phys,* **18**, 402-7, 1991.

[223] G. G. Poludniowski and P. M. Evans, "Calculation of x-ray spectra emerging from an x-ray tube. Part I. electron penetration characteristics in x-ray targets," *Med Phys,* **34**, 2164-74, 2007.

[224] M. R. Ay, M. Shahriari, S. Sarkar, M. Adib, and H. Zaidi, "Monte carlo simulation of x-ray spectra in diagnostic radiology and mammography using MCNP4C," *Phys Med Biol,* **49**, 4897-917, 2004.

[225] M. Bhat, J. Pattison, G. Bibbo, and M. Caon, "Off-axis x-ray spectra: a comparison of Monte Carlo simulated and computed x-ray spectra with measured spectra," *Med Phys,* **26**, 303-9, 1999.

[226] R. E. Alvarez, "Estimator for photon counting energy selective x-ray imaging with multibin pulse height analysis," *Med Phys,* **38**, 2324-34, 2011.

[227] H. Ding and S. Molloi, "Image-based spectral distortion correction for photon-counting x-ray detectors," *Med Phys,* **39**, 1864-76, 2012.

[228] S. Y. Huang, K. Yang, C. K. Abbey, and J. M. Boone, "A semiempirical linear model of indirect, flat-panel x-ray detectors," *Med Phys,* **39**, 2108-18, 2012.

[229] T. P. Szczykutowicz and C. A. Mistretta, "Design of a digital beam attenuation system for computed tomography: part I. System design and simulation framework," *Med Phys,* **40**, 021905, 2013.

[230] J. H. Siewerdsen, A. M. Waese, D. J. Moseley, S. Richard, and D. A. Jaffray, "Spektr: a computational tool for x-ray spectral analysis and imaging system optimization," *Med Phys,* **31**, 3057-67, 2004.

[231] T. R. Fewell, R. E. Shuping, K. R. Hawkins, and P. United States. Bureau of Radiological Health. Division of Electronic, *Handbook of computed tomography X-ray spectra*. Rockville, Md.: U.S. Dept. of Health and Human Services, Public Health Service, Food and Drug Administration, Bureau of Radiological Health, 1981.

[232] K. Meghzifene, H. Aiginger, and R. Nowotny, "A fit method for the determination of inherent filtration with diagnostic x-ray units," *Phys Med Biol,* **51**, 2585-97, 2006.

[233] R. Nowotny and K. Meghzifene, "Simulation of the effect of anode surface roughness on diagnostic x-ray spectra," *Phys Med Biol,* **47**, 3973-83, 2002.

[234] M. R. Ay, S. Sarkar, M. Shahriari, D. Sardari, and H. Zaidi, "Assessment of different computational models for generation of x-ray spectra in diagnostic radiology and mammography," *Med Phys,* **32**, 1660-75, 2005.

[235] R. Birch, M. Marshall, and G. M. Ardran, *Catalogue of spectral data for diagnostic X-rays*. London: Hospital Physicists' Association, 1979.

[236] M. Endo, T. Tsunoo, N. Nakamori, and K. Yoshida, "Effect of scattered radiation on image noise in cone beam CT," *Med Phys,* **28**, 469-74, 2001.

[237] G. H. Glover, "Compton scatter effects in CT reconstructions," *Med Phys,* **9**, 860-7, 1982.

[238] P. C. Johns and M. Yaffe, "Scattered radiation in fan beam imaging systems," *Med Phys,* **9**, 231-9, 1982.

[239] R. Ning, X. Tang, and D. Conover, "X-ray scatter correction algorithm for cone beam CT imaging," *Med Phys,* **31**, 1195-202, 2004.

[240] L. Zhu, N. Strobel, and R. Fahrig, "X-ray scatter correction for cone-beam CT using moving blocker array," *Proc. SPIE,* **5745**, 251, 2005.

[241] L. Zhu, Y. Xie, J. Wang, and L. Xing, "Scatter correction for cone-beam CT in radiation therapy," *Med Phys,* **36**, 2258-68, 2009.

[242] X. Liu, C. C. Shaw, T. Wang, L. Chen, M. C. Altunbas, and S. C. Kappadath, "An Accurate Scatter Measurement and Correction Technique for Cone Beam Breast CT Imaging Using Scanning Sampled Measurement (SSM) Technique," *Proc Soc Photo Opt Instrum Eng,* **6142**, 6142341-6142347, 2006.

[243] M. Bertram, J. Wiegert, and G. Rose, "Potential of software-based scatter corrections in cone-beam volume CT," *Proc. SPIE*, **5745**, 259, 2005.

[244] L. A. Love and R. A. Kruger, "Scatter estimation for a digital radiographic system using convolution filtering," *Med Phys*, **14**, 178-85, 1987.

[245] D. Lazos and J. F. Williamson, "Monte Carlo evaluation of scatter mitigation strategies in cone-beam CT," *Med Phys*, **37**, 5456-70, 2010.

[246] G. Bootsma, F. Verhaegen, and D. Jaffray, "SU-F-BRCD-04: Efficient Scatter Distribution Estimation and Correction in CBCT Using Concurrent Monte Carlo Fitting," *Med Phys*, **39**, 3856, 2012.

[247] A. P. Colijn and F. J. Beekman, "Accelerated simulation of cone beam X-ray scatter projections," *IEEE Transactions on Medical Imaging*, **23**, 584-90, 2004.

[248] G. Poludniowski, P. M. Evans, V. N. Hansen, and S. Webb, "An efficient Monte Carlo-based algorithm for scatter correction in keV cone-beam CT," *Phys Med Biol*, **54**, 3847-64, 2009.

[249] W. Zbijewski and F. J. Beekman, "Efficient Monte Carlo based scatter artifact reduction in cone-beam micro-CT," *IEEE Transactions on Medical Imaging*, **25**, 817-27, 2006.

[250] Y. Kyriakou and W. Kalender, "Efficiency of antiscatter grids for flat-detector CT," *Phys Med Biol*, **52**, 6275-93, 2007.

[251] G. J. Day and D. R. Dance, "X-ray transmission formula for antiscatter grids," *Phys Med Biol*, **28**, 1429-33, 1983.

[252] R. L. Siddon, "Fast calculation of the exact radiological path for a three-dimensional CT array," *Med Phys*, **12**, 252-5, 1985.

[253] A. Badal and A. Badano, "SU-E-I-68: Fast and Accurate Estimation of Organ Doses in Medical Imaging Using a GPU-Accelerated Monte Carlo Simulation Code," *Med Phys*, **38**, 3411, 2011.

[254] N. Otsu, "A Threshold Selection Method from Gray-Level Histograms," *IEEE Transactions on Systems, Man and Cybernetics*, **9**, 62-66, 1979.

[255] A. L. Kwan, J. M. Boone, and N. Shah, "Evaluation of x-ray scatter properties in a dedicated cone-beam breast CT scanner," *Med Phys*, **32**, 2967-75, 2005.

[256] J. H. Siewerdsen, D. J. Moseley, B. Bakhtiar, S. Richard, and D. A. Jaffray, "The influence of antiscatter grids on soft-tissue detectability in cone-beam computed tomography with flat-panel detectors," *Med Phys*, **31**, 3506-20, 2004.

[257] http://www.itis.ethz.ch. Last Accessed: April 2013

[258] A. Christ, *et al.*, "The Virtual Family—development of surface-based anatomical models of two adults and two children for dosimetric simulations," *Phys Med Biol*, **55**, N23, 2010.

[259] N. D. Prionas, G. W. Burkett, S. E. McKenney, L. Chen, R. L. Stern, and J. M. Boone, "Development of a patient-specific two-compartment anthropomorphic breast phantom," *Phys Med Biol*, **57**, 4293-307, 2012.

[260] H. H. Barrett, S. K. Gordon, and R. S. Hershel, "Statistical limitations in transaxial tomography," *Comput Biol Med*, **6**, 307-323, 1976.

[261] P. C. Johns and M. J. Yaffe, "Coherent scatter in diagnostic radiology," *Med Phys*, **10**, 40-50, 1983.

[262] D. M. Cunha, A. Tomal, and M. E. Poletti, "Evaluation of scatter-to-primary ratio, grid performance and normalized average glandular dose in mammography by Monte Carlo simulation including interference and energy broadening effects," *Phys Med Biol*, **55**, 4335-59, 2010.

[263] C. J. Leliveld, J. G. Maas, V. R. Bom, and C. W. E. Van Eijk, "Monte Carlo modeling of coherent scattering: influence of interference," in *IEEE Nuclear*

Science Symposium and Medical Imaging Conference (NSS/MIC), 1995, 1543-1547.

[264] G. Poludniowski, P. M. Evans, and S. Webb, "Rayleigh scatter in kilovoltage x-ray imaging: is the independent atom approximation good enough?," *Phys Med Biol,* **54**, 6931-42, 2009.

[265] A. Tartari, A. Taibi, C. Bonifazz, and C. Baraldi, "Updating of form factor tabulations for coherent scattering of photons in tissues," *Phys Med Biol,* **47**, 163-75, 2002.

[266] M. Almajdub, M. Nejjari, G. Poncet, L. Magnier, E. Chereul, C. Roche, and M. Janier, "In-vivo high-resolution X-ray microtomography for liver and spleen tumor assessment in mice," *Contrast Media Mol Imaging,* **2**, 88-93, 2007.

[267] A. L. Goertzen, "Development of a combined microPET and microCT system for mouse imaging," University of California, Los Angeles, 2003.

[268] N. Hayasaka, N. Nagai, N. Kawao, A. Niwa, Y. Yoshioka, Y. Mori, H. Shigeta, N. Kashiwagi, M. Miyazawa, T. Satou, H. Higashino, O. Matsuo, and T. Murakami, "In Vivo Diagnostic Imaging Using Micro-CT: Sequential and Comparative Evaluation of Rodent Models for Hepatic/Brain Ischemia and Stroke," *PLoS ONE,* **7**, e32342, 2012.

[269] M. Kachelriess, K. Sourbelle, and W. A. Kalender, "Empirical cupping correction: a first-order raw data precorrection for cone-beam computed tomography," *Med Phys,* **33**, 1269-74, 2006.

[270] C. Badea, L. W. Hedlund, and G. A. Johnson, "Micro-CT with respiratory and cardiac gating," *Med Phys,* **31**, 3324-9, 2004.